CỘNG HOÀ XÃ HỘI CHỦ NGHĨA VIỆT NAM
Độc lập - Tự do - Hạnh phúc

HỒ SƠ ĐĂNG KÝ XÉT CÔNG NHẬN ĐẠT TIÊU CHUẨN CHỨC DANH: PHÓ GIÁO SƯ

Tập II

Họ và tên: **NGUYỄN BÁ THỦY**

Đối tượng: **GIẢNG VIÊN THỈNH GIẢNG**

Ngành: **KHOA HỌC TRÁI ĐẤT - MỎ**

Chuyên ngành: **HẢI DƯƠNG HỌC**

Quốc tịch: **VIỆT NAM**

Cơ quan công tác:

TRUNG TÂM DỰ BÁO KHÍ TƯỢNG THỦY VĂN QUỐC GIA

TỔNG CỤC KHÍ TƯỢNG THỦY VĂN

Điện thoại: **097 585 3471**

Đăng ký xét tại Hội đồng Chức danh giáo sư cơ sở:

VIỆN KHOA HỌC KHÍ TƯỢNG THỦY VĂN VÀ BIẾN ĐỔI KHÍ HẬU

Đăng ký xét tại Hội đồng Chức danh giáo sư ngành/liên ngành:

KHOA HỌC TRÁI ĐẤT - MỎ

Năm 2019

CỘNG HOÀ XÃ HỘI CHỦ NGHĨA VIỆT NAM
Độc lập - Tự do - Hạnh phúc

HỒ SƠ ĐĂNG KÝ XÉT CÔNG NHẬN ĐẠT TIÊU CHUẨN CHỨC DANH: PHÓ GIÁO SƯ

Tập II

Họ và tên: **NGUYỄN BÁ THỦY**

Đối tượng: **GIẢNG VIÊN THỈNH GIẢNG**

Ngành: **KHOA HỌC TRÁI ĐẤT - MỎ**

Chuyên ngành: **HẢI DƯƠNG HỌC**

Quốc tịch: **VIỆT NAM**

Cơ quan công tác:

TRUNG TÂM DỰ BÁO KHÍ TƯỢNG THỦY VĂN QUỐC GIA
TỔNG CỤC KHÍ TƯỢNG THỦY VĂN

Điện thoại: **097 585 3471**

Đăng ký xét tại Hội đồng Chức danh giáo sư cơ sở:

VIỆN KHOA HỌC KHÍ TƯỢNG THỦY VĂN VÀ BIẾN ĐỔI KHÍ HẬU

Đăng ký xét tại Hội đồng Chức danh giáo sư ngành/liên ngành:

KHOA HỌC TRÁI ĐẤT - MỎ

Năm 2019

MỤC LỤC

Trang

GIAI ĐOẠN TRƯỚC KHI BẢO VỆ LUẬN ÁN TIẾN SĨ (17/09/2010)

1.TẠP CHÍ QUỐC TẾ (6)

CONSENT LETTER

To whom it may concern

Journal title: Science of tsunami hazards, Journal of Tsunami Society International

Article title: Flow and potential force due to runup tsunami around a coastal forest with a gap – experiments and numerical simulations (2010). Science of tsunami hazards, Journal of Tsunami Society International, Vol. 29/2, pp. 43-69.

Authors: Nguyen Ba Thuy, Katsutoshi Tanimoto, Norio Tanaka

I am the supervisor of Dr. Nguyen Ba Thuy during doctor course in Saitama University, Japan from October 2007 to September 2010. I am also the corresponding author of this paper.

On behalf of all co-authors I would like to inform you that we are totally aware and agree that the content of this paper is one part on the doctor thesis of Dr. Nguyen Ba Thuy, and he is principal author for this paper.

On behalf of all co-authors

Norio Tanaka
Dr. Engineering, Prof.
Graduate School of Science and
Engineering, Saitama University
255 Shimo-okubo, Sakura-ku, Saitama
338-8570, Japan

ISSN 8755-6839

SCIENCE OF TSUNAMI HAZARDS

Journal of Tsunami Society International

Volume 29 **Number 2** **2010**

TSUNAMI SOCIETY INTERNATIONAL, 1741 Ala Moana Blvd. #70, Honolulu, HI 96815,USA.

WWW.TSUNAMISOCIETY.ORG

SCIENCE OF TSUNAMI HAZARDS is a CERTIFIED OPEN ACCESS Journal included in the prestigious international academic journal database DOAJ maintained by the University of Lund in Sweden with the support of the European Union. 'SCIENCE OF TSUNAMI HAZARDS is also preserved and archived at the National Library, The Hague, NETHERLANDS, at the Library of Congress, Washington D.C., USA, at the Electronic Library of Los Alamos, National Laboratory, New Mexico, USA and at the EBSCO Publishing databases, which give the journal additional global exposure and readership in 90% of the academic institutions worldwide, including nation-wide access to databases in more than 70 countries.

OBJECTIVE: Tsunami Society International publishes this journal to increase and disseminate knowledge about tsunamis and their hazards.

Submit manuscripts of articles, notes or letters to the Editor. If an article is accepted for publication the author(s) must submit a scan ready manuscript, a Doc, TeX or a PDF file in the journal format. Issues of the journal are published electronically in PDF format. Issues of the journal (ISSN 8755-6839) from 1982 thru 2005 are available in PDF format at http://epubs.lanl.gov/tsunami/and at **WWW.TSUNAMISOCIETY.ORG** or on a CD-ROM that may be purchased by contacting Tsunami Society International at tsunamisociety@hawaiiantel.net
Recent and all past journal issues are also available at: http://www.TsunamiSociety.org

Tsunami Society International members are notified by e-mail when a new issue is available. There are minimal page charges for authors who are members of Tsunami Society International for three years and slightly higher for non-members. Permission to use figures, tables and brief excerpts from this journal in scientific and educational works is hereby granted provided that the source is acknowledged.

ISSN 8755-6839

SCIENCE OF **TSUNAMI HAZARDS**

Journal of Tsunami Society International

Volume 29 **Number 2** **2010**

FLOW AND POTENTIAL FORCE DUE TO RUNUP TSUNAMI AROUND A COASTAL FOREST WITH A GAP – EXPERIMENTS AND NUMERICAL SIMULATIONS

Nguyen Ba Thuy [a], Katsutoshi Tanimoto [b], Norio Tanaka [c,*]

[a] Graduate School of Science and Engineering, Saitama University, 255 Shimo-okubo, Sakura-ku, Saitama, 338-8570, Japan.
[b] Emeritus Professor of Saitama University, 255 Shimo-okubo, Sakura-ku, Saitama 338-8570, Japan.
[c,*] Professor, Institute for Environmental Science and Technology, Saitama University, 255 Shimo-okubo, Sakura-ku, Saitama 338-8570, Japan.
Tel./Fax: +81-48-858-3564. E-mail address: tanaka01@mail.saitama-u.ac.jp

ABSTRACT

In the present study, laboratory experiments were conducted to validate the applicability of numerical model based on two-dimensional nonlinear long-wave equations including drag resistance of trees and turbulence induced shear forces to tsunami flow around a simplified forest with a gap in a wave channel. It was confirmed that the water surface elevation and flow velocity by the numerical simulations agree well with the experimental results for various forest conditions of width and tree density. Then the numerical model was applied to a prototype scale condition of a coastal forest of *Pandanus odoratissimus* with a gap to investigate the effects of forest conditions (width and tree density) and incident tsunami conditions (period and height) on a potential tsunami force. The potential tsunami force at the gap exit is greatly enhanced and the maximum in the spatial distribution around and inside the forest. The potential tsunami forces at four representative points at front and back of forest including the center of gap exit were analyzed for various conditions and formulated as function of forest and tsunami conditions in the non-dimensional form. The potential tsunami forces calculated by the curve-fit formula agree well with the simulated potential tsunami forces within ±10% error.

Key words: Runup tsunami, Coastal forest, Gap, *Pandanus odoratissimus*, Tsunami force

1. INTRODUCTION

Since the Indian Ocean tsunami in 2004, numerous studies have elucidated the effects of coastal vegetation in reducing tsunami forces and the damage to humans and property based on post-tsunami surveys (for example, Danielsen et al. 2005; Kathiresan and Rajendran, 2005; Tanaka et al., 2007). Currently, coastal forests are widely considered to be effective for mitigating tsunami damage from both economic and environmental points of view, although their role is still questioned due to the absence of adequate studies (Kerr and Baird, 2007). In fact, several projects to plant vegetation on coasts as a bioshield against tsunamis have been started in South and Southeast Asian countries (Tanaka et al., 2009; Tanaka, 2009).

The reduction in tsunami damage behind a coastal forest depends on the vegetation species and their dimensions (tree height, diameter, and density), scale and arrangement of the forest (along-shore length and cross-shore width), and tsunami conditions. In relation to forest arrangement, Mascarenhas and Jayakumar (2008) pointed out that roads perpendicular to the beach in a coastal forest served as a passages for a tsunami to travel inland in many places in Tamil Nadu-India on the occasion of the 2004 Indian Ocean tsunami. Fernando et al. (2008) reported that the destruction of coral by the tsunami was remarkable in some places in Hikkaduwa and Akuralla in Sri Lanka, and that the inundation depth behind the destroyed coral reefs was much larger than that behind unbroken coral reefs. Fernando et al. (2008) also conducted a laboratory experiment to verify the effect of an open gap in submerged porous barriers and found that the flow velocity at the gap exit was significantly higher than the case with no gap. Although the latter case was not a coastal forest, those indicate a negative effect of a gap in tsunami runup.

Tanaka et al. (2007) pointed out that *Pandanus odoratissimus*, which is dominant coastal vegetation in South and Southeast Asia, is especially effective in providing protection from tsunami damage due to its density and complex aerial root structure. To study the effect of a gap in a coastal forest of *P. odoratissimus*, Nandasena et al. (2008) performed a numerical simulation including resistance by the forest for limited conditions and found that a narrow gap has a significant effect on the exit flow, but an insignificant effect on the runup height. Thuy et al. (2009a) conducted experiments on a costal forest with a gap by using a simplified model in a 0.4-m-wide wave channel and validated that the numerical results, including the turbulence-induced shear force in addition to the forest resistance, agreed well with experimental results for both runup height and velocity at the gap exit. They also applied the numerical model to a coastal forest of *P. odoratissimus* with a gap and found that a 15-m-wide gap caused the highest velocity under their calculated conditions of a fixed condition of incident tsunami. Based on the discussions in experiment and prototype scale, they confirmed that the turbulence induced shear force gives a significant effect on the flow velocity at the gap exit. Furthermore, Thuy et al. (2009b) discussed the effects of forest and incident tsunami conditions on inundation depth and flow velocity at the gap exit and behind the vegetation patch based on the numerical results.

The tsunami forces are directly related with the damage of trees and other obstacles; however, tsunami forces were not discussed in previous studies using numerical simulations mentioned above. In the present paper, potential tsunami forces due to runup tsunami around a coastal forest of *P. odoratissimus* with a gap are studied by numerical simulations. The potential tsunami force is defined as the total drag force on a virtual high column with unit width and unit drag coefficient. The numerical model is based on two-dimensional nonlinear long-wave equations incorporating drag resistance of trees and the sub-depth scale (*SDS*) turbulence model by Nadaoka and Yagi (1998). Laboratory experiments on tsunami flow around a simplified forest model with various width and tree density are conducted in a wave channel to validate the applicability of numerical model. The numerical model is then applied to a prototype scale condition of coastal forest of *P. odoratissimus* with a gap to investigate the effects of forest conditions (width and tree density) and incident tsunami conditions (height and period) on the potential tsunami forces. The potential tsunami forces at four representative points at front and back of forest including the center of gap exit are analyzed and formulated in the non-dimensional form.

2. MATHEMATICAL MODEL AND NUMERICAL METHOD

2.1. Governing equations

The governing equations are two-dimensional nonlinear long-wave equations that include drag and eddy viscosity forces due to interaction with vegetation. The continuity and the momentum equations are respectively:

$$\frac{\partial \zeta}{\partial t} + \frac{\partial (dV_x)}{\partial x} + \frac{\partial (dV_y)}{\partial y} = 0 \tag{1}$$

$$\frac{\partial V_x}{\partial t} + V_x \frac{\partial V_x}{\partial x} + V_y \frac{\partial V_x}{\partial y} + g\frac{\partial \zeta}{\partial x} + \frac{\tau_{bx}}{\rho d} + \frac{F_x}{\rho d} - \frac{E_{Vx}}{d} = 0 \tag{2}$$

$$\frac{\partial V_y}{\partial t} + V_x \frac{\partial V_y}{\partial x} + V_y \frac{\partial V_y}{\partial y} + g\frac{\partial \zeta}{\partial y} + \frac{\tau_{by}}{\rho d} + \frac{F_y}{\rho d} - \frac{E_{Vy}}{d} = 0 \tag{3}$$

where,

$$\vec{\tau}_b = \frac{\rho g n^2}{d^{1/3}} \vec{V}\left|\vec{V}\right| \tag{4}$$

$$\vec{F} = \gamma \frac{1}{2} \rho C_{D-all} b_{ref} \vec{V}\left|\vec{V}\right| d \tag{5}$$

$$E_{vx} = 2\frac{\partial}{\partial x}\left(d\nu_e \frac{\partial V_x}{\partial x}\right) + \frac{\partial}{\partial y}\left(d\nu_e \frac{\partial V_x}{\partial y} + d\nu_e \frac{\partial V_y}{\partial x}\right) \tag{6}$$

$$E_{vy} = 2\frac{\partial}{\partial y}\left(d\nu_e \frac{\partial V_y}{\partial y}\right) + \frac{\partial}{\partial x}\left(d\nu_e \frac{\partial V_x}{\partial y} + d\nu_e \frac{\partial V_y}{\partial x}\right) \tag{7}$$

x and y are the horizontal coordinates; V_x and V_y are the depth-averaged velocity components in x and y directions respectively; t is the time; d the total water depth ($d=h+\zeta$); h the local still water depth (on land, the negative height of the ground surface); ζ the water surface elevation; g the gravitational acceleration; ρ the water density; n the Manning roughness coefficient; γ the tree density (number of trees/m^2). $C_{D\text{-}all}$ is the depth-averaged equivalent drag coefficient considering the vertical stand structure of the trees, which was defined by Tanaka et al. (2007) as:

$$C_{D-all}(d) = C_{D-ref}\frac{1}{d}\int_0^d \frac{b(z_G)}{b_{ref}}\frac{C_D(z_G)}{C_{Dref}})dz_G \tag{8}$$

where $b(z_G)$ and $C_D(z_G)$ are the projected width and drag coefficient of a tree at height z_G from the ground surface, and b_{ref} and $C_{D\text{-}ref}$ are the reference width of the trunk and the reference drag coefficient at breast height, respectively. The eddy viscosity v_e is given by the *SDS* turbulence model as described below.

2.2. Turbulence model

The *SDS* turbulence model of Nadaoka and Yagi (1998) was applied to evaluate the eddy viscosity with modifications related to the bottom friction and vegetation resistance.

$$\frac{\partial k_D}{\partial t} + V_x\frac{\partial k_D}{\partial x} + V_y\frac{\partial k_D}{\partial y} = \frac{1}{d}\frac{\partial}{\partial x}\left(d\frac{v_e}{\sigma_k}\frac{\partial k_D}{\partial x}\right) + \frac{1}{d}\frac{\partial}{\partial y}\left(d\frac{v_e}{\sigma_k}\frac{\partial k_D}{\partial y}\right) + p_{kh} + p_{kv} + p_{kd} - \varepsilon_D \tag{9}$$

$$p_{kh} = v_e\left[2\left(\frac{\partial V_x}{\partial x}\right)^2 + \left(\frac{\partial V_x}{\partial y} + \frac{\partial V_y}{\partial x}\right)^2 + 2\left(\frac{\partial V_y}{\partial y}\right)^2\right] \tag{10}$$

$$p_{kv} = \frac{gn^2}{d^{4/3}}(V_x^2 + V_y^2)^{1.5} \tag{11}$$

$$p_{kd} = \frac{\gamma b_{ref} C_{D-all}}{2}(V_x^2 + V_y^2)^{1.5} \tag{12}$$

$$v_e = c_w\frac{k_D^2}{\varepsilon_D} \tag{13}$$

$$\varepsilon_D = c_d \frac{k_D^{\ 1.5}}{l_D} \tag{14}$$

where k_D is the kinetic energy and $l_D = \lambda\, d$ is the length scale (λ : turbulence length scale coefficient). For the model parameters, standard values are adopted: c_w=0.09, c_d=0.17, σ_k=1.0 and λ=0.08.

2.3. Method of numerical simulations

A set of the above equations is solved by the finite-difference method of a staggered leap-frog scheme, which is widely used in numerical simulations of tsunami (for example, Liu et al., 1994; Titov and Synolakis, 1997; Imamura et al., 1998; Koh et al., 2009). An upwind scheme was used for nonlinear convective terms in order to maintain numerical stability. A semi-Crank–Nicholson scheme was used for the terms of bed friction, drag, and turbulence-induced shear force. On the offshore sides, a wave generation zone with a constant water depth in which the governing equations were reduced to linear long-wave equations was introduced to achieve non-reflective wave generation by using the method of characteristics. A sinusoidal incident tsunami was given as a time-dependent boundary condition at the most offshore side of the wave-generation zone. For a moving boundary treatment, a number of algorithms were necessary so that the flow occurring when the water surface elevation is high enough can flow to the neighboring dry cells. The initial conditions were given for a waveless state in the computational domain including the wave-generation zone.

3. EXPERIMENTS AND VALIDATION OF NUMERICAL MODEL

3.1. Experimental setup and conditions

The present experiments are follow-up from Thuy et al. (2009a) in which the effect of gap width on flow around a simplified forest model of vertical cylinders with a fixed width and tree density was investigated by a fixed condition of long waves in a wave channel with 0.4 m wide. It was found that a 0.07 m-wide gap causes the largest velocity at the gap exit under their conditions. In this study, the effects of forest conditions on the flow velocity and water surface elevation at the gap exit and behind the vegetation patch are mainly investigated.

Fig. 1 shows the experimental setup in the wave channel where the forest model was set in the water area for the convenience of velocity measurements. Trees were simply modeled by wooden cylinders with a diameter of 0.005 m mounted in a staggered arrangement as seen in Fig. 2. The gap width b_G was fixed as 0.07 m in the present experiments. The forest width B_F was changed in cases of 0.2, 0.5, 0.7 and 1.0 m with the fixed density of 2200 trees/m^2 (0.22 trees/cm^2). The end of forest was fixed at x=11.36 m (see Fig. 1), where the still water depth is 0.037 m. Three cases of tree density for the fixed forest width of 1.0 m were tested; lower density (γ=500 tree/m^2), moderate density (γ=1000 trees/m^2), and higher density (γ=2200 trees/m^2). In addition to those cases, experiments for cases of no forest (B_F=γ=0) and full vegetation (no gap) were also conducted. Wave condition was fixed as that the incident wave height H_i at still water depth of 0.44 m is 0.02 m and the wave period T is 20 s as same as the previous experiments (Thuy et al., 2009a).

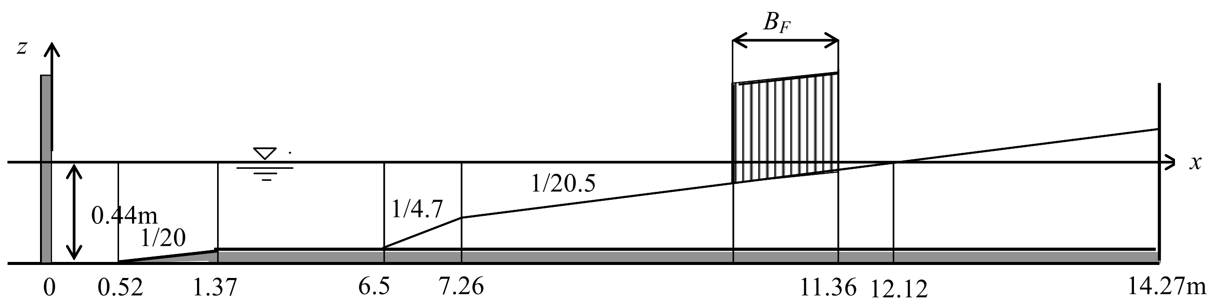

Fig. 1. Experimental setup in wave channel.

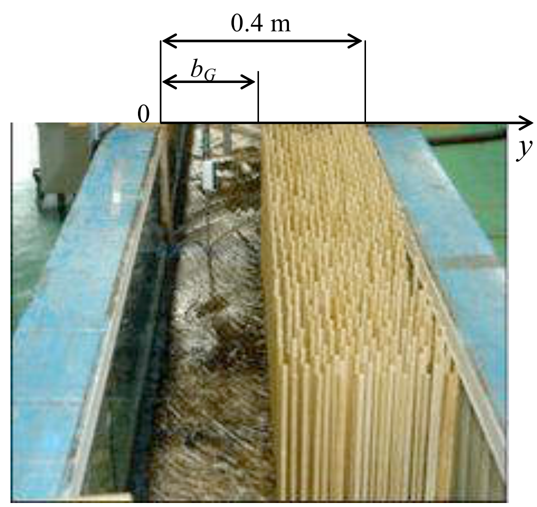

Fig. 2. Photo of forest model (example of b_G=0.15 m).

3.2. Conditions of numerical simulation for laboratory scale

For numerical simulations of the experimental conditions, the uniform grid size of 0.005 m and time step of 0.002 s were selected. The Manning roughness coefficient n was given as 0.012 s/m$^{1/3}$ for the relatively rough wooden bottom. For parameters in the turbulence model, standard values as indicated in *2.2.* were applied. The drag coefficient $C_{D\text{-}ref}$ depends on both the Reynolds number and relative spacing of vegetation (s/D), where s is the distance between cylinders and D is the diameter of cylinder. However, Chakrabati (1991) showed that the interaction between multiple cylinders becomes small when s/D is larger than 2, and the drag coefficient of multiple cylinders approaches to a single cylinder. In the present experimental conditions, the drag coefficient may be assumed as a single cylinder because the s/D is considerably greater than 2. The drag coefficient C_{Dref} was determined to be 1.5 after some trial calculations, which is consistent with the drag coefficient of a circular cylinder in the laboratory scale corresponding to the Reynolds number of 300.

The measurements of water surface elevation and horizontal velocity in the experiments were made in a steady state in multi-reflection system of wave channel between reflective wave paddle and coastal model with forest. Consequently, the incident wave height in the numerical simulations must be given with consideration of the effect of reflected waves. Fig. 3 shows examples of wave height measured at six locations in cases of no vegetation and full vegetation. In the figure, two distributions simulated with the incident wave height H_i of 0.02 m are plotted for the actual channel length and for the channel length extended by 21 m, which corresponds to a half of wavelength at the still water depth of 0.44 m. Both results coincide well as the difference is not observed in the figure, because of non-reflective wave generation in the numerical simulations. The simulated distributions also agree well with measured wave heights and the separated incident wave heights on the basis of small amplitude theory at the extended channel are about 0.02 m. Therefore, H_i =0.02 m can be considered as the incident wave height at the still water depth of 0.44 m in the multi-reflection system of wave channel in the present experimental conditions.

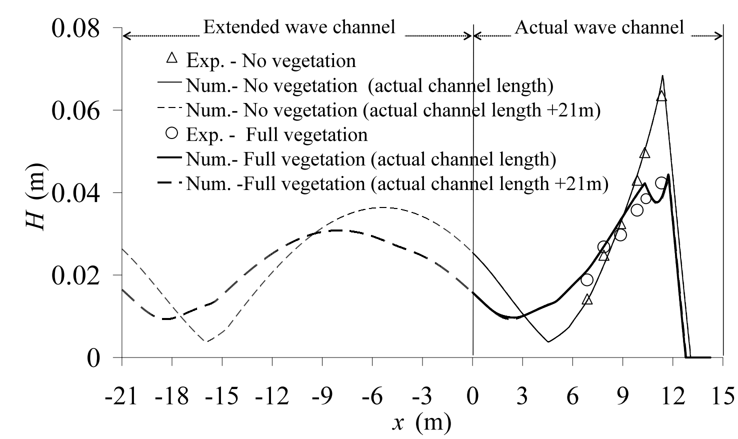

Fig. 3. Wave height distributions in wave channel.

Fig. 4 shows examples of time variation of velocity at the center of vegetation end (y=0.235 m) and the center of gap exit (y=0.035 m) at x=11.4 m during the analyzed time interval of measurements. It is confirmed that the flow velocity is almost steady and the simulated maximum value in particular agrees well with the measured maximum values as already shown in the previous study (Thuy et al., 2009a). The velocity is defined by the following equation because the tsunami flow dominated in the direction of the x-axis in the present study:

$$V = \mathrm{sign}(V_x)\left|\vec{V}\right| \qquad (15)$$

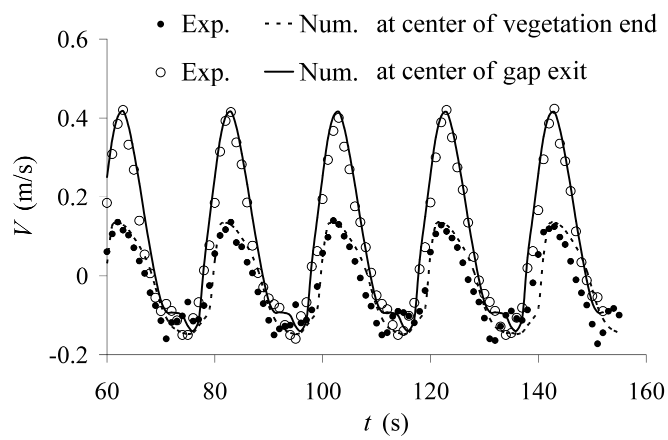

Fig. 4. Time variations of flow velocity (b_G=0.07 m).

3.3. Validation of numerical model with respect to forest conditions

Fig. 5 shows the distribution of maximum velocity in *y*-direction at the forest end (*x*=11.4m) for three cases of tree density. The change of velocity gradient around the edge of gap is remarkable, which suggests the importance of turbulence induced shear force at the gap as already discussed by Thuy et al. (2009a). It is also noted that the increase in tree density reduces the velocity behind the vegetation patch, whereas it increases in the velocity at the gap exit. Those are fairly well realized in the present numerical model simulations.

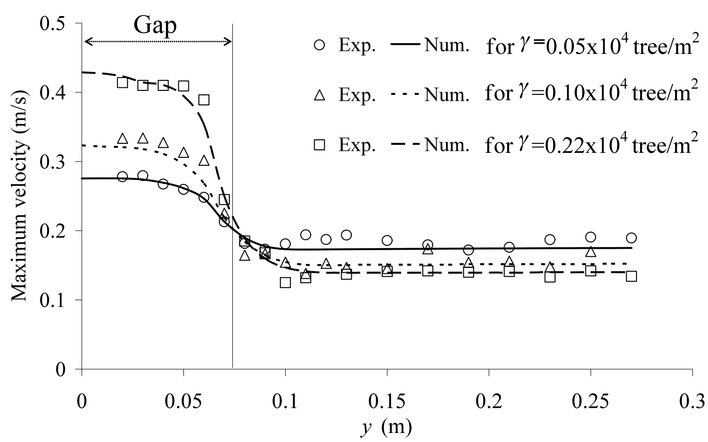

Fig. 5. Distribution of maximum velocity (*x*=11.4 m).

Fig. 6 shows the variation of the change of wave crest (ζ_{max}), maximum velocity at the gap exit ($V_{G\max}$) and maximum velocity at the center behind the vegetation patch ($V_{VP\max}$) against the forest width. The wave crest and velocity behind the vegetation patch decreases and the maximum velocity at the gap exit increases as forest width increases. The numerical results agree fairly well with the experimental results.

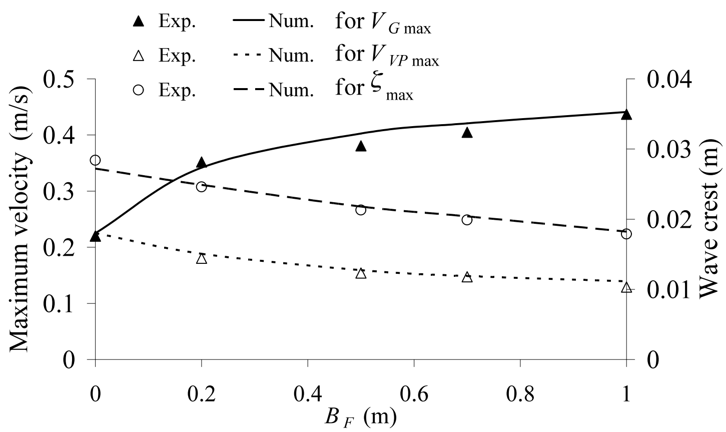

Fig. 6. Effect of forest width on maximum velocity and wave crest height.

4. EFFECT OF FOREST AND TSUNAMI CONDITIONS ON POTENTIAL TSUNAMI FORCES IN ACTUAL SCALE

4.1. Topography, forest and tsunami conditions, and definitions of potential tsunami force

4.1.1. Topography and forest conditions

A uniform coastal topography with the cross-shore section perpendicular (x-axis) to a straight shoreline, as shown in Fig.7 (a), was selected as a model case. The bed profile of the domain consists of four slopes, S=1/10, 1/100, 1/50, and 1/500. The offshore water depth at an additional wave-generation zone with a horizontal bottom is 100 m below the datum level of z=0. The tide level at the attack of the tsunami was considered to be 2 m, and therefore the still water level is 2 m above the datum level. The direction of the incident tsunami is perpendicular to the shoreline.

The coastal forest starts at the starting point of the 1/500 slope on the land (x=5700 m), where the ground is 4 m above the datum level (2 m above the tide level at the tsunami event). The forest was assumed to extend in the direction of the shoreline (y-axis) with the arrangement of a gap and vegetation patches with an along-shore unit length of L_F and a cross-shore width of B_F, as shown in Fig. 7(b). Both side boundaries, shown by dot-and-dash lines in the figure, are mirror image axes in which no cross flow exists. A gap with a width b_G is perpendicular to the shoreline and located at the center of the along-shore forest length. In the present study, the forest length L_F and gap width b_G were fixed as 200 m and 15 m respectively. The forest width B_F was changed from 0 m (no forest) to

200 m for selected cases, and the forest width of 1000 m was additionally considered in order to investigate an extreme condition. According to Thuy et al. (2009a), the forest (L_F=200 m) is long enough to avoid the effect of a gap around the mirror image boundary, so that tsunami flow becomes one-dimensional there as in the case of coastal forest without a gap. In the numerical simulations, the uniform grid size of 2.5 m was applied. In Fig. 7(b), representative checkpoints of simulated results are shown as A (x=5700+B_F+1.25 m, y=100 m), B (x=5700+B_F+1.25 m, y=156.25 m), C (x=5701.25 m, y=108.75 m) and D (x=5701.25 m, y=156.25 m). The Manning roughness coefficient n was set as 0.025 s/m$^{1/3}$ for a relatively rough bare ground, which is widely used in numerical simulations of tsunami runup (for example, Harada and Imamura, 2005).

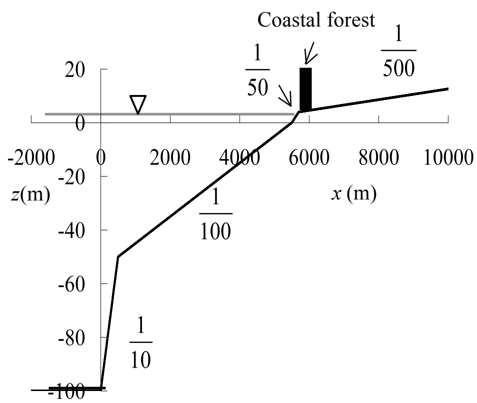

(a)

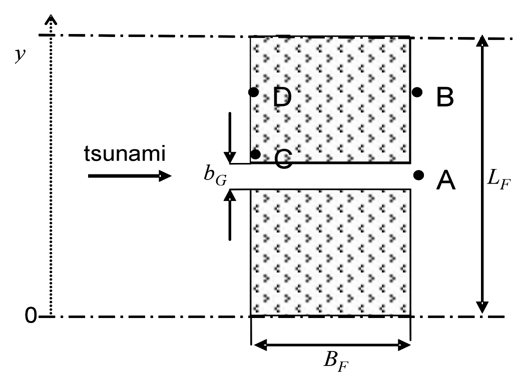

(b)

Fig. 7. Schematic topography. (a) Cross section, (b) sketch of forest and gap arrangement.

In the present study, a coastal forest consisting of *P. odoratissimus* was considered. As shown in Fig. 8(a), *P. odoratissimus* has a complex aerial root structure that provides additional stiffness and increases the drag coefficient. Fig. 8(b) shows the $b(z_G)/b_{ref}$, $C_D(z_G)/C_{Dref}$, and $C_{D\text{-}all}$ of *P. odoratissimus* based on Tanaka et al. (2007) for the conditions of the tree height H_{Tree}=8 m (for a mature tree), the reference diameter b_{ref}=0.195 m. The reference drag coefficient $C_{D\text{-}ref}$ of 1.0 was adopted for a trunk with a circular section and a rough surface in the region of high Reynolds number. The value of $C_{D\text{-}all}$ varied with the total depth d (inundation depth) because the projected width b and the drag coefficient C_D vary with the height from the ground surface z_G as shown in the figure. The tree density γ was changed from 0 (no forest) to 0.4 trees/m^2 in numerical simulations.

(a)

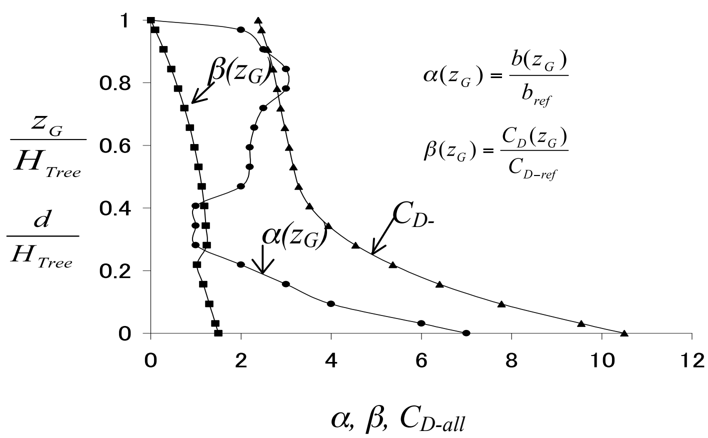

(b)

Fig. 8. Characteristics of *P. odoratissimus*. (a) Photographs of a stand, and (b) vertical distribution of α, β , and $C_{D\text{-}all}$.

4.1.2. Tsunami conditions

As already described, the tsunami attack on the coast is perpendicular to the shoreline at a tide level of 2 m. An incident tsunami at the offshore boundary is a sinusoidal wave starting positive with period T and height H_i from 600 to 3600 s and from 2 to 8 m, respectively. In the present paper, the runup of only the first wave was analyzed because it has the largest runup height among continuous waves.

The incident tsunami height (H_i) at the offshore boundary is rather arbitrary because the offshore boundary may be set at an arbitrary depth. Therefore, the tsunami height (H_{sl0}) above the ground surface at the shoreline was used instead of H_i and called the 'incident tsunami height' for the simplicity in the present paper. The range of H_{sl0} is from 3.08 to 8.51 m corresponding to H_i=2 to 8 m with T=1200 s. Note that the suffix 0 in the present paper indicates the absence of a coastal forest.

Fig. 9 shows the spatial distributions of water surface elevation ζ, mean velocity V and $\sqrt{gd}$ of the first runup wave of T=1200 s and H_i=6 m without forest at the time when the water surface elevation at the shoreline is the maximum as H_{sl0}=6.94 m. It is apparent that the runup tsunami is no more like a sinusoidal wave but a bore-like wave and the front is a super-critical flow.

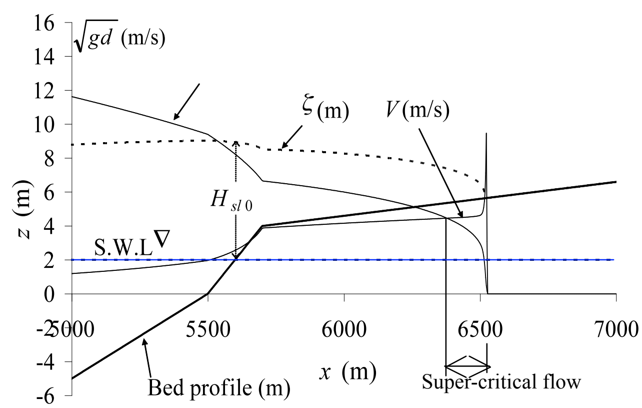

Fig. 9. Spatial distribution of runup tsunami (T=1200 s, H_i=6 m) in the case of no forest at the time when the water surface elevation at the shoreline is the maximum.

4.1.3. Summary of combined conditions of forest and tsunami

Table 1 summarizes combined condition of forest and tsunami in the numerical simulations.

Table 1. Summary of all simulation cases for combined conditions of forest and tsunami.

Series	B_F (m)	γ (trees/m^2)	H_{sl0} (m)	T (s)
		Change of forest conditions		
1	0–200, 1000	0.226	6.94	1200
2	100	0–0.4	6.94	1200
		Change of tsunami conditions		
3	100	0.226	3.08–8.51	1200
4	100	0.226	6.94	600–3600
		Change of tree density and tsunami conditions		
5	100	0.05	4.21–7.73	1200
6	100	0.05	6.94	600–3600
7	100	0.1	4.21–7.73	1200
8	100	0.1	6.94	600–3600
		Change of forest width and tsunami conditions		
9	20	0.226	4.21–7.73	1200
10	20	0.226	6.94	600–3600
11	50	0.226	4.21–7.73	1200
12	50	0.226	6.94	600–3600

4.1.4. Definition of a potential tsunami force and the time variation

The tsunami force vector ($\vec{F}^*$) in the present paper is defined by the following equation:

$$\vec{F}^* = \frac{1}{2}\rho d\vec{V}\left|\vec{V}\right| \tag{16}$$

This is a potential tsunami force integrated over the inundation depth and corresponds to the total drag force due to the tsunami acting on a virtual tall column of unit width and a unit drag coefficient. For an example, the integrated drag force vector ($\vec{F}_{Tree}$) on a single tree with a height of H_{Tree} can be calculated by the following relationship:

$$\begin{aligned} \vec{F}_{Tree} &= C_{D-all} b_{ref} \vec{F}^*, \qquad H_{Tree} \geq d \\ &= C_{D-all} b_{ref} \frac{H_{Tree}}{d} \vec{F}^*, \quad H_{Tree} < d \end{aligned} \tag{17}$$

Similarly, the total drag force on a human body as an application may be calculated with appropriate $C_{D\text{-}all}$ and b_{ref} specified to the human body.

Fig. 10 shows the time variations of inundation depth d, mean velocity V, tsunami force F^* for the condition of B_F=100 m, γ=0.226 trees/m^2, H_{sl0}=6.94 m and T=1200 s at the representative checkpoint C. As observed in the figure, the temporal maxima appear at different times. In particular, the maximum of V appeared early in the tsunami arrival when the inundation depth is low, and consequently, the tsunami force was not maximal. Therefore, the representative inundation depth and velocity are defined as values at the time of the temporal maxima of tsunami force ($F^*_{\max}$; hereafter, simply called 'tsunami force'). They are denoted as $d_{F^*\max}$, $V_{F^*\max}$.

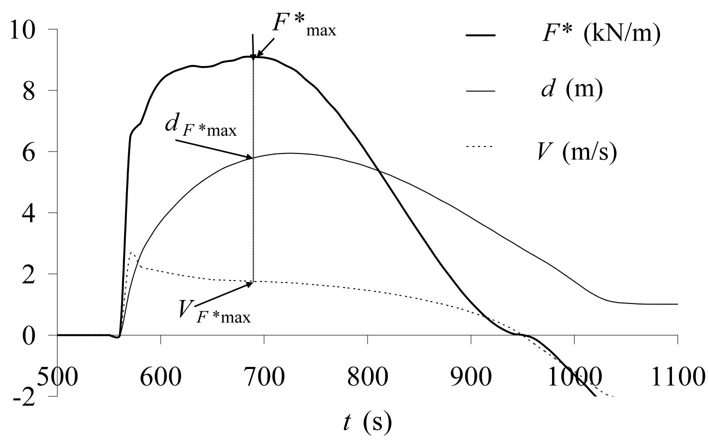

Fig. 10. Time profiles of inundation depth (d), mean velocity (V) and tsunami force (F^*) at C.

4.2. Results and discussions

4.2.1. Overview of tsunami runup around forest

In this section, the tsunami runup around a forest with a width of 100 m and a density of 0.226 trees/m^2 is summarized as an example for the incident tsunami conditions of T=1200 s and H_{sl0}=6.94 m. Fig. 11(a) and (b) show the x-y distributions of the maximum inundation depth $d_{\max}$ and the representative inundation depth $d_{F^*\max}$, respectively. The distribution of the maximum inundation depth decreases monotonously from about 6 m at the front of the forest to about 3.5 m at the back of the forest. The distribution of the representative inundation depths for the maximum tsunami force is different from that of the maximum inundation depth. In particular, the representative inundation depth in front of the forest is small as 2–3 m. This is because the maximum tsunami force occurred early in the tsunami's arrival and the velocity at the time of the maximum inundation depth was reduced by reflected waves from the forest.

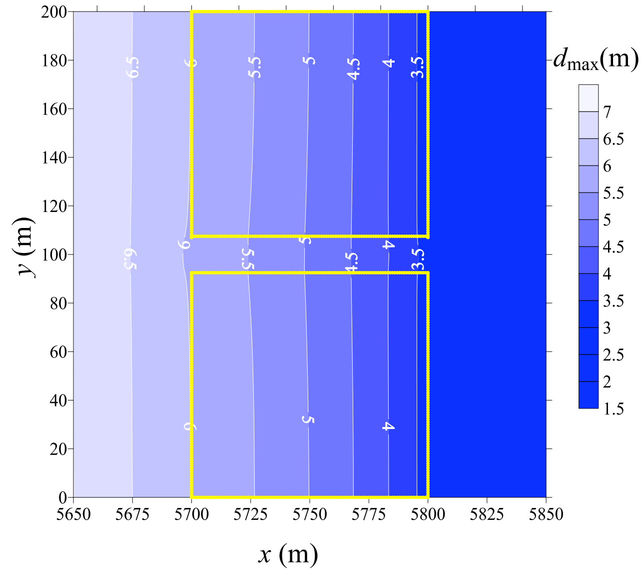

(a

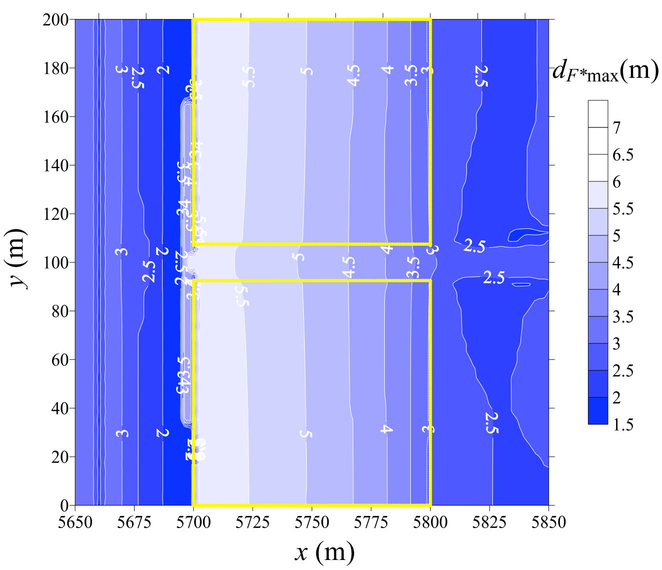

(b)

Fig. 11. Distributions of (a) maximum inundation depth (d_{max}), and (b) representative inundation depth (d_{F^*max}).

Fig. 12 (a) and (b) show the distributions of the maximum and representative velocity, respectively. As already pointed out by Thuy et al. (2009a), the velocity increased in the gap and became large around the gap exit. The spatial maximum appears behind the gap exit and exceeds 7.5 m/s in the temporal maximum velocity and 7.0 m/s in the representative velocity for the maximum tsunami force. Fig. 13

shows the distributions of the maximum tsunami force. The spatial maximum tsunami force appears at the gap exit (checkpoint A) and exceeds 75 kN/m.

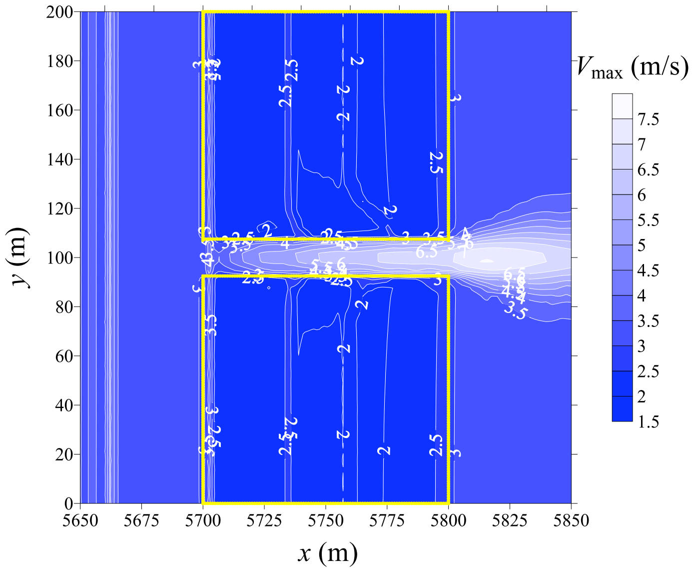

(a)

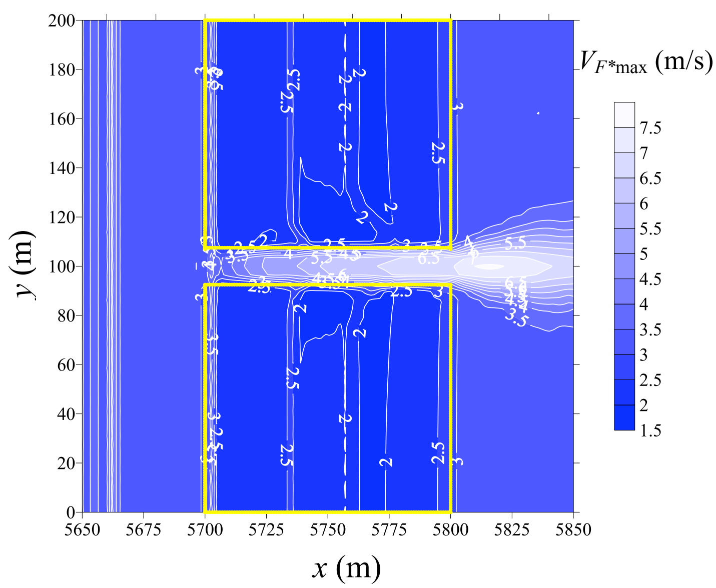

(b)

Fig. 12. Distribution of (a) maximum velocity (V_{max}), and (b) representative velocity (V_{F*max}).

Figs. 11-13 show that the contour line tends to become straight and parallel to the y-axis as the distance from the gap increases. This implies that the tsunami runup near the side boundaries is one-dimensional like the case with no gap. In the present paper, the representative checkpoints D and B were selected as corresponding to the case with no gap, although only a slight difference was apparent.

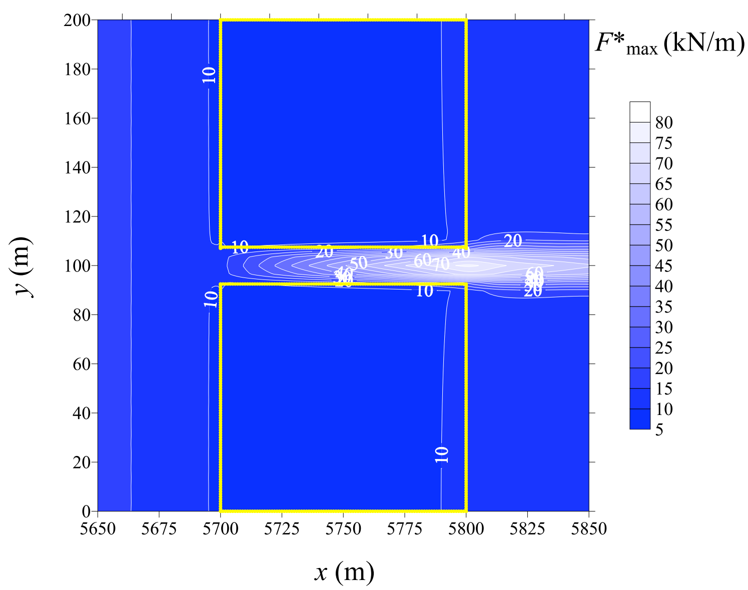

Fig. 13. Distribution of maximum tsunami force (F^*_{max}).

4.2.2. Effect of forest conditions

The tsunami force obtained by the incident tsunami condition of T=1200 s and H_{sl0}=6.94 m for different forest conditions were plotted in Fig. 14(a) and (b) against the following forest thickness B_{dNall}:

$$
\begin{aligned}
B_{dNall} &= \gamma\left(1 \times B_F\right) b_{ref} C_{D-all} \\
&= \gamma B_F b^*_{ref} C_{D-all}
\end{aligned}
\qquad (18)
$$

where, b_{ref} is the reference width per tree and b^*_{ref} is a logical reference width so that B_{dNall} has a unit of meters in the simple form (Note that b^*_{ref} has the same value as b_{ref} , but the unit is m^2/tree). The original form of forest thickness was proposed by Shuto (1987) for the combined effect of forest width and tree density. Tanaka et al. (2009) improved it to include resistance characteristic (C_{D-all}) due to the tree species as the upper expression in the right hand side of Eq.(18). In the present paper, the lower expression is used to make brief.

The forest width was changed with fixed tree density of 0.226 trees/m^2 and the tree density was changed with fixed forest width of 100 m. Tsunami forces F^*_{maxB}, F^*_{maxC} and F^*_{maxD} at points B, C and D decrease as the forest width and tree density increase due to mainly decrement of velocity with increase of forest resistance. On the other hand, the tsunami force F^*_{maxA} at point A is enhanced greatly but behaves in different ways by the forest width or tree density. This difference could be understood by the fact that the tsunami force with the increase of tree density increases to an extreme value corresponding to a rigid forest with the infinite density at the fixed point, while the tsunami force with the increase of forest width increases at first and then decreases to 0 finally because of the moving point. The enhancement of tsunami force at point A with the increase of density and width is due to the increase of velocity at the gap exit in spite of decrease of inundation depth as explained as the followings.

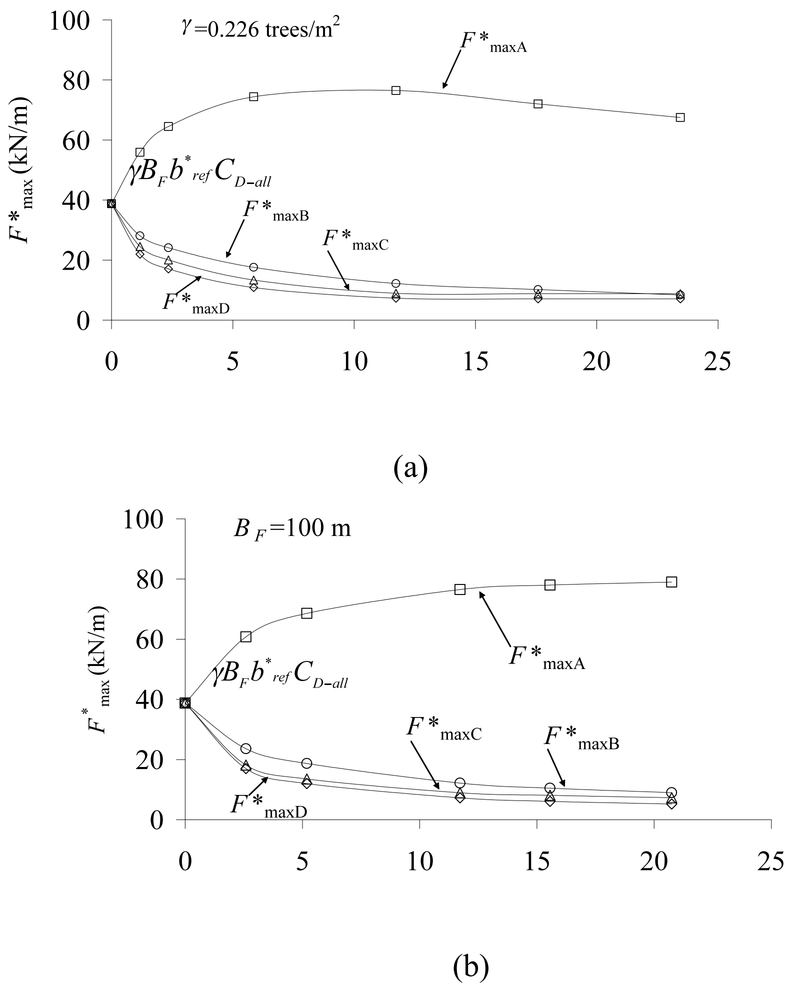

Fig. 14. Variation of tsunami force at A, B, C and D with (a) forest width (Series 1), (b) tree density (Series 2).

Fig. 15 (a) and (b) shows the variations of the representative velocity ($V_{F*\max}$) and total depth ($d_{F*\max}$) at the time of maximum tsunami force together with variations of average maximum discharge fluxes ($\overline{Q}_{in\max}$, $\overline{Q}_{out\max}$, and $\overline{Q}_{side\max}$) against the forest width and the tree density, respectively, where $Q_{in\max}$ and $Q_{out\max}$ are the maximum inflow and outflow at the gap inlet and exit, and $Q_{side\max}$ is the total inflow from both sides to the gap. The over-bar indicates the average discharge flux divided by the gap width. As the width and density increase, the inflow at the gap inlet decreases because of the increase of resistance of forest (in other word, the increase of reflection). In contrast, the outflow at the gap exit is increased slightly at first and does not decrease so much due to the increasing inflow from sides. On the other hand, the inundation depth behind the forest decreases due to the increase of forest resistance. Consequently, the representative velocity at the gap exit increases to result in the increase of tsunami force there. For the change of forest width, however, the point A moves as the forest width increases, while it is fixed in the change of density. Therefore the tsunami force decreases as the forest width becomes considerably wide and reduces to 0 as the forest width reaches to about 1000 m in the present condition.

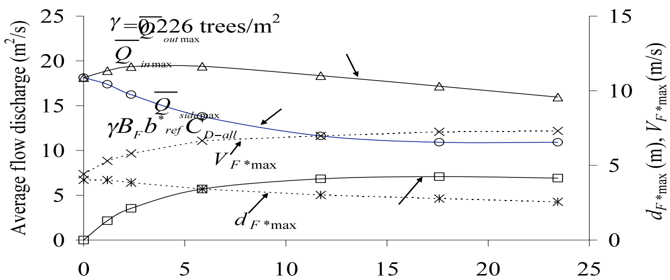

(a)

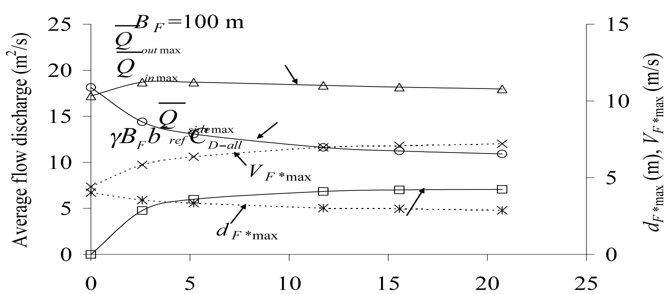

(b)

Fig. 15. Variation of representative water depth, representative velocity and maximum average discharge fluxes against (a) forest width (Series 1), (b) tree density (Series 2).

4.2.3. Effects of incident tsunami conditions

Fig. 16 (a) and (b) shows tsunami forces at four check points and the tsunami force $F^*_{\max 0}$ in the case of no forest against the incident tsunami height and period. The conditions are B_F=100 m, γ=0.226 trees/m^2, T=1200 s (for the change of tsunami height) and H_{sl0}=6.94 m (for the change of tsunami period). The tsunami force in the case with no forest was taken at D, but it is almost the same with the tsunami force at B in the present forest condition. The tsunami force increases as the incident tsunami height increases. The relationship between the tsunami force and incident tsunami height can be expressed in the form of the following equation:

$$F^*_{\max} = a_{Hf}\left(H_{sl0} - H_{cf}\right)^{b_{Hf}}, \quad H_{sl0} \geq H_{cf} \qquad (19)$$

where H_{cf} is the threshold incident tsunami height at which the tsunami force becomes 0 and a_{Hf} has a dimension. In the present study, b_{Hf} was fixed as 2, because it may be reasonable to assume that tsunami force is proportional to the second power of the inundation depth and that the inundation depth is proportional to (H_{sl0}-H_{cf}). H_{cf} was also fixed as 2.5 m in the present study after considering the effect on the result and simplicity although, strictly speaking, it is a function of forest condition and tsunami period. The empirical constant of a_{Hf} is given in Fig.16 (a).

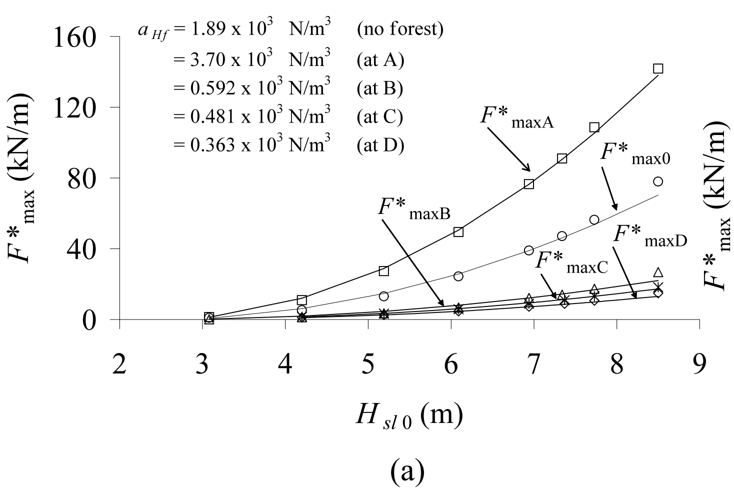

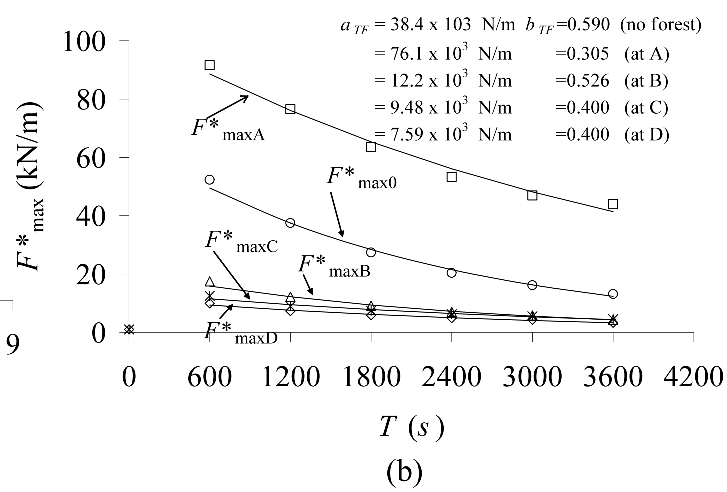

Fig. 16. Tsunami forces against (a) incident tsunami height (Series 3), and (b) tsunami period (Series 4).

On the other hand, the tsunami force decreases as the tsunami period increases in case of the fixed incident tsunami height. The relationship of the tsunami force and the tsunami period can be expressed in the form of the following equation:

$$F^{*}_{\max} = a_{Tf} \exp\left\{ - b_{Tf} \left(\frac{T}{T_{rep}} - 1 \right) \right\} \tag{20}$$

where T_{rep} is the representative tsunami period and was taken as 1200 s in the present study, and a_{Tf} has a dimension. The determined empirical constants of a_{Tf} and b_{Tf} are given in Fig.16 (b). Both curve-fit relations against the incident tsunami height and period agree well with numerical results.

4.2.4. Non-dimensional tsunami forces for all simulation results

In the present paper, the following non-dimensional forest thickness combining forest and tsunami conditions is considered:

$$\frac{B_{dNall}}{T_{rep}\sqrt{gH_{rep}}} = \frac{\gamma B_F b^{*}_{ref} C_{D-all}\left(H_{rep}\right)}{T_{rep}\sqrt{gH_{rep}}} \tag{21}$$

where $T_{rep}\sqrt{gH_{rep}}$ corresponds to a wavelength of long waves with period of T_{rep} at the depth of H_{rep}. It should be noted, however, that the non-dimensional forest thickness represents the forest condition only, since the tsunami condition is fixed to the representative tsunami condition in Eq.(21). The representative tsunami height H_{rep} is arbitrary as well as the representative tsunami period T_{rep} and was taken as 7 m in the present study.

On the other hand, the tsunami force $F^{*}_{\max}$ is made dimensionless by the following relationship in consideration of the curve-fit equations in 4.2.3 as:

$$\begin{aligned} \frac{F^{*}_{\max}}{\rho g H_{sl0}^{2}} &= \frac{a_f \left(H_{sl0} - H_{cf}\right)^{b_{Hf}} \exp\left\{- b_{Tf}\left(T / T_{rep} - 1\right)\right\}}{\rho g H_{sl0}^{2}} \frac{F^{*}_{\max rep}}{a_f \left(H_{rep} - H_{cf}\right)^{b_{Hf}}} \\ &= \alpha_f f_{Hf} f_{Tf} \end{aligned} \tag{22}$$

where $\rho g H_{sl0}^{2}$ (unit: N/m) corresponds to double the hydrostatic force acting on a virtual high wall per unit length by inundation depth of H_{sl0}, and $F^{*}_{\max rep}$ is the representative tsunami force by incident tsunami with the representative height H_{rep} and arbitrary period T. α_f, f_{Hf} and f_{Tf} are non-dimensional and expressed as follows:

$$\alpha_f = \frac{F^{*}_{\max rep}}{\rho g H_{rep}^{2}} = \frac{F^{*}_{\max}}{f_{Hf} f_{Tf} \rho g H_{sl0}^{2}} \tag{23}$$

$$f_{Hf} = \left(\frac{1 - H_{cf} / H_{sl0}}{1 - H_{cf} / H_{rep}} \right)^{b_{Hf}} = 2.42 \left(1 - \frac{2.5}{H_{sl0}} \right)^2 \tag{24}$$

$$f_{Tf} = \exp\left\{ -b_{Tf} \left(\frac{T}{T_{rep}} - 1 \right) \right\} \tag{25}$$

The empirical constant of b_{Tf} at A, B, C and D was determined based on the numerical results as:

$$\left. \begin{aligned} b_{Tf} &= 0.307 + 0.279 \exp\left(-3.13 \times 10^3 \frac{\gamma B_F b^*{}_{ref} C_{D-all}(H_{rep})}{T_{rep}\sqrt{gH_{rep}}} \right), && \text{at A} \\ &= 0.526, && \text{at B} \\ &= 0.400, && \text{at C and D} \end{aligned} \right\} \tag{26}$$

The empirical constant b_{Tf} at A is given as function of forest condition (B_F and γ), because the relation of tsunami force and forest condition is complex as shown in Fig.14 (a) and (b). The meaning of modification factors will be explained later.

All simulated results of non-dimensional value of α_f in Eq. (22) are plotted against the non-dimensional forest thickness of Eq. (21) in Fig. 17 (a) and (b). As being apprehensible by Eq. (23), f_{Hf} and f_{Tf} are modification factors so that the non-dimensional tsunami force is normalized to the non-dimensional tsunami force due to the incident tsunami with the representative height of H_{rep}. The α_f is called the normalized tsunami force. Due to the changes in tsunami conditions, many data were plotted at the same point on the abscissa, and some data are superimposed.

In Fig. 17(a) and (b), relationships calculated by the following curve-fit equations are shown:

$$\left. \begin{aligned} \alpha_f &= 0.164 - 0.0824 \exp\left(-4.09 \times 10^3 \frac{\gamma B_F b^*{}_{rep} C_{D-all}(H_{rep})}{T_{rep}\sqrt{gH_{rep}}} \right), && \text{at A} \\ &= 0.0794 \exp\left(-0.0311 \times 10^3 \left[\frac{\gamma B_F b^*{}_{ref} C_{D-all}(H_{rep})}{T_{rep}\sqrt{gH_{rep}}} \right]^{0.492} \right), && \text{at B} \\ &= 0.0186 + 0.0633 \exp\left(-4.22 \times 10^3 \frac{\gamma B_F b^*{}_{ref} C_{D-all}(H_{rep})}{T_{rep}\sqrt{gH_{rep}}} \right), && \text{at C} \\ &= 0.0139 + 0.0678 \exp\left(-4.05 \times 10^3 \frac{\gamma B_F b^*{}_{ref} C_{D-all}(H_{rep})}{T\sqrt{gH_{rep}}} \right), && \text{at D} \end{aligned} \right\} \tag{27}$$

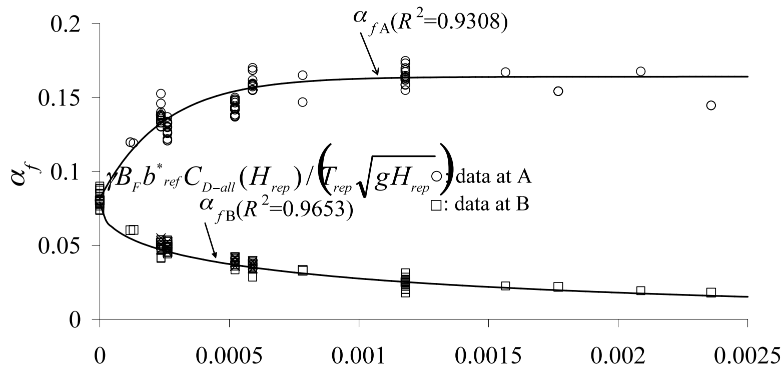

(a)

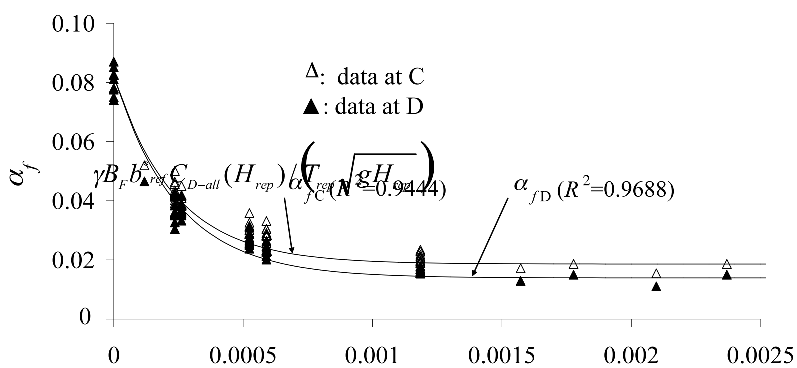

(b)

Fig. 17. Normalized tsunami force against non-dimensional forest thickness, (a) at A and B, (b) at C and D (Series 1-12).

In the figure, the relationships are indicated with the subscript A, B, C and D. Those curve-fit equations represent the average relationship of the non-dimensional tsunami force against non-dimensional forest thickness fairly well although the data are considerably scattered due to variety of conditions.

Fig. 18 shows the correlation of tsunami force at A, B, C and D estimated from the normalized tsunami force by Eq. (27) and tsunami force obtained by a numerical simulation with the absolute values. The agreement is fairly good. In the figure, the relations for y=1.1x and y=0.9x are also shown.

The error was within 10%. Eq. (27) can be applied to calculate tsunami force at A, B, C and D respectively if all information of forest and tsunami conditions are available. Note, however, that α_f at A is effective for the condition of B_F<200 m.

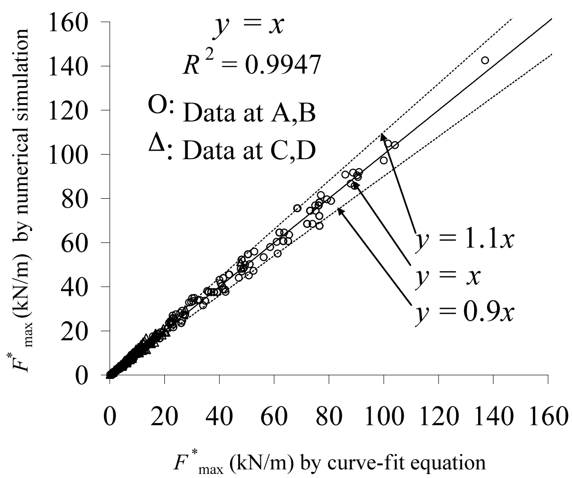

Fig. 18. Correlation of tsunami force by numerical simulations and by curve-fit equation at A, B, C and D (Series 1-12).

5. SUMMARY AND CONCLUSIONS

The summary and conclusions of the present study are as follows:

1. Laboratory experiments were carried out to validate the applicability of numerical model based on two-dimensional nonlinear long-wave equations including drag resistance of trees and turbulence induced shear forces to flow around a simplified forest model with a gap. It was confirmed that the water surface elevation and flow velocity by the numerical simulations agree well with the experimental results for various forest conditions of width and tree density.

2. The numerical model was applied to a prototype scale condition of a coastal forest of *Pandanus odoratissimus* with a gap to investigate the effects of forest conditions (width B_F and tree density γ) and incident tsunami conditions (period T and height at shoreline H_{sl0}) on a potential tsunami force which is defined as the total drag force on a virtual high column with unit width and unit drag coefficient. The potential tsunami force at the gap exit is greatly enhanced due to mainly the inflow to the gap through sides of vegetation patch and the maximum in the spatial distribution around and inside the forest, which reaches to twice of the potential tsunami force in the case of no forest in unfavorable conditions.

3. The potential tsunami forces at four representative points at front and back of forest including the center of gap exit were analyzed for various conditions and formulated as function of forest and tsunami conditions in the non-dimensional form. The potential tsunami forces at the gap exit increases as the increase of forest resistance due to the increase of forest width (B_F<100 m) and tree density, as the incident tsunami height increases and as the tsunami period decreases. The potential tsunami force at other points behind the vegetation patch and the front of forest decreases as the forest resistance increases. The potential tsunami forces calculated by the curve-fit formula in the non-dimensional form agree well with the simulated potential tsunami forces within ±10% error (B_F<200 m).

In the present paper, mature *P. odoratissimus* trees distributed uniformly in a forest were considered. However, tree conditions are not uniform in the actual forest and differ in the growth stage. To investigate the effects of non-uniform distribution of the various growth stages on tsunami forces is an exciting subject to be studied. Further, including the breaking of trees in numerical simulations is another subject of future study, as well as verification of the method of numerical simulations including tree breaking by field data.

ACKNOWLEDGEMENTS

This work was supported in part by JSPS AA Science Platform Program. The first author would like to acknowledge the financial support of the Government of Vietnam for his postgraduate study at Saitama University.

REFERENCES

Chakrabati, SK., 1991. Wave force on offshore structures. In: J.B. Herbich, Editor, Handbook of Coastal and Ocean engineering, Vol. 2 (1991), pp. 1-54.

Danielsen, F., Sorensen, M.K., Olwig, M.F., Selvam, V., Parish, F., Burgess, N.D., Hiraishi, T., Karunagaran, V.M., Rasmussen, M.S., Hansen, L.B., Quarto, A., Suryadiputra, N., 2005. The Asian tsunami: A protective role for coastal vegetation. Science 310, 643.

Fernando, H.J.S., Samarawickrama, S.P., Balasubramanian, S., Hettiarachchi, S.S.L., Voropayev, S., 2008. Effects of porous barriers such as coral reefs on coastal wave propagation. Journal of Hydro-environment Research 1, 187-194.

Harada, K., Imamura, F., 2005. Effects of coastal forest on tsunami hazard mitigation – A preliminary investigation, Tsunamis: Case studies and Resent Development, ed. K. Satake (Advances in natural and Technological Hazards Research, Springer) pp. 279-292.

Imamura, F., Shuto, N., Goto, C., 1998. Numerical simulation of the transoceanic propagation of tsunami. Proceedings of paper presented at the Sixth Congress of the Asian and Pacific Regional Division, Int. Assoc. Hydraul. Res., Kyoto, Japan.

Kathiresan, K., Rajendran, N., 2005. Coastal mangrove forests mitigated tsunami. Estuarine, Coastal and Shelf Science 65, 601-606.

Kerr, A.M., Baird, H.B., 2007. Natural barriers to natural disasters. BioScience. 57(2), 102-103.

Koh, H.L., Tek, S.Y., Liu, P.L., Ismail, A.I., Lee, H.L., 2008. Simulation of Andaman 2004 tsunami for assessing impact on Malaysia. Journal of Asian Earth Sciences 36, 74-83.

Liu, P.L., Cho, Y.S., Yoon, S.B., Seo S.N., 1994. Numerical simulations of the 1960 Chilean tsunami propagation and inundation at Hilo, Hawaii. In: M.I. El-Sabh, Editor, Recent Development in Tsunami Research, Kluwer Academic Publishers (1994), pp. 99–115.

Mascarenhas, A., Jayakumar, S., 2008. An environmental perspective of the post-tsunami scenario along the coast of Tamil Nadu, India: Role of sand dunes and forests. Journal of Environmental Management 89, 24-34.

Nadaoka, K., Yagi, H., 1998. Shallow-water turbulence modeling and horizontal larger eddy computation of river flow. Journal of Hydraulic Engineering 124(5), 493-500.

Nandasena, N. A. K., Tanaka, N., Tanimoto, K., 2008. Perspective of coastal vegetation patches with topography variations for tsunami protection in 2D-numerical modeling. Annual Journal of Hydraulic Engineering, JSCE 52, 133-38.

Shuto N., 1987. The effectiveness and limit of tsunami control forests. Coastal Engineering in Japan. 30(1), 143-153.

Tanaka, N., Sasaki, Y., Mowjood, M.I.M., Jinadasa, K.B.S.N., 2007. Coastal vegetation structures and their functions in tsunami protection: Experience of the recent Indian Ocean tsunami. Landscape and Ecological Engineering 3, 33-45.

Tanaka, N., 2009. Vegetation bioshields for tsunami mitigation: review of the effectiveness, limitations, construction, and sustainable management. Landscape and Ecological Engineering 5, 71-79.

Tanaka, N., Nandasena, N. A. K., Jinadasa, K. S. B. N., Sasaki, Y., Tanimoto, K. Mowjood, M. I. M., 2009. Developing effective vegetation bioshield for tsunami protection. Journal of Civil and Environmental Engineering Systems 26, 163-180.

Thuy, N.B., Tanimoto, K., Tanaka, N., Harada K., Iimura, K., 2009a. Effect of open gap in coastal forest on tsunami run-up – Investigations by experiment and numerical simulation. Ocean Engineering 36, 1258-1269.

Thuy, N.B., Tanaka, N., Tanimoto, K., Harada K., Iimura, K., 2009b. Tsunami flow behind the coastal forest with an open gap-effects of tsunami and tree condition. Proceedings of the 6th International Conference on Coastal Dynamic, Tokyo-Japan (CD-Rom). DOI No: 10.1142/9789814282475_0050

Titov, V.V., Synolakis, C.E., 1997. Extreme inundation flows during the Hokkaido Nansei-Oki tsunami. Geophys. Res. Lett. 24(11), 1315-1318.

CONSENT LETTER

To whom it may concern

Journal title: Annual Journal of Coastal Engineering, JSCE

Article title: Bending moment on a tree (Pandanus odoratissimus) due to tsunami flow around edge of coastal forest (2010). Annual Journal of Coastal Engineering, JSCE, Vol. 66/1, pp. 276-280. (in Japanese, abstract in English)

Authors: Nguyen Ba Thuy, Katsutoshi Tanimoto, Norio Tanaka, Kenji Harada, Kosuke Iimura

I am the supervisor of Dr. Nguyen Ba Thuy during doctor course in Saitama University, Japan from October 2007 to September 2010.

On behalf of all co-authors I would like to inform you that we are totally aware and agree that the content of this paper is one part on the doctor thesis of Dr. Nguyen Ba Thuy, and he is principal author for this paper.

On behalf of all co-authors

Norio Tanaka
Dr. Engineering, Prof.
Graduate School of Science and
Engineering, Saitama University
255 Shimo-okubo, Sakura-ku, Saitama
338-8570, Japan

Journal of Japan Society of Civil Engineers, Ser. B2 (Coastal Engineering)

Online ISSN : 1883-8944
Print ISSN : 1884-2399
ISSN-L : 1883-8944

Journal home Journal issue About the journal

Volume 66 , Issue 1

Showing 51-100 articles out of 291 articles from the selected issue

Study on the Evaluation of Tsunami Inundation in Real time with Database and its Accuracy

Ikuo ABE, Fumihiko IMAMURA

2010 Volume 66 Issue 1 Pages 261-265
Published: 2010
Released: November 09, 2010

DOI https://doi.org/10.2208/kaigan.66.261

JOURNALS FREE ACCESS

Show abstract

Download PDF (870K)

2010 Chilean Tsunami Observed by GPS-mounted Buoy Network on Tohoku to Shikoku Coast, Japan

Hiroyasu KAWAI, Makoto SATOH, Toshihiko NAGAI, Koji KAWAGUCHI

2010 Volume 66 Issue 1 Pages 266-270
Published: 2010
Released: November 09, 2010

DOI https://doi.org/10.2208/kaigan.66.266

JOURNALS FREE ACCESS

Show abstract

Download PDF (1151K)

Tsunami-trace Distribution around Buildings and Its Practical Use - Examples in the 2009 Samoa Earthquake Tsunami -

Hideo MATSUTOMI, Kenji HARADA

2010 Volume 66 Issue 1 Pages 271-275
Published: 2010
Released: November 09, 2010

DOI https://doi.org/10.2208/kaigan.66.271

JOURNALS FREE ACCESS

Show abstract

Download PDF (3108K)

Bending Moment on a Tree (*Pandanus odoratissimus*) due to Tsunami Flow around Edge of Coastal Forest

N. B. THUY, Katsutoshi TANIMOTO, Norio TANAKA, Kenji HARADA, Kosuke II ...

2010 Volume 66 Issue 1 Pages 276-280
Published: 2010
Released: November 09, 2010

DOI https://doi.org/10.2208/kaigan.66.276

JOURNALS FREE ACCESS

Hide abstract

Pandanus odoratissimus grown on sandy beach is considered as effective tree species providing tsunami mitigation due to its density and complex aerial root structure, but it is not strong enough to preclude the risk of breaking by action of high tsunami. In the present paper, the bending moment acting at a critical position (top of aerial root) of mature *P. odoratissimus* around edge of coastal forest has been investigated by numerical simulations. The bending moment is greatly influenced by forest condition (forest width and tree density) as well as tsunami conditions (period and height) and was formulated in the non-dimensional form for three representative points including the front corner of forest. The bending moment calculated by the curve-fit formula agrees with the simulated bending moment within 10% error.

Download PDF (1129K)

Tsunami Mitigation Effects by the Combination of Vegetation with Different Tree Density

Kosuke IIMURA, Norio TANAKA, Kenji HARADA, Katsutoshi TANIMOTO

2010 Volume 66 Issue 1 Pages 281-285
Published: 2010
Released: November 09, 2010

DOI https://doi.org/10.2208/kaigan.66.281

JOURNALS FREE ACCESS

Show abstract

Download PDF (701K)

Damage Assessment of Houses due to the 2006 Java Tsunami

Gaku SHOJI, Yusuke TANI

2010 Volume 66 Issue 1 Pages 286-290
Published: 2010
Released: November 09, 2010

DOI https://doi.org/10.2208/kaigan.66.286

JOURNALS FREE ACCESS

Show abstract

Download PDF (2352K)

土木学会論文集B2（海岸工学）
Vol. 66，No.1，2010，276-280

海岸樹林端部付近における樹木（アダン）に働く津波曲げモーメント

Bending Moment on a Tree (*Pandanus odoratissimus*) due to Tsunami Flow around Edge of Coastal Forest

N. B. THUY [1]・谷本勝利 [2]・田中規夫 [3]・原田賢治 [4]・飯村耕介 [5]

N. B. THUY, Katsutoshi TANIMOTO, Norio TANAKA, Kenji HARADA and Kosuke IIMURA

Pandanus odoratissimus grown on sandy beach is considered as effective tree species providing tsunami mitigation due to its density and complex aerial root structure, but it is not strong enough to preclude the risk of breaking by action of high tsunami. In the present paper, the bending moment acting at a critical position (top of aerial root) of mature *P. odoratissimus* around edge of coastal forest has been investigated by numerical simulations. The bending moment is greatly influenced by forest condition (forest width and tree density) as well as tsunami conditions (period and height) and was formulated in the non-dimensional form for three representative points including the front corner of forest. The bending moment calculated by the curve-fit formula agrees with the simulated bending moment within 10% error.

1. はじめに

熱帯において砂浜に生育するアダン（*Pandanus odoratissimus*）は気根を有し密生することから，感潮帯に生育するマングローブとともに，津波防御樹林（バイオシールド）の樹種として有望視される．しかしながら，2004年のインド洋大津波や2006年のジャワ津波に際して折損の例（例えば，Tanaka et al., 2007）が見られたように，津波に対する抵抗に限界があることは明らかであり，Tanaka et al.（2009）は主としてスリランカにおける現地試験等によりその破断曲げモーメントの算定法を提案している．

一方，樹林があるときの津波の流速は樹林端部近くや通路出口において顕著に増幅されることが実験や数値計算によって明らかにされているが（たとえば，Thuy et al., 2009），破断に直接関わる曲げモーメントは流速のみならず没水深も関係する．谷本ら（2009）は半無限のアダン林を対象として，潜在的津波力やそれによってアダンに働く曲げモーメントの樹林幅による変化の特性を検討している．また，Yanagisawa et al.（2009）は樹木の破壊を考慮したマングローブ林の津波減災効果に関する事例研究を行っている．

しかしながら，これら既往研究は樹林密度や津波条件が固定されているなど特定条件での検討であり，樹林および津波条件が曲げモーメントにどのように影響するかについてはいまだ十分には明らかにされていない．そのため，本研究においては，谷本ら（2009）と同様な半無限樹林を対象として津波遡上に関する二次元数値計算を行い，アダンに働く津波曲げモーメントに及ぼす樹林および入射津波条件の影響を系統的に検討するものである．特に，結果の無次元表示を試みる．

1		修（工）	埼玉大学大学院理工学研究科理工学専攻
2	フェロー	工博	埼玉大学名誉教授
3	正会員	工博	埼玉大学教授大学院理工学研究科
4	正会員	博（工）	埼玉大学助教大学院理工学研究科
5	学生会員	修（工）	埼玉大学大学院理工学研究科理工学専攻

2. 数値計算の方法と計算条件

（1）基礎方程式と数値計算法

数値計算法はThuy et al.（2009）および谷本ら（2009）と基本的に同じであるが，基礎方程式は津波力や曲げモーメントの計算の便宜から水深平均流速を用いた非線形長波方程式に変えている．ただし，平均流速を用いても，全水深が非常に小さいときの流速を除き，線流量を用いたときの計算結果と違いはなく，数値計算モデルの実験的検証と現地スケールへの適用に対する考え方に変わりはない（Thuyら，2010）．

平均流速を用いたときの樹林による抵抗力ベクトル$\vec{F}$（没水深積分値として表示）は次式のとおりである．

$$\vec{F} = \gamma \frac{1}{2} \rho C_{D-all}(d) b_{ref} \vec{V} \left| \vec{V} \right| d \quad \text{(1)}$$

ここに，γは樹林密度（単位面積あたりの樹木の本数），ρは水の密度，C_{D-all}（d）は樹木の水深平均抵抗係数（dの関数），b_{ref}は樹木の基準投影幅（胸高での幹の直径），$\vec{V}$は流速ベクトル，dは全水深（没水深）である．C_{D-all}は次式で与える（田中・佐々木，2007）．

$$C_{D-all}(d) = C_{Dref} \frac{1}{d} \int_0^d \frac{b(z_G)}{b_{ref}} \frac{C_D(z_G)}{C_{Dref}} dz_G \quad \text{(2)}$$

ここに，C_{Dref}は基準抵抗係数（胸高での幹に対する抗力係数で与える），bおよびC_Dは地面からの高さz_Gでの幹と枝の投影幅およびその高さでの樹木の抗力係数である．このように，$C_{D\text{-}all}$は高さ方向における抗力係数の変化ばかりでなく，投影幅の変化を含んだもので，全水深（没水深）の関数であるところに特色がある．

数値計算は基礎式を差分式に変換して行うが，本論文での差分間隔Δx，Δyは5mとする．

(2) 対象とする海岸と津波および樹林条件

対象としたのは図-1に示した断面が汀線方向（y軸方向）に一様に続く海岸であり，そこに津波がまっすぐ（x軸方向）に来襲する条件である．汀線付近は基準面（z=0m）までが1/100勾配，基準面上+4.0mまでが1/50勾配であり，続く陸地の勾配は1/500である．この断面形状は比較的緩勾配の海岸における砕波帯と浜の典型的地形を念頭に単純化したもので，特定の地点を対象としたものではない．津波来襲時の潮位は+2.0mとし，入射津波は水深100mの沖側境界で押し波スタートの正弦波で与えており，周期Tを600～3600s，波高H_iを2～8mの範囲で変化させる．ただし，沖側境界をどこにとるかは任意性があるので，本論文では飯村ら（2009）と同様に入射津波高を樹林なしの場合の汀線（z=2.0m）での津波高H_{sl0}で表す．

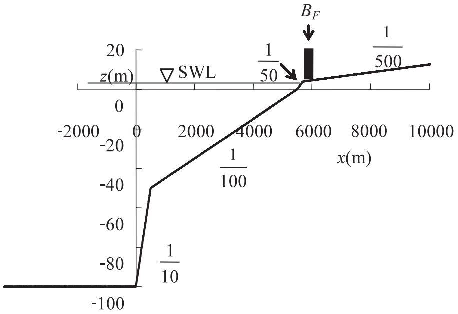

図-1　海岸断面と樹林位置

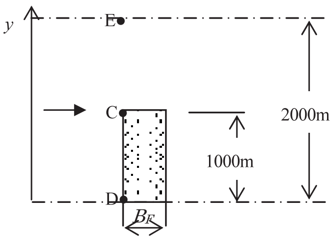

図-2　樹林の配置と代表地点

写真-1　スリランカにおけるアダン林の例

海岸樹林は1/500斜面の沖側端（x=5700m，z=4.0m）から幅B_Fにわたってあるものとし，図-2に示しているように計算領域のy方向距離は2000mであり，樹林はその半分の1000mにわたって配置する．図中のC，D，Eは計算結果を解析する代表地点を示している．地点C（x=5702.5m，y=997.5m）は樹林帯最前列の端部である．地点D（x=5702.5m，y=2.5m），E（x=5702.5m，y=1997.5m）は端部の影響をほとんど受けない十分に離れた地点に設定しており，それぞれ樹林あり，なしの場合の一次元結果に対応する地点である．対象とした樹木は熱帯海岸樹のアダンで気根があり，写真-1に示したように砂浜海岸に密生して生育するので，津波防御樹林（バイオシールド）として注目される樹木である．本研究ではほぼ最大に生長したアダンを考え，樹高H_{Tree}を8m，基準投影幅b_{ref}を0.2mとし，基準抗力係数$C_{D\text{-}ref}$は1.0とする．なお，アダンの水深平均抵抗係数$C_{D\text{-}all}$（d）は2004年インド洋大津波，2006年ジャワ津波に際しての樹木特性や破壊事例の調査結果（田中・佐々木，2007）に基づき与えている．

3. 数値計算結果と考察

(1) 津波曲げモーメントの定義と時間変化および平面分布の例

本研究では次式で定義するアダンに働く津波曲げモーメント$\vec{M}_P$を議論する．

$$\vec{M}_P=\frac{1}{2}\rho C_{Dref}b_{ref}\vec{V}\left|\vec{V}\right|\int_{h_c}^{d}\frac{b(z_G)}{b_{ref}}\frac{C_D(z_G)}{C_{Dref}}(z_G-h_c)dz_G,\quad h_c\le d \qquad \cdots(3)$$

ここに，h_cは樹木の破断位置の地面からの高さであり，アダンの場合気根上端部の高さで与え2mとする．

図-3に代表地点C，Eにおける全水深d，流速Vおよび津波曲げモーメントM_Pの時間変化（第1波）を示している（B_F=50m，γ=0.2本/m^2，H_{sl0}=6.94m，T=1200sの条件での例）．ここに，VおよびM_Pは流速および津波曲げモーメントの絶対値にx方向流速成分の符号を付したものである．この場合，地点Eの津波曲げモーメントは樹林帯の影響をほとんど受けない地点に単独にあるアダンに働く津波曲げモーメントに相当する．地点Dを含めた代表3地点における津波曲げモーメントの最大値M_{Pmax}（以降，これを単に津波曲げモーメントと呼ぶ），そのときの全水深d_{MPmax}，流速V_{MPmax}を表-1に示している．このように地点Eでの津波曲げモーメントが大きく，端部コーナー

表-1　代表地点における津波曲げモーメントの最大値等
（B_F=50m，γ=0.2本/m²，H_{sl0}=6.94m，T=1200s）

	$M_{Pmax}/10^3$ (kNm)	d_{MPmax} (m)	V_{MPmax} (m/s)
C	8.56	5.08	2.96
D	7.47	5.87	2.06
E	15.6	4.88	4.25

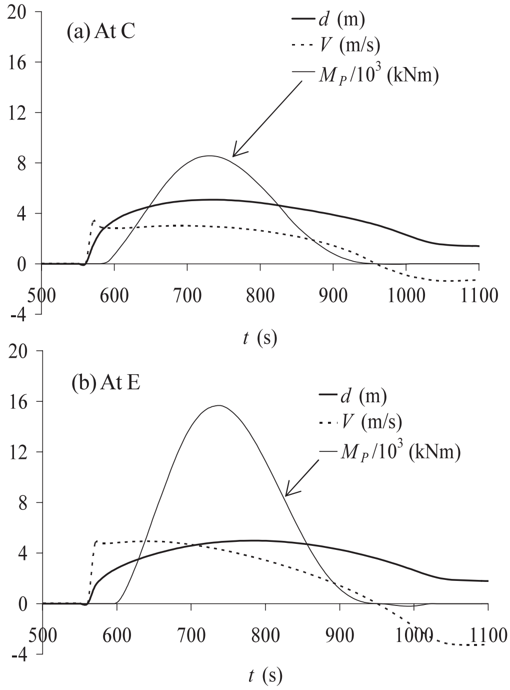

図-3　代表地点における津波曲げモーメントの時間変化等
（B_F=50m，γ=0.2本/m²，H_{sl0}=6.94m，T=1200s）

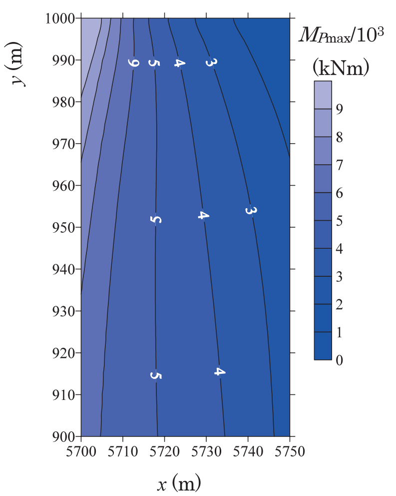

図-4　樹林帯端部付近における津波曲げモーメントの最大値の平面分布

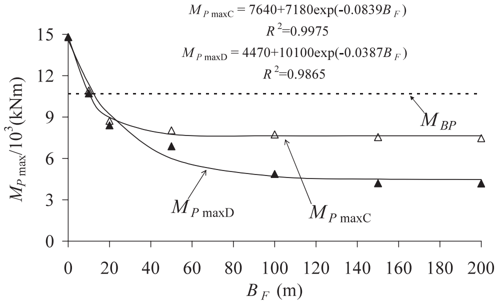

図-5　樹林幅による津波曲げモーメントの変化

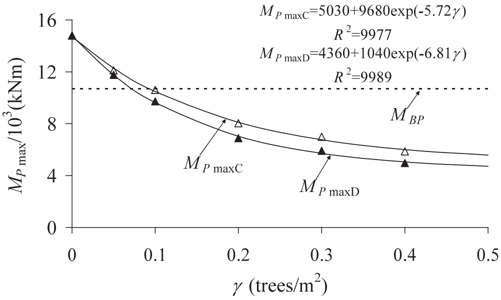

図-6　樹林密度による津波曲げモーメントの変化

地点Cおよび樹林帯が無限に続く場合に相当する地点Dでの津波曲げモーメントは地点Eのそれぞれ55%，48%と小さい．これは，同表に示してある津波曲げモーメント最大時の全水深と流速からもわかるように，樹林帯による反射によって，最前列での水位は上昇するものの，流速が大きく減じることによっている．図-4は樹林帯内の端部付近における津波曲げモーメントM_{Pmax}の平面分布である．樹林帯の中では最前列端部の地点Cでの津波曲げモーメントが最大で，そこで破断の危険性が最も高いことが確認できる．

（2）樹林条件の影響

図-5，6はH_{sl0}=6.94m，T=1200sの津波条件での樹林幅B_F（γ=0.2本/m²に固定），樹林密度γ（B_F=50mに固定）による津波曲げモーメントM_{Pmax}の変化である．図中，M_{Pmax}の後の添字CおよびDはそれぞれ地点CおよびDでの値であることを示している（B_F=0，γ=0は地点Eでの値）．樹林幅，樹林密度が増大することは樹林抵抗が増大することを意味しており，いずれの結果においても樹林抵抗が増大するにつれて津波曲げモーメントは減少し，一定値に近づく変化を示している．図中，当てはめ曲線とその式を示しているが，樹林幅による変化ではB_F=25m付近まで地点Dの値がわずかに大きくなっているけれども，これは当てはめ式による結果にすぎない．また，図中のM_{BP}は現地調査の結果得られたTanaka et al.(2009）によるアダンの破断限界曲げモーメント（単位：Nm）

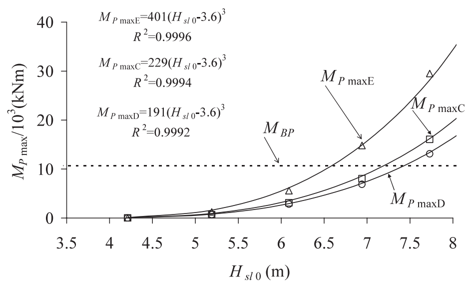

図-7　入射津波高による津波曲げモーメントの変化

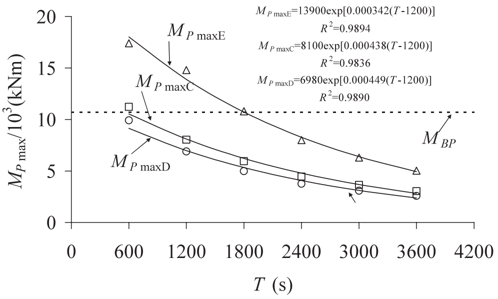

図-8　周期による津波曲げモーメントの変化

$$M_{BP} = 4.45\left(100 b_{ref}\right)^{2.62} \quad \cdots\cdots (4)$$

を示しており，樹林幅が狭い場合や樹林密度が小さい場合には津波曲げモーメントは破断モーメント（10.7kNm）を超え，折損の危険性が高いことがわかる．

（3）津波条件の影響

図-7，8はB_F=50m，γ=0.2本/m^{2}の樹林条件のもとでの入射津波高H_{sl0}（T=1200sに固定），周期T（H_{sl0}=6.94mに固定）による津波曲げモーメントの変化を示したものである．図中，M_{PmaxE}は地点Eでの津波曲げモーメントである．津波曲げモーメントはいずれの代表地点においても入射津波高が大きくなるにつれて増大し，周期が長くなるにつれて減少する．図中の曲線は

$$M_{P\max} = a_{Hm}\left(H_{sl0} - H_{cm}\right)^{b_{Hm}} \quad \cdots\cdots (5)$$

$$M_{P\max} = a_{Tm}\exp\left\{-b_{Tm}\left(\frac{T}{T_{rep}} - 1\right)\right\} \quad \cdots\cdots (6)$$

の関数で当てはめた式による変化である．ここにa_{Hm}，a_{Tm}は有次元係数，b_{Hm}，b_{Tm}は無次元指数，H_{cm}は遡上津波がh_cに達する限界の入射津波高，T_{rep}は津波の代表周期である．このうちH_{cm}は厳密に言えば樹林条件および地点の関数であるが，本研究の範囲ではそれほど変化しないので，その平均的な値である3.6mに固定する．また，b_{Hm}は津波曲げモーメントが津波高の3乗に比例すると考え3としている．代表周期は任意性のあるところであるが，本研究では20分を考え，T_{rep}=1200sとする．そうした上での当てはめ曲線であるが，適合度は良好である．

（4）無次元化の試み

Shuto（1987）は樹林条件を表すのに樹林厚を定義し，田中ら（2005）はそれに樹種による抵抗特性の違いを取り入れた式を提案した．式（7）は田中ら（2005）の式をSI単位系に変更して書き換えたものである．

$$B_{d\,Nall} = \gamma\left(1\times B_F\right)b_{ref}C_{D-all} = \gamma B_F b^*{}_{ref}C_{D-all} \quad \cdots\cdots (7)$$

ここに，B_{dNall}は樹林厚（単位：m），$b^*{}_{ref}$は数値は樹木の基準投影幅b_{ref}に同じであるが，表記の簡単のため単位をm^2/本とした便宜的なものである．$C_{D\text{-}all}$を与える没水深としては飯村ら（2009）と同様に汀線での津波高を用いる．

本研究では，これを次のように代表津波条件に対する長さスケールを導入して無次元化する（Thuyら，2010）．

$$\frac{B_{dNall}}{T_{rep}\sqrt{gH_{rep}}} = \frac{\gamma B_F b^*{}_{ref}C_{D-all}\left(H_{rep}\right)}{T_{rep}\sqrt{gH_{rep}}} \quad \cdots\cdots (8)$$

ここに，H_{rep}は汀線における代表津波高で，任意性があるところであるが，本研究では7mと設定する．したがって，この無次元パラメータは津波条件は入っているものの固定条件であり，単に樹林条件を表すにすぎない．なお，上式の分母は周期T_{rep}の長波の水深H_{rep}における波長に相当する．

一方，津波曲げモーメントは，入射津波による汀線での単位幅あたりの全静水圧に比例した力（$\rho gH_{sl0}{}^2$）に樹木の基準幅b_{ref}，抵抗特性を表す$C_{D\text{-}all}$（H_{sl0}）を乗じ，さらに腕の長さに比例するものとしてH_{sl0}を乗じてモーメントの単位とした値で割って，次のように無次元化する．

$$\frac{M_{P\max}}{\rho g b_{ref}C_{D-all}\left(H_{sl0}\right)H_{sl0}{}^3} = \alpha_m f_{C_{D-all}} f_{Hm} f_{Tm} \quad \cdots\cdots (9)$$

ここに，α_mは無次元値，$f_{C_{D-all}}$は水深平均抵抗係数$C_{D\text{-}all}$，f_{Hm}は入射津波高H_{sl0}，f_{Tm}は津波周期Tに関するそれぞれ無次元関数であり，次のように与える．

$$f_{C_{D-all}} = \frac{C_{D-all}(7)}{C_{D-all}\left(H_{sl0}\right)} \quad \cdots\cdots (10)$$

$$f_{Hm} = 8.73\left(1 - \frac{3.6}{H_{sl0}}\right)^3 \quad \cdots\cdots (11)$$

$$f_{Tm} = \exp\left\{-b_{Tm}\left(\frac{T}{1200} - 1\right)\right\} \quad \cdots\cdots (12)$$

これについては後で説明を加える．図-9は全データについて，式（8）の無次元樹林厚を横軸にとり，式（9）の無次元値α_m（地点を表す添字C，Dを付加）をプロットしたものである．無次元関数f_{Tm}に含まれる未定係数b_{Tm}については，地点ごとに次のように与えている．

$$\begin{aligned} b_{Tm} &= 0.530, \quad \text{at C} \\ &= 0.560, \quad \text{at D} \end{aligned} \quad \cdots\cdots (13)$$

なお，α_mは式（9）からわかるように，入射津波による

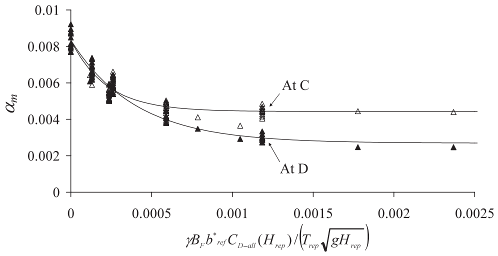

図-9 無次元樹林厚による無次元津波曲げモーメント

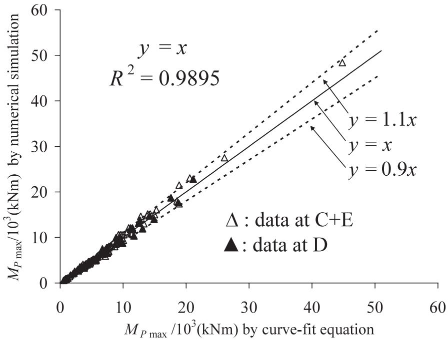

図-10 あてはめ式と数値シミュレーションによる結果の相関

汀線での全静水圧を考えたときのモーメントに比例した値で無次元化した遡上域での津波曲げモーメントを無次元関数$f_{C_{D\text{-}all}}$，f_{Hm}，f_{Tm}で除して補正した値であり，本論文ではこれを単に無次元津波力と呼ぶ．

このように無次元関数$f_{C_{D\text{-}all}}$，f_{Hf}，f_{Tf}は横軸の津波条件を代表津波条件の値に固定化したことによる津波曲げモーメントの補正関数で，これにより樹林条件が同じであれば津波高あるいは周期による変化は横軸の同じ位置にプロットされ，無次元津波曲げモーメントは代表津波条件による値とほぼ同じ値をとるように基準化したものである．図-9の曲線はそうした無次元津波力に対する次のような当てはめ式による関係を表している．

$$\alpha_{mC} = 0.00443 + 0.00392\exp\left(-4553\frac{\gamma B_F b^*_{ref} C_{D-all}\left(H_{rep}\right)}{T_{rep}\sqrt{gH_{rep}}}\right) \qquad \cdots\cdots\cdots\cdots\cdots(14)$$

$$\alpha_{mD} = 0.00269 + 0.00566\exp\left(-2507\frac{\gamma B_F b^*_{ref} C_{D-all}\left(H_{rep}\right)}{T\sqrt{gH_{sl0}}}\right) \qquad \cdots\cdots\cdots\cdots\cdots(15)$$

ただし，式中の数値の有効数字が結果の有効数字を表すものではない．図-10は当てはめ式による津波力とシミュレーションによる津波力の相関である．多様な条件での結果であるためばらついているが，ほぼ±10％の誤差に収まっている．

4. おわりに

本研究により，遡上津波によるアダンの折損に関する津波曲げモーメントに及ぼす樹林および入射津波条件の影響を明らかにした．津波高が大きいほど破断の危険性は高いのはもとより，幅や密度といった樹林条件の影響が大きいことが特筆される．樹林幅が狭いほど，樹林密度が小さいほど津波曲げモーメントは大きい．そうした津波曲げモーメントの無次元式を示したが，広範な条件に対し，誤差はほぼ±10％の範囲に収まっている．今後，津波力や曲げモーメントに関する実験的検討，さらには現地事例に対する適用性を明らかにしていく考えである．

謝辞：本研究の一部に，（独）日本学術振興会の「アジア・アフリカ学術基盤形成事業」の助成（コーディネータ：田中規夫）を使用した．記して謝意を表します．

参考文献

飯村耕介・田中規夫・谷本勝利・田中茂信（2009）：海岸樹林による津波減災効果の評価式の構築，海岸工学論文集，第56巻，pp.366-370.

田中規夫・佐々木寧・湯谷賢太郎・Samang Homchern（2005）：津波防御に対する樹林帯幅と樹種の影響について－インド洋大津波に対するタイでの痕跡調査－，海岸工学論文集，第52巻，pp.1346-1350.

田中規夫・武村 武・佐々木 寧・M.I.M. Mowjood（2006）：スリランカ海岸林の樹種による破壊条件と津波到達遅延時間の相違，海岸工学論文集，第53巻，pp.281-285.

田中規夫・佐々木寧（2007）：2006年ジャワ津波災害において海岸林が果たした役割とその破断・なぎ倒し限界，水工学論文集，第51巻，pp.1445-1450.

谷本勝利・田中規夫・N.B. Thuy・飯村耕介・原田賢治（2009）：海岸樹林端部付近における津波の流れ－実験と数値計算－，海岸工学論文集，第56巻，pp.361-365.

Thuy, N.B.・飯村耕介・田中規夫・谷本勝利（2010）：切れ間を有する海岸樹林の潜在的津波力に関する樹林および津波条件の影響，海洋開発論文集，第26巻，pp.291-296.

Shuto N. (1987) : The effectiveness and limit of tsunami control forests, Coastal Engineering in Japan, 30 (1), pp.143-153.

Tanaka, N., N.A.K. Nandasena, K.S.B.N. Jinadasa, Y. Sasaki, K. Tanimoto and M.I.M. Mowjood (2009) : Developing effective vegetation bioshield for tsunami protection, Journal of Civil Engineering and Environmental Systems, Taylor & Francis, 26, pp.163-180.

Tanaka, N., Y. Sasaki, M.I.M. Mowjood and K.B.S.N. Jinadasa, (2007) : Coastal vegetation structures and their functions in tsunami protection: Experience of the recent Indian Ocean tsunami, Landscape and Ecological Engineering, 3, pp.33-45.

Thuy, N.B., K. Tanimoto,. N. Tanaka, K. Harada and K. Iimura (2009) : Effect of open gap in coastal forest on tsunami run-up – Investigations by experiment and numerical simulation, Ocean Engineering, 36, pp.1258-1269.

Yanagisawa, H., S. Koshimura, K. Goto, T. Miyagi, F. Imamura, A. Ruangrassamee and C. Tanavud, (2009) : The reduction effects of mangrove forest on a tsunami based on field surveys at Pakarang Cape, Thailand and numerical analysis, Estuarine, Coastal and Shelf Science, 81, pp.27-37.

CONSENT LETTER

To whom it may concern

Journal title: Ocean Engineering

Article title: Effect of open gap in coastal forest on tsunami Run-up-Investigations by experiment and numerical simulation (2009). Ocean Engineering, Elsevier, Vol 36, 1258–1269.

Authors: Nguyen Ba Thuy, Katsutoshi Tanimoto, Norio Tanaka, Kenji Harada, Kosuke Iimura.

I am the supervisor of Dr. Nguyen Ba Thuy during doctor course in Saitama University, Japan from October 2007 to September 2010. I am also the corresponding author of this paper.
On behalf of all co-authors I would like to inform you that we are totally aware and agree that the content of this paper is one part on the doctor thesis of Dr. Nguyen Ba Thuy, and he is principal author for this paper.

On behalf of all co-authors

Norio Tanaka
Dr. Engineering, Prof.
Graduate School of Science and
Engineering, Saitama University
255 Shimo-okubo, Sakura-ku, Saitama
338-8570, Japan

Ocean Engineering 36 (2009) 1258–1269

Contents lists available at ScienceDirect

Ocean Engineering

journal homepage: www.elsevier.com/locate/oceaneng

Effect of open gap in coastal forest on tsunami run-up—investigations by experiment and numerical simulation

Nguyen Ba Thuy, Katsutoshi Tanimoto, Norio Tanaka *, Kenji Harada, Kosuke Iimura

Institute of Environmental Science and Technology, Saitama University, 255 Shimo-okubo, Sakura-ku, Saitama 338-8570, Japan

A R T I C L E I N F O

Article history:
Received 17 December 2008
Accepted 20 July 2009
Available online 25 July 2009

Keywords:
Gap
Bioshield
Tsunami run-up
Pandanus odoratissimus
Coastal forest
Drag force
Turbulence induced shear force

A B S T R A C T

The objective of this study is to investigate the effects of an open gap, such as a road, in a coastal forest on tsunami run-up. A numerical model based on two-dimensional nonlinear long-wave equations was developed to account for the effects of drag and turbulence induced shear forces due to the presence of vegetation. Experiments were conducted on a forest simulated with vertical cylinders by changing the gap width. The numerical model was validated in good agreement with the experimental results. The numerical model was then applied to a wide forest of *Pandanus odoratissimus*, a tree species that is a dominant coastal vegetation on a sand dune in South and Southeast Asia. The effect of vertical stand characteristics of *P. odoratissimus* with aerial roots was considered on the drag resistance. A straight open gap perpendicular to the shoreline was used to investigate the effect of gap width. As the gap width increases, the flow velocity at the end of the open gap first increases, reaches a maximum, and then decreases, while the run-up height increases monotonously. The maximum velocity in the present condition is 1.7 times the maximum velocity without a coastal forest. The effects of different gap arrangements in the forest on tsunami run-up were also investigated in this paper. The flow velocity at the end of an open gap can be reduced by a staggered arrangement.

1. Introduction

The effect of a coastal forest on tsunami mitigation has long been a topic of interest. Shuto (1987) pointed out various aspects of the effects of coastal forests in the mitigation of tsunami damage. Many field observations, particularly after the 2004 Indian Ocean tsunami, have elucidated the effects of coastal vegetation on tsunami energy reduction (Danielsen et al., 2005; Kathiresan and Rajendran, 2005; Tanaka et al., 2007; Mascarenhas and Jayakumar, 2008). Currently, coastal forests are widely considered to be an effective measure to mitigate tsunami damage from both economic and environmental points of view. In fact, several projects to plant vegetation on coasts as a bioshield against tsunamis have been started in South and Southeast Asian countries (Tanaka et al., 2009a; Tanaka, 2009b). The effect of coastal forest on tsunami mitigation, however, is still questioning. Kerr and Baird (2007) pointed out that the significance of coastal vegetation in tsunami mitigation remains an open question due to the absence of adequate studies, and more data and more powerful approaches may well find an association.

Related to the capacity of coastal forests to mitigate tsunami damage, many studies have been done using laboratory experiments and numerical simulations as well as field investigations. Among these, the numerical simulation is very effective, and various numerical models based on nonlinear long-wave equations have been proposed. Harada and Imamura (2005) proposed a model of a numerical simulation in which the resistance of vegetation was evaluated by drag forces on trees and the drag coefficients of pines were estimated on the basis of field observations and laboratory experiments. Tanaka et al. (2007) improved the expression of drag force so that the vertical stand characteristics of tree were considered more realistically, and proposed the depth-averaged equivalent drag coefficients for various tropical trees on the basis of field investigations in Sri Lanka, Thailand, and Indonesia. Tanaka et al. (2007) also pointed out that *Pandanus odoratissimus* grown on beach sand is especially effective in providing protection from tsunami damage due to its density and complex aerial root structure for a less than 5 m tsunami.

The capacity of coastal forests to mitigate a tsunami run-up is primarily dependent on the streamwise length of the forest in the direction of the tsunami flow (for example, Tanaka et al., 2009a). In the present paper, the streamwise length is called the cross-shore width of the forest (or simply, the forest width) because a coastal forest extending like an along-shore green belt proposed by Hiraishi and Harada (2003) is considered. Tanimoto et al. (2007) investigated the effects of forest width on the run-up height and flow velocity behind the forest for several species of

* Corresponding author. Tel./fax: +81 48 858 3564.
E-mail address: tanaka01@mail.saitama-u.ac.jp (N. Tanaka).

0029-8018/$ - see front matter © 2009 Elsevier Ltd. All rights reserved.
doi:10.1016/j.oceaneng.2009.07.006

tropical trees, and confirmed that the flow velocity, and consequently, the tsunami force, was significantly reduced by a coastal forest of *P. odoratissimus* with the increase of the forest width.

On the other hand, on the basis of field investigations on the Indian coast after the 2004 tsunami, Mascarenhas and Jayakumar (2008) pointed out that roads perpendicular to the coast serve as pathways for a tsunami to travel inland. Fernando et al. (2008) demonstrated by laboratory experiments that the exit flow velocity from a coastal perpendicular gap in submerged porous barriers simulated corals was significantly higher compared to the case with no gap. These results suggest that an open gap, like a road, in a coastal forest has a negative effect on tsunami run-up behind the forest.

Nandasena et al. (2008) investigated the effect of an open gap in a forest of *P. odoratissimus* on tsunami run-up by numerical simulations and found that a narrow gap has an insignificant effect on the run-up height, but that it significantly affects the exit flow velocity. Because the investigation by Nandasena et al. (2008) was restricted to two-gap widths, Tanimoto et al. (2008) systematically investigated it by changing the gap width and found that a specific gap width (15 m) causes the highest velocity in their simulated conditions.

Water flowing within vegetation and an open gap is not only resisted by drag force and bottom friction, but also by the turbulence induced shear force. In the gap, the flow is fast, while inside the vegetation the drag due to the vegetation slows it. Mazda et al. (2005) revealed that both drag force and turbulence induced shear force play dominant roles in the tidal scale hydrodynamics of mangrove swamps. The drag force in tsunamis has been evaluated in the numerical simulations as already described. However, the role of turbulence induced shear force was not discussed in previous studies. According to Mazda et al. (2007), the turbulence induced shear force along a creek might reduce the tsunami energy going up the creek.

Turbulent flow in an open channel with a vegetation bank was investigated numerically by Nadaoka and Yagi (1998) and Su and Li (2002). The sub-depth scale (*SDS*) turbulence model developed by Nadaoka and Yagi (1998) which includes the turbulence generated by the vegetation performs with high accuracy on experimental results and is better than the depth-integrated $k-\varepsilon$ model. In a numerical model of a tsunami run-up, Thuy et al. (2008) included the turbulence induced shear force based on the *SDS* turbulence model of Nadaoka and Yagi (1998). The numerical model, however, was not validated for long waves like tsunamis.

In the present paper, the effect of an open gap in coastal forests on tsunami run-up was investigated on the basis of experiments and numerical simulations. The numerical model is based on two-dimensional nonlinear long-wave equations and incorporates the *SDS* turbulence model. Experiments were conducted in a wave channel by changing the gap width in a simplified forest model of vertical cylinders. The numerical model then was applied to a coastal forest of *P. odoratissimus*, which is a dominant coastal vegetation in South and Southeast Asia. The effect of vertical stand characteristics of *P. odoratissimus* on the drag resistance is considered on the basis of Tanaka et al. (2007, 2009a). This study will provide basic information for designing and establishing a vegetation bioshield against tsunamis.

2. Mathematical model and numerical method

2.1. Governing equations

The governing equations are two-dimensional nonlinear long-wave equations that include drag and turbulence induced shear forces due to interaction with vegetation. The continuity and the momentum equations are respectively:

$$\frac{\partial \zeta}{\partial t}+\frac{\partial Q_x}{\partial x}+\frac{\partial Q_y}{\partial y}=0 \tag{1}$$

$$\begin{aligned}&\frac{\partial Q_x}{\partial t}+\frac{\partial}{\partial x}\left(\frac{Q_x^2}{d}\right)+\frac{\partial}{\partial y}\left(\frac{Q_xQ_y}{d}\right)+gd\frac{\partial \zeta}{\partial x}+\frac{\rho g n^2}{\rho d^{7/3}}Q_x\sqrt{Q_x^2+Q_y^2}\\&+\frac{1}{2\rho}\frac{\rho\gamma C_{D-all}b_{ref}}{d}Q_x\sqrt{Q_x^2+Q_y^2}-2\frac{\partial}{\partial x}\left(\nu_e\frac{\partial Q_x}{\partial x}\right)-\frac{\partial}{\partial y}\left(\nu_e\frac{\partial Q_x}{\partial y}\right)\\&-\frac{\partial}{\partial y}\left(\nu_e\frac{\partial Q_y}{\partial x}\right)=0\end{aligned} \tag{2}$$

$$\begin{aligned}&\frac{\partial Q_y}{\partial t}+\frac{\partial}{\partial x}\left(\frac{Q_xQ_y}{d}\right)+\frac{\partial}{\partial y}\left(\frac{Q_y^2}{d}\right)+gd\frac{\partial \zeta}{\partial y}+\frac{\rho g n^2}{\rho d^{7/3}}Q_y\sqrt{Q_x^2+Q_y^2}\\&+\frac{1}{2\rho}\frac{\rho\gamma C_{D-all}b_{ref}}{d}Q_y\sqrt{Q_x^2+Q_y^2}-2\frac{\partial}{\partial y}\left(\nu_e\frac{\partial Q_y}{\partial y}\right)-\frac{\partial}{\partial x}\left(\nu_e\frac{\partial Q_y}{\partial x}\right)\\&-\frac{\partial}{\partial x}\left(\nu_e\frac{\partial Q_x}{\partial y}\right)=0\end{aligned} \tag{3}$$

where Q_x and Q_y are the discharge flux in x and y directions respectively, t is the time, d the total water depth ($d=h+\zeta$), h the local still water depth, ζ the water surface elevation, g the gravitational acceleration, ρ the water density, n the Manning roughness coefficient, γ the tree density (number of trees/m^2), and $C_{D\text{-}all}$ the depth-averaged equivalent drag coefficient considering the vertical stand structure of tree, which was defined by Tanaka et al. (2007) as:

$$C_{D-all}(d)=C_{D-ref}\frac{1}{d}\int_0^d \alpha(z_G)\beta(z_G)dz_G \tag{4}$$

$$\alpha(z_G)=\frac{b(z_G)}{b_{ref}} \tag{5}$$

$$\beta(z_G)=\frac{C_D(z_G)}{C_{D-ref}} \tag{6}$$

where $b(z_G)$ and $C_D(z_G)$ are the projected width and drag coefficient of a tree at the height z_G from the ground surface, and b_{ref} and $C_{D\text{-}ref}$ are the reference projected width and reference drag coefficient of the trunk at $z_G=1.2$ m in principle, respectively. The eddy viscosity coefficient ν_e is expressed in the *SDS* turbulence model as described below.

2.2. Turbulence model

The *SDS* turbulence model given by Nadaoka and Yagi (1998) was applied to evaluate the eddy viscosity coefficient with modifications related to the bottom friction and vegetation resistance.

$$\begin{aligned}&\frac{\partial k_D}{\partial t}+u\frac{\partial k_D}{\partial x}+v\frac{\partial k_D}{\partial y}=\frac{1}{d}\frac{\partial}{\partial x}\left(d\frac{\nu_e}{\sigma_k}\frac{\partial k_D}{\partial x}\right)+\frac{1}{d}\frac{\partial}{\partial y}\left(d\frac{\nu_e}{\sigma_k}\frac{\partial k_D}{\partial y}\right)\\&+p_{kh}+p_{kv}+p_{kd}-\varepsilon_D\end{aligned} \tag{7}$$

$$p_{kh}=\nu_e\left[2\left(\frac{\partial u}{\partial x}\right)^2+\left(\frac{\partial u}{\partial y}+\frac{\partial v}{\partial x}\right)^2+2\left(\frac{\partial v}{\partial y}\right)^2\right] \tag{8}$$

$$p_{kv}=\frac{gn^2}{d^{4/3}}(u^2+v^2)^{1.5} \tag{9}$$

$$p_{kd}=\frac{\gamma b_{ref}C_{D-all}}{2}(u^2+v^2)^{1.5} \tag{10}$$

$$\nu_e=c_w\frac{k_D^2}{\varepsilon_D} \tag{11}$$

$$\varepsilon_D = c_d \frac{k_D^{1.5}}{l_D} \tag{12}$$

where k_D is the kinetic energy, $l_D = \lambda d$ the length scale (λ: turbulence length scale coefficient), and u and v are the depth-averaged velocity components in x and y directions, respectively. For the model parameters, standard values are adopted: $c_w = 0.09$, $c_d = 0.17$, and $\sigma_k = 1.0$. The value of λ will be discussed later.

2.3. Numerical method

A set of the above equations is solved by the finite-difference method of a staggered leap-frog scheme. An upwind scheme is used for nonlinear convective terms in order to maintain numerical stability. A semi-Crank–Nicholson scheme was used for the terms of bed friction, drag, and turbulence induced shear force.

On the offshore sides, a wave generation zone with a constant water depth in which governing equations are reduced to linear long-wave equations was introduced to achieve the non-reflective wave generation by using the method of characteristics. The incident sinusoidal tsunami was given as a time-dependent boundary condition at the most offshore side of the wave generation zone. For a moving boundary treatment, a number of algorithms are necessary so that the flow occurring when the water surface elevation is high enough can flow to the neighboring dry cells. The initial conditions were given for a state of no wave in the computational domain including the wave generation zone.

3. Experiments and validation of numerical model

3.1. Experimental setup and conditions

The laboratory experiments for long waves were carried out in a wave channel of 40 cm wide and 15 m long at Saitama University. Fig. 1 shows the experimental setup including a 1 m wide vegetation model which was set in the water area for the convenience of velocity measurements. The vegetation is simply modeled by wooden cylinders with a diameter of 5 mm mounted in a staggered arrangement (see Fig. 1(c) and (d)). In the

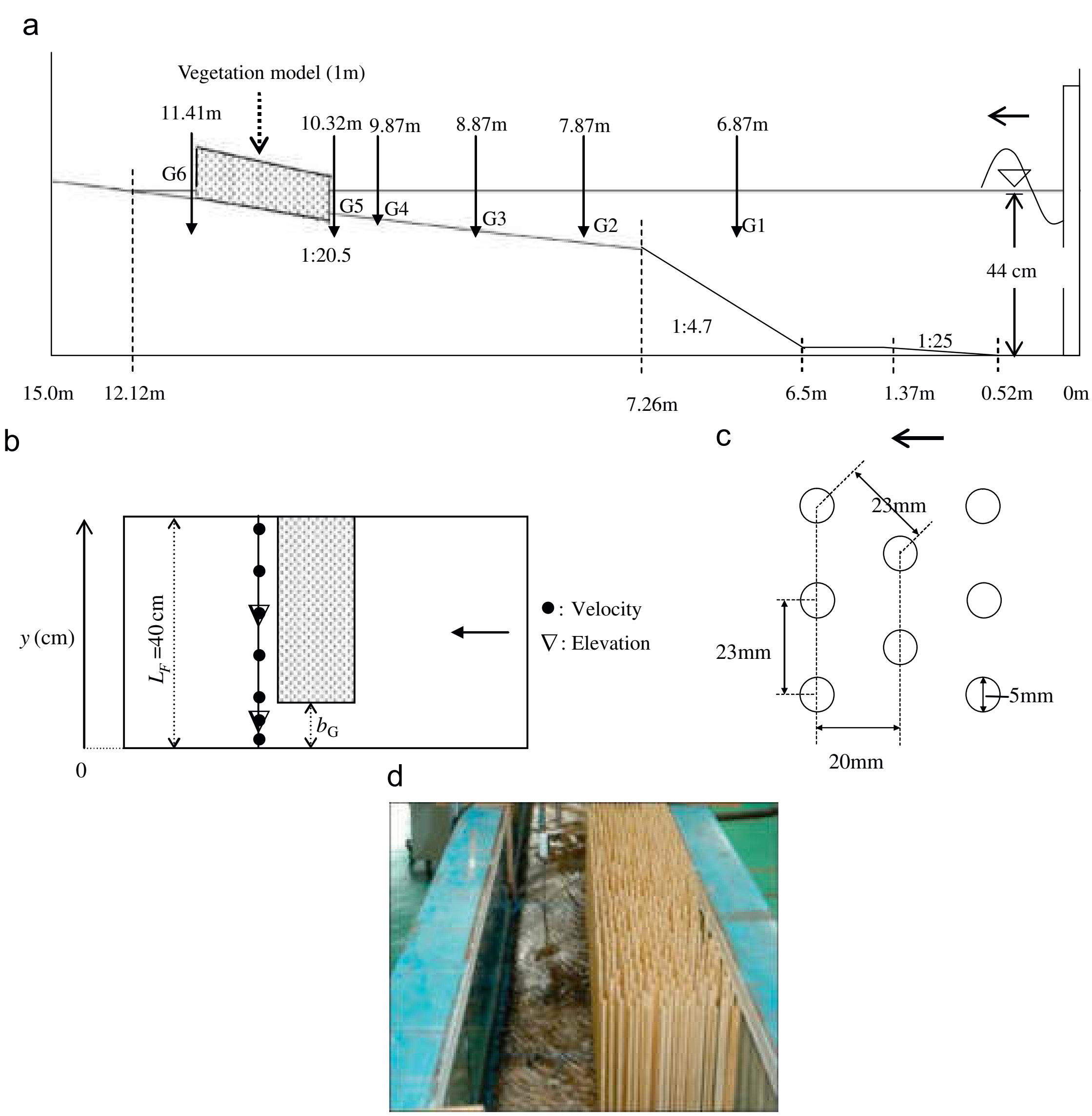

Fig. 1. Experimental setup of wave channel. (a) Longitudinal section. (b) Plan in vicinity of vegetation model and measuring points. (c) Details of vegetation arrangement. (d) Photo of vegetation model with a gap.

experiments, 8 widths of the open gap (b_G) were examined: 0 cm (full vegetation), 4, 7, 11, 15, 20, 30, and 40 cm (no vegetation, $=L_F$; the width of the channel here. Later, it is redefined.). In the cases of full vegetation and no vegetation, flow velocity and water surface elevation were measured at six positions (G1–G6) along the center of the flume (see Fig. 1(a)). In other cases, flow velocity and water surface elevation were measured at locations in the cross section just behind the vegetation (on the line passing G6). The flow velocity was measured at 1 cm intervals in the vicinity of the gap and 2 cm intervals in the vegetation region, while the water surface elevation was measured at the centers of the two regions (see Fig. 1(b)). Water surface elevations were measured using capacitance wave gauges, while flow velocities were measured using electromagnetic current meters for two horizontal components at the middle of the still water depth. The final run-up height above the still water level (hereafter, simply run-up height) was measured by tracing the water front moving by eyes with a scale on the slope. In the data analysis, five waves in a steady state and digitalized at 5 Hz were used. Several wave conditions were tested in the experiments. In the present paper, however, the results of relatively low waves with the period of $T=20$ s are presented.

3.2. Validation of numerical model with experimental results

For the numerical simulations of the experimental conditions, the uniform grid size of 0.05 m and time step of 0.002 s were selected. The Manning's roughness coefficient n was given as 0.012 for the relatively rough wooden bottom. Other computational parameters were determined by trial simulations as follows. First, the incident wave height H_i at the offshore boundary was determined for the case without vegetation so that the best fit between the measured and calculated results at G1 was obtained. The determined incident wave height is 2.0 cm. Second, the best fit value of the drag coefficient $C_{D\text{-}ref}$ was investigated for the case of full vegetation and was determined to be 1.5, which is consistent with the drag coefficient for a circular cylinder in the laboratory scale corresponding to the Reynolds number of 300. This $C_{D\text{-}ref}$ is equal to $C_{D\text{-}all}$, because the vegetation model is composed of vertical cylinders with a constant diameter in the experiments. Third, the best fit value of the turbulence length scale coefficient λ was investigated for a representative case with a 7-cm wide gap and was determined to be 0.08. Finally, numerical simulations for all cases were carried out using the determined values, and comparisons of measured and simulated results were made to confirm the agreement. Some of the comparisons are shown below.

Fig. 2 shows the crest and trough elevations and the wave height in cases of (a) no vegetation and (b) full vegetation. Results of both experiments (Exp. in the figure) and numerical simulations (Num. in the figure) are plotted against the distance from the wave paddle (wave source), where the black circles are the measured run-up height. As already shown by Tanaka et al. (2009a), the wave height increases due to shoaling as waves propagate to the shore. In the case of full vegetation, however, the increase of wave height is damped by the effect of vegetation resistance. It is confirmed that the experimental and numerical results agree well over the whole range, although the incident wave height was determined for the results at the deepest gage G1.

Fig. 3 shows examples of the time series of flow velocity for the conditions of $b_G=7$ cm. Both experimental and numerical results of flow velocities at (a) the center of the gap width, and (b) the center of the vegetation region on the cross line at G6 are plotted. Here, the flow velocity is a resultant velocity of two components,

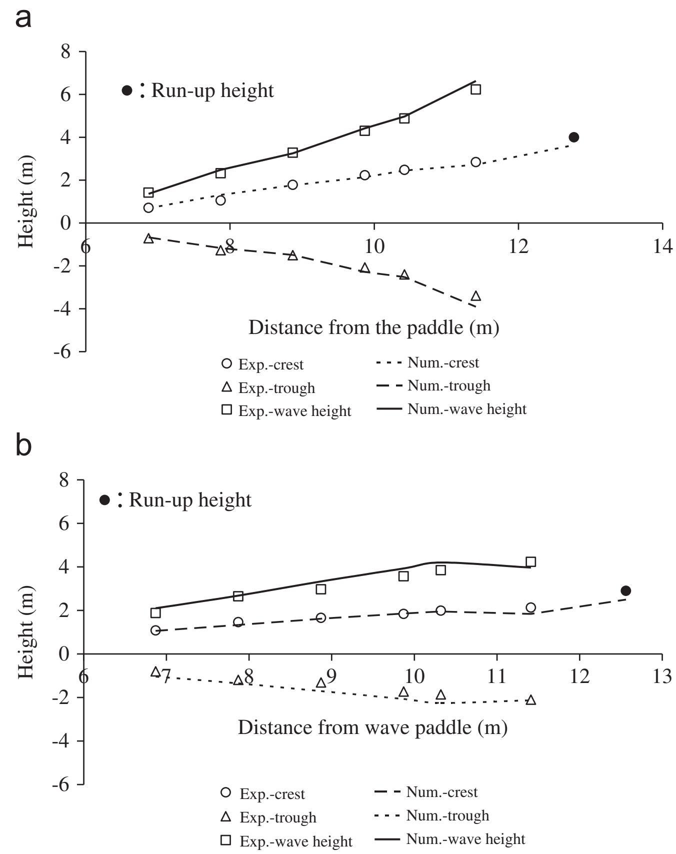

Fig. 2. Changes of wave crest, wave trough, and wave height. (a) Case with no vegetation, and (b) case with full vegetation. Exp. and Num. denote experiment and numerical simulation, respectively.

although the transverse component is very small. The numerical results agree fairly well with the experimental results. The average of five peak values of flow velocity obtained from the time series is plotted in Fig. 4 for all measuring points on the cross line at G6, where the distance y is defined in Fig. 1(b). In the figure, numerical results from the model without turbulence terms (excluded TT in the figure) and the depth averaged $k-\varepsilon$ model with standard values of parameters (Rodi, 2000) are also shown for comparison. Compared with the results from the model without turbulence terms and the depth averaged $k-\varepsilon$ model, the result from the present *SDS* turbulence model is closer to the experimental data. These results indicate that turbulence has a significant effect on reducing the velocity slightly in the open gap, but an insignificant effect inside a vegetation region.

Fig. 5 shows the relationships of the normalized height of a wave crest (ζ_c/ζ_1), normalized maximum velocity ($V_{G\max}/V_1$) at the gap exit, and normalized run-up height (R/R_1) to the normalized gap width (b_G/L_F), where ζ_1, V_1 and R_1 are the height of the wave crest, the temporal maximum velocity at G6 and the run-up height, respectively, in the case of $b_G=L_F$, namely without vegetation, and the maximum velocity $V_{G\max}$ is the largest spatial velocity in the gap width. The run-up height R observed in the experiment was almost uniform in the y-direction, and it was uniform in the numerical result. In the figure, it is noted that the results of experiments and numerical simulations agree well. According to the results, the height of the wave crest and run-up height increase monotonously as the gap width increases. The reduction due to the full vegetation ($b_G/L_F=0$) is 30% and 26% from the case of no vegetation for the wave crest and run-up height, respectively. In contrast, the change of flow velocity is different from that of the height. It first increases, reaching the

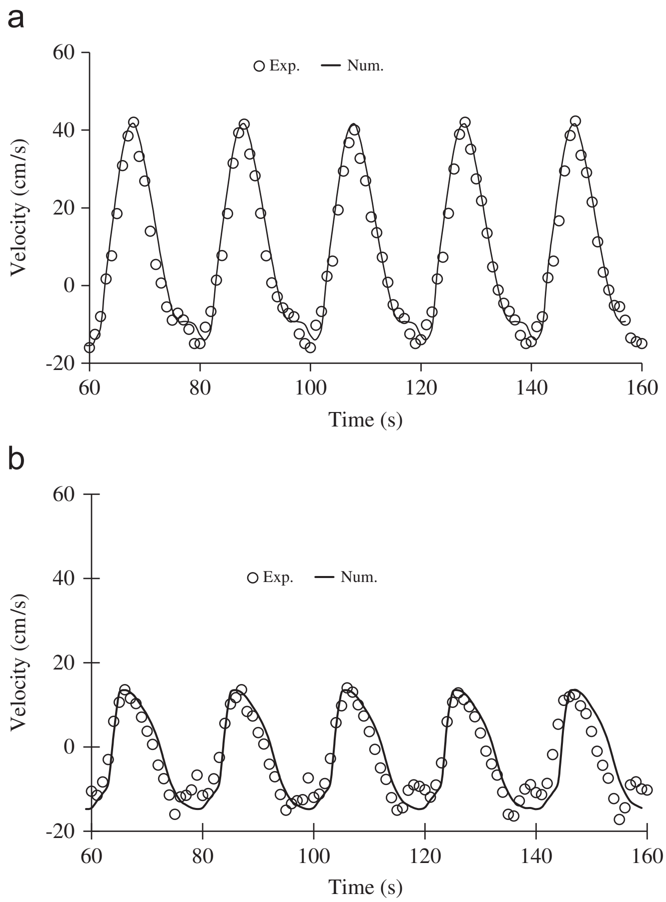

Fig. 3. Time series of flow velocity ($b_G = 7$ cm). (a) At the center of gap exit, and (b) at the center of vegetation end.

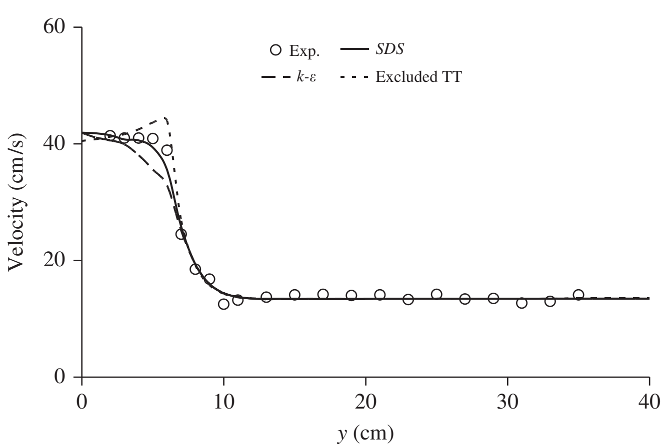

Fig. 4. Transverse profiles of maximum velocity behind the gap ($b_G = 7$ cm).

maximum value at $b_G/L_F = 0.175$, and then decreases. The maximum value is 1.8 times that of the case with no vegetation ($b_G/L_F = 1$), and 3.0 times that of the case with full vegetation ($b_G/L_F = 0$). The enhancement of flow velocity behind the gap was also observed in the experimental results for porous barriers by Fernando et al. (2008). The increase of velocity behind the gap is mainly due to the inflow from the vegetation region to the gap, which is generated by large scale eddies at the interface of the gap and vegetation. The generation of these eddies is due to the

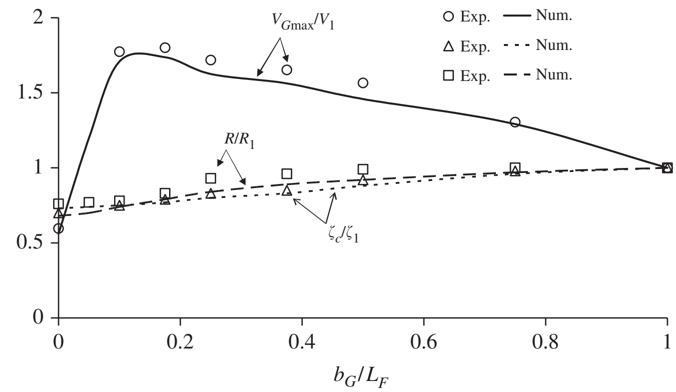

Fig. 5. Variation of normalized wave crest (ζ_c/ζ_1), maximum velocity behind the gap (V_{Gmax}/V_1) and normalized run-up height (R/R_1).

difference in velocities between the gap and vegetation region. As the gap width increases the inflow averaged by the gap width is decreased, and consequently the magnitude of the jetting flow in the gap decreases. In the case of a relatively narrow gap (on the order of the distance between cylinders), however, the flow velocity is reduced due to the drag of vegetation.

4. Effect of open gap in forest on tsunami run-up in actual scale

4.1. Topography, tsunami and vegetation conditions

4.1.1. Vegetation species

In the present study, *P. odoratissimus*, a dominant coastal vegetation in South and Southeast Asia, was considered as a tree species consistent with a coastal forest. As shown in Fig. 6(a), *P. odoratissimus* has a complex aerial root structure that provides additional stiffness and increases the drag coefficient. Fig. 6(b) shows the α, β, and $C_{D\text{-}all}$ of *P. odoratissimus* modified slightly from those proposed by Tanaka et al. (2007) to the following conditions: the tree height $H_{Tree} = 8$ m (for adult tree), the reference diameter $b_{ref} = 0.2$ m, the density $\gamma = 0.22$, and the reference drag coefficient $C_{D\text{-}ref} = 1.0$. The reference drag coefficient of 1.0 was adopted for the trunk with a circular section and a rough surface in the region of high Reynolds number (order of 10^6) in the actual scale. The value of $C_{D\text{-}all}$ varies by the total depth d (inundated depth) because the projected width b and the drag coefficient C_D vary with the height from the ground surface z_G.

4.1.2. Topography and tsunami conditions

A uniform coastal topography with a straight shoreline with the cross section perpendicular (x-axis) to the shoreline, as shown in Fig. 7(a), was selected as a test case. The bed profile of the domain consists of 4 slopes $S = 1/10$, $1/100$, $1/50$, and $1/500$. The offshore water depth at an additional wave generation zone with a horizontal bottom is 100 m below the datum level of $z = 0$. The tide level at the attack of a tsunami is considered to be 2 m, and therefore the still water level is located at 2 m above the datum level. The incident tsunami is assumed to be a sinusoidal wave of 3 m in amplitude and 20 min in period. The direction of the incident tsunami is perpendicular to the shoreline. In the present paper, the run-up of the first wave only is discussed.

The coastal forest starts at the starting point of the slope of 1/500 on the land, where the height of the ground is 4 m above the datum level (2 m above the tide level at tsunami attack). The forest is assumed to extend in the direction of the shoreline

(y-axis) with the same arrangement of gaps and vegetation patches with an along-shore unit length of L_F, as shown in Fig. 7(b), where three different gap arrangements are shown. Both side boundaries, shown by dot-and-dash lines in the figure, are mirror image axes in which no cross flow exists. The cross-shore width of the forest is denoted as B_F. The width of the open gap is denoted as b_G. In the present study, the forest width B_F was fixed at 200 m.

In the numerical simulation, a uniform grid size in x and y directions was set as 2.5 m and the time interval was 0.04 s. The Manning's roughness coefficient (n) was set as 0.025 for a relatively rough bare ground, which is widely used in numerical simulations of tsunami run-up (for example, Harada and Imamura, 2005). The turbulence length scale coefficient (λ) was set as 0.08, the same value obtained from the experimental results.

Fig. 8 shows the spatial variation of temporal maximum water surface elevations of the first wave for the two extreme cases of no vegetation (bare ground) and full vegetation (no gap). In the case of no vegetation, the maximum water surface elevation on the steep slope of $\frac{1}{50}$ increases due to shoaling. Near the mild slope of $\frac{1}{500}$, however, it decreases because the flow velocity on the mild slope is accelerated. The run-up height above the still water level is 6.88 m, slightly greater than the 6.64 m at the beginning of the mild slope. In the case of full vegetation, the maximum water surface elevation is increased at the front of vegetation due to a

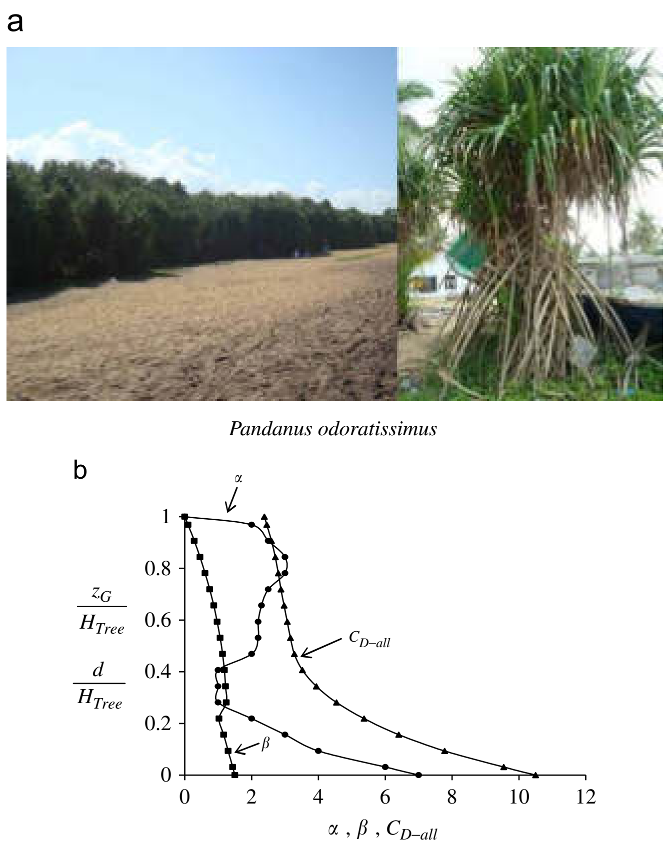

Fig. 6. Characteristics of *Pandanus odoratissimus*. (a) Photographs of a stand, and (b) vertical distribution of α, β, and $C_{D\text{-}all}$.

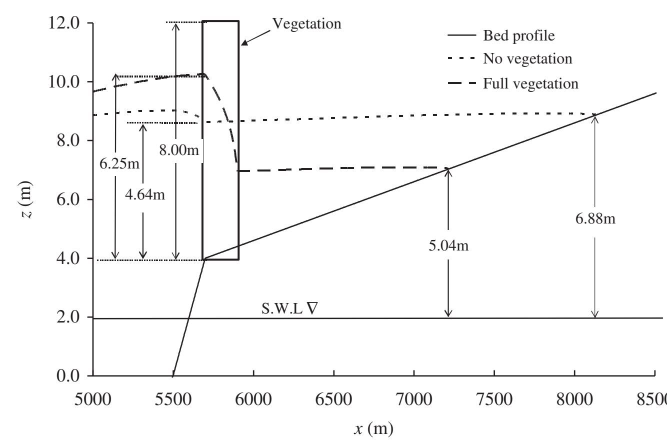

Fig. 8. Maximum water surface elevation of the first wave.

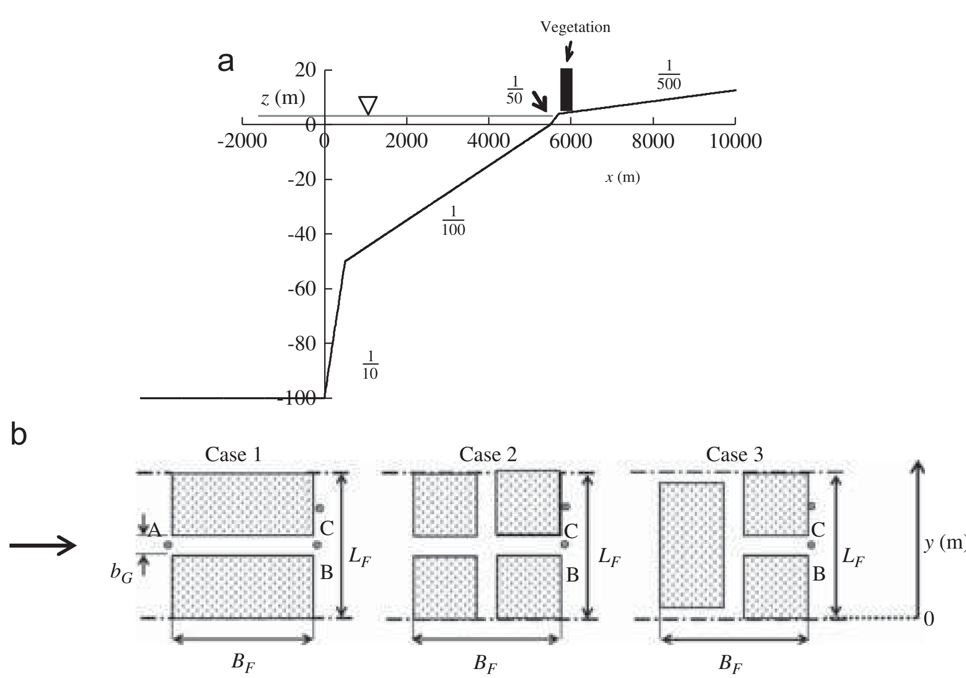

Fig. 7. Schematic of topography for numerical simulation. (a) Cross-section of topography, and (b) sketch of gap arrangement.

back up in the flow, decreases remarkably in the vegetation zone, and becomes almost constant behind the vegetation. The run-up height above the still water level is 5.04 m, which is 73% of that in the case of no vegetation. The maximum water surface elevation above the ground surface (inundated depth) at the front of vegetation is 6.25 m, which is slightly less than 80% of the height of *P. odoratissimus*.

The inundated depth 6.25 m exceeds a critical tsunami height of 5 m which is suggested for the breaking and collapse of *P. odoratissimus* species by Tanaka et al. (2007, 2009a). The inundated depth, however, includes the increase of water surface elevation due to the back up by the vegetation, in other word, reflection from the coastal forest. The reflection from the coastal forest is greatly effected by the forest width and reduces the flow velocity at the front of coastal forest. In an extreme state of no vegetation, the inundated depth reduces to 4.64 m as shown in Fig. 8, which is less than 5 m. On the other hand, the maximum flow velocity is 4.51 m/s, while it is 2.36 m/s in the case of full vegetation.

Tanaka et al. (2007) reported on the basis of field investigations for the 2004 Indian Ocean tsunami that some trees of *P. odoratissimus* at Medilla, Sri Lanka were broken in the front region of 2–5 m under the tsunami height by 5–6 m. The forest width in this case, however, is narrow as 10 m. In the present paper, the forest width is wide as 200 m which may be enough width to reduce tsunami forces on trees and scouring risk so as to avoid the tree breaking and collapse. The present condition of the incident tsunami height was selected under above-mentioned considerations. For the higher tsunami, the risk of tree breaking and collapse increases the more, and a new simulation model included the effect of tree breaking and scouring on tsunami run-up is necessary to be developed.

4.2. Flow patterns and effect of turbulence induced shear force

First, flow patterns and the effect of turbulence induced shear force on the tsunami run-up in the coastal forest with a gap are discussed. The gap arrangement of Case 1 was selected with the conditions of $L_F = 200$ m and $b_G = 15$ m for the examination. Fig. 9(a)–(d) shows the distribution of the flow velocity vector. The time t in these figures indicates the time after the start of calculations. These figures show the change of flow pattern for 144 s from $t = 624$ s, when the tip of the first wave reached the end of the gap to $t = 768$ s. Because there is no resistance by vegetation at the gap, the flow is fast there and reaches the end quickly to spread out from the exit. As time passes, however, the flow behind the vegetation gradually becomes uniform, except in the neighborhood of the gap exit. Finally, the first wave runs up to

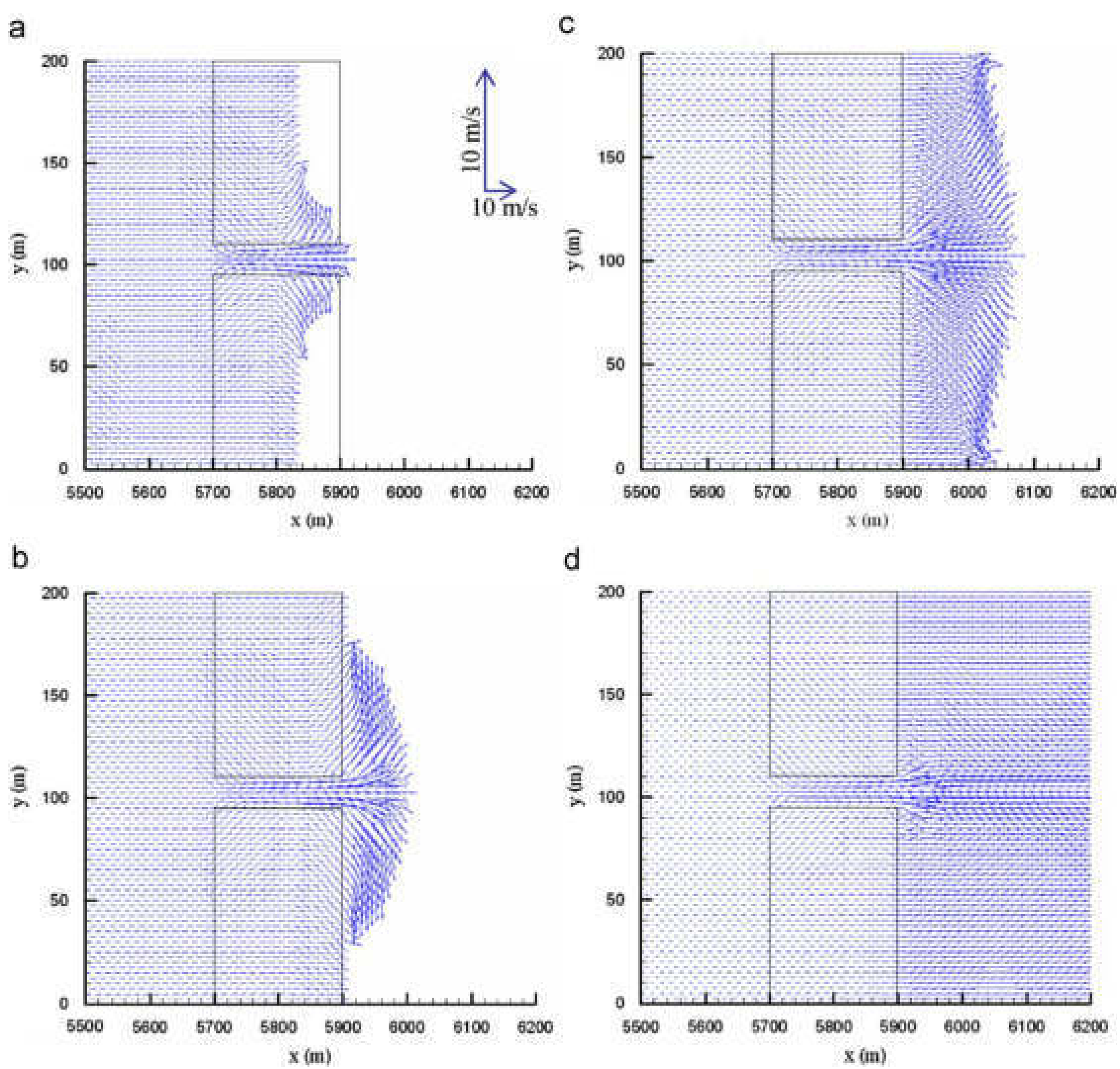

Fig. 9. Flow pattern in Case 1. (a) t=624 s; (b) t=664 s; (c) t=696 s; (d) t=768 s.

the ground elevation of 7.19 m above the datum level (5.19 m above the still water level), which is 1.7 km from the shoreline at the tide level of 2 m.

Fig. 10(a) and (b) shows the time profiles of water surface elevations measured from the datum level and flow velocity at point B (the middle at the end of the open gap) and point C (the middle behind the vegetation patch) as shown in Fig. 7(b). It is noticed that the turbulence induced shear force has little effect on water surface elevations behind the gap and vegetation patch. The maximum inundation depths at B and C are almost the same. This was also observed in the experiments, although the results are not shown in the present paper. On the other hand, the modification in flow velocity due to the turbulence induced shear force is visible at point B, where the peak magnitude of the eddy viscosity coefficient ν_e is increased greatly, as shown in Fig. 11(a). The maximum decrease of flow velocity due to the turbulence induced shear force at point B is about 0.51 m/s (7.0%). This reduction is due to the energy dissipation by the eddy viscosity, which is strongly dependent on the transverse shear of the flow. The total discharge flux that passed through the open gap is decreased to 6.5% due to the turbulence induced shear force, as shown in Fig. 11(b). It can be concluded that the turbulence induced shear force slows the water flow in the gap, and therefore, it is better to include these effects appropriately in the numerical model.

In actual scale, the reduction of maximum velocity due to the turbulence induced shear force was observed similarly in the laboratory scale, despite their large difference of Reynolds number. The effect of turbulence induced shear force, however, depends on the turbulence length scale coefficient. Trial numerical results show that the reduction rate of maximum velocity at point B is increased as the turbulence length scale coefficient increases. Therefore, an appropriate value of the turbulence length scale coefficient in the actual scale as well as other turbulence parameters is a further subject to be investigated with field observation data.

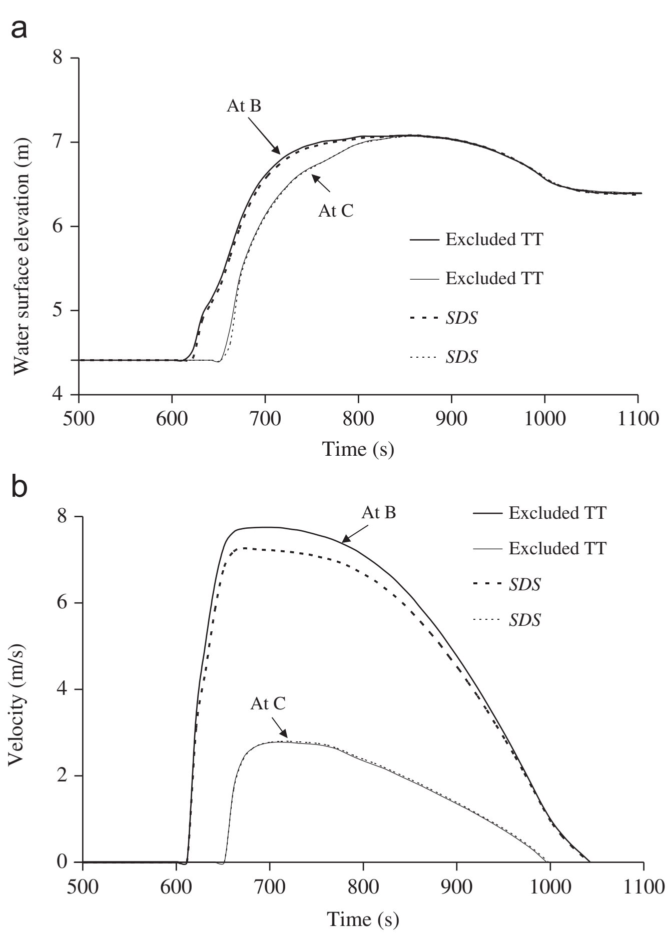

Fig. 10. Time profile of (a) water surface elevation, and (b) flow velocity.

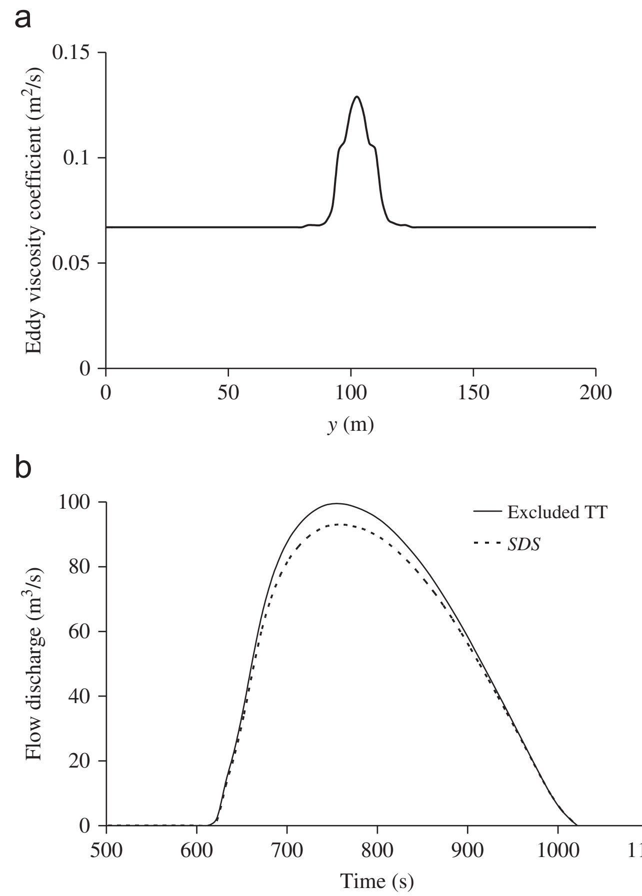

Fig. 11. (a) Along-shore distribution of maximum eddy viscosity coefficient, and (b) time profile of total flow discharge passing the exit of the gap section.

4.3. *Effects of open gap and arrangement of vegetation patch*

4.3.1. *Effect of gap width*

To investigate the effect of the gap width in a forest on a tsunami run-up, numerical simulations for Case 1 were carried out with L_F fixed as 200 m and by varying b_G.

The normalized maximum discharge flux (Q_{max}/Q_1), representative flow velocity (V_{rep}/V_{rep1}), representative inundation depth (d_{rep}/d_{rep1}) at point B, and run-up height (R/R_1) are plotted against the normalized gap width (b_G/L_F) in Fig. 12, where the representative flow velocity V_{rep} and the representative inundation depth d_{rep} are the flow velocity and inundation depth (total water depth) at the time when the discharge flux reaches the maximum in the time variation. Suffix 1 indicates the corresponding values in the case of $b_G/L_F = 1$, namely no vegetation. The representative values are not always the temporal maximum but are close to the temporal maximum. The run-up height R above the still water level is uniform along the direction parallel to the shoreline because the flow far from the forest becomes like a one-dimensional. These results are consistent with the experimental results: as the gap is widened, the flow velocity at the end of the open gap increases first, reaches the maximum at the open ratio $b_G/L_F = 0.075$ in this case, and then decreases, while the inundation depth increases

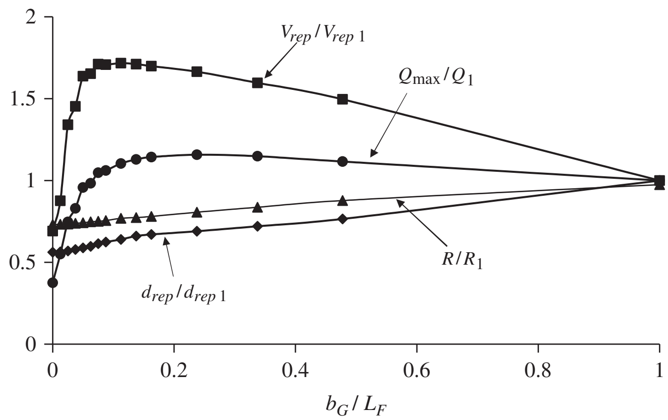

Fig. 12. Variation of normalized maximum discharge flux (Q_{max}/Q_1), representative of velocity (V_{rep}/V_{rep1}), representative of inundation depth (d_{rep}/d_{rep1}) at point B and run-up height (R/R_1).

monotonously. The run-up height has the same tendency as the inundation depth at the gap exit. The maximum velocity is 2.5 times in comparison with the case with full vegetation and 1.7 times in the case with no vegetation. These values of discharge flux and representative flow velocity are slightly smaller than the results of Tanimoto et al. (2008) due to the effect of turbulence induced shear force.

The increases of discharge flux and velocity at the end of the gap are related to the inflow from both sides of the open gap, as the physical explanation was already given in Section 3.2. Here, the time variation of the discharge flux can be examined by averaging with the gap width ($\bar{Q}_{in}$ at the inlet, $\bar{Q}_{out}$ at the outlet, and $\bar{Q}_{side}$ at the sides), as shown in Fig. 13(a), where $\bar{Q}_{side}$ is defined as the value of total inflow (positive) from both sides to the gap divided by the gap width and called the average inflow from (both) sides. Consequently, $\bar{Q}_{out}$ corresponds to a summation of $\bar{Q}_{in}$ and $\bar{Q}_{side}$ with consideration of their phase differences and is strongly dependent on the inflow coming from both sides. Fig. 13(b) shows the variation of maximum values of the average discharge fluxes and the average inflows from the sides ($\bar{Q}_{in\max}$, $\bar{Q}_{out\max}$, and $\bar{Q}_{side\max}$) against the normalized gap width. It can be seen that the average inflows from both sides vary with the gap width, similar to the representative velocity in Fig. 12, and the largest value appears at the open ratio $b_G/L_F = 0.075$, being the same as the case of the representative velocity. Fig. 14 shows the distribution of the representative x component of flow velocity (V_{xrep}) along the end line of the forest for four gap widths. The results very clearly show the effect of gap width on the velocity distribution on the along-shore section. Based on these numerical results, it can be concluded that the effect of gap width is particularly significant on flow in the open gap.

4.3.2. Effect of along-shore unit length of forest

The along-shore unit length of forest of 200 m is rather arbitrary, and the opening ratio depends on it. Therefore, in order to examine the effect of the unit length of the forest L_F on inundation depth and flow velocity at the gap exit, numerical simulations for the gap arrangement of Case 1 were conducted with conditions of $b_G = 15$ m by varying L_F. Fig. 15(a) shows the relationship of the normalized representative inundation depth (d_{rep}/d_{rep1}) and the normalized representative flow velocity (V_{rep}/V_{rep1}) at point B with the normalized unit length of forest to the gap width (L_F/b_G), where d_{rep1} and V_{rep1} are the representative inundation depth and representative flow velocity for the case of

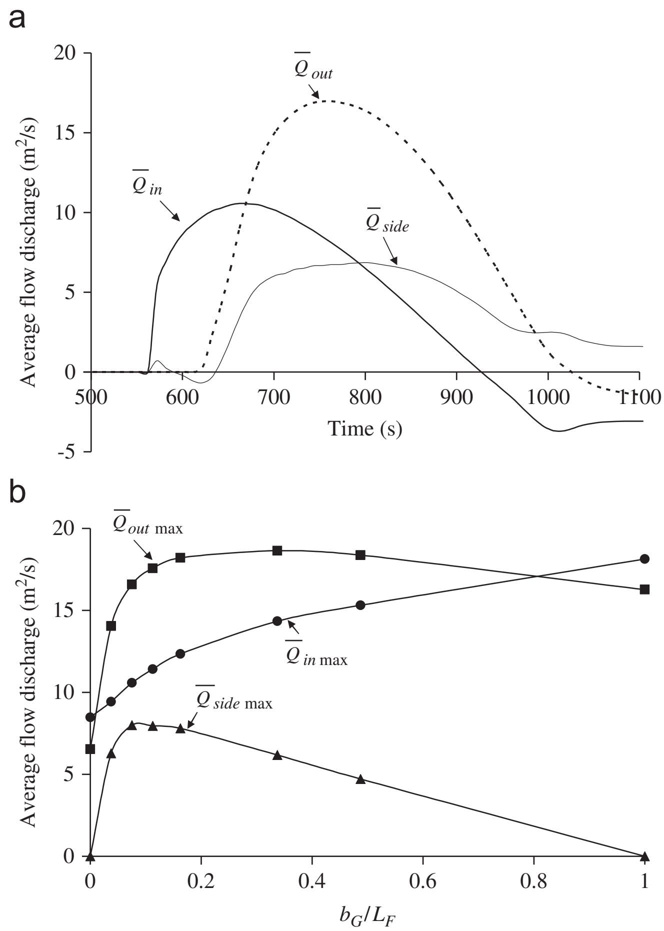

Fig. 13. (a) Time profile of average discharge flux ($\bar{Q}_{in}$ at the inlet, $\bar{Q}_{out}$ at the outlet, and $\bar{Q}_{side}$ at the sides), and (b) variation of maximum average discharge fluxes and the average inflows from the sides ($\bar{Q}_{in\max}$ at the inlet, $\bar{Q}_{out\max}$ at the outlet, and $\bar{Q}_{side\max}$ at the sides).

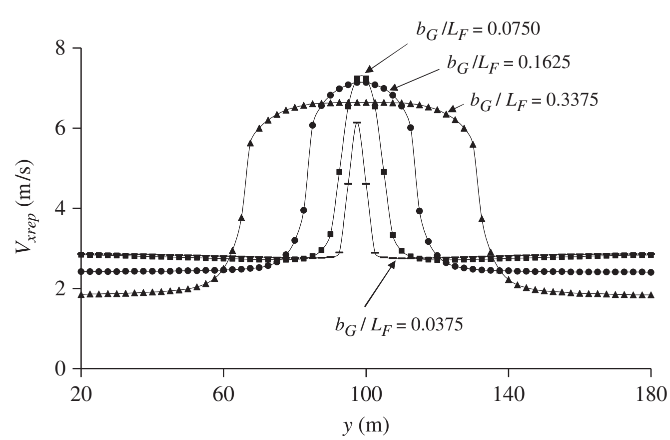

Fig. 14. Along-shore distribution of V_{xrep} at end of the forest.

$L_F/b_G = 1$, namely no vegetation. The inundation depth decreases and the flow velocity increases with the increasing unit length of forest. However, the change rate decreases as the unit length of forest increases and becomes almost zero around $L_F/b_G = 14$, where d_{rep}/d_{rep1} and V_{rep}/V_{rep1} are about 0.6 and 1.7, respectively. The enhancements of velocity at the end of the gap depend on the magnitude of the average inflow from both sides. This is examined in Fig. 15(b), where the variations of $\bar{Q}_{sidemax}$ with L_F/b_G are shown. In the figure, the average inflow from both sides varies with the unit length of forest, similar to the representative velocity shown in Fig. 15(a). It becomes constant when L_F/b_G exceeds 14, being same as the case of representative velocity.

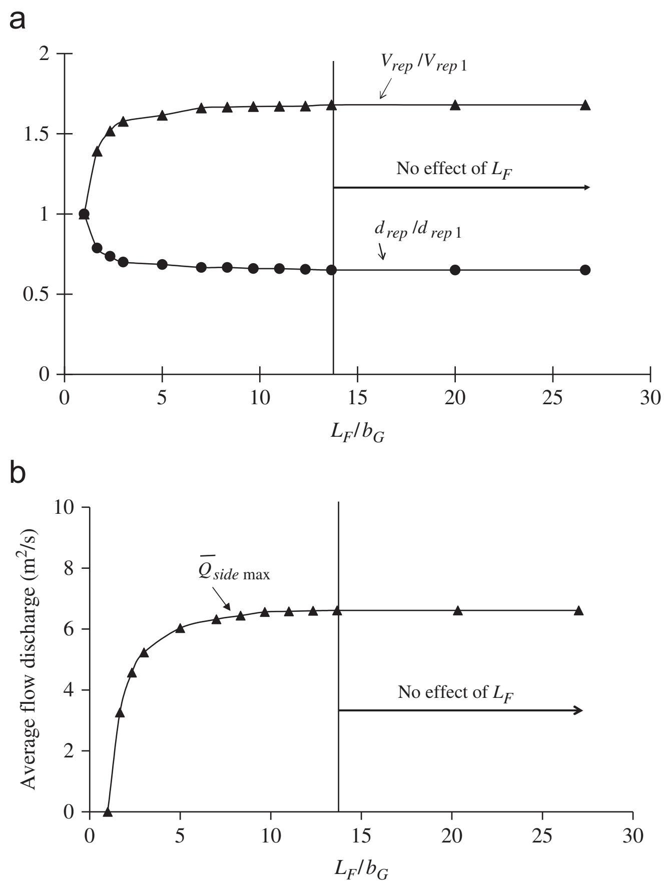

Fig. 15. The effect of unit forest length. (a) Variation of normalized representative inundation depth (d_{rep}/d_{rep1}) and representative velocity (V_{rep}/V_{rep1}) at point B, and (b) maximum of average inflow from sides ($\bar{Q}_{sidemax}$).

4.3.3. *Effect of gap arrangement (arrangement of vegetation patches)*

In addition to the gap arrangement of Case 1 (a single open gap), the two-gap arrangements of Case 2 (cross open gaps) and Case 3 (staggered open gaps) shown in Fig. 7(b) were examined to elucidate the effect of gap arrangement. In both cases, the open gap parallel to the shoreline was set at the middle of the forest width B_F. The size of the forest is the same at $B_F = 200$ m and $L_F = 200$ m. The gap width b_G is also kept constant at 15 m. Consequently, the gap width at both sides in Case 3 is set as 7.5 m in the numerical simulation due to the mirror image, so that the total gap width is kept as a constant at the inlet and outlet for all cases. Fig. 16 illustrates the effect of gap arrangement on the flow patterns in the two cases. The difference in flow patterns due to the gap arrangement is clear.

Fig. 17(a) and (b) shows the time profiles of water surface elevation at points B and C for the two cases. The difference in the water surface elevation is not large in either case, and the maximum difference is only 0.1 m (1.5%) at point B. The run-up heights are plotted in Fig. 18, including cases of no forest and full vegetation and Case 1. In consequence, the effect of the gap arrangement on the run-up height is small. On the other hand, the gap arrangement has considerable effect on the flow velocity. Fig. 19(a) and (b) shows the time profiles of flow velocities at points B and C for Cases 2 and 3. Compared with Case 2, the maximum flow velocity of Case 3 is decreased by about 0.91 m/s (13.0%) at point B, and it is increased 0.23 m/s (7.0%) at point C. The reduction of flow velocity at the gap exit in Case 3 is caused by the resistance of vegetation before water enters the gap in the landside vegetation patch, while in Case 2, the flow comes directly to the gap and is increased by inflow from both sides in the process of propagation.

It is concluded that, in the conditions of the present study, the gap arrangement has a significant effect on flow velocity in the gap, particularly flow velocity at the exit, while it has an insignificant influence on the run-up height. The gap arrangement of Case 3 exhibits a considerably reduced maximum velocity at the gap exit.

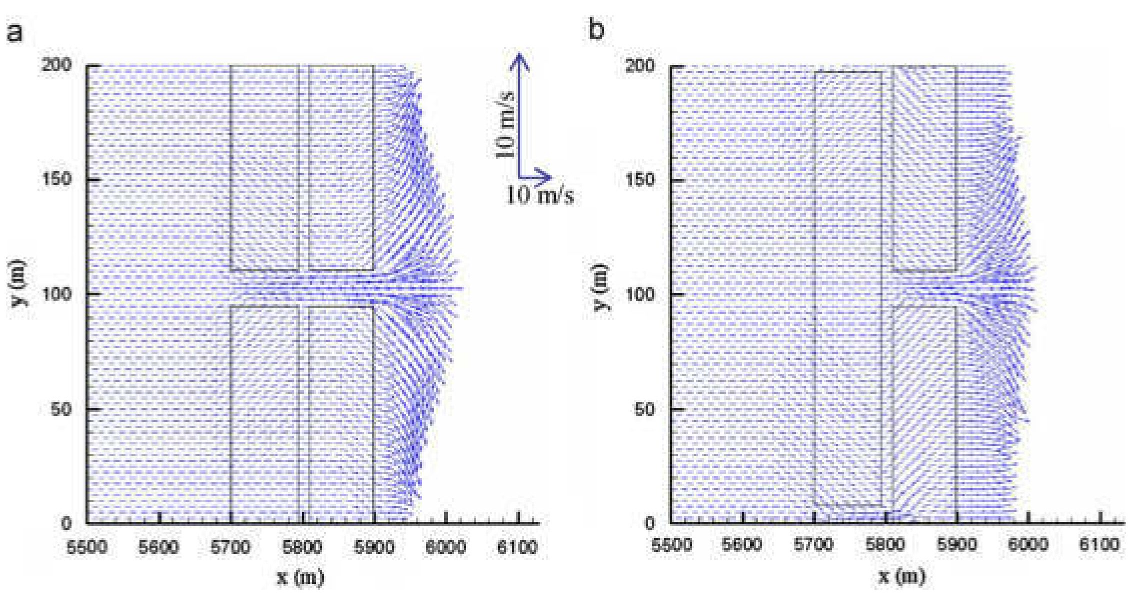

Fig. 16. Flow patterns at 680 s, (a) Case 2, and (b) Case 3.

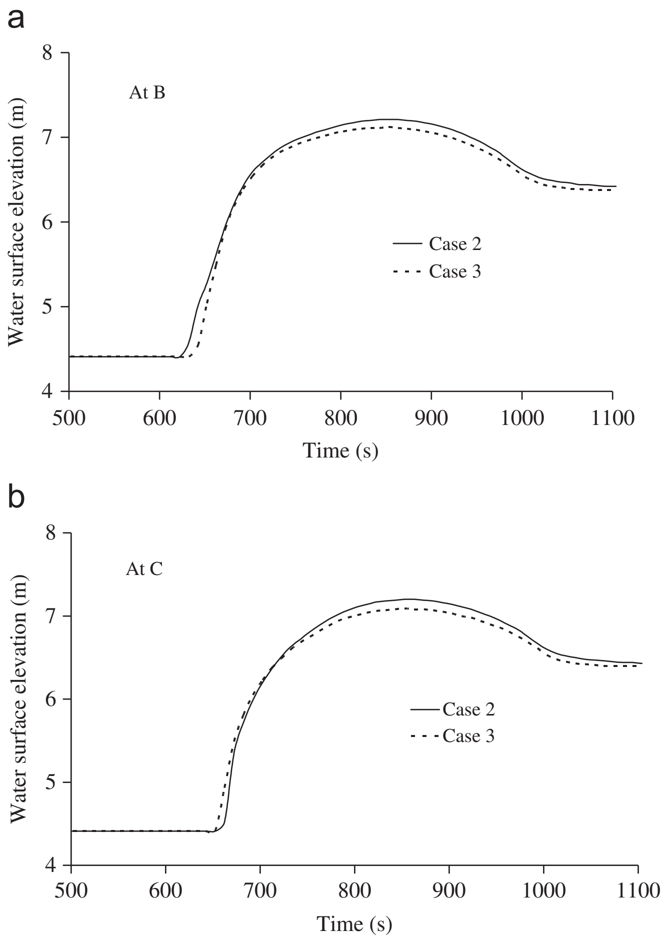

Fig. 17. Time profiles of water surface elevation. (a) At point B, and (b) at point C.

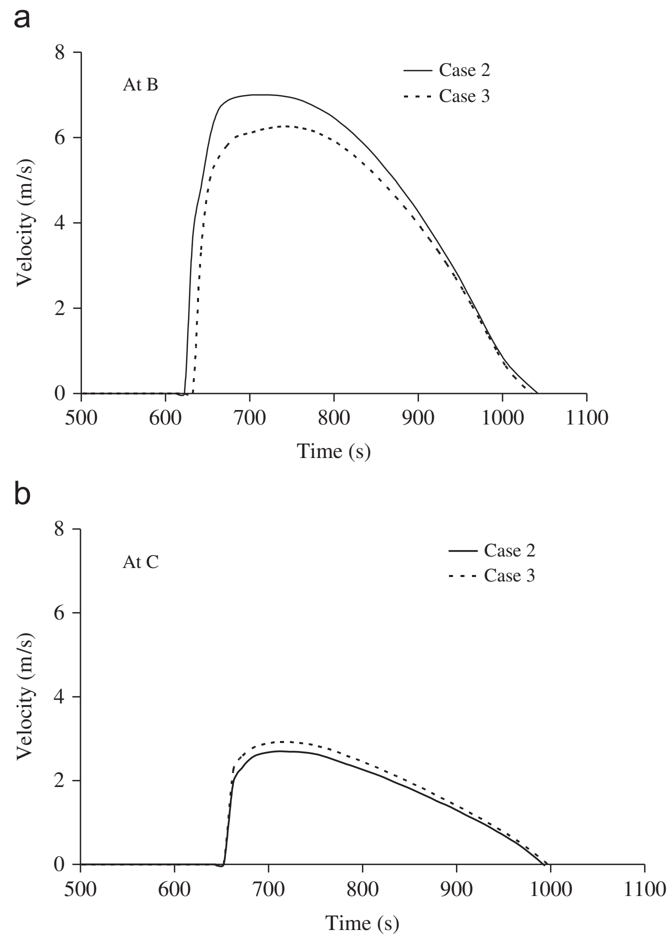

Fig. 19. Time profiles of flow velocity. (a) At point B, and (b) at point C.

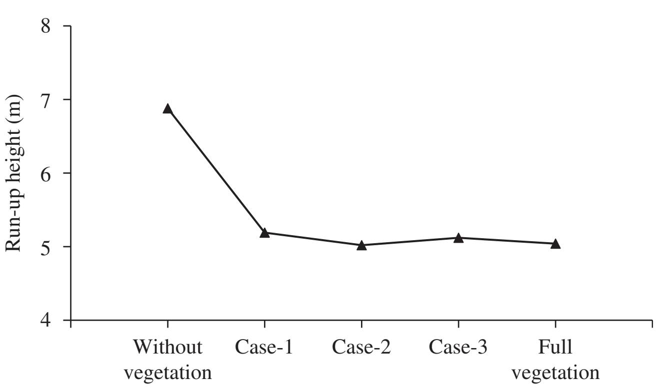

Fig. 18. Run-up height in five cases.

5. Conclusions

Laboratory experiments using a wave channel and numerical simulations were carried out to investigate the effects of an open gap in a coastal forest on tsunami run-up. The effects of gap width, forest length, and gap arrangement were discussed based on the results. The present study can be summarized as follows:

1. A two-dimensional numerical model of nonlinear long waves including resistance due to vegetation and turbulence induced shear force was developed, and the applicability was confirmed by good agreement with experimental results. In the numerical model, the eddy viscosity coefficient is evaluated by a sub-depth scale turbulence model by Nadaoka and Yagi (1998) with a modification related to the bottom friction and vegetation drag. The evaluation of the resistance due to vegetation is based on drag forces on trees proposed by Tanaka et al. (2007) with due consideration of the vertical characteristics.
2. In general, the turbulence induced shear force plays a significant role in slowing the water flow slightly in the open gap. The flow velocity in the gap is reduced by the effect of turbulence induced shear force, while the turbulence induced shear force has little effect on the inundation depth and consequently the run-up height. These results were confirmed by experiments and numerical simulations.
3. A coastal topography with an along-shore forest which is uniform in the direction of a straight shoreline was used to investigate the effect of an open gap on tsunami run-up. Three types of gap arrangements were considered: a straight gap perpendicular to the shoreline, cross gaps with a gap parallel to the shoreline, and staggered gaps in the direction perpendicular to the shoreline with the straight parallel gap. *P. odoratissimus* of 8 m in height was considered as the tree species consisting the forest. A sinusoidal tsunami with a period of 20 min was considered to attack the coast perpendicularly to the shoreline. The maximum tsunami height was set so that the inundation depth in the forest due to the tsunami run-up is about 80% of the tree height at the front of the forest to avoid over-wash.

The gap width affects primarily flow velocity and inundation depth. The flow velocity in the gap, however, is different from the tendency in the inundation depth and the run-up height. As the gap width increases, the flow velocity at the gap exit increases at first, reaches the maximum value, and then decreases. This variation is caused by the difference in total inflow averaged with the gap width from the vegetation patches to the gap in the forest. When the forest width is 200 m in the direction perpendicular to the shoreline and the along-shore forest is long enough to avoid the effect of flow from the ends of the forest in the direction parallel to the shoreline, the flow velocity at the end of the 15 m wide gap located in the middle of the forest length reaches the maximum value of 2.5 times in comparison with the case of no gap and 1.7 times the case of no vegetation belt.

4. The flow velocity in the gap can be reduced by the appropriate gap arrangement. In the case of a staggered arrangement in a 200-m-wide forest, the flow velocity at the gap exit is reduced about 13% in comparison with the case of a cross arrangement, while the arrangement of the gap(s) has little effect on the inundation depth and consequently the run-up height.

In the present paper, the forest width was fixed as 200 m. The mitigation of tsunami run-up behind a forest strongly depends on the forest width. The effect of forest width on tsunami run-up with the presence of open gap will be investigated for various vegetation species in future work.

In particular, this study considered a single layer of *P. odoratissimus* in the vertical direction of vegetation. Tanaka et al. (2007) pointed out that the application of *P. odoratissimus* as a vegetation bioshield has a limitation due to the relatively weak strength for high incoming tsunamis and two layers of vegetation by *P. odoratissimus* and *Casuarina equisetifolia* have a strong potential as an effective vegetation bioshield. Also, the flow velocity was discussed mainly in the present paper, however the tsunami forces and breaking moments which are related with square of velocity are more directly related with possible damages. Those are subjects of follow-up studies.

Another important problem is scouring around the vegetation. This problem as well as validation of the numerical model against field measurements is the subject of future studies.

Acknowledgements

This study is partially funded by the Sumitomo Foundation. The authors wish to acknowledge Mr. N.A.K. Nandasena for his contribution in setting up the laboratory experiments.

References

Danielsen, F., Sorensen, M.K., Olwig, M.F., Selvam, V., Parish, F., Burgess, N.D., Hiraishi, T., Karunagaran, V.M., Rasmussen, M.S., Hansen, L.B., Quarto, A., Suryadiputra, N., 2005. The Asian tsunami: a protective role for coastal vegetation. Science 310, 643.

Fernando, H.J.S., Samarawickrama, S.P., Balasubramanian, S., Hettiarachchi, S.S.L., Voropayev, S., 2008. Effects of porous barriers such as coral reefs on coastal wave propagation. Journal of Hydro-environment Research 1, 187–194.

Harada, K., Imamura, F., 2005. Effects of coastal forest on tsunami hazard mitigation—a preliminary investigation, tsunamis: case studies and resent development. In: Satake, K. (Ed.), Advances in Natural and Technological Hazards Research. Springer, pp. 279–292.

Hiraishi, T., Harada, K., 2003. Greenbelt tsunami prevention in South-Pacific region. Report of the Port and Airport Research Institute 42 (2) 23 p.

Kathiresan, K., Rajendran, N., 2005. Coastal mangrove forests mitigated tsunami, short note. Estuarine, Coastal and Shelf Science 65, 601–606.

Kerr, A.M., Baird, H.B., 2007. Natural Barriers to Natural Disasters. View point of BioScience. 57(2), 102–103. February.

Mascarenhas, A., Jayakumar, S., 2008. An environmental perspective of the post-tsunami scenario along the coast of Tamil Nadu, India: Role of sand dunes and forests. Journal of Environmental Management 89, 24–34.

Mazda, Y., Kobashi, D., Okada, S., 2005. Tidal-scale hydrodynamics within mangrove swamps. Wetlands Ecology and Management 13, 647–655.

Mazda, Y., Parish, F., Danielsen, F., Imamura, F., 2007. Hydraulic functions of mangroves in relation to tsunamis. Mangrove Science 4–5, 57–67.

Nadaoka, K., Yagi, H., 1998. Shallow-water turbulence modeling and horizontal larger-eddy computation of river flow. Journal of Hydraulic Engineering 124 (5), 493–500.

Nandasena, N.A.K., Tanaka, N., Tanimoto, K., 2008. Perspective of coastal vegetation patches with topography variations for tsunami protection in 2D-numerical modeling. Annual Journal of Hydraulic Engineering, JSCE 52, 133–138.

Rodi, W., 2000. Turbulence models and their application in hydraulics, IAHR Monograph, third ed. Taylor & Francis, London and New York.

Shuto, N., 1987. The effectiveness and limit of tsunami control forests. Coastal Engineering in Japan 30 (1), 143–153.

Su, X., Li, C.W., 2002. Large eddy simulation of free surface turbulent flow in partly vegetated open channels. International Journal for Numerical Methods in Fluids 39, 919–937.

Tanaka, N., Sasaki, Y., Mowjood, M.I.M., Jinadasa, K.B.S.N., 2007. Coastal vegetation structures and their functions in tsunami protection: Experience of the recent Indian Ocean tsunami. Landscape and Ecological Engineering 3, 33–45.

Tanaka, N., Nandasena, N.A.K., Jinadasa, K.S.B.N., Sasaki, Y., Tanimoto, K., Mowjood, M.I.M., 2009a. Developing effective vegetation bioshield for tsunami protection. Journal of Civil and Environmental Engineering Systems 26, 163–180 (Taylor & Francis).

Tanaka, N., 2009b. Vegetation bioshields for tsunami mitigation: review of the effectiveness, limitations, construction, and sustainable management. Landscape and Ecological Engineering 5, 71–79.

Tanimoto, K., Tanaka, N., Nandasena, N.A.K., Iimura, K., Shimizu, T., 2007. Numerical simulation of tsunami prevention by coastal forest with several species of tropical tree. Annual Journal of Coastal Engineering, JSCE 54 (2), 1381–1385 (in Japanese).

Tanimoto, K., Tanaka, N., Thuy, N.B., Nandasena, N.A.K., Iimura, K., 2008. Effect of open gap in coastal forest on tsunami run-up—investigation by 2-dimensional numerical simulation. Annual Journal of Civil Engineering in the Ocean, JSCE 24, 87–92 (in Japanese).

Thuy, N.B., Tanimoto, K., Tanaka, N., 2008. Numerical investigation of the effects of opening gap width in forest on tsunami run-up in the coast. In: Proceedings of the 10th International Summer Symposium. JSCE, Japan, pp. 61–64.

Journal of Japan Society of Civil Engineers, Ser. B2 (Coastal Engineering)

Online ISSN : 1883-8944
Print ISSN : 1884-2399
ISSN-L : 1883-8944

Journal home Journal issue About the journal

Volume 65 , Issue 1

Showing 51-100 articles out of 295 articles from the selected issue

---

Dynamic Tsunami Generation Process by 3-Diminsion Simulation

Tetsuji IMAI, Tatsuo OHMACHI, Shusaku INOUE

2009 Volume 65 Issue 1 Pages 251-255
Published: 2009
Released: February 23, 2010

DOI https://doi.org/10.2208/kaigan.65.251

JOURNALS FREE ACCESS

Show abstract

Download PDF (545K)

Applicability of the Lattice Boltzmann Method for Tsunami Modeling

Shunichi KOSHIMURA, Kazuyuki MURAKAMI

2009 Volume 65 Issue 1 Pages 256-260
Published: 2009
Released: February 23, 2010

DOI https://doi.org/10.2208/kaigan.65.256

JOURNALS FREE ACCESS

Show abstract

Download PDF (747K)

DOI https://doi.org/10.2208/kaigan.65.356

JOURNALS FREE ACCESS

Show abstract

Download PDF (4188K)

Tsunami Flow around Edge of Coastal Forest-Experiments and Numerical Simulations-

Katsutoshi TANIMOTO, Norio TANAKA, N. B. THUY, Kosuke IIMURA, Kenji HA ...

2009 Volume 65 Issue 1 Pages 361-365
Published: 2009
Released: March 05, 2010

DOI https://doi.org/10.2208/kaigan.65.361

JOURNALS FREE ACCESS

Hide abstract

In the present study, laboratory experiments have been carried out to confirm the applicability of numerical method based on two-dimensional non-linear long wave equations incorporated with drag resistance of trees and eddy viscosity forces to tsunami flow around the edge of coastal forest. Then the method has been applied to a prototype scale condition to investigate tsunami flow around edge of coastal forest of Pandanus odoratissimus. The flow velocity outside and around the edge of coastal forest is increased, consequently the potential tsunami force is considerably increased there. On the other hand, the moment due to drag force at the top of aerial root of P. odoratissimus near the edge of the forest is decreased significantly to reduce the risk of breaking as the forest width increases.

Download PDF (964K)

Analysis and Evaluation of Tsunami Mitigation Effects by Coastal Vegetation

Kosuke IIMURA, Norio TANAKA, Katsutoshi TANIMOTO, Shigenobu TANAKA

2009 Volume 65 Issue 1 Pages 366-370
Published: 2009
Released: March 05, 2010

DOI https://doi.org/10.2208/kaigan.65.366

JOURNALS FREE ACCESS

Show abstract

Download PDF (821K)

Global Storm Surges by Tropical Cyclones and Vulnerability Projection in Coastal Zones

土木学会論文集B2（海岸工学）
Vol. B2-65，No.1，2009，361-365

海岸樹林端部付近における津波の流れ－実験と数値計算－

Tsunami Flow around Edge of Coastal Forest -Experiments and Numerical Simulations-

谷本勝利[1]・田中規夫[2]・N. B. THUY[3]・飯村耕介[4]・原田賢治[5]

Katsutoshi TANIMOTO, Norio TANAKA, N. B. THUY, Kosuke IIMURA and Kenji HARADA

In the present study, laboratory experiments have been carried out to confirm the applicability of numerical method based on two-dimensional non-linear long wave equations incorporated with drag resistance of trees and eddy viscosity forces to tsunami flow around the edge of coastal forest. Then the method has been applied to a prototype scale condition to investigate tsunami flow around edge of coastal forest of *Pandanus odoratissimus*. The flow velocity outside and around the edge of coastal forest is increased, consequently the potential tsunami force is considerably increased there. On the other hand, the moment due to drag force at the top of aerial root of *P.odoratissimus* near the edge of the forest is decreased significantly to reduce the risk of breaking as the forest width increases.

1. はじめに

2004年インド洋大津波に際して，珊瑚礁の切れ間や海岸樹林内の汀線に直角方向の道路背後での被害が大きいことが報告され（Fernando et al. 2008；Mascarenhas and Jayakumar，2008），これまでにも2次元数値計算によって，海岸樹林切れ間での津波の流れに及ぼす影響等が検討されている（谷本ら，2008a）．しかしながら，それらの数値計算においては，速度勾配の大きい流れに対する渦粘性の効果が考慮されておらず，また実験的検証も行われていない．そのため，本研究では，まず切れ間を有する樹林を対象とした実験を行い，灘岡・八木（1993）によるSub-Depth Scale乱流モデルに基づく渦粘性項を取り入れた数値計算法を検証する．次に，まだ十分には解明されていない海岸樹林端部付近における遡上津波の挙動について現地スケールでの数値計算を行い，特に津波による力（潜在的津波力や樹木に働く破断モーメント）に及ぼす樹林幅の影響を検討する．対象とした樹木はアダン（*Pandanus odoratissimus*）である．

2. 数値計算の基礎方程式

数値計算は，式（1）～（3）に示している水深積分型の非線形長波方程式に基づく．

$$\frac{\partial \zeta}{\partial t}+\frac{\partial Q_x}{\partial x}+\frac{\partial Q_y}{\partial y}=0 \quad \cdots\cdots(1)$$

$$\frac{\partial Q_x}{\partial t}+\frac{\partial}{\partial x}\left(\frac{Q_x^2}{d}\right)+\frac{\partial}{\partial y}\left(\frac{Q_xQ_y}{d}\right)+gd\frac{\partial \zeta}{\partial x}+\frac{\tau_{bx}}{\rho}+\frac{F_x}{\rho}-E_{vx}=0 \quad \cdots\cdots(2)$$

$$\frac{\partial Q_y}{\partial t}+\frac{\partial}{\partial x}\left(\frac{Q_xQ_y}{d}\right)+\frac{\partial}{\partial y}\left(\frac{Q_y^2}{d}\right)+gd\frac{\partial \zeta}{\partial y}+\frac{\tau_{by}}{\rho}+\frac{F_y}{\rho}-E_{vy}=0 \quad \cdots\cdots(3)$$

ここに，x，yは平面座標，tは時間，ζは水位，Q_x，Q_yはx，y方向線流量成分，dは全水深（$=h+\zeta$，h：静水深），ρは水の密度，gは重力加速度である．また，τ_{bx}，τ_{by}は水底摩擦応力，F_x，F_yは単位面積あたりの樹林による抵抗力，E_{vx}，E_{vy}は渦粘性項のそれぞれx，y方向成分であり，摩擦応力ベクトル$\vec{\tau}_b$および樹林による抵抗力ベクトル$\vec{F}$は次式で与える（田中ら，2006）．

$$\vec{\tau}_b=\frac{\rho g n^2}{d^{4/3}}\frac{\vec{Q}|\vec{Q}|}{d} \quad \cdots\cdots(4)$$

$$\vec{F}=\gamma\frac{1}{2}\rho C_{D-all}b_{ref}\frac{\vec{Q}|\vec{Q}|}{d} \quad \cdots\cdots(5)$$

$$C_{D-all}(d)=C_{Dref}\frac{1}{d}\int_0^d\frac{C_D(z_G)}{C_{Dref}}\frac{b(z_G)}{b_{ref}}dz_G \quad \cdots\cdots(6)$$

ここに，nはManningの粗度係数，$\vec{Q}$は線流量ベクトル，γは単位面積あたりの樹木本数，b_{ref}は樹木の基準投影幅（胸高における幹の直径），C_{Dref}は基準抗力係数（胸高における幹に対する値），b，C_Dは地面からの高さz_Gでの樹木の幹と枝の投影幅とその高さでの抗力係数である．

また，渦粘性項は次式で与える．

$$E_{vx}=\frac{\partial}{\partial x}\left(2\nu_e\frac{\partial Q_x}{\partial x}\right)+\frac{\partial}{\partial y}\left\{\nu_e\left(\frac{\partial Q_y}{\partial x}+\frac{\partial Q_x}{\partial y}\right)\right\} \quad \cdots(7)$$

$$E_{vy}=\frac{\partial}{\partial x}\left\{\nu_e\left(\frac{\partial Q_x}{\partial y}+\frac{\partial Q_y}{\partial x}\right)\right\}+\frac{\partial}{\partial y}\left(2\nu_e\frac{\partial Q_y}{\partial y}\right) \quad \cdots\cdots(8)$$

ここに，ν_eは渦動粘性係数であり，灘岡・八木（1993）のSDS（Sub-Depth Scale）乱流モデルに倣い，次の乱れ

1 フェロー 工博 埼玉大学名誉教授
2 正会員 工博 埼玉大学教授大学院理工学研究科
3 修（工） 埼玉大学大学院理工学研究科理工学専攻
4 学生会員 修（工） 埼玉大学大学院理工学研究科理工学専攻
5 正会員 博（工） 埼玉大学助教大学院理工学研究科

エネルギーk_Dの輸送方程式を解くことによって与える．

$$\frac{\partial k_D}{\partial t}+V_x\frac{\partial k_D}{\partial x}+V_y\frac{\partial k_D}{\partial y} =\frac{1}{d}\frac{\partial}{\partial x}\left(d\frac{\nu_e}{\sigma_k}\frac{\partial k_D}{\partial x}\right)+\frac{1}{d}\frac{\partial}{\partial y}\left(d\frac{\nu_e}{\sigma_k}\frac{\partial k_D}{\partial y}\right) + p_{kh}+p_{kv}+p_{kd}-\varepsilon_D \quad\cdots\cdots(9)$$

渦動粘性係数：$\nu_e = c_w \dfrac{k_D{}^2}{\varepsilon_D}$ ………………(10)

乱れエネルギー消散率：$\varepsilon_D = c_d \dfrac{k_D{}^{1.5}}{\alpha d}$ ……(11)

水平せん断変形による乱れエネルギー生産：

$$p_{kh}=\nu_e\left[2\left(\frac{\partial V_x}{\partial x}\right)^2+\left(\frac{\partial V_x}{\partial y}+\frac{\partial V_y}{\partial x}\right)^2+2\left(\frac{\partial V_y}{\partial y}\right)^2\right] \quad\cdots(12)$$

底面摩擦によるSDSエネルギー生産：

$$p_{kv}=\frac{gn^2}{d^{4/3}}(V_x{}^2+V_y{}^2)^{1.5} \quad\cdots\cdots(13)$$

樹林抵抗によるSDSエネルギー生産：

$$p_{kd}=\frac{\gamma b_{ref}\,C_{D-all}}{2}\left(V_x{}^2+V_y{}^2\right)^{1.5} \quad\cdots\cdots(14)$$

ここに，V_x，V_yは水深平均流速成分である．また，式中のモデル係数については標準的な次の値を用いる．

$$\sigma_k=1.0,\ c_w=0.09,\ c_d=0.17 \quad\cdots\cdots(15)$$

乱れ長さスケールの係数αについては後述する．

実際の計算は基礎式を差分式に変換して行う．差分化の方法等は基本的には谷本ら(2008b)に同じである．

3. 数値計算モデルの適用性に関する実験的検証

（1）実験条件

実験は幅（L_Fと表記）40cmの造波水路の斜面上（勾配1/20.5）汀線から70cm沖側に水路延長方向1mの樹林模型を設け（**図-1**参照），**図-2**に示しているように水路側面からの切れ間の幅b_Gを0cm（切れ間無し）から40cm（樹林無し）の範囲で8種類に変化させて行った．樹林模型は直径5mmの木製円柱を中心間隔23mmで千鳥状に配置したもので，樹林密度は0.22本/cm²であり，イメージとしては密生したマングローブ林に相当する．波は周期20sの長周期波で，**図-1**に示したG1からG6の測点で容量式波高計により水位を，また測点G6では水路幅方向に1あるいは2cm間隔で水平2成分電磁流速計により流速を測定している．流速測点の高さ位置は静水深中央である．

（2）結果と考察

実験は，多重反射系水路においてほぼ定常状態になるのを待って測定する手法で行っている．**図-3**に樹林模型が無い状態での測点G1～G6における測定波高と数値計算による水路での波高分布を示している．数値計算におけ

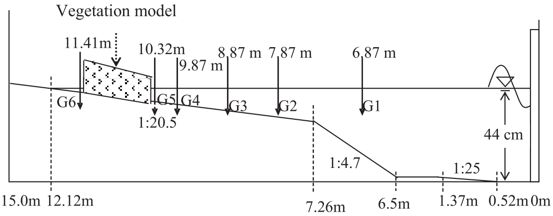

図-1　造波水路における模型と測点

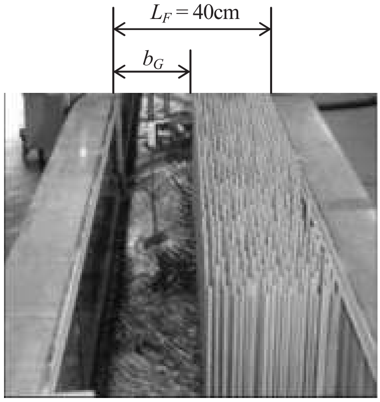

図-2　樹林模型とギャップ

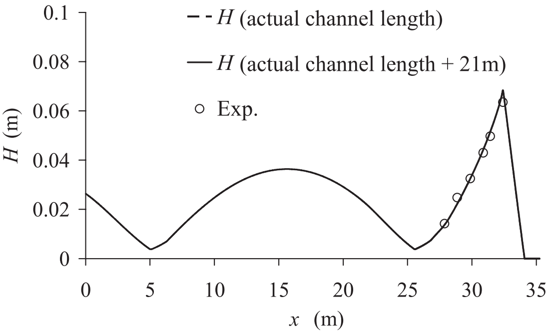

図-3　水路における波高分布（樹林模型なし）

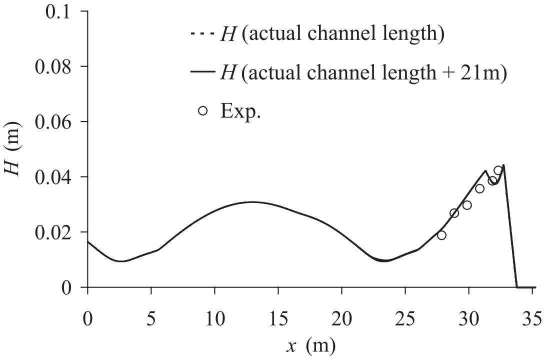

図-4　水路における波高分布（樹林模型あり）

る入射波高は測点G1での実験および数値計算による波高が一致するように，造波水深0.44mで0.020mを与えている．数値計算による波高分布は実際の水路長と造波水深

部（線形方程式の領域）を約半波長（21m）延長した水路での結果を示しているが，無反射性造波境界を採用しているため，実際の水路長の範囲で両者はほとんど完全に一致している．延長の一定水深領域でHealyの方法により反射率と分離入射波高を求めると0.82，0.020mである．この結果と計算波高分布が測定波高と全体によく合っていることから，数値計算で与えた入射波高は実際の水路における多重反射後の分離入射波高と考えられる．なお，数値計算における格子間隔は0.05m，時間間隔は0.002sであり，マニングの粗度係数nは比較的粗い木製床に対し0.012としている．

一方，図-4は樹林模型が水路幅一杯（b_G=0）の条件で入射波高を0.020mとしたときの結果である．ここに，抗力係数は実験スケールでのレイノルズ数10^2のオーダーでの単円柱に対する代表値として1.5を用いている．この場合の反射率は0.53と変化するが，波高分布はよく合っている．そのため，本研究においては，樹林がある場合においても入射波高を0.020mとして以下の計算結果を示すことにする．

最後に，b_G=7cmのケースを対象として，SDSモデルにおける乱れ長さスケール係数αを検討し，0.08を採用した．以上のような値を用いて，全実験ケースに対する数値計算を行い，実験値との比較を行っているが，以下その主なものを示す．

図-5にb_G=7cm，切れ間後端中央および樹林帯後端中央での流速Vの時間変化を，図-6にそのピーク流速V_p（5波の平均値）の水路幅方向（y方向）分布を示している．ともに実験と数値計算の結果を示しており，樹林帯後端での流速の負のところでやや違いが目立つものの，全体的にはよく合っていることが確認できる．また，図-6では渦粘性項を無視した結果（Excluded EV）とk-ε法（Rodi, 2000）による結果を示しているが，本計算で採用したSDSモデルの適合性が高いことがわかる．なお，流速Vは次式で算出している．

$$V = \mathrm{sign}(V_x)\sqrt{V_x^{\ 2} + V_y^{\ 2}} \quad \cdots\cdots\cdots\cdots\cdots\cdots\cdots\cdots\cdots (16)$$

図-7は同じ波の条件で切れ間幅b_Gを変化させたときの切れ間の直ぐ背後での波峰高ζ_c，切れ間幅内での最大流速$V_{G\max}$，および最終遡上高Rをそれぞれ樹林がないときの値で割って無次元化してプロットしたものである．谷本ら（2008a）による既往の数値計算結果と同様に，切れ間幅が大きくなるにつれて波峰高や遡上高が単調な増加を示すのに対し，最大流速は極大値を有するような変化を示している．なお，遡上高は斜面上のスケールによる目視観測によっており，実験および数値計算によるb_G/L_F=1での値は表-1に示すとおりである．

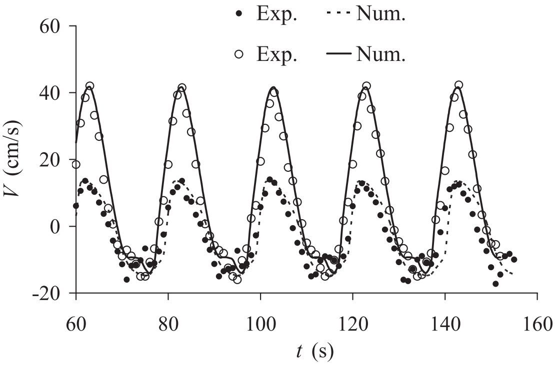

図-5　切れ間および樹林帯後端中央での流速

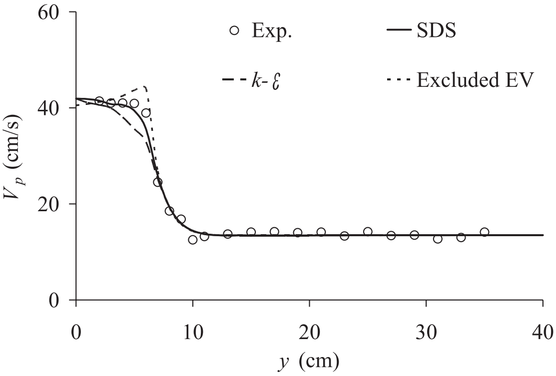

図-6　切れ間－樹林帯後端でのピーク流速の分布

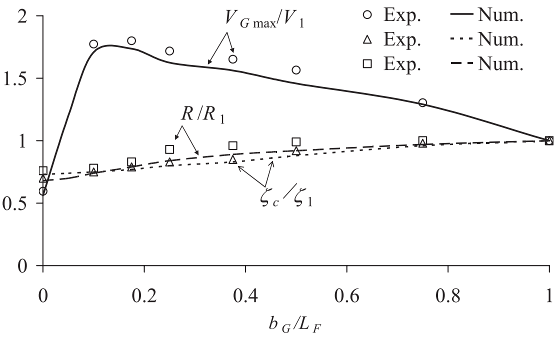

図-7　切れ間幅による切れ間後端での波峰高，最大流速，および遡上高の変化

表-1　b_G/L_F=1での波峰高，ピーク流速，遡上高

	ζ_1(cm)	V_1(cm/s)	R_1(cm)
実験	2.84	22.5	4.1
計算	2.72	24.1	3.8

4. 現地スケールでの2次元数値計算

（1）計算条件

以上のように，切れ間と樹林の境界で流速が急変し，切れ間が適当に広いと流速が樹林のないときと比べて顕著に増大することが大きな特色である．同様なことは有限

長の海岸樹林の端部付近でも生じる．そのため，本研究では十分に長い延長の海岸樹林（半無限樹林）を対象として現地スケールでの数値計算による検討を行った．

図-8は想定した海岸の断面と海岸樹林の位置を示したものであり，谷本ら（2008a）と同じである．対象とした樹種は熱帯性海岸樹のアダン（*Pandanus odoratissimus*）で，樹高H_{Tree}=8m，b_{ref}=0.2m，γ=0.22（間隔4mで千鳥状配置）であり，基準抗力係数C_{Dref}は高レイノルズ数域での表面の粗い円柱と考え1.0とした．式（5），（6）に示したように，高さによる投影幅と抗力係数の変化を考慮した抗力による樹林抵抗を考えている．なお，アダンの諸元やその抵抗特性の詳細については，田中ら（2006）および田中・佐々木（2007）を参照されたい．対象とした津波は周期が20分で，海岸線に直角に入射し，想定樹林沖側端での樹林がないとしたときの押し波第1波の地盤上津波高さ（最大没水深）が4.64mという規模のものである．

数値計算における格子間隔は10m，計算時間間隔は0.2sであり，Manningの粗度係数nは通常よく用いられている0.025とし，乱れ長さスケールの係数αについては実験条件に対して得られた0.08をそのまま用いる．

（2）結果と考察

静水面上遡上高は海岸樹林から十分離れたところ（y=4495m）で6.85m，端部から十分樹林側（y=5m）で5.40mであり，樹林端部付近背後ではこの範囲で変化する．**図-9**は樹林端部付近に限った式（17）で定義した潜在的津波力F^*（抗力係数が1で，単位投影幅で高さ方向に一様な仮想物体に働く抗力に相当，谷本ら，2007参照）のピーク値F^*_pの分布である．樹林端近傍で津波力が樹林のないとき（想定樹林沖側端で38kN/m）と比べて大きくなっていることがわかる．**図-10**はそうした分布における潜在的津波力の空間的最大値$F^*_{p\max}$の樹林幅B_Fによる変化を示している．樹林幅が広くなるにつれて，$F^*_{p\max}$は大きくなり，B_F=50m付近で極大に達し，その後は緩やかに低下する変化となる．

$$F^* = \frac{F}{\gamma C_{D-all} b_{ref}} = \frac{1}{2}\rho\frac{\vec{Q}|\vec{Q}|}{d} \quad \cdots\cdots (17)$$

ところで，樹高8mというのはアダンとして最も生長した高さに相当する．田中・佐々木（2007）は，アダンには気根があり，密集度も高く津波減殺のための海岸林として適しているものの，強度は比較的弱く，耐力に限界があることを指摘している．そのため，Tanakaら（2009）は主としてスリランカにおける海岸樹を対象として強度・破壊の現地試験を実施し，アダン等の気根上端での破断モーメントM_{GP1}（単位はb_{ref}をcm単位にとってN・m）について次の推定式を提案している（定数は次元を有す）．

$$M_{GP1} = 4.45 b_{ref}^{\ 2.62} \quad \cdots\cdots (18)$$

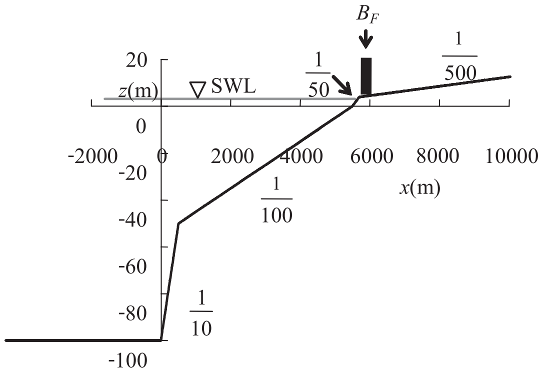

図-8　海岸断面と樹林位置

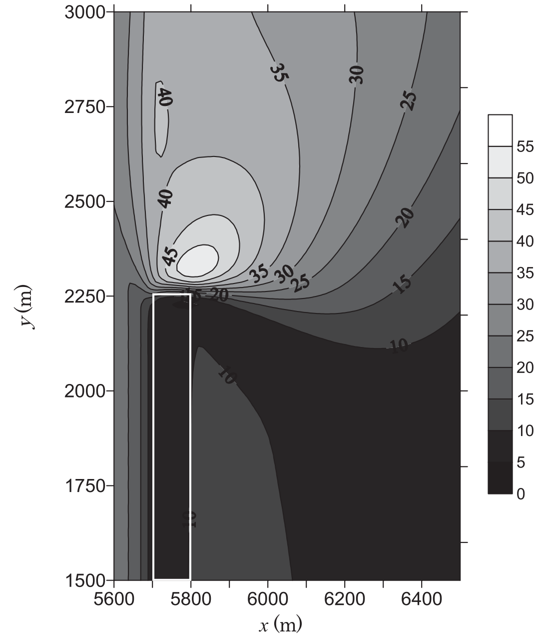

図-9　樹林端部付近における潜在的津波力のピーク値F^*_p（kN/m）の分布

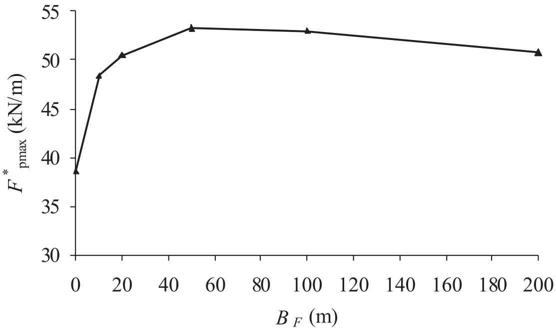

図-10　潜在的津波力の空間的最大値$F^*_{p\max}$の樹林幅による変化

そこで，以下，本計算条件の下で，気根上端での抗力によるモーメントベクトル$\vec{M}_D$を次式により計算して検討する．

$$\overrightarrow{M}_D=\frac{1}{2}\rho C_{Dref}b_{ref}\vec{V}\left|\vec{V}\right|\int_{z_1}^{d}\frac{C_D(z_G)}{C_{Dref}}\frac{b(z_G)}{b_{ref}}z_G dz_G \cdots(19)$$

ここに，$\vec{V}$は線流量を全水深で割った平均流速ベクトル，z_1は地盤面からの気根上端の高さであり，$d<z_1$ではモーメントは働かない．

図-11はB_F=100mの場合の樹林端部の沖側端付近（x=5715m，y=2245m）での抗力モーメントベクトルの大きさM_Dの時間変化を，全水深d，線流量Q，水深平均流速V，潜在的津波力F^*とともに示したものである．ここに，ベクトルの大きさM_DやQ，F^*は式（16）のVと同様に定義している．線流量と潜在的津波力のピークがほぼ同時，それより少し遅れて抗力モーメントと全水深のピークがほぼ同時に現われている．全水深と潜在的津波力のピークの起時がそれほど違わないのは，谷本ら（2007）の結果と大きく異なっているが，これは主として陸上の勾配を1/100から1/500へと緩くしたことによっている．

図-12は樹林幅を変化させたときの抗力モーメントのピーク値M_{Dp}とそのときの全水深d_{MDp}および流速V_{MDp}を示したものである．B_F=0の結果は，樹林が無いときの流れの中にアダンが単独であるときの結果であり，Tanakaら（2009）による破断モーメントを上回っている．抗力モーメントは樹木が群生し帯状となることによって急減し，樹林幅が広くなるにつれて減少することがかわかる．これは樹林内で流速が減じることと樹林帯によって津波が一部反射されることによっている．なお，樹林幅20m程度で抗力モーメントがほぼ落ち着く傾向は，本論文の条件で，樹林密度を半分にしても，また津波周期を15～30分の範囲で変化させても変わらない．

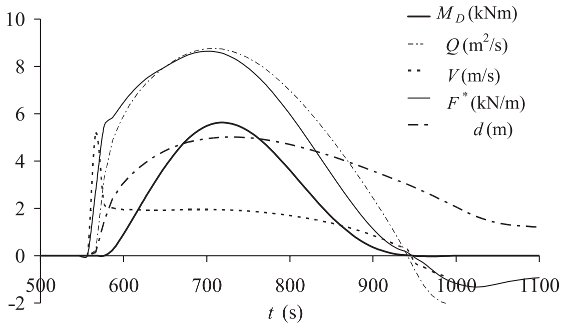

図-11　抗力モーメント等の時間変化（B_F=100m）

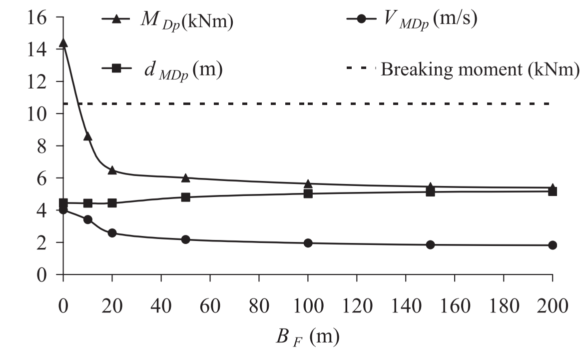

図-12　抗力モーメント等の樹林幅による変化

5. おわりに

本研究により，流速が急変する条件において，SDSモデルの適用性が高いこと，樹林切れ間において流速が増大することを実験的に検証し，延長の十分に長い樹林端部付近における津波流れの特性を検討した．樹林端部付近では流速が増大し，したがって潜在的津波力が増大する．また，樹木に働く抗力モーメントは樹林幅に大きく依存し，樹林幅が広くなるにつれて小さくなる．ただし，本研究では計算条件が限られており，今後地形や樹林特性など幅広い条件での検討が必要である．

参　考　文　献

田中規夫・武村　武・佐々木寧・M.I.M. Mowjood（2006）：スリランカ海岸林の樹種による破壊条件と津波到達遅延時間の相違，海岸工学論文集，第53巻，pp.281-285.

田中規夫・佐々木寧（2007）：2006年ジャワ津波災害において海岸林が果たした役割とその破断・なぎ倒し限界，水工学論文集，第51巻，pp.1445-1450.

谷本勝利・田中規夫・N.A.K. Nandasena・飯村耕介・清水 隆（2007）：種々の熱帯性海岸樹の組合せによる津波防御効果に関する数値計算，海岸工学論文集，第54巻，pp.1381-1385.

谷本勝利・田中規夫・N.B. Thuy・N.A.K. Nandasena・飯村耕介（2008a）：津波遡上に対する海岸樹林内通路の影響－2次元数値計算による検討－，海洋開発論文集，第24巻，pp.87-92.

谷本勝利・田中規夫・N.B. Thuy・飯村耕介（2008b）：津波の河川遡上へ及ぼす海岸および河道内樹林の影響，海岸工学論文集，第55巻，pp.260-230.

灘岡和夫・八木　宏（1993）：SDS & 2DHモデルを用いた開水路水平せん断乱流の数値シミュレーション，土木学会論文集，No.473/Ⅱ-24，pp.35-44.

Fernando, H.J.S., S.P. Samarawickrama, S. Balasubramanian, S.S.L. Hettiarachchi and S. Voropayev (2008): Effects of porous barriers such as coral reefs on coastal wave propagation. Journal of Hydro-environment Research, 1, pp.187-194.

Mascarenhas, A. and S. Jayakumar (2008): An environmental perspective of the post-tsunami scenario along the coast of Tamil Nadu, India: Role of sand dunes and forests, Journal of Environmental Management, 89, pp.24-34.

Tanaka, N., N.A.K. Nandasena, K.S.B.N. Jinadasa, Y. Sasaki, K. Tanimoto and M.I.M. Mowjood (2009): Developing effective vegetation bioshield for tsunami protection, Journal of Civil Engineering and Environmental Systems, Taylor & Francis, 26, pp.163-180.

Rodi, W. (2000): Turbulence models and their application in hydraulics, IAHR Monograph, third ed., Taylor & Francis, London and New York, 104p.

Available online at www.sciencedirect.com
SCIENCE DIRECT
Ocean Engineering 33 (2006) 350–364
OCEAN ENGINEERING
www.elsevier.com/locate/oceaneng

Numerical study of propagation of ship waves on a sloping coast

Khanh Toan Dam[a,*], Katsutoshi Tanimoto[a], Ba Thuy Nguyen[b], Yoshiyuki Akagawa[a]

[a]*Department of Civil and Environmental Engineering, Saitama University, 255 Shimo-okubo, Sakura-ku, Saitama-shi, Saitama 338-8570, Japan*
[b]*Department of Research, Marine and Meteorological Center, 18 Nguyen Chi Thanh, Dong Da District, Hanoi, Vietnam*

Received 15 November 2004; accepted 4 May 2005
Available online 8 August 2005

Abstract

The aim of this paper is to investigate the propagation of ship waves on a sloping coast on the basis of results simulated by a 2D model. The governing equations used for the present model are the improved Boussinesq-type equations. The wave breaking process is parameterized by adding a dissipation term to the depth-integrated momentum equation. To give the boundary conditions at the ship location, the slender-ship approximation is used. It was verified that, although ship waves are essentially transient, the Snell's law can be applied to predict crest orientation of the wake system on a sloping coast. Based on simulated results, an applicable empirical formula to predict the maximum wave height on the slope is introduced. The maximum wave height estimated by the proposed method agrees well with numerical simulation results.

Keywords: Depth Froude number; Divergent wave; Maximum wave height; Sailing line; Shoaling; Transverse wave

* Corresponding author. Tel.: +81 48 858 3561; fax: +81 48 858 7374.
E-mail address: sgd3053@post.saitama-u.ac.jp (K.T. Dam).

0029-8018/$ - see front matter
doi:10.1016/j.oceaneng.2005.05.003

Nomenclature

A	empirical parameter of breaking term
B	correction factor of the dispersion term
B_S	ship beam
C	wave celerity
C_1	reference wave celerity
d	ship draft
D	total depth
F_h	depth Froude number
g	gravitational acceleration
h	still water depth
H_0	deep water wave height
H_1	reference maximum wave height at $y=100$ m
H_b	limited breaking wave height
H_{max}	maximum wave height
K_d'	relative damping coefficient
K_r'	relative refraction coefficient
K_s	shoaling coefficient
K_s'	relative shoaling coefficient
K_{s1}	shoaling coefficient at $y=100$ m
L	wave length
L_0	deep water wave length
L_S	ship length
n	damping coefficient
Q_x, Q_y	depth-integrated velocity components in x and y direction
R_{bx}, R_{by}	eddy viscosity terms in x and y direction
S	transverse section area of the ship below still water level
S_0	mid-ship section area
t	time
T_1	reference wave period at $y=100$ m
T_{max}	maximum wave period
U	ship speed
x	distance in x-direction
x_S	distance from the mid-ship
y	distance from the sailing line
α	mid-ship section coefficient
β	wave angle
β_1	reference wave angle at $y=100$ m
δ	mixing length coefficient
ζ	water surface elevation
ν	eddy viscosity
π	the ratio of the circumference to the diameter of a circle

1. Introduction

Waves generated by navigating ships contain a massive amount of energy that can seriously damage the marine environment, degradation of coastal structures, and being responsible for nuisance or damage to beach users as well as other floating bodies. Since the middle of the 19th century, many investigations have been done with the aim to predict the characteristics of these waves as a function of ship hull geometry, ship speed, water depth, and the distance from the sailing line.

Havelock (1908) shows the wave height decreases exponentially with distance from the sailing line. He predicted that in sub-critical speed, the decay of divergent waves has an exponent of $n=0.33$. Sorensen (1969) used model test to show that the bow waves are generally similar to this predicted rate of decay. For super-critical ship speed, Kofoed-Hansen et al. (1999) suggested that the value of $n=0.55$ can be used. Furthermore, based on experimental result, Whittaker et al. (2001) proposed the lowest value of $n=0.2$ for shallow water. Although their studies were carried out in constant water depth only, these approaches are more practical for coastal engineering purposes and result only in an additional constant in the equation.

However, transformation due to shoaling, refraction, and breaking must be considered in addition to damping by the distance, when ship waves propagate on a sloping coast. Especially, the wakes generated by ships operating at near-critical and critical speeds, with wave heights noticeable higher, wave periods longer, and associated with shoaling and breaking, are being much more complicated.

In computation of ship waves, the wave generation by ship moving in constant water depth can be predicted using Kadomtsev–Petviashvili (KP) type equations, see e.g. Chen and Sharma (1995), where the near ship flow is approximated by a slender-ship theory. Recent advances in dispersive, nonlinear long-wave theory (Madsen and Sørensen, 1992; Nwogu, 1993; Wei et al., 1995; Beji and Nadaoka, 1996; Madsen and Schäffer, 1998) now permit the use of Boussinesq model for large computational domain. Since the basic restriction of the KP equation is not valid for unsteady cases, a set of modified Boussinesq equations, which are valid not only for long waves but also for waves of moderate length, was applied to compute ship waves in shallow water, see e.g. Tanimoto et al. (2000) and Jiang et al. (2002). Recently, Dam et al. (2004) investigated the transformation of ship waves on sloping bottom by a Boussinesq model and suggested that the refraction on slope of ship waves are similar to the ordinary wind waves.

However, none of these models described the breaking effect, which is an essential phenomenon occurred usually when waves propagate on a natural coast. In the present model, transformation of ship waves are simulated by solution of 2D depth integrated Boussinesq equations, including wave energy loss due to wave breaking. Based on simulated results, the effect of shoaling, refraction, and breaking is evaluated to estimate the travel direction and the maximum height of ship waves on slope.

2. Governing equations

The simulation method is used to solve numerically Boussinesq-type equations (Madsen and Sørensen, 1992) with a moving ship boundary (Chen and Sharma, 1995).

In the coordinate system Oxy, where the origin O lies on the calm water-plane, the x-axis points in the direction of ship's forward motion, the y-axis pointing toward the shore, the governing equations are written as:

$$\frac{\partial \zeta}{\partial t} + \frac{\partial Q_x}{\partial x} + \frac{\partial Q_y}{\partial y} = 0 \tag{1}$$

$$\begin{aligned}
&\frac{\partial Q_x}{\partial t} + \frac{\partial}{\partial x}\left(\frac{Q_x^2}{D}\right) + \frac{\partial}{\partial y}\left(\frac{Q_x Q_y}{D}\right) + gD\frac{\partial \zeta}{\partial x} \\
&\quad = \left(B + \frac{1}{3}\right)h^2\left(\frac{\partial^3 Q_x}{\partial t \partial x^2} + \frac{\partial^3 Q_y}{\partial t \partial x \partial y}\right) + Bgh^3\left(\frac{\partial^3 \zeta}{\partial x^3} + \frac{\partial^3 \zeta}{\partial x \partial y^2}\right) + h \\
&\qquad \times \frac{\partial h}{\partial x}\left(\frac{1}{3}\frac{\partial^2 Q_x}{\partial t \partial x} + \frac{1}{6}\frac{\partial^2 Q_y}{\partial t \partial y}\right) + h\frac{\partial h}{\partial y}\left(\frac{1}{6}\frac{\partial^2 Q_y}{\partial t \partial x}\right) \\
&\qquad + Bgh^2\left\{\frac{\partial h}{\partial x}\left(2\frac{\partial^2 \zeta}{\partial x^2} + \frac{\partial^2 \zeta}{\partial y^2}\right) + \frac{\partial h}{\partial y}\frac{\partial^2 \zeta}{\partial x \partial y}\right\} + R_{bx}
\end{aligned} \tag{2}$$

$$\begin{aligned}
&\frac{\partial Q_y}{\partial t} + \frac{\partial}{\partial y}\left(\frac{Q_y^2}{D}\right) + \frac{\partial}{\partial x}\left(\frac{Q_x Q_y}{D}\right) + gD\frac{\partial \zeta}{\partial y} \\
&\quad = \left(B + \frac{1}{3}\right)h^2\left(\frac{\partial^3 Q_y}{\partial t \partial y^2} + \frac{\partial^3 Q_x}{\partial t \partial x \partial y}\right) + Bgh^3\left(\frac{\partial^3 \zeta}{\partial y^3} + \frac{\partial^3 \zeta}{\partial x^2 \partial y}\right) + h \\
&\qquad \times \frac{\partial h}{\partial y}\left(\frac{1}{3}\frac{\partial^2 Q_y}{\partial t \partial y} + \frac{1}{6}\frac{\partial^2 Q_y}{\partial t \partial x}\right) + h\frac{\partial h}{\partial y}\left(\frac{1}{6}\frac{\partial^2 Q_y}{\partial t \partial y}\right) \\
&\qquad + Bgh^2\left\{\frac{\partial h}{\partial y}\left(\frac{\partial^2 \zeta}{\partial x^2} + 2\frac{\partial^2 \zeta}{\partial y^2}\right) + \frac{\partial h}{\partial x}\frac{\partial^2 \zeta}{\partial x \partial y}\right\} + R_{by}
\end{aligned} \tag{3}$$

Herein, $\zeta(x, y, t)$ is the water surface elevation, $Q_x(x, y, t)$ and $Q_y(x, y, t)$ are the depth-integrated velocity components in x and y directions, t is the time, $h(x, y)$ the still water depth, $D(x, y, t)$ is the total depth ($D = \zeta + h$), g is the gravitational acceleration, and B is the correction factor of the dispersion term ($B = 1/15$). R_{bx} and R_{by} are eddy viscosity term in x and y direction, respectively.

3. Breaking model

To simulate surf zone hydrodynamics, energy dissipation due to wave breaking is modeled by introducing two additional eddy viscosity terms (R_{bx} and R_{by}) into the momentum equations (Eqs. (2) and (3)). These momentum mixing terms are modified and improved by Kennedy et al. (2000) and Chen et al. (2000), as follows:

$$R_{bx} = \frac{\partial}{\partial x}\left(\nu\frac{\partial Q_x}{\partial x}\right) + \frac{1}{2}\left[\frac{\partial}{\partial y}\left(\nu\frac{\partial Q_x}{\partial y}\right) + \frac{\partial}{\partial y}\left(\nu\frac{\partial Q_y}{\partial x}\right)\right] \tag{4}$$

$$R_{by} = \frac{\partial}{\partial y}\left(\nu\frac{\partial Q_y}{\partial y}\right) + \frac{1}{2}\left[\frac{\partial}{\partial x}\left(\nu\frac{\partial Q_x}{\partial y}\right) + \frac{\partial}{\partial x}\left(\nu\frac{\partial Q_y}{\partial x}\right)\right] \tag{5}$$

The eddy viscosity ν, which is a function of both space and time localized on the front face of breaksing wave, is determined in a similar formula proposed by Zelt (1991).

$$\nu = A\delta^2(h+\zeta)\frac{\partial\zeta}{\partial t} \tag{6}$$

where δ is a mixing length coefficient with an empirical value of 1.2. The quantity A that controls the occurrence of energy dissipation is smoothly varied from 0 to 1.0 to avoid an impulsive start of breaking. Detailed formulation of the quantity A can be found in Kennedy et al. (2000).

In the case of 2D wave breaking, implementation of the breaking model requires determination of wave directions in order to estimate the age of a breaking event. The incident wave angle β relative to the x direction can be written as:

$$\beta = \tan^{-1}\left(\frac{\zeta_y}{\zeta_x}\right) \tag{7}$$

In the present model, we used four points around the calculation point for estimating the wave angle, once the wave direction is determined, the model can estimate the age of a breaking event at a given location by tracking the breaking history at the grid points along the wave ray.

4. Ship boundary conditions

Since the main interest in the present study is the wave propagation far from the ship, therefore, a slender ship theory (Chen and Sharma, 1995) is assumed to give the boundary conditions at the ship location, as follows:

$$Q_y = \pm\frac{1}{2}U\frac{dS}{dx} \tag{8}$$

In which U is the ship speed, S is the transverse section area of the ship below still water level. The transverse section area is approximated by the following equation:

$$S(x_S) = S_0\left[1-\left(\frac{2x_S}{L_S}\right)^2\right], \quad -1 \le \frac{2x_S}{L_S} \le 1 \tag{9}$$

where S_0 is the mid-ship section area, x_S is the distance from the mid-ship, and L_S is the ship length. The mid-ship section area is given in the following expression:

$$S_0 = \alpha B_S d \tag{10}$$

in which, α is the mid-ship section coefficient, B_S is the ship beam, and d is the ship draft. In the present study, the ship conditions are: $L_S = 82$ m, $B_S = 14.6$ m, $d = 5.88$ m, and $\alpha = 0.62$.

The most important parameter for the characterization of ship waves in shallow water is depth Froude number. The depth Froude number (F_h) is defined as:

$$F_h = \frac{U}{\sqrt{g h_S}} \tag{11}$$

where h_S is the water depth at the sailing line. In the present study, ship speed is ranged from 7.28 to 16.98 m/s, the corresponding depth Froude numbers (F_h) from 0.6 to 1.4, respectively.

5. Numerical solution technique

The equations are solved by implicit finite difference techniques with the variables defined on a space staggered rectangular grid. The Alternating Direction Implicit (ADI) algorithm is used in the solution to avoid the necessity for iteration.

The ADI algorithm implies that at each time step a solution is first made in the x-momentum equations followed by a similar solution in the y-direction. By using this method, the system of implicit finite difference equations is reduced to a tridiagonal system of equations for each grid line in the model, and then will be solved by the Double Sweep algorithms, a very fast and accurate form of Gauss elimination.

6. Results and discussions

The ship, as shown in Fig. 1, is steadily traveling on an open coast with straight and parallel contours. Computational grid size in both x and y-direction is 2.5 m. The channel length is 4000 m from the ship start position. The ship is assumed to start from rest and accelerate uniformly to a final velocity. The computation domain was of 48.8 ship lengths long and 25.6 ship lengths wide. The grid size was 2.5 m×2.5 m, yielding a total of 1,432,200 grid points.

Figs. 2–4 show top views of wave crests for three cases: $F_h = 0.6$; $F_h = 1.0$; and $F_h = 1.4$, respectively. In theses figures, the darker (bigger) spot the higher elevation of wave

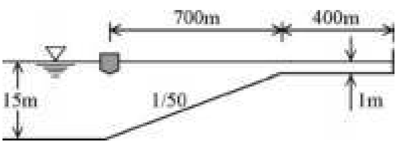

Fig. 1. Cross-section of computational channel.

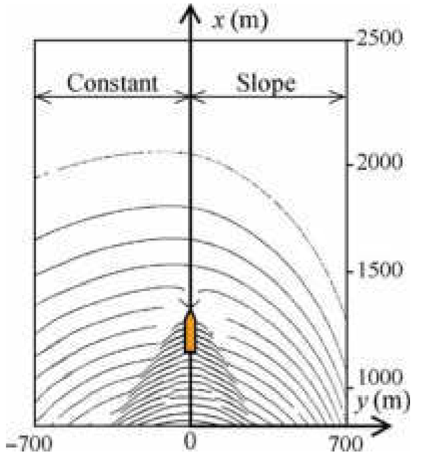

Fig. 2. Top view of wave crests at sub-critical speed (F_h=0.6).

crest. At a sub-critical speed (F_h=0.6) in Fig. 2, the wave pattern is close to a Kelvin–Havelock wave pattern, and number of leading waves ahead of the ship increase correspondingly with the sailing time. At a critical speed (F_h=1.0) in Fig. 3, the wave system is characterized by significant divergent waves, with only one leading wave. At a super-critical speed (F_h=1.4) in Fig. 4, the wave system comprises only divergent waves, the transverse waves are almost disappear. They simply cannot keep up with the ship since the water depth limits their speed.

In constant water depth, the distance between wave crests increases with distance from the sailing line. In the slope side, however, this tendency is not occurred due to shoaling and refraction effects. In both constant side and slope side, the directions of travel of the subsequent waves are different with the direction of propagation of the leading wave.

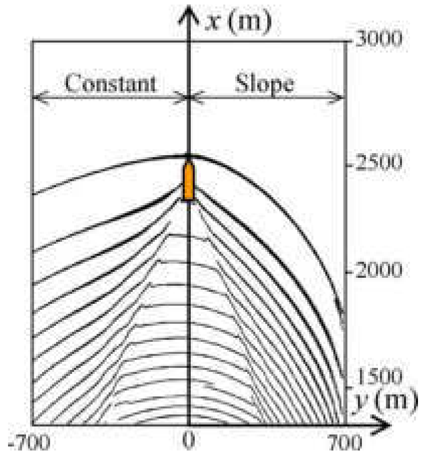

Fig. 3. Top view of wave crests at critical speed (F_h=1.0).

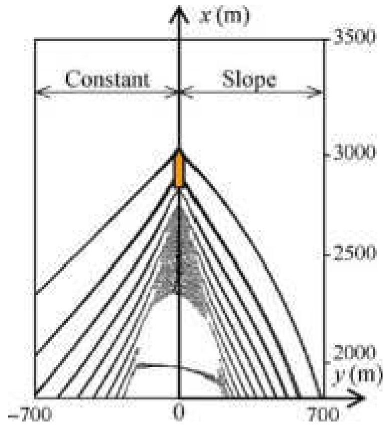

Fig. 4. Top view of wave crests at super-critical speed ($F_h = 1.4$).

On sloping coast, the effect of wave refraction is clearly observed in the wave pattern. It may cause the decrease in the wave height as the water depth becomes shallow. Besides, the effect of wave shoaling increases the wave height.

Fig. 5 illustrates a time profile of water surface elevation (at $x = 2000$ m, and $y = 200$ m), and definition of maximum wave height (H_{max}) and maximum wave period (T_{max}). In the case of depth Froude number less than 0.95, the wave period increases as the depth Froude number increases. However, in the case of the depth Froude number larger than 0.95, the wave period gradually decreases as the depth Froude number increases. The remarkable increase in wave period at near-critical and critical speeds is of particular concern as the long-periodic wave can build up to considerable height on reaching a sloping shoreline.

Fig. 6 shows the maximum wave height at a range of depth Froude numbers. It is obvious from this figure that the largest and most energetic waves are produced at approximately $F_h = 0.95$. Wave heights are sharply increased when F_h from 0.8 to 0.95. However, the decay rate of near-critical wave (with distance from the sailing line) differs greatly from the decay rate of super-critical wave. This point is illustrated in Fig. 7 where the decay of the maximum wave height is plotted for a range of near-critical

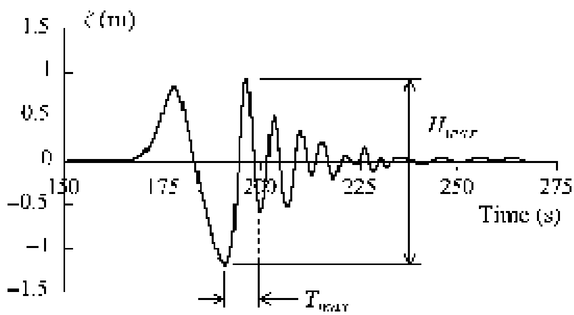

Fig. 5. Definition of H_{max} and T_{max}.

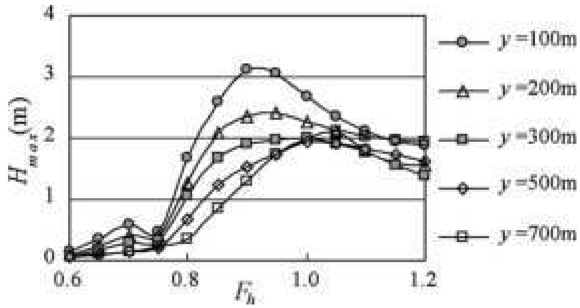

Fig. 6. $H_{\max}$ against depth Froude number.

and super-critical Froude number. It can be seen from these results that the maximum wave height on the sloping coast is not only dependent upon its transverse distance from the sailing line (due to wave decay) and interaction between the divergent and transverse waves, but also due to shoaling and refraction.

Fig. 8 illustrates a plan view of plotted tracks of the pointed end of velocity vector at different locations in the case the ship travels at critical speed ($F_h = 1.0$). On the left-hand side (constant water depth), the dominant directions of propagation are mostly alike. Meanwhile, on the right-hand side (slope), these dominant directions (indicated the direction of propagation for ship waves on slope, or $\tan\beta$) are apparently changed according to the distance from the sailing line. The dark curves in the figure are the wave rays that constructed from the flow vectors of water particles.

Fig. 9 shows the inclination of wave direction ($\tan\beta$) on the slope, which can be formulated as a function of the distance from the sailing line (y). The approximate functions are shown in the figure. These functions are also strongly influenced by the value of depth Froude number. With $y = 100$ m value as a reference level, based on the Snell's law, the value of $\tan\beta$ at a certain position is given by:

$$\tan\beta = \sqrt{\frac{(C/C_1 \times \sin\beta_1)^2}{1-(C/C_1 \times \sin\beta_1)^2}} \tag{12}$$

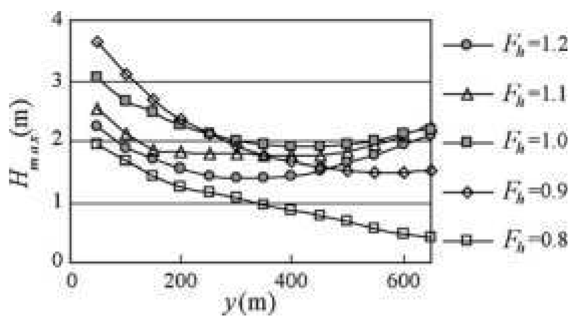

Fig. 7. H_{max} against distance from the sailing line.

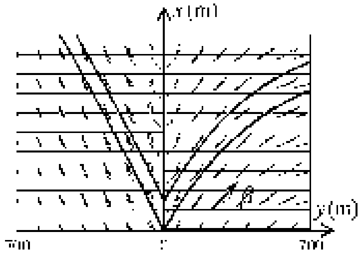

Fig. 8. Motion time history of water particles ($F_h = 1.0$).

in which, C is wave celerity at the optional position of y, C_1 and β_1 are the reference wave celerity and wave angle at the reference location of $y = 100$ m.

Fig. 10 illustrates the plotted wave rays on the slope that obtained from three different methods. The dash–dot curve is the wave ray obtained from the Snell's law. The continuously dark curved line is the wave ray created from flow vectors. And the dashed curve is the wave ray that constructed from wave crest lines. As shown in the figure, these methods give almost the same result. In other words, on a gently sloping coast, ship waves refracted as same as the way the ordinary wind waves did. Therefore, the Snell's law can be applied for ship waves and the relative refraction coefficient is $K_r^{\prime}$ given by:

$$K_r^{\prime} = \left\{ 1 + \left[1 - \left(\frac{C}{C_1} \right)^2 \right] \tan^2 \beta_1 \right\}^{-1/4} \tag{13}$$

7. Empirical formula for maximum wave height

To predict the maximum wave height on slope, an empirical formula is proposed as follows:

$$H_{\max} = \min[(K_s^{\prime} \times K_r^{\prime} \times K_d^{\prime} \times H_1), H_b] \tag{14}$$

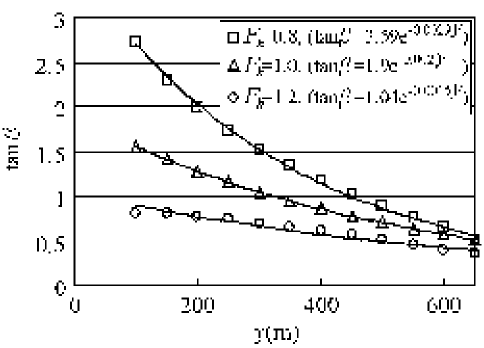

Fig. 9. Inclination of wave direction on slope.

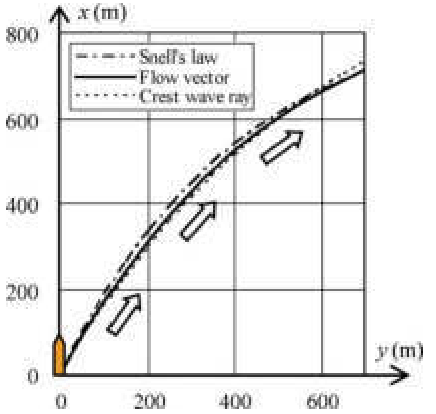

Fig. 10. Wave rays on sloping coast ($F_h = 1.0$).

Herein, K'_s, K'_r, K'_d are the relative shoaling, refraction, and damping coefficients, respectively. H_1 is reference maximum wave height at $y = 100$ m, and H_b is the limiting wave height in the surf zone due to wave breaking, which is proposed by Goda (1985) as follows:

$$H_b = 0.17 \times L_0 \times \left\{1 - \exp\left[-1.5\frac{\pi h}{L_0}\left(1 + 15 \times i^{4/3}\right)\right]\right\} \tag{15}$$

in which L_0 is the deep water wave length, and i is tangent of bottom slope.

The relative refraction coefficient K'_r can be obtained from Eq. (13), on the basis of the Snell's law. To compute the relative shoaling coefficient K'_s, the finite amplitude wave theory is used, as follows:

$$K'_s = K_s/K_{s1} \tag{16}$$

where

$$K_s = K_{si} + 0.0015 \times (h/L_0)^{-2.9} \times (H_0/L_0)^{1.3} \tag{17}$$

$$K_{si} = \frac{1}{\sqrt{\tanh\frac{2\pi h}{L} + \frac{2\pi h}{L}\left(1 + \tanh^2\frac{2\pi h}{L}\right)}} \tag{18}$$

$$H_0 = H_1/K_{s1} \tag{19}$$

$$L_0 = gT_1^2/2\pi \tag{20}$$

$$L = \frac{gT_1^2}{2\pi}\tanh\frac{2\pi h}{L} \tag{21}$$

in which, H_0 is deep water wave height and T_1, H_1 are reference wave period and reference maximum wave height at $y=100$ m.

Finally, the relative damping coefficient $K_d^\prime$ can be obtained from the following formula:

$$K_d^\prime = (y/100)^{-n} \tag{22}$$

In the present study, we found that the value of $n=0.2$ gives best agreement of the model evaluated based on analytical results.

8. Comparison between empirical formula and simulation results

Fig. 11 presents the comparison between results by numerical simulation and empirical formula for three cases: $F_h=0.8$, $F_h=1.0$ and $F_h=1.2$. At sub-critical speed, the maximum wave height gradually decreases until slope end, due to combined interaction between shoaling and damping effects. On the other hand, in critical and super-critical regimes, the maximum wave height on slope reduces by the damping and refraction at first, then increases by shoaling, and finally markedly decreases after broken.

The relative maximum wave height from simulated result (circle mark) agrees well with the result calculated by empirical formula (thickly solid line), except in very shallow water depth. In the figure, the straight thin line indicated limited breaking wave height due to limitation of water depth (H_b).

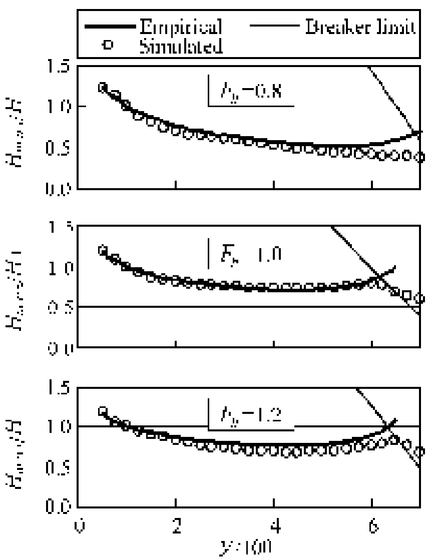

Fig. 11. Results of simulation and empirical formula.

9. Reference value of maximum wave height, wave period, and angle of wave direction

As mentioned before, at a certain datum point, if reference values of maximum wave height H_1, maximum wave period T_1, and incidence angle β_1 are given, maximum wave height at any optional position on the slope can be obtained by using empirical formula in Eq. (14).

Based on numerical simulation, these reference values of maximum wave height (at $x = 2000$ m, $y = 100$ m) are illustrated in Fig. 12. These approximate functions, which are displayed as the solid line in the figure can be formulated as follows:

Reference wave height H_1:

$$\begin{aligned} F_h \leq 0.89: \quad H_1 &= 0.0004\,\mathrm{e}^{9.871F_h} \\ F_h \geq 0.89: \quad H_1 &= 6.4636\,\mathrm{e}^{-1.0531F_h} \end{aligned} \tag{23}$$

Reference wave period T_1:

$$\begin{aligned} F_h \leq 0.95: \quad T_1 &= 0.7264\,\mathrm{e}^{2.697F_h} \\ F_h \geq 0.95: \quad T_1 &= 18.022\,\mathrm{e}^{-0.6729F_h} \end{aligned} \tag{24}$$

Reference wave angle β_1:

$$\begin{aligned} F_h \leq 0.80: \quad \beta_1 &= 48.003\,\mathrm{e}^{0.473F_h} \\ F_h \geq 0.80: \quad \beta_1 &= 256.9\,\mathrm{e}^{-1.6108F_h} \end{aligned} \tag{25}$$

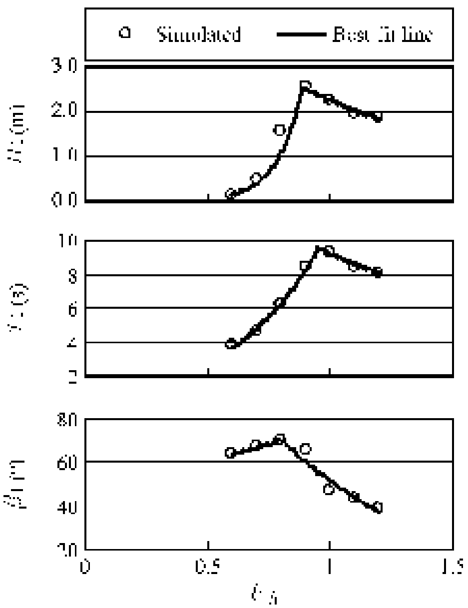

Fig. 12. Reference components of maximum wave height.

10. Conclusions

To predict the characteristics of waves generated by a ship, the present model with improved Boussinesq type equations for the far-field flow and the slender-ship approximation for the near-field flow provided satisfactory results. To estimate the maximum wave height on a sloping coast at a given distance from the sailing line, the proposed analytical solution can be applied. For shallow water depth, to compute the relative damping coefficient, the value of $n = 0.2$ is suggested. The relative shoaling coefficient is calculated by using the finite amplitude wave theory, and to calculate the relative refraction coefficient, the Snell's law can be used.

The reference values of maximum wave components, such as maximum wave height, maximum wave period, and wave angle can be formulated as a function of depth Froude number. However, to generalize the proposed formula, further investigations including lab data and field data for various slopes and various ships geometric conditions (e.g. ship length, ship draft) are essentially needed.

Acknowledgements

The first author would like to acknowledge the financial support of the Ministry of Education, Culture, Sport, Science, and Technology of Japan (Monbu-kagaku-sho) for his postgraduate study in Saitama University.

References

Beji, S., Nadaoka, K., 1996. A formal derivation and numerical modelling of the improved Boussinesq equations or varying depth. Ocean Eng. 23 (8), 691–704.

Chen, X.N., Sharma, S.D., 1995. A slender ship moving at a near-critical speed in a shallow channel. J. Fluid Mech. 291, 263–285.

Chen, Q., Kirby, J.T., Dalrymple, R.A., Kennedy, A.B., Chawla, A., 2000. Boussinesq modeling of wave transformation, breaking and runup. II: 2D. J. Waterway, Port, Coastal, Ocean Eng., ASCE 126 (1), 48–56.

Dam, K.T., Tanimoto, K., Thuy, N.B., Akagawa, Y., 2004. Investigation of waves generated by ships on an open coast, Proceedings of the 6th International Summer Symposium, JSCE, Saitama, Japan 2004 pp. 173–176.

Goda, Y., 1985. Random Seas and Design of Maritime Structures. University of Tokyo Express, Tokyo pp. 41–86.

Havelock, T.H., 1908. The propagation of groups of waves in dispersive media, with application to waves on water produced by a traveling disturbance, Proceedings of the Royal Society of London, A81 1908 pp. 398–430.

Jiang, T., Henn, R., Sharma, S.D., 2002. Wash waves generated by ships moving on fairways of varying topography, Proceedings of the 24th Symposium on Naval Hydrodynamics, Fukuoka, Japan 2002 pp. 441–457.

Kennedy, A.B., Chen, Q., Kirby, J.T., Dalrymple, R.A., 2000. Boussinesq modeling of wave transformation, breaking and runup. I: 1D. J. Waterway, Port, Coastal, Ocean Eng., ASCE 126 (1), 39–47.

Kofoed-Hansen, H., Jensen, T., Kirkegaard, J., Fuchs, J., 1999. Prediction of wake wash from high-speed craft in coastal areas, Proceedings of the International Conference on Hydrodynamics of High Speed Craft, London, UK 1999 pp. 1–10.

Madsen, P.A., Schäffer, H.A., 1998. Higher order Boussinesq-type equations for surface gravity waves: Derivation and analysis. Phil. Trans. Roy. Soc. London A356, 1–59.
Madsen, P.A., Sørensen, O.R., 1992. A new form of Boussinesq equations with improved linear dispersion characteristics. Part 2: a slowly-varying bathymetry. Coastal Eng. 18, 183–204.
Nwogu, O., 1993. Alternative form of Boussinesq equations for nearshore wave propagation. J. Waterway, Port, Coastal, Ocean Eng., ASCE 119 (6), 618–638.
Sorensen, R.M., 1969. Waves generated by model ship hull. J. Waterways, Harbours Div., ASCE 95, 513–538.
Tanimoto, K., Kobayashi, H., Ca, V.T., 2000. Ship waves in a shallow and narrow channel, Proceedings of the 27th Conference on Coastal Engineering, ASCE, Sidney, Australia 2000 pp. 1141–1154.
Wei, G., Kirby, J.T., Grilli, S.T., Subramanya, R., 1995. A fully nonlinear Boussinesq model for surface waves. Part I: highly nonlinear unsteady waves. J. Fluid Mech. 294, 71–92.
Whittaker, T.J.T., Doyle, R., Elsaesser, B., 2001. An experimental investigation of the physical characteristics of fast ferry wash, Proceedings of the 2nd International EuroConference on High Performance Marine Vehicles, Hamburg, Germany 2001 pp. 480–491.
Zelt, J.A., 1991. The run-up of nonbreaking and breaking solitary waves. Coastal Eng. 15, 205–246.

ISSN 0916−7897

海岸工学論文集

第 52 巻（1）

ANNUAL JOURNAL OF COASTAL ENGINEERING, JACE

VOL. 52 （1）

2005 年 10 月

土 木 学 会

JAPAN SOCIETY OF CIVIL ENGINEERS

海岸工学論文集　第52巻

目　次

第一分冊

ANNUAL JOURNAL OF COASTAL ENGINEERING, JSCE
VOL. 52

CONTENTS

PART I

海岸工学論文集，第52巻（2005）
土木学会，036-040

航走波の砕波を考慮した数値計算と最大波高算定法

赤川嘉幸*・Dam Khanh Toan**・Nguyen Ba Thuy***
Vu Hai Dang****・谷本勝利*****

航走波の数値計算に砕波・遡上モデルを取り入れた．採用した砕波モデルは運動方程式に砕波減衰項を導入することで砕波による減衰を評価するものであり，局所的な水位の上昇速度を砕波の指標としている．一方，遡上モデルは地盤面下を非常に小さな間隙率を有した透水層とすることで，水域と陸域を同時に計算するものである．1次元規則波を対象とした数値計算を行って砕波・遡上モデルの再現性を確認した後，航走波の数値計算に適用した．平行等深線海岸を対象とした計算結果に基づき，砕波変形を含めた航走波の最大波高を簡便に推定する手法を検討した．提案した算定法を用いれば，砕波帯を含んだ航走波の最大波高を数値計算に頼らなくとも推定することが可能である．

1. はじめに

浅水域を高速で航行する船舶によって発生する航走波は，水辺利用者を危険にさらし，水産養殖施設へ深刻な被害を与えるなど，沿岸環境に及ぼす影響が無視できなくなってきている．こうした航走波が海岸のような浅水域を伝播する際には航走波特有の減衰特性の他に浅水変形，屈折変形，砕波変形等を受けるため非常に複雑な現象となり，現地観測や模型実験では詳細なデータを得ることは難しい．これに対し，近年，航走波の数値計算法の開発が行われ（例えば，土井ら，2005；細川ら，2003），著者らはBoussinesq方程式を基本式とした手法を開発してきた（Tanimotoら，2001）．さらに，平行等深線海岸を対象とした計算結果を基に航走波の最大波高算定法を提案した（谷本ら，2004）．しかしながら，これまでの研究では砕波変形を考慮していないため砕波帯における航走波の変形は検討されていない．一方，Boussinesq方程式に適した砕波・遡上モデルの開発が試みられ，その実用化へ向けて研究が進められている（例えば，平山・平石，2004；Kennedyら，2000）．

本研究は，航走波の数値計算法に砕波・遡上モデルを取り入れ，砕波変形を含めた簡便な航走波の最大波高算定法を提案することを目的としたものである．砕波・遡上モデルとしては，Kennedyら（2000）の手法を採用している．本論文では，1次元規則波を対象とした数値計算を行い，砕波変形・遡上の再現性を確認する．次いで，平行等深線海岸における航走波の数値計算に適用し，その結果に基づき，航走波の最大波高の簡便な算定法を検討する．

2. 数値計算の方法と砕波・遡上モデル

（1）数値計算の方法

数値計算はMadsen & Sørensen（1992）によるBoussinesq型の基本式を，微小船幅を仮定して，船舶に相当する湧き出しと吸い込みを分布させた線状移動境界条件の下にADI法で解いていくものである．砕波・遡上モデルを取り入れた基本式は以下のとおりである．

$$b(\eta)\frac{\partial \eta}{\partial t}+\frac{\partial Q_x}{\partial x}+\frac{\partial Q_y}{\partial y}=0 \cdots\cdots(1)$$

$$\frac{\partial Q_x}{\partial t}+\frac{\partial}{\partial x}\left(\frac{Q_x^2}{A}\right)+\frac{\partial}{\partial y}\left(\frac{Q_xQ_y}{A}\right)+gA\frac{\partial \eta}{\partial x}-R_{bx}$$
$$=\left(\beta+\frac{1}{3}\right)h^2\left(\frac{\partial^3 Q_x}{\partial t\partial x^2}+\frac{\partial^3 Q_y}{\partial t\partial x\partial y}\right)+h\frac{\partial h}{\partial y}\left(\frac{1}{6}\frac{\partial^2 Q_y}{\partial t\partial x}\right)$$
$$+\beta gh^3\left(\frac{\partial^3 \eta}{\partial x^3}+\frac{\partial^3 \eta}{\partial x\partial y^2}\right)+h\frac{\partial h}{\partial x}\left(\frac{1}{3}\frac{\partial^2 Q_x}{\partial t\partial x}+\frac{1}{6}\frac{\partial^2 Q_y}{\partial t\partial y}\right)$$
$$+\beta gh^2\left[\frac{\partial h}{\partial x}\left(2\frac{\partial^2 \eta}{\partial x^2}+\frac{\partial^2 \eta}{\partial y^2}\right)+\frac{\partial h}{\partial y}\frac{\partial^2 \eta}{\partial x\partial y}\right] \cdots\cdots(2)$$

$$\frac{\partial Q_y}{\partial t}+\frac{\partial}{\partial x}\left(\frac{Q_xQ_y}{A}\right)+\frac{\partial}{\partial y}\left(\frac{Q_y^2}{A}\right)+gA\frac{\partial \eta}{\partial y}-R_{by}$$
$$=\left(\beta+\frac{1}{3}\right)h^2\left(\frac{\partial^3 Q_x}{\partial t\partial x\partial y}+\frac{\partial^3 Q_y}{\partial t\partial y^2}\right)+h\frac{\partial h}{\partial x}\left(\frac{1}{6}\frac{\partial^2 Q_x}{\partial t\partial y}\right)$$
$$+\beta gh^3\left(\frac{\partial^3 \eta}{\partial x^2\partial y}+\frac{\partial^3 \eta}{\partial y^3}\right)+h\frac{\partial h}{\partial y}\left(\frac{1}{6}\frac{\partial^2 Q_x}{\partial t\partial x}+\frac{1}{3}\frac{\partial^2 Q_y}{\partial t\partial y}\right)$$
$$+\beta gh^2\left[\frac{\partial h}{\partial y}\left(\frac{\partial^2 \eta}{\partial x^2}+2\frac{\partial^2 \eta}{\partial y^2}\right)+\frac{\partial h}{\partial x}\frac{\partial^2 \eta}{\partial x\partial y}\right] \cdots\cdots(3)$$

$$R_{bx}=\frac{\partial}{\partial x}\left(v\frac{\partial Q_x}{\partial x}\right)+\frac{1}{2}\left[\frac{\partial}{\partial y}\left(v\frac{\partial Q_x}{\partial y}\right)+\frac{\partial}{\partial y}\left(v\frac{\partial Q_y}{\partial x}\right)\right]$$
$$\cdots\cdots(4)$$

$$R_{by}=\frac{\partial}{\partial y}\left(v\frac{\partial Q_y}{\partial y}\right)+\frac{1}{2}\left[\frac{\partial}{\partial x}\left(v\frac{\partial Q_y}{\partial y}\right)+\frac{\partial}{\partial x}\left(v\frac{\partial Q_y}{\partial x}\right)\right]$$
$$\cdots\cdots(5)$$

ここに，ηは水位，Q_x，Q_yはそれぞれx方向（船の進行方向），y方向（船の進行方向と直角方向）の線流量，tは時間，hは静水深，gは重力加速度，βは分散項

* 正会員 工修 セントラルコンサルタント(株)
** 工修 埼玉大学大学院理工学研究科博士後期過程
*** 工修 Marine hydrometeorological center, Vietnam
**** 工修 Hanoi Institute of Oceanography, Vietnam
***** フェロー 工博 埼玉大学教授 工学部建設工学科

の補正係数で1/15としている．R_{bx}，R_{by}はそれぞれx，y方向の砕波減衰項，νは渦動粘性係数，b，Aは後述するように透水層の間隙率，水面下の単位幅あたりの通水断面積である．

船舶境界条件式についてはこれまでのもの（Tanimoto ら，2001）と同様であるので，ここでは省略する．

（2）砕波モデル

本研究では，Kennedy ら（2000）によって提案された手法を採用した．この砕波モデルは，運動方程式に砕波減衰項を導入することで砕波による減衰を評価するもので，砕波減衰項における渦動粘性係数νは次式を用いて算出する．

$$\nu = B\delta_b^2(h+\eta)\eta_t \cdots\cdots\cdots\cdots(6)$$

ここに，η_tは水位の上昇速度，δ_bは混合距離係数である．すなわち，砕波によるエネルギーの減衰は局所的な水位の上昇速度に依存することになる．また，Bは砕波が急激に発生することを抑えるために0～1の値をとるもので，次式で与えられる．

$$B = \begin{cases} 1 & ,2\eta_t^* \leqq \eta_t \\ \eta_t/\eta_t^* - 1 & ,\eta_t^* < \eta_t \leqq 2\eta_t^* \\ 0 & ,\eta_t \leqq \eta_t^* \end{cases} \cdots\cdots\cdots\cdots(7)$$

さらに，η_t^*は砕波の開始と終了を決定するパラメーターであり，砕波開始からの時間に依存して次式のように線形的に変化する．

$$\eta_t^* = \begin{cases} \eta_t^{(F)} & ,T^* \leqq t-t_0 \\ \eta_t^{(I)} + \dfrac{t-t_0}{T^*}\left(\eta_t^{(F)} - \eta_t^{(I)}\right) & ,0 \leqq t-t_0 < T^* \end{cases} \cdots\cdots\cdots\cdots(8)$$

ここに，$\eta_t^{(I)}$は開始値，$\eta_t^{(F)}$は終了値，T^*は遷移時間，t_0は砕波開始時刻である．すなわち，水位の上昇速度η_tがある限界値$\eta_t^{(I)}$を超えると砕波が発生し，砕波継続後，η_tがその値を下回っても終了値$\eta_t^{(F)}$を下回るまでは砕波は継続することになる．

（3）遡上モデル

遡上モデルは水際線近傍における波の運動を再現すると同時に，極浅海域における波浪変形計算を安定に実行させる役割も担っている．現在までに提案されている遡上モデルを大きく分けると，汀線位置での流速を外挿により求め移動させるものと，地盤を透水性とするものがある．本研究では，Kennedy ら（2000）による透水性モデルを採用することにした．このモデルは，地盤面下を非常に小さな間隙率を有した透水層とすることによって，特別な考慮無しに遡上域の計算を行うものである．これより地盤面下を含めた流動の計算が可能であり，地盤面と水面との交点を各時間における波の先端とするものである．透水層の間隙率は次の式で与える．

$$b_{(z)} = \begin{cases} 1 & ,z^* \leqq z \\ \delta + (1-\delta)\exp\left(\lambda\dfrac{z-z^*}{h_0}\right) & ,z < z^* \end{cases} \cdots\cdots(9)$$

さらに，水面下における単位幅あたりの通水断面積Aは，次のように$b(z)$を水深方向に基準深さから水面まで積分することで得られる．

$$A_{(z)} = \begin{cases} (z-z^*) + \delta(z^*+h_0) + \dfrac{(1-\delta)h_0}{\lambda}\left(1-e^{-\lambda(1+z^*/h_0)}\right) \\ \qquad ,z^* \leqq z \\ \delta(z+h_0) + \dfrac{(1-\delta)h_0}{\lambda}e^{\lambda(z-z^*)/h_0}\left(1-e^{-\lambda(1+z/h_0)}\right) \\ \qquad ,z < z^* \end{cases}$$

$$\cdots\cdots\cdots\cdots(10)$$

ここに，δ，λは間隙率を支配する定数である．また，z^*は仮想的な地盤面の位置であり，次式で定義する．

$$z^* = \frac{-h}{(1-\delta)} + h_0\left(\frac{1}{1-\delta} + \frac{1}{\lambda}\right) \cdots\cdots\cdots\cdots(11)$$

このように，z^*を実際の地盤面の位置と定義しないことで，最大遡上高を算定する際，誤差を小さくすることができる．

（4）1次元 Boussinesq 方程式による砕波・遡上計算

Kennedy らは断面実験結果との比較から砕波モデルに必要な各パラメーターの標準値を提案している．しかし，彼らの基礎式は Nwogu（1993）による任意水深の流速を用いた形の Boussinesq 方程式であり，Madsen & Sørensen の Boussinesq 方程式にこのモデルを適用した例はない．そこで，1次元規則波の砕波・遡上について数値計算を行い，実験結果と比較を行うことで，砕波変形・遡上の再現性を確認する．

図-1は崩れ巻き波砕波に対する波の峰と谷の水位，平均水位，波高分布について Bowen（1968）による実験結果との比較を示したものである．波の峰の水位は砕波点近傍において過小評価であり，砕波後は過大評価となっている．波高分布についても同様のことが言える．また，平均水位は砕波点近傍までは良く合っているものの，砕波後は過小評価されている．これは Boussinesq 方程式の弱非線形性によるものなので，こうしたことを除けば，本モデルは概ね砕波変形を再現しているといえる．さらに，遡上に関しても数値計算による再現性は良い．

以上のことより，Madsen & Sørensen タイプの本基礎式においても Kennedy らが提案したようなパラメーターを適切に用いることで，砕波変形・遡上の計算ができることが確認される．

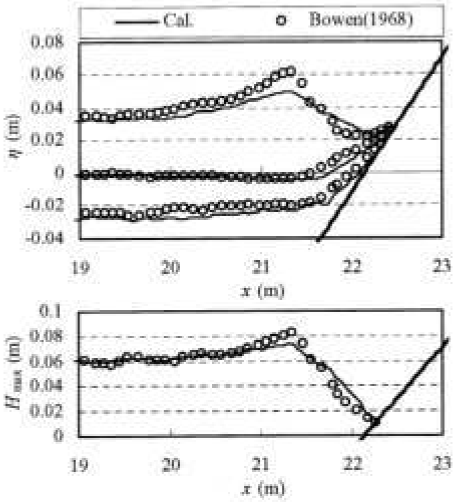

図-1　計算結果と実験結果の比較
（上：波の峰と谷および平均水位，下：波高分布）

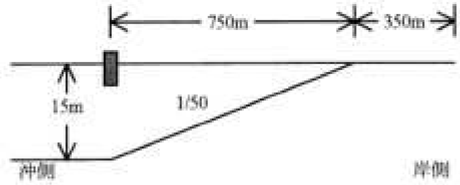

図-2　平行等深線海岸の断面図

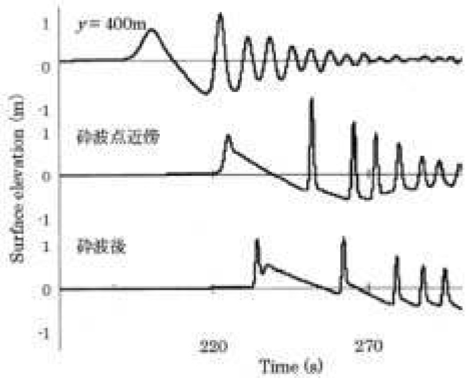

図-3　斜面上における航走波の時間波形（F_h=1.0）

3. 航走波の数値計算への適用

続いて，航走波の数値計算に砕波・遡上モデルを適用し，その結果に基づき，砕波を含めた航走波の最大波高算定法を検討する．

（1）計算条件

図-2のように勾配1/50の平行等深線海岸を汀線と平行して船が走る場合について航走波の数値計算を行った．海岸形状と船舶条件は谷本ら（2004）とほぼ同様であるが，砕波・遡上モデルを取り入れたため汀線までの計算が可能となった．ただし，陸域を設けると安定した計算が十分続かなかったため，汀線より外側は水深0mの水平床とした．陸域を含めた条件下における安定した計算は今後の課題である．格子間隔はx，y方向ともに2.5mとし，x方向の長さは航走開始位置から4000mとした．

なお，浅水航走波を支配する重要なパラメーターである水深フルード数F_hの定義は次式の通りである．

$$F_h = U/\sqrt{gh_s} \quad \cdots\cdots(12)$$

ここに，Uは船速，h_sは航走水深（15m），gは重力加速度である．本研究では，F_h=0.6〜2.0を対象とした．

（2）計算結果

図-3はx = 2000m地点の斜面上における航走波の時間波形を示したもので，それぞれ航走線（y = 0m）から400mの地点，砕波点近傍，砕波後の波形である．F_h=1.0，すなわち船速が限界速度のときである．本研究では，こうした航走波の最大波に着目して議論を進める．最大波は航走線の近傍を除く斜面上では第2波目以降に現れることから，データ解析においては第1波を除く谷から峰までの水位差を最大波高H_{max}とし，谷から次の谷までの時間差を最大波周期T_{max}と定義した．また，第1波の波高H_1は静水面から峰までの高さと定義する．

図-4は航走波の最大波高と第1波の波高，および最大水位，最低水位の空間分布を示したものである．航走線から離れるに従い，すなわち斜面を伝播するとともに，航走波特有の減衰と屈折変形による減衰を受けて一度波高は減少するが，水深が浅くなってくると浅水変形の影響を強く受けて再び増加するといった傾向を示す．最大波はy = 640m（水深2.2m）の地点において砕波するのに対し，第1波はさらに水深が浅いy = 700m（水深1.0m）の地点において砕波する．そして，その時の波高が1.0m以上にもなることから，水辺利用者が突然現れる航走波によって危険にさらされる可能性が指摘できる．

図-5は航走波の等値線分布であり，左側（沖側）が一定水深領域，右側（岸側）が斜面領域である．斜面上において航走波が大きく屈折し，波峰が長く連なって連続的に岸に押し寄せる傾向が確認できる．

（3）最大波高算定法

傾斜海岸を伝播する航走波は，航走波特有の距離による減衰のほかに，浅水変形，屈折変形，砕波変形を受け

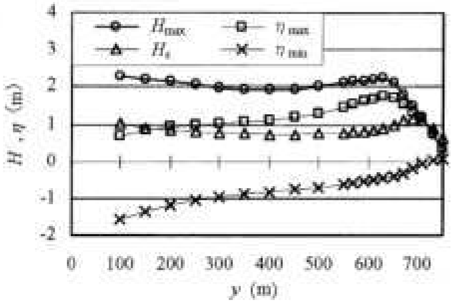

図-4　波高と水位の空間分布（F_h=1.0）

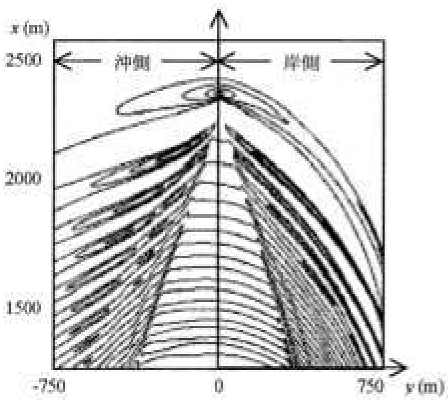

図-5　航走波の等値線分布（F_h=1.0）

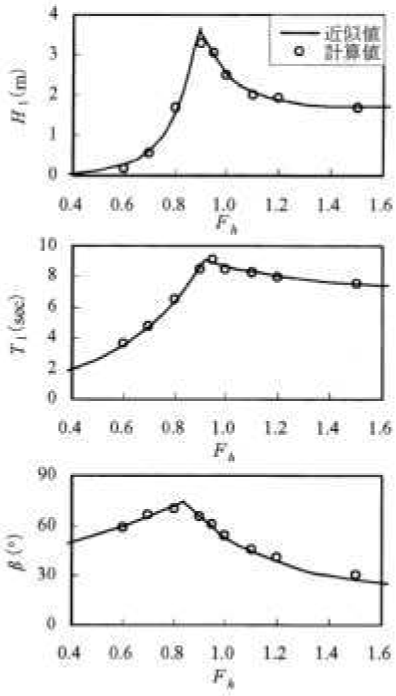

図-6　基準値の定式化

る．著者らはそうした航走波の減衰特性，浅水変形，屈折変形を考慮した最大波高の算定法を提案した（谷本ら，2004）．本研究では，さらに砕波変形を考慮した次式によって航走波の最大波高を推定する手法を検討する．

$$H_{max}=\min\{K_s'\times K_r'\times K_d'\times H_1, H_b\} \quad \cdots\cdots\cdots\cdots(13)$$

ここに，H_1はy = 100 m の地点における最大波高（基準波高）で，K_s'，K_r'，K_d'はそれぞれのy = 100 m における値で割った相対浅水係数，相対屈折係数，相対減衰係数である．相対浅水係数は有限振幅波理論，相対屈折係数はスネルの法則に基づき与え，相対減衰係数は距離の－1/5乗に比例して減衰するものとした．各々の式については谷本ら（2004）と同様であるのでここでは省略する．また，砕波限界波高H_bは合田（1973）の砕波限界式によって算出し，定数Aの値とし0.20を採用した．

この算定法は，ある基準点（y = 100 m）における最大波の基準値（波高，周期，入射角）を与えることで，任意の地点における最大波高を算定するものである．各基準値については数値計算結果に基づいて以下のように水深フルード数F_hで定式化し，そこから値を算出した．

基準波高H_1：

$$\begin{aligned} &H_1=30e^{-8(F_h-0.55)}+1.7 && ,0.89\leq F_h \\ &H_1=0.0012e^{9F_h} && ,F_h<0.89 \end{aligned} \quad \cdots\cdots\cdots(14)$$

基準波周期T_1：

$$\begin{aligned} &T_1=30e^{-3F_h}+7.2 && ,0.92\leq F_h \\ &T_1=0.6e^{3(F_h-0.01)} && ,F_h<0.92 \end{aligned} \quad \cdots\cdots\cdots\cdots\cdots\cdots(15)$$

基準入射角β_1：

$$\begin{aligned} &\beta_1=150e^{-3(F_h-0.5)}+20 && ,0.84<F_h \\ &\beta_1=35e^{0.9F_h} && ,F_h\leq 0.84 \end{aligned} \quad \cdots\cdots\cdots\cdots(16)$$

提案した式は既発表（谷本ら，2004）のものとは異なるが，これは各基準値により一般性を持たせるためにF_h＝2.0までの傾向を考慮したためである．図-6はこうして定式化した基準値と数値計算結果の比較である．

図-7は各相対係数と基準波高で割った最大波高の算定値，および数値計算によって得られた最大波高比を示したものである．ただし，横軸はyを100 m で割って無次元化して表示してある．F_hが0.8，1.0，1.2の例であり，減衰定数はいずれも1/5を使用している．従って，相対減衰係数は3ケースとも同じ減衰曲線である．これに対し，相対屈折係数は低下曲線であることは同じであるが，F_hが大きくなるにつれて低下率がやや減じると

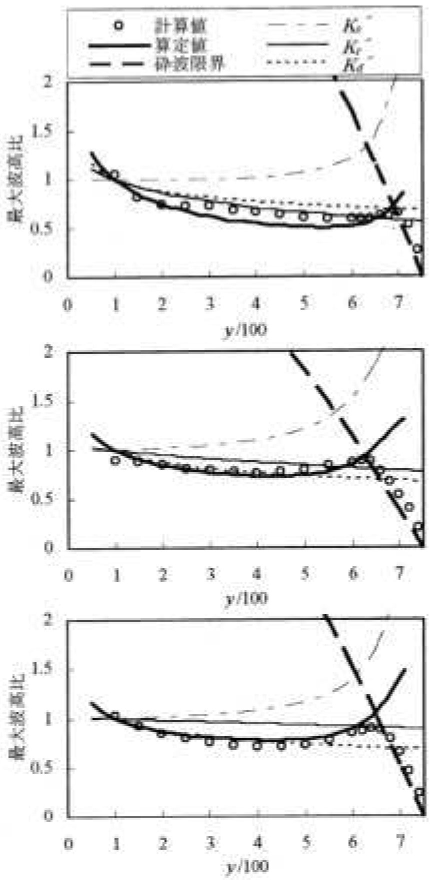

図-7　各相対係数と最大波高比の計算値と算定値
（上：F_h=0.8，中：F_h=1.0，下：F_h=1.2）

いう傾向を示している．相対浅水係数はyが大きくなるにつれて，すなわち水深が浅くなるにつれて増加傾向を示し，特に水深が非常に浅いところで非線形性のため急増するという変化を示している．これら3つの係数の積である最大波高比の算定値は，斜面上を伝播するに従い航走波特有の減衰特性や屈折変形の影響を受けて一度低減しつつも，浅水変形の影響を受けて増加に転じ，砕波によって再び減衰するといった変化を示している．また，砕波限界式は砕波点および砕波による波高減衰を適切に表現している．ここで，計算値における砕波点が過小評価となるのは，弱非線形性を有するBoussinesq方程式の性質によるものと考えられる．

以上のことから，斜面上を伝播する航走波は，ある基準点における基準波高に相対浅水係数，相対屈折係数，相対減衰係数を乗じることで得られた値と，砕波限界波高のうちどちらか小さい値を用いることによって算定が可能である．相対浅水係数については有限振幅波理論，相対屈折係数についてはスネルの法則に基づき与え，航走波特有の相対減衰係数については距離の－1/5乗に比例するものとして与えることができる．さらに，航走波の砕波減衰は合田の砕波限界式を適用することで推定が可能であり，定数Aは0.20とするのが適切である．

4. む す び

航走波の数値計算に砕波・遡上モデルを取り入れるとともに，砕波変形を含めた簡便な航走波の最大波高算定法を検討した．砕波・遡上モデルの適用性を1次元規則波を対象とした数値計算を行うことで確認した．提案した算定法を用いれば，砕波帯を含んだ航走波の最大波高を数値計算に頼らなくとも簡単に推定することができる．ただし，砕波モデルについては観測データとの検証が必要であり，陸域を含んだ数値計算も今後の課題である．

参 考 文 献

合田良実(1973)：防波堤の設計波圧に関する研究，港湾技術研究所報告，第12巻第3号，pp. 31-69.

谷本勝利・赤川嘉幸・茂木勇佑・D. K. Toan(2004)：平行等深線海岸における航走波の変形，海洋開発論文集，第20巻，pp. 779-784.

土井康明・C. B. Hong・南本隼人・陸田秀実(2005)：Wave-breaking on shore by ship wash，第18回海洋工学シンポジウム，日本造船学会

平山克也・平石哲也(2004)：ブシネスクモデルによる砕波・遡上計算法とその適用性，海工論文集，第51巻，pp. 11-15.

細川真也・福岡捷二・渡辺明英・泊　宏(2003)：荒川における航走波の数値解析，第58回年次学術講演会講演概要集，Ⅱ-258，pp. 515-516.

Bowen, A. J., D. L. Inman, V. P. Simons(1968): Wave set-down and set-up. J. Geophysical Research, Vol.73, pp. 2569-2577.

Kennedy, A. B., Q. Chen, J. T. Kirby and R. A. Dalrymple(2000)：Boussinesq modeling of wave transformation, breaking, and runup. Ⅰ:1D, Journal of Waterway, Port, Coastal, and Ocean Engineering, ASCE, Vol.126, No.1, pp. 39-47.

Madsen, P. A. and O. R. Sørensen (1992)：A new form of Boussinesq equations with improved linear dispersion characteristics. Part2. A slowly-varying bathymetry, Coastal Eng., Vol.18, pp. 183-204.

Nwogu, O.(1993)：Alternative form of Boussinesq equations for nearshore wave propagation, Journal of Waterway, Port, Coastal, and Ocean Engineering, ASCE, Vol.119, No.6, pp. 618-638.

Tanimoto, K., H. Kobayashi and V. T. Ca(2001): Ship waves in a shallow and narrow channel, Proceeding of 27th Conference on Coastal Engineering, pp. 1141-1154.

2. TẠP CHÍ TRONG NƯỚC (4)

CỘNG HÒA XÃ HỘI CHỦ NGHĨA VIỆT NAM
Độc lập – Tự do – Hạnh phúc

GIẤY XÁC NHẬN LÀ TÁC GIẢ CHÍNH CỦA BÀI BÁO KHOA HỌC

Tạp chí: Khí tượng thủy văn

Tên bài báo: Một số kết quả dự báo nghiệp vụ nước dâng do bão năm 2006 (2007). Tạp chí Khí tượng Thủy văn, số 556, trang 17-22

Tác giả: Trần Hồng Lam, Nguyễn Bá Thủy, Bùi Mạnh Hà

Chúng tôi công nhận TS. Nguyễn Bá Thủy là người đóng góp chính trong các nội dung của bài báo này và xác nhận TS. Nguyễn Bá Thủy là tác giả chính của bài báo.

Họ và tên tác giả	Chữ ký	Ngày/tháng/năm
TS. Trần Hồng Lam		28/6/2019
TS. Nguyễn Bá Thủy		3/7/2019
CN. Bùi Mạnh Hà		1/7/2019

000083

Tạp chí

ISSN 0866 - 8744

KHÍ TƯỢNG THỦY VĂN

Scientific and Technical Hydro-Meteorological Journal

Số 556 * Tháng 4-2007

Số đặc biệt kỷ niệm 20 năm thành lập

Trung tâm Khí tượng Thuỷ văn Biển

20 năm trưởng thành và phát triển

TRUNG TÂM KHÍ TƯỢNG THUỶ VĂN QUỐC GIA
National Hydro-Meteorological Service of Vietnam

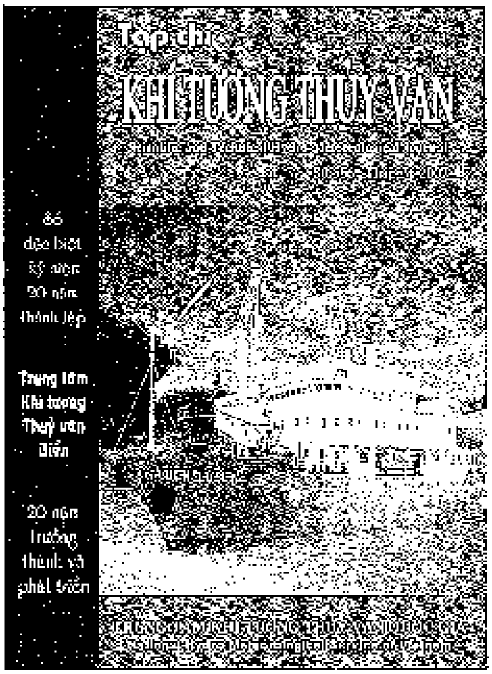

TẠP CHÍ KHÍ TƯỢNG THUỶ VĂN

Giấy phép xuất bản:
Số: 25/GP-BVHTT - Bộ Văn hoá Thông tin
cấp ngày 5/4/2004
In tại: Công ty in Khoa học Kỹ thuật

Toà soạn
Số 4 Đặng Thái Thân - Hà Nội
Điện thoại: 04.8241405
Fax: 04.8260779
Email: ducbv@fpt.vn

Giá bán: 10.000đồng

Số 556 * Tháng 4 năm 2007

Nghiên cứu và trao đổi

Tổng kết tình hình Khí tượng Thuỷ văn

MỘT SỐ KẾT QUẢ DỰ BÁO NGHIỆP VỤ NƯỚC DÂNG DO BÃO NĂM 2006

TS. Trần Hồng Lam

ThS. Nguyễn Bá Thủy, CN. Bùi Mạnh Hà

Trung tâm Khí tượng Thủy văn Biển

Nước dâng do bão là hiện tượng thiên tai rất nguy hiểm. Tổng thiệt hại do bão nói chung và nước dâng do bão nói riêng hàng năm là rất lớn. Đó không chỉ là mối đe dọa đối với một Quốc gia mà còn là sự cảnh báo cho cộng đồng quốc tế về hiểm họa thiên tai bão lũ có thể gây ra trong thời gian tới.

Với nhiệm vụ được giao và tính cấp bách của việc dự báo và cảnh báo nước dâng do bão, Trung tâm Khí tượng Thuỷ văn Biển đã xây dựng "Quy trình dự báo nghiệp vụ nước dâng do bão cho vùng ven biển Việt Nam dựa trên mô hình Delft3D - FLOW". Bài báo này tác giả giới thiệu khái quát về quy trình dự báo và một số kết quả dự báo nước dâng cho một số cơn bão điển hình trong mùa bão năm 2006.

1. Tóm tắt quy trình dự báo nước dâng do bão

Trên cơ sở mô hình Delft3D - FLOW Trung tâm Khí tượng Thuỷ văn Biển đã xây dựng một quy trình dự báo nước dâng do bão gồm các bước chính sau:

** Bước 1: Lựa chọn khu vực để lấy các kết quả dự báo và phát bản tin*

Đây là khâu mở đầu trong quy trình dự báo, sở dĩ có công đoạn này vì mô hình được chạy trên một lưới tính rất lớn, phạm vi bao phủ rất rộng. Do vậy, nếu không hạn chế số điểm cần lấy kết quả tính toán thì sẽ mất nhiều thời gian để chạy mô hình và dung lượng file kết quả ra cũng rất lớn. Chính vì vậy, khi biết được khả năng bão sẽ đổ bộ vào khu vực nào thì các dự báo viên phải lựa chọn file chứa các điểm trong khu vực đó đưa vào tính toán và phát bản tin. Sự lựa chọn này có thể thay đổi khi bão bất ngờ thay đổi quỹ đạo và đổ bộ vào vùng khác.

** Bước 2. Công tác chuẩn bị các số liệu khí tượng*

- Thu thập các tham số bão (bước thời gian là 06h, lấy từ các bản tin dự báo của Trung tâm dự báo Khí tượng Thủy văn (KTTV) Trung ương phát trên mạng Internet và có tham khảo các bản tin dự báo bão của Nhật Bản, Hồng Kông, Mỹ và Philippin), tiếp theo là nội suy các số liệu dự báo tại các bước thời gian chưa có trong dự báo bão và chuyển các số liệu bão theo format chuẩn của mô hình gió bão..

- Thu thập trường gió và trường áp nền tại các bước thời gian dự báo (lấy từ kết quả dự báo của mô hình MM5 đang chạy dự báo thử nghiệm tại Phòng Khí tượng biển - Trung tâm KTTV biển) và chuyển theo format chuẩn của mô hình.

Người phản biện: TS. Nguyễn Tài Hợi

- Tổng hợp trường gió bão (được mô phỏng theo mô hình gió bão) và trường gió nền và chuyển về lưới tính của Delft3D - Flow bằng mô hình WES (Win Enhancement Scheme).

** Bước 3. Mô phỏng thuỷ triều trong thời đoạn dự báo*

Việc mô phỏng thủy triều trong thời đoạn dự báo gồm hai tính toán:

- Thứ nhất: Xác định thuỷ triều thực để làm điều kiện ban đầu cho mô hình. Các tính toán thử nghiệm trước đó đã cho thấy dự tính thuỷ triều trước thời gian ba ngày là đủ để cho ra một trường thuỷ triều thực trong khu vực Biển Đông để làm điều kiện ban đầu cho mô hình;

- Thứ hai: Tính toán thuỷ triều trong khoảng thời gian dự báo sẽ xác định được giá trị nước dâng tại các điểm khi so sánh với kết quả trong trường hợp mô hình tính cả nước dâng và thuỷ triều, đồng thời cũng đánh giá được nước dâng rơi vào các pha nào của thuỷ triều.

** Bước 4. Tính toán dự báo nước dâng do bão*

Đây là bước chủ yếu trong dự báo nghiệp vụ nước dâng do bão. Thông thường thì thời hạn dự báo là 72h, tuy nhiên, thời gian tính toán có thể được thực hiện dài hơn.

Sau khi nhận được thông tin dự báo bão thì mô hình sẽ cập nhật cho kết quả dự báo theo kịch bản dự báo bão mới. Do vậy, bão càng gần vào bờ thì độ chính xác của dự báo sẽ càng cao vì các số liệu đưa vào mô hình có nhiều giá trị thực và những số liệu dự báo gần cũng sẽ sát với thực tế hơn.

** Bước 5. Thảo luận, phân tích các kết quả dự báo và thiết lập các bản tin dự báo*

Sản phẩm của mô hình là kết quả dao động mực nước, mô đun và hướng dòng chảy tại các vị trí cần tính toán và cảnh báo, phân bố trường mực nước, trường dòng chảy theo không gian tại các thời điểm. Một việc rất quan trọng trong cảnh báo nước dâng do bão là xác định giá trị nước dâng lớn nhất có thể xẩy ra tại các vị trí bị ảnh hưởng và thời điểm xẩy ra nước dâng lớn nhất. Do vậy chúng tôi đã xây dựng một chương trình phân tích trong việc xây dựng quy trình dự báo nghiệp vụ nước dâng do bão.

2. Một số kết quả dự báo nước dâng do bão năm 2006

Năm 2006 là năm điển hình về tần suất bão đổ bộ vào Việt Nam. Có nhiều cơn bão xuất hiện với cường độ mạnh và có hướng di chuyển tương đối phức tạp. Rút kinh nghiệm từ công tác dự báo nước dâng bão năm 2005, công tác dự báo nước dâng bão năm 2006 được thực hiện nghiêm túc, những kết quả của dự báo đã góp phần giảm thiểu thiệt hại về người và tài sản do bão gây ra.

Quy trình dự báo nước dâng do bão được vận hành khi có thông tin về bão và áp thấp nhiệt đới xuất hiện trên khu vực Biển Đông và có xu thế đổ bộ vào Việt Nam. Công việc dự báo nước dâng cho một cơn bão được hoàn tất khi bão đổ bộ vào bờ hoặc khi bão tan hoặc đi chuyển ra ngoài lãnh thổ Việt Nam. Dưới đây là một số kết quả dự báo nước dâng cho một số cơn bão điển hình năm 2006.

a. Dự báo nước dâng do bão số 1 (Typhoon Chanchu)

Bão Chanchu đổ bộ vào khu vực miền đông Trung Quốc. Trong mùa bão Thái Bình Dương năm 2006, cơn bão này còn được gọi là "siêu bão Chanchu". Đây là cơn bão mạnh nhất tính đến thời điểm tháng 5 năm 2006 tại khu vực Biển Đông và là siêu bão thứ hai đã được ghi nhận tại Biển Đông, trận siêu bão thứ nhất trong khu vực này là "siêu bão Ryan" trong năm 1995. Mặc dù, không đe dọa khu vực đất liền của nước ta nhưng đã gây thiệt hại rất lớn và cũng để lại dấu ấn rất khó quên cho những người làm dự báo khí tượng thủy văn.

Bảng1. Kết quả dự báo nước dâng do bão Chanchu (cm)

Thời gian dự báo	Khu vực		
	HongKong	N1	N2
36h	110	180	210
12h	60	120	160
06h	80	130	190

b. Dự báo nước dâng do bão số 5

Bão số 5 được hình thành ngoài Biển Đông và có hướng di chuyển ít biến đổi là Tây - Tây Bắc. Khi bão số 5 cách bờ biển Thừa Thiên Huế - Hà Tĩnh khoảng 320km về phía Đông Nam, sức gió ở gần tâm bão mạnh cấp 8, giật trên cấp 8, tức là khoảng 62 đến 74km/h. Mỗi giờ đi được từ 10 đến 15km, ảnh hưởng trực tiếp đến các tỉnh từ Nghệ An đến Quảng trị.

Nhìn chung, theo tính toán thì nước dâng bão số 5 không lớn. Nước dâng do bão lớn nhất có thể xảy ra theo tính toán là 70cm tại Tĩnh Gia - Thanh Hoá, tính theo mô hình Delft3D và 72cm Hòn Ngư - Nghệ An, tính theo mô hình CTS. Theo kết quả tính toán dự báo cho thấy, không có sự khác biệt lớn về trị số nước dâng tính toán giữa hai mô hình Delft3D và CTS (bảng 2).

Bảng 2. Kết quả dự báo nước dâng bão số 5 tại một số khu vực

Tỉnh	Khu vực	Nước dâng lớn nhất dự báo (cm)	
		Delft3D - Flow	CTS Model
Hải Phòng	Hòn Dấu	50	53
Thái Bình	Diêm Điền	50	47
Thanh Hóa	Tĩnh Gia	70	67
Nghệ An	Cầu Giát	70	69
Nghệ An	Hòn Ngư	69	72
Hà Tĩnh	Cửa Nhượng	60	62

b. Dự báo nước dâng do bão số 6 (Typhoon Xangsane)

Có thể nói, bão Xangsane có hướng di chuyển không phức tạp nhưng cường độ của cơn bão này rất mạnh. Trung tâm đã phân công các cán bộ dự báo tiến hành theo dõi sự di chuyển của bão Xangsane ngay từ khi nó có xu thế đổ bộ vào Philippines. Thường xuyên theo dõi các bản tin của Trung tâm Dự báo KTTV Trung ương.

Theo số liệu chúng tôi thu thập được, vào thời điểm bão Xangsane đổ bộ vào Đà Nẵng, tốc độ gió dao động trong khoảng từ 18m/s đến 22m/s, tốc độ gió giật là 38m/s (đo được tại Trạm Sơn Trà) và 44m/s (đo được tại Thành Phố Đà Nẵng). Theo như dự báo của chúng tôi thì cơn bão Xangsane sẽ gây nước dâng lớn trên diện rộng dọc khu vực ven biển từ Quảng Bình đến Đà Nẵng, đặc biệt là ở khu vực ven biển tỉnh Thừa Thiên Huế, nước dâng lớn nhất có thể trên 2,0m. Khu vực từ Quảng Nam đến Bình Định mặc dù nước dâng không lớn, nhưng có thể xảy ra vào lúc triều cường, đây là trường hợp rất nghiêm trọng. Cũng theo dự báo, thời gian nước dâng có thể diễn ra khá lâu, khoảng 4 giờ. Nước dâng do bão lớn nhất sẽ xảy ra sớm hơn thời gian bão đổ bộ khoảng 2 giờ.

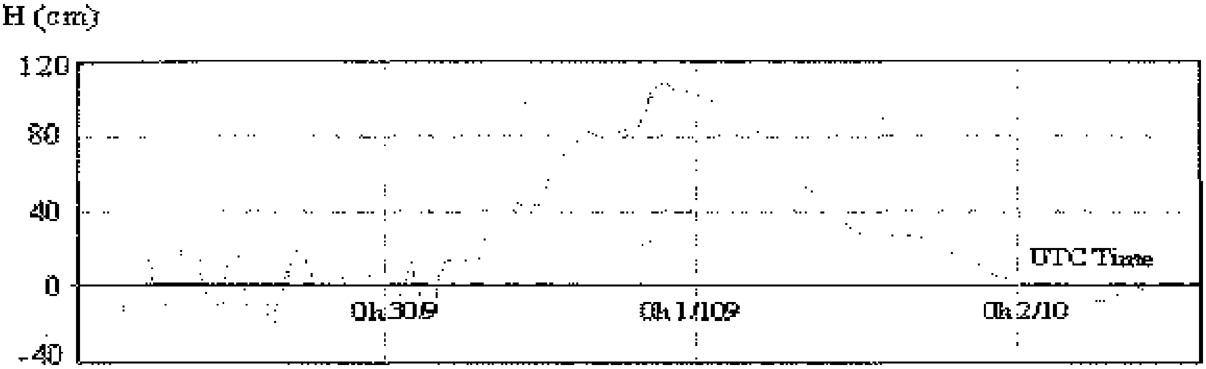

Hình 1. Biến trình nước dâng bão Xangsane tại Tam Kỳ - Quảng Nam

Bảng 3. Kết quả dự báo nước dâng bão Xangsane

Tỉnh	Khu vực	Dự báo	Thực đo	Sai số %
Nghệ An	Cửa Hội	150	130	13
Hà Tĩnh	Cẩm Nhượng	170	144	15
Quảng Bình	Lệ Thủy	200	178	11
Quảng Trị	Triệu Phong	200	178	11
Huế	Vinh Tu	210	218	4
Đà Nẵng	Sơn Trà	160	145	9
Quảng Nam	Tam Kỳ	110	120	9
Sai số tuyệt đối (tính trung bình)				10%

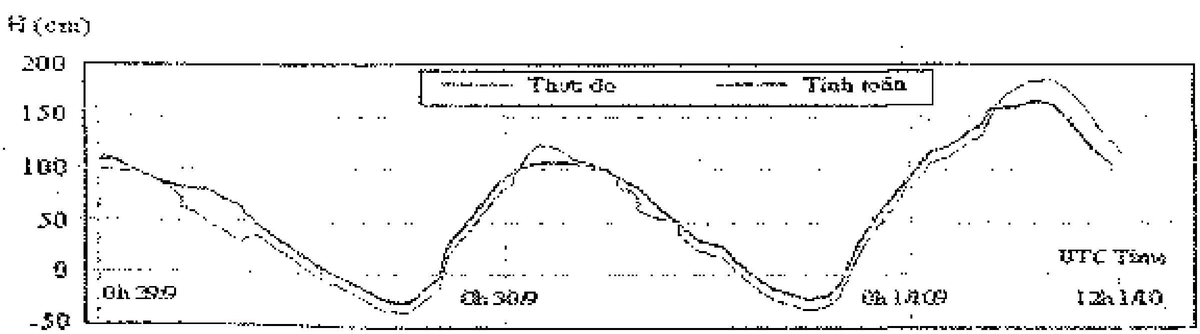

Hình 2. Biến trình mực nước trong bão Xangsane tại Trạm Ngọc Trà - Thanh Hoá

Qua so sánh giữa kết quả tính toán dự báo nước dâng bão Xangsane và thực đo cho thấy, sai số dự báo có thể chấp nhận được (sai số tương đối trung bình là 10%, tương đương với sai số tuyệt đối khoảng 20cm, bảng 3).

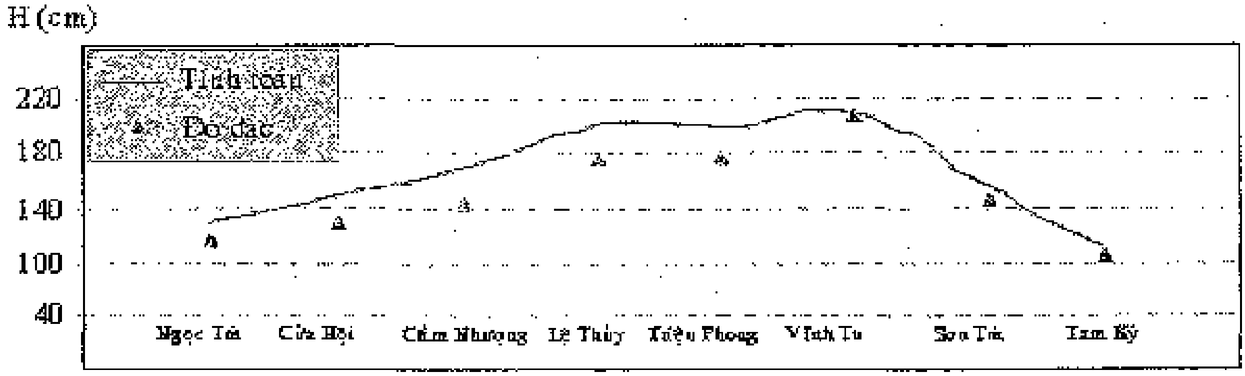

Hình 3. Đường bao nước dâng bão Xangsane

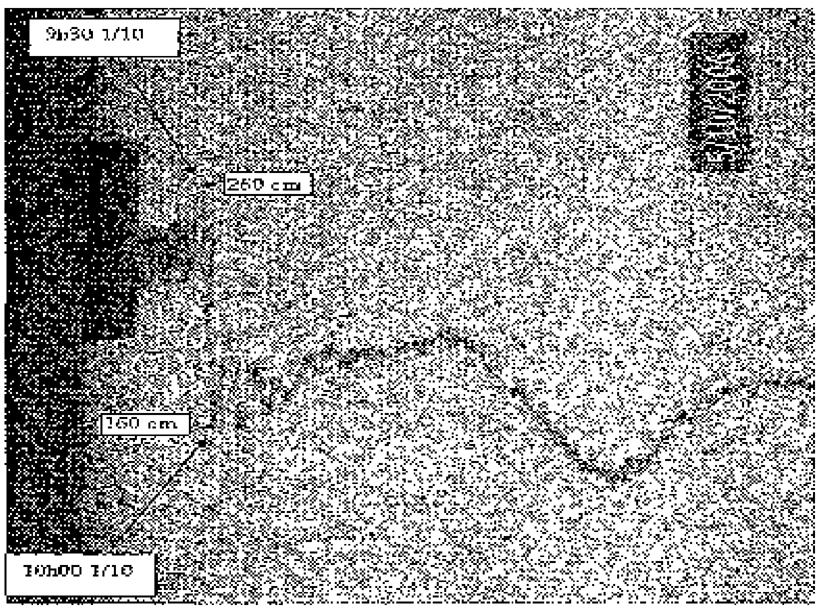

Hình 4. Biến trình mực nước quan trắc tại Sơn Trà vào thời điểm bão Xangsane đổ bộ

Một vấn đề lý thú mà mô hình Delft3D đã phản ánh được trong tính toán dao động mực nước trong bão đó là hiện tượng nước rút trước khi bão đổ bộ vào bờ. Đây là một vấn đề rất khó mà một số mô hình dự báo nước dâng hiện nay chưa phản ánh được. Biến thiên theo thời gian của dao động mực nước tại Sơn Trà cho thấy trước lúc bão đổ bộ vào bờ mực nước đã bị rút xuống khoảng 0,5m so với thuỷ triều tại thời điểm đó. Tuy nhiên, khi khảo sát thì tại Sơn Trà mực nước đã rút xuống khoảng 1m, nhưng điều đặc biệt là nó diễn ra chỉ trong thời gian là 1h (hình 4). Đây cũng là công việc mà mô hình cần phải hiệu chỉnh trong thời gian tới.

d. Dự báo nước dâng do bão số 9 (Typhoon Durian)

Bão số 9 hay còn gọi là bão Durian, đây là cơn bão có cường độ tương đối mạnh, lại xuất hiện vào cuối mùa bão. Chính vì vậy, có thể có những diễn biến rất phức tạp. Theo bản tin của Trung tâm Dự báo KTTV Trung ương, hồi 7h ngày 02/12, sức gió mạnh nhất ở gần tâm bão mạnh cấp 11, cấp 12 và giật trên cấp 12, *Bảng 4. Kết quả dự báo nước dâng do bão Durian tại một số khu vực*

Tỉnh	Khu vực	Nước dâng lớn nhất có thể xảy ra (m)
Ninh Thuận	Cà Ná	0,3
Bình Thuận	Phan Thiết	0,4
Tp. HCM	Cần Giờ	0,7
ĐB Sông Cửu Long	Cửa Định An	0,5
Kiên Giang	Vịnh Rạch Gía	0,5

Theo kết quả tính toán dự báo, nước dâng do bão Durian gây ra nhìn chung là không lớn, dao động trong khoảng từ 0,3 - 0,7m. Trị số nước dâng lớn nhất có thể xảy ra theo dự báo là 0,7m, bảng 4.

3. Kết luận và kiến nghị

- Qua việc áp dụng quy trình để dự báo nước dâng do bão trong mùa bão năm 2005 và 2006, cộng với phân tích, so sánh kết quả dự báo với số liệu thực đo cho thấy mô hình Delft3D - FLOW có khả năng dự báo nước dâng do bão với độ tin cậy cao, sai số dự báo có thể chấp nhận được;

- Việc triển khai dự báo nghiệp vụ dự báo nước dâng do bão bằng mô hình Delft3D trong mùa bão năm 2006 là rất kịp thời, những kết quả của dự báo một phần nào đó đã góp phần giảm thiểu thiệt hại về người và của do bão gây ra;

Cần tiếp tục triển khai dự báo nghiệp vụ nước dâng do bão bằng mô hình Delft3D. Lựa chọn, phối hợp với Delft Hydraulics để bảo hành và cập nhật phiên bản mới nhất của mô hình nhằm hoàn thiện mô hình cho phù hợp với thực tế như việc chính xác hơn về pha của biến trình nước dâng bão theo thời gian, chính xác về giá trị nước dâng đối với các cơn bão có cường độ mạnh và hướng di chuyển phức tạp.

- Phối hợp với Trung tâm Dự báo KTTV Trung ương thiết lập một "kênh riêng" nhằm thuận lợi cho việc thu nhận các tham số dự báo bão;

- Các bản tin dự báo cần được phát báo tới công chúng một cách sâu rộng hơn, kết hợp với giáo dục nhằm phổ thông hóa các thuật ngữ dự báo đối với cộng đồng;

Nên xây dựng những kịch bản ngập lụt do nước dâng do bão gây ra và tiếp tục phải duy trì việc điều tra, khảo sát nước dâng do bão góp phần hiệu chỉnh mô hình dự báo ngày càng hoàn thiện hơn.

Tài liệu tham khảo

1. *Bảng thủy triều năm. Tập I và Tập II. Trung tâm Khí tượng Thủy văn Biển phát hành. 2006*
2. *Báo cáo dự báo và điều tra khảo sát nước dâng bão năm 2005. Trung tâm Khí tượng Thủy văn Biển, 2005.*
3. *Trần Hồng Lam, Nguyễn Tài Hợi, Nguyễn Bá Thủy. Nước dâng do bão, công tác triển khai dự báo nghiệp vụ tại Việt Nam. Tạp chí KTTV số 543, tháng 3/2006.*
4. *The SCM regional model and VCM detail model. Report March 2001, WL/Delft Hydraulics.*

Tạp chí

ISSN 0866 - 8744
Số 545 * Tháng 5 - 2006

KHÍ TƯỢNG THỦY VĂN

Scientific and Technical Hydro-Meteorological Journal

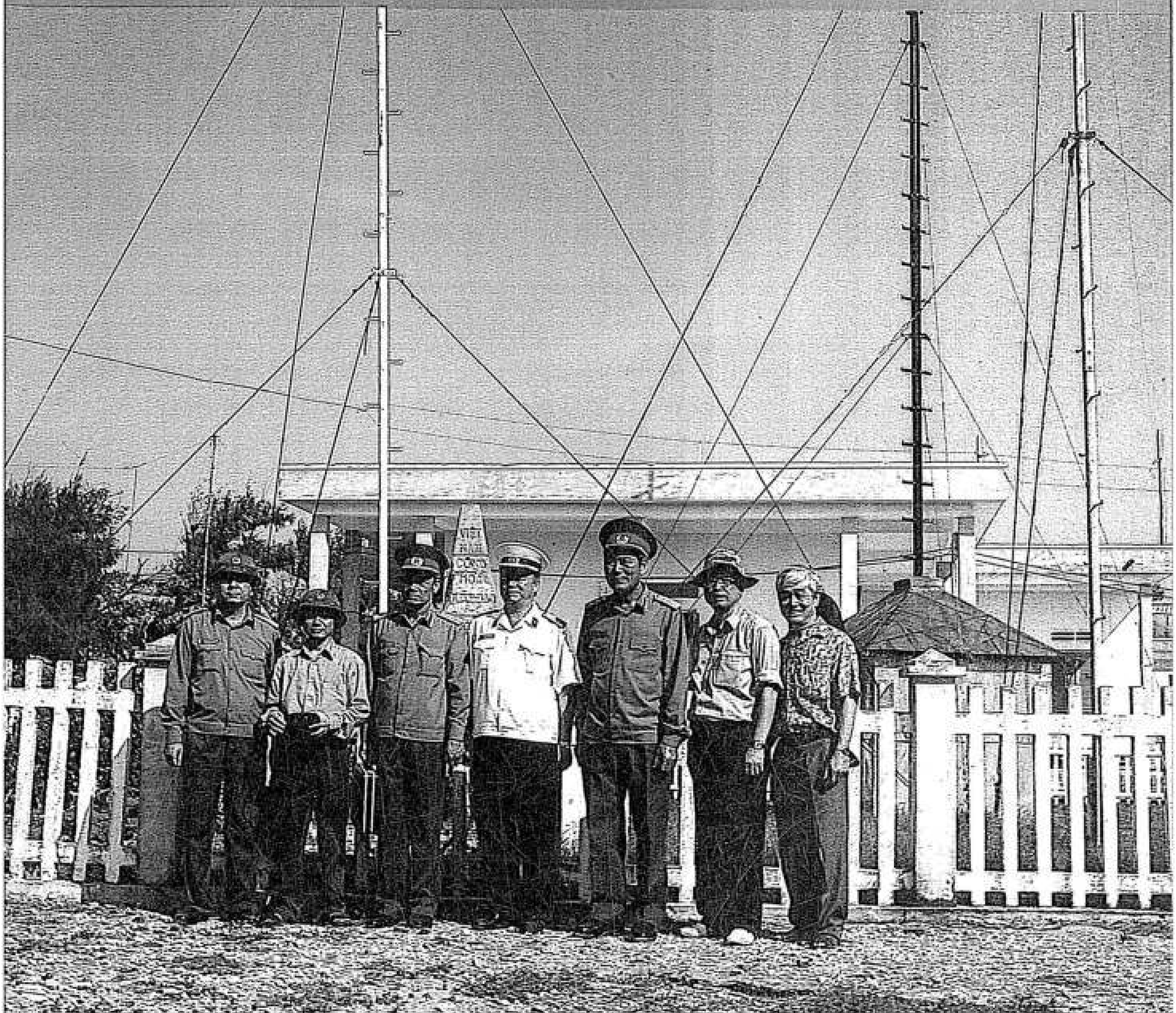

TRUNG TÂM KHÍ TƯỢNG THỦY VĂN QUỐC GIA
National Hydro-Meteorological Service of Vietnam

Contents

Page

NGHIÊN CỨU QUÁ TRÌNH PHÁT TRIỂN VÀ LAN TRUYỀN CỦA SÓNG TẦU TRONG VÙNG VEN BỜ

ThS. **Nguyễn Bá Thủy**, CN. **Trần Đức Trứ**
CN. **Bùi Mạnh Hà**, KS. **Đặng Minh Tuấn**
Trung tâm Khí tượng Thủy văn Biển

Nghiên cứu các hiện tượng trong quá trình phát triển và lan truyền của sóng như hiệu ứng nước nông, khúc xạ, nhiễu xạ, phản xạ, sóng đổ và sóng leo bờ của sóng gió và sóng lừng từ trước đến nay đã được thực hiện khá kỹ lưỡng. Tuy nhiên, sóng sinh ra do tầu chuyển động biến đổi như thế nào vẫn còn là vấn đề ít được nghiên cứu. Trong bài báo này quá trình lan truyền của sóng tầu trong vùng bờ thoải đều với các đường đẳng sâu song song sẽ được đưa ra thảo luận trên cơ sở mô hình lan truyền Boussinesq 2D kết hợp với việc sử dụng biên sóng tầu của Tanimoto (2000).

1. Mở đầu

Sóng sinh ra do sự di chuyển của tầu tại vùng ven biển cũng như trong cảng, sông tác động lên các công trình ven bờ, gây nguy hiểm cho các tầu nhỏ, cho sự ổn định đường bờ. Trên quan điểm về bảo vệ môi trường, sóng tầu có thể gây ra sự xáo động mạnh, ảnh hưởng đến việc nuôi trồng hải sản như rong, tảo biển. Những năm gần đây sóng tầu đã được các nhà thiết kế và đóng tầu quan tâm nhiều vì tác động của nó tới các tầu lân cận. Do vậy, một vấn đề quan trọng được đặt ra là làm sao giảm tối thiểu tác động nguy hiểm của sóng tầu thông qua việc hiểu cơ chế phát sinh và những đặc điểm trong quá trình lan truyền của sóng tầu.

Những nghiên cứu trước (Havelock (1908), Tanimoto (2000) [5]) cho thấy rằng sóng do tầu sinh ra và lan truyền phụ thuộc vào hình dạng vỏ tầu, tốc độ di chuyển của tầu, độ sâu và khoảng cách đến đường tầu chạy. Các tính chất của hiện tượng nước nông, khúc xạ, nhiễu xạ, phản xạ, sóng đổ và sóng leo của sóng gió và sóng biển sâu đã được nghiên cứu khá kỹ lưỡng. Tuy nhiên trong sóng tầu, điều này vẫn còn mới mẻ. Do vậy, vấn đề đặt ra là phải tìm hiểu xem cơ chế phát sinh và đặc trưng của quá trình sóng khi lan truyền vào bờ cụ thể là độ cao sóng lớn nhất, giá trị cực đại của sóng leo bờ và năng lượng của sóng tầu từ đó đưa ra sơ đồ thích hợp trong việc hạn chế tác động của sóng tầu.

2. Cơ sở lý thuyết của mô hình tính sóng tầu

Mô hình tính sóng tầu được thiết lập trên cơ sở giải phương trình Bousinessq 2 chiều của Madsen và Sorensen (1992 [4]). Đây là phương trình đã được cải tiến những đặc trưng về biến đổi sóng tuyến tính ở vùng nước sâu từ phương trình Boussinesq nguyên thuỷ của Penegrine (1967). Mô hình đã sử dụng điều kiện biên sóng tầu của Tanimoto (2000, [5]). Trong trường hợp 2 chiều, hệ phương trình được diễn tả:

(a). Phương trình liên tục:

$$\frac{\partial \zeta}{\partial t}+\frac{\partial Q_x}{\partial x}+\frac{\partial Q_y}{\partial y}=0 \qquad (1)$$

(b).Phương trình động lượng:

- Theo phương x:

$$\frac{\partial Q_x}{\partial t}+\frac{\partial}{\partial x}\left(\frac{Q_x^2}{D}\right)+\frac{\partial}{\partial y}\left(\frac{Q_xQ_y}{D}\right)+gD\frac{\partial \zeta}{\partial x}=\left(\beta+\frac{1}{3}\right)h^2\left(\frac{\partial^3 Q_x}{\partial t\partial x^2}+\frac{\partial^3 Q_y}{\partial t\partial x\partial y}\right)+\beta g h^3\left(\frac{\partial^3\zeta}{\partial x^3}+\frac{\partial^3\zeta}{\partial x\partial y^2}\right)$$
$$+h\frac{\partial h}{\partial x}\left(\frac{1}{3}\frac{\partial^2 Q_x}{\partial t\partial x}+\frac{1}{6}\frac{\partial^2 Q_y}{\partial t\partial y}\right)+h\frac{\partial h}{\partial y}\left(\frac{1}{6}\frac{\partial^2 Q_y}{\partial t\partial x}\right)+\beta g h^2\left\{\frac{\partial h}{\partial x}\left(2\frac{\partial^2\zeta}{\partial x^2}+\frac{\partial^2\zeta}{\partial y^2}\right)+\frac{\partial h}{\partial y}\frac{\partial^2\zeta}{\partial x\partial y}\right\}+R_{bx} \qquad (2)$$

- Theo phương y

$$\frac{\partial Q_y}{\partial t}+\frac{\partial}{\partial y}\left(\frac{Q_y^2}{D}\right)+\frac{\partial}{\partial x}\left(\frac{Q_xQ_y}{D}\right)+gD\frac{\partial \zeta}{\partial y}=\left(\beta+\frac{1}{3}\right)h^2\left(\frac{\partial^3 Q_y}{\partial t\partial y^2}+\frac{\partial^3 Q_x}{\partial t\partial x\partial y}\right)+\beta g h^3\left(\frac{\partial^3\zeta}{\partial y^3}+\frac{\partial^3\zeta}{\partial x^2\partial y}\right)$$
$$+h\frac{\partial h}{\partial y}\left(\frac{1}{3}\frac{\partial^2 Q_y}{\partial t\partial y}+\frac{1}{6}\frac{\partial^2 Q_y}{\partial t\partial x}\right)+h\frac{\partial h}{\partial y}\left(\frac{1}{6}\frac{\partial^2 Q_y}{\partial t\partial y}\right)+\beta g h^2\left\{\frac{\partial h}{\partial y}\left(\frac{\partial^2\zeta}{\partial x^2}+2\frac{\partial^2\zeta}{\partial y^2}\right)+\frac{\partial h}{\partial x}\frac{\partial^2\zeta}{\partial x\partial y}\right\}+R_{by} \qquad (3)$$

Trong đó:

ζ - là dao động mực nước, Q_X, Q_Y là tích phân của vận tốc theo hướng x và y, h là độ sâu thời điểm ban đầu

d - là độ sâu tức thời $d=h+\zeta$

g - là gia tốc trọng trường

ζ - là hệ số phân tán (ζ = 0,15).

Tính sóng đổ ven bờ được thực hiện qua kết hợp với mô hình rối nhớt với việc thêm vào phương trình động lượng thành phần nhớt rối (R_{bx}, R_{by}).

Thành phần gây sóng đổ được diễn tả theo phương trình (4), (5):

$$R_{bx}=\frac{\partial}{\partial x}\left(\nu\frac{\partial Q_x}{\partial x}\right)+\frac{1}{2}\left[\frac{\partial}{\partial y}\left(\nu\frac{\partial Q_x}{\partial y}\right)+\frac{\partial}{\partial y}\left(\nu\frac{\partial Q_y}{\partial x}\right)\right]$$

$$R_{by}=\frac{\partial}{\partial y}\left(\nu\frac{\partial Q_y}{\partial v}\right)+\frac{1}{2}\left[\frac{\partial}{\partial x}\left(\nu\frac{\partial Q_x}{\partial y}\right)+\frac{\partial}{\partial x}\left(\nu\frac{\partial Q_y}{\partial x}\right)\right]$$

Độ nhớt rối được tính:

$$\nu = B\delta_b(h+\zeta)\frac{\partial \zeta}{\partial t} \qquad (6)$$

Trong đó δ_b là hệ số kích thước pha trộn, thường được lấy theo giá trị thực nghiệm bằng 1,2; hệ số B là đại lượng kiểm soát quá trình phân tán năng lượng khi sóng đổ xuất hiện, đại lượng này biến đổi một cách nhuần nhuyễn trong khoảng từ 0 tới 1, để tránh quá trình đổ bị sốc.

Trường hợp mô hình kết hợp với tính sóng leo bờ, kỹ thuật biên khe hẹp của Tao&Kennedy (2000, [3]) đã được sử dụng với bề rộng khe truyền sóng và diện tích tương đối của kênh khi có sóng leo được xác định:

$$b(\zeta)=\begin{cases}1, & \geq z^*\\ \delta+(1-\delta)e^{-\lambda(\eta-z^*)/ho} & \zeta<z^*\end{cases} \quad (7) \qquad A(x,y,t)=A(\zeta)\equiv\int_{ho}^{\eta} b(z)dz \quad (8)$$

$$A(\zeta)=\begin{cases}(\zeta-z^*)+\delta(z^*+ho)+\dfrac{(1-\delta)ho}{\lambda}(1-e^{-\lambda(1+z^*/ho)})\\ \delta(\zeta+ho)+\dfrac{(1-\delta)ho}{\lambda}e^{-\lambda(\eta-z^*)/ho}(1-e^{-\lambda(1+z^*/ho)})\end{cases} \quad (9)$$

Giá trị z* được tính theo công thức:

$$z^*=\frac{-h}{(1-\delta)}+ho\left(\frac{\delta}{1-\delta}+\frac{1}{\lambda}\right) \quad (10)$$

Trong đó: δ là độ rộng của khe hẹp, là hệ số điều khiển quá trình biến đổi của diện tích kênh truyền sóng, ho là độ sâu, z* là giá trị mực nước mà tại đó b = 1.

Kết hợp phương trình Bousinesq 2 chiều với mô hình sóng đổ và sử dụng kỹ thuật biên khe hẹp, hệ phương trình cuối cùng của mô hình tính như sau:

* Phương trình liên tục

$$b\frac{\partial\zeta}{\partial t}+\frac{\partial Q_x}{\partial x}+\frac{\partial Q_y}{\partial y}=0 \quad (11)$$

* Phương trình động lượng

- Phương trình theo phương x:

$$\frac{\partial Q_x}{\partial t}+\frac{\partial}{\partial x}\left(\frac{Q_x^{\,2}}{A}\right)+\frac{\partial}{\partial y}\left(\frac{Q_xQ_y}{A}\right)+gA\frac{\partial\zeta}{\partial x}-R_{bx}+E_x+...=0 \quad (12)$$

- Phương trình theo phương y:

$$\frac{\partial Q_y}{\partial t}+\frac{\partial}{\partial x}\left(\frac{Q_xQ_y}{A}\right)+\frac{\partial}{\partial y}\left(\frac{Q_y^{\,2}}{A}\right)+gA\frac{\partial\zeta}{\partial y}-R_{by}+E_y+...=0 \quad (13)$$

Trong đó, R_{bx}, R_{by} là thành phần gây sóng đổ theo phương x và y đã được mô tả ở trên. E_x và E_y là thành phần gây hấp thụ sóng để tránh hiện tượng phản xạ từ biên. b và A là bề rộng và diện tích tương đối của kênh truyền sóng. Hệ phương trình trên được sai phân hoá trung tâm theo thời gian và sai phân tiến theo không gian với các điểm tính được xác định theo ô lưới hình chữ nhật. Phương pháp ADI (Alternating Direction Implicit) là phương pháp truy đuổi luân hướng đã được áp dụng cho việc giải hệ phương trình sai phân.

3. Các điều kiện biên của mô hình

- Điều kiện về biên tầu chuyển động

Đây là dạng biên di động, sóng được sinh trên các điểm biên này lúc tầu đi qua. Để xác định độ cao (hay năng lượng sóng) tạo ra do tầu, Chen và Sharma (1995) [2] giả thuyết rằng bề rộng tầu là mảnh và coi đó như 1 đoạn thẳng mà tại đó sóng được sinh ra ở hai bên khi tầu đi qua. Với giả thiết này năng lượng sóng do tầu đi qua được xác định:

$$Q_y = \pm\frac{1}{2}U\frac{dS}{dx}$$

Trong đó U là tốc độ di chuyển của tầu, S là diện tích tầu chiếm trên bề mặt nước tại các thời điểm, các điểm trên hành trình của tầu, được tính:

$$S(x_s) = S_0\left[1-(\frac{2x_s}{L_s})\right],\ -1 \le \frac{2x_s}{L_s} \le 1$$

Trong đó S_0 là diện tích phần nổi trên bề mặt nước của tầu.

$$S_0 = \alpha B_s d$$

Với α là hệ số, B_s là kích thước bề ngang của tầu, d là ngấn nước của tầu.

Khi tầu di chuyển, những nhiễu động được sinh ra gồm 2 phần: Nửa phía trước của tầu sẽ là nguồn phát sóng trong khi đó nửa phía sau sóng có hướng đi ngược lại.

Trong nghiên cứu sóng tầu, khái niệm về hệ số Froude được đưa ra:

$$F_h = \frac{U}{\sqrt{gh_s}}$$

Với h_s là độ sâu tại điểm tầu đi qua. Đại lượng $\sqrt{gh_s}$ ở đây được xác định là vận tốc truyền sóng. Trong nghiên cứu sóng tầu thì tính toán với sự thay đổi của hệ số F_h cho các trường hợp nhỏ hơn 1, bằng 1 và lớn hơn 1 là rất ý nghĩa vì điều này cho ta thấy sự thay đổi độ cao của sóng như thế nào khi vận tốc tầu thay đổi.

4. Kết quả tính toán

Để tính toán thử nghiệm mô hình, một kênh tính với đường bờ thẳng, các đường đẳng sâu song song. Tầu di chuyển tại độ sâu h = 15m, độ dốc của đáy kênh tính từ vị trí tầu tới độ sâu h = 1m là 1/50. Trong tính toán, một miền với độ sâu đồng nhất được mở rộng từ phần đáy dốc với mục đích là tránh được sự phản xạ sóng của đường bờ để cho việc phân tích và đánh giá kết quả được thuận tiện hơn. Trên hình 1 biểu diễn mặt cắt ngang của miền tính.

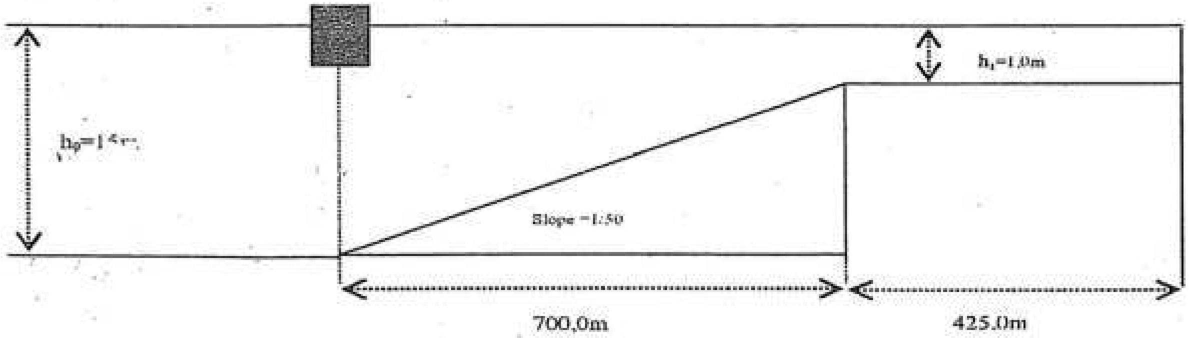

Hình 1. Sơ đồ mặt cắt ngang của miền tính sóng tầu

Các chỉ số của tầu dùng trong mô hình với: Chiều dài là 41m, bề rộng là 14,6m, ngấn nước tầu là 5,58m hệ số là 0,62. Các thông số này sẽ được dùng tính toán cho tất cả các trường hợp trong báo cáo này.

Tốc độ tầu được chọn cho mô phỏng sóng tầu với 3 trường hợp; U_0 = 9,7; 12,13; 14,45m/s, tương ứng với hệ số Froud là 0,8; 1,0 và 1,2. Việc chọn các giá trị về vận tốc tầu như trên nhằm để đánh giá xem sự khác biệt của độ cao sóng tầu như thế nào khi vận tốc tầu thay đổi.

Trên các hình từ 2 - 5 biểu diễn kết quả tính toán trong trường hợp mô hình có tính tới hiện tượng sóng đổ (wave breaking).

Trên các hình 4 biểu diễn dao động mực nước theo thời gian tại các vị trí (x=2000m, y=200m), (x=2000m, y=600m), (x=2000m, y=650m) và (x=2000m, y=700m) trong trường hợp F_h=1. Chúng ta thấy rằng tại một điểm quan trắc sóng tầu luôn quan trắc được nhiều sóng có độ cao và chu kỳ khác nhau. Kết quả tính toán cho thấy, sóng thứ 2 trong nhóm sóng là sóng có biên độ lớn nhất. Các thông số của sóng này thường được đưa ra để đánh giá mức độ ảnh hưởng của sóng do tầu gây nên. Kết quả tính toán cũng cho thấy chỉ có những sóng có biên độ lớn trong chuỗi nhóm sóng là bị đổ, đây là một trong những đặc trưng được phát hiện của sóng tầu.

Tại hình 2, giá trị độ cao sóng cực đại dọc theo các đường cắt ngang ở vị trí x=1000m, 1500m và 2000m với trường hợp F_h = 1 được diễn tả. Có thể có một số nhận xét như sau về sự biến đổi của độ cao lớn nhất của sóng tầu khi lan truyền vào bờ, lúc đầu độ cao sóng giảm bởi hiện tượng tắt dần (damping) và khúc xạ, sau đó độ cao sóng tăng dần do hiệu ứng nước nông và cuối cùng giảm do sóng bị đổ tại vùng nước nông gần bờ. Kết quả tính toán cũng cho thấy, trong khu vực gần bờ, giá trị độ cao sóng cực đại dọc theo mặt cắt x=2000m là lớn nhất và nhỏ hơn cả là tại mặt cắt x=1000m. Điều này cho thấy rằng khi tầu di chuyển, độ cao sóng theo các mặt cắt ngang là biến đổi và có xu hướng tăng dần, tuy nhiên trong kết quả tính toán của mô hình cũng cho thấy rằng độ cao sóng lớn nhất sẽ tăng tới giá trị ổn định ở một khoảng cách mà từ đó khi tầu tiếp tục chuyển động nhưng giá trị độ cao sóng không thay đổi, trong điều kiện đang tính ở đây thì giá trị đó là 2000m. Trong quá trình lan truyền vào bờ, nếu gặp phải vùng nước nông, sóng sẽ bị đổ. Vị trí các điểm sóng đổ theo các mặt cắt là tuỳ thuộc vào độ cao sóng tại đó. Với các mặt cắt như trên, sóng đổ suất hiện tại các độ sâu h=2,65m; 2,45m và 1,55m tương ứng tại x=2000m, 1500m và 1000m.

Để xác định sự biến đổi độ cao sóng tầu theo tốc độ di chuyển của tầu như thế nào, mô hình đã tính thử nghiệm cho 3 trường hợp với hệ số Froud khác nhau là F_h=0,8; 1,0 và 1,2. Trên hình 3 biểu diễn kết quả tính toán độ cao sóng cực đại dọc mặt cắt có toạ độ x = 2000m cho 3 trường hợp như trên. Kết quả tính toán cho thấy về xu thế biến đổi độ cao sóng trong 3 trường hợp là giống nhau, tuy nhiên với trường hợp F_h = 0,8 không có hiện tượng sóng đổ xuất hiện ở mặt cắt này. Một điều lý thú được phát hiện trong kết quả tính của mô hình là khi so sánh độ cao sóng tại 1 điểm thì không phải khi vận tốc tầu lớn thì độ cao sóng sẽ tăng.Trong trường hợp này độ cao sóng lớn hơn cả khi so sánh là trường hợp F_h = 1. Chúng tôi đã thử nghiệm tính toán nhiều với các hệ số F_h khác nhau và nhận thấy rằng giá trị độ cao sóng lớn nhất khi hệ số F_h gần bằng 1 có nghĩa là khi vận tốc của tầu xấp xỉ vận tốc truyền sóng.

Hiện tại chúng ta chưa có số liệu quan trắc sóng tầu để kiểm chứng độ chính xác và hiệu chỉnh mô hình. Báo cáo đã dùng kết quả phân tích giải tích của Tanimoto (2004) [4] để so sánh.

Trên hình 5 là so sánh giữa kết quả tính toán độ cao sóng cực đại của mô hình và kết quả phân tích trong cùng 1 điều kiện cho trường hợp tại mặt cắt x = 2000m và với 3 hệ số Froud là F_h=0,8; 1,0 và 1,2. Có thể nhận xét rằng có sự khá phù hợp giữa 2 tính toán trên trừ trường hợp trong vùng gần bờ. Với trường hợp F_h = 1,0 kết quả so sánh là phù hợp hơn cả.

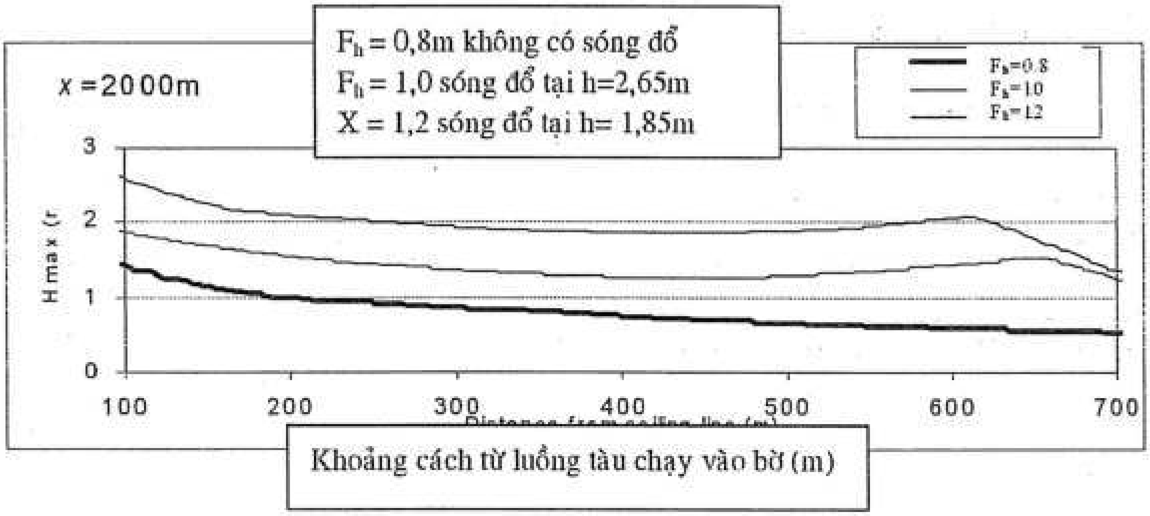

Hình 2. Sự biến đổi giá trị lớn nhất của sóng tầu dọc theo mặt cắt (Fh=1)

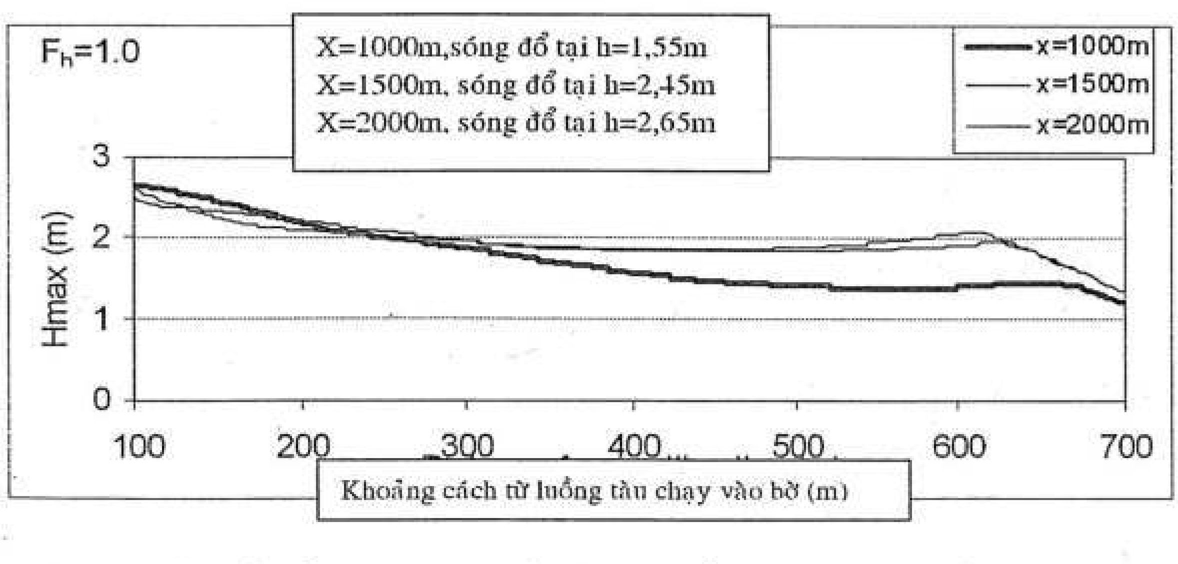

Hình 3. Sự biến đổi giá trị lớn nhất của sóng tầu dọc theo mặt cắt (x=2000m)

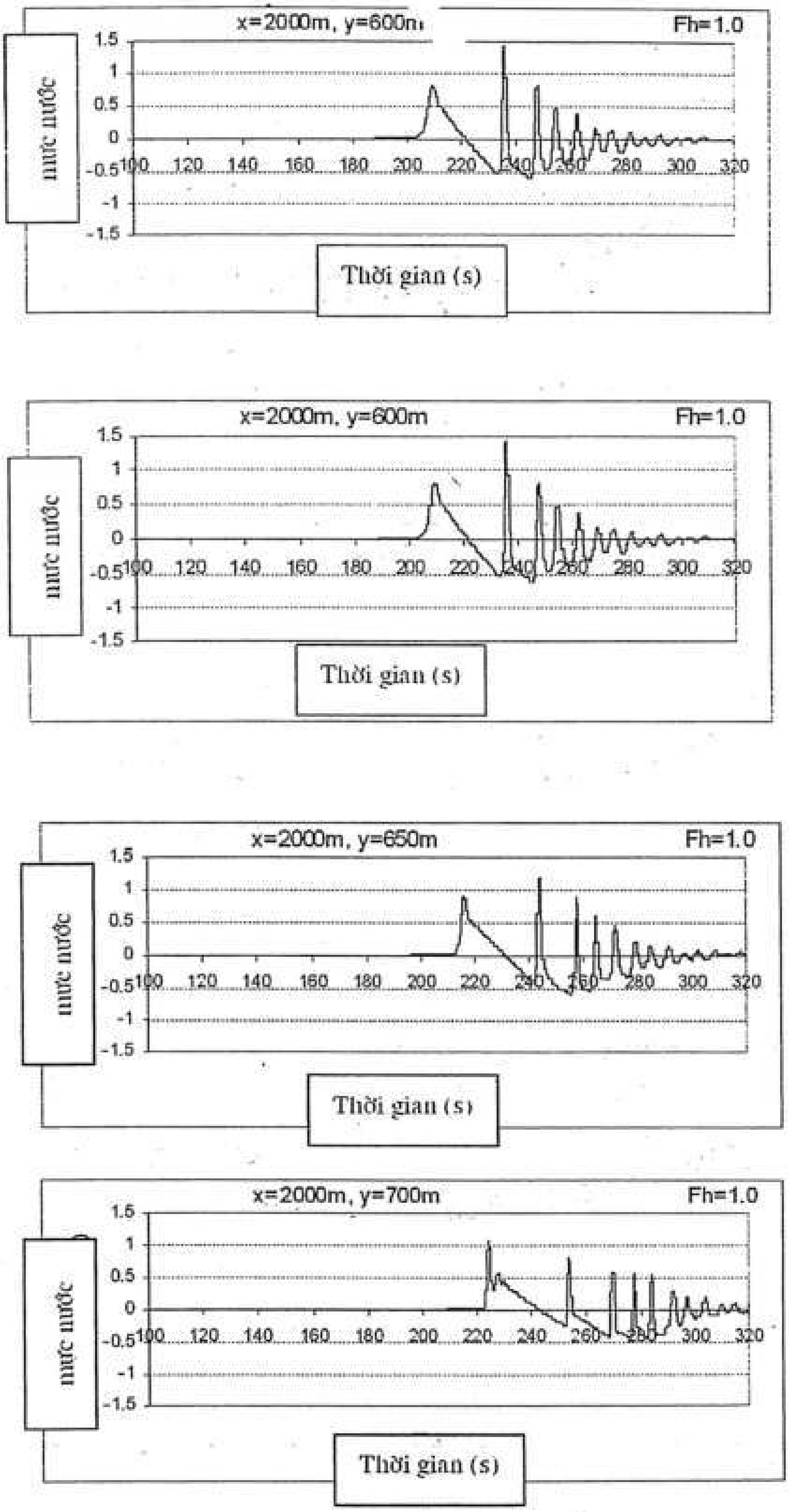

Hình 4. Dao động mực nước theo thời gian của sóng tầu ($x = 2000, F_h = 1,0$)

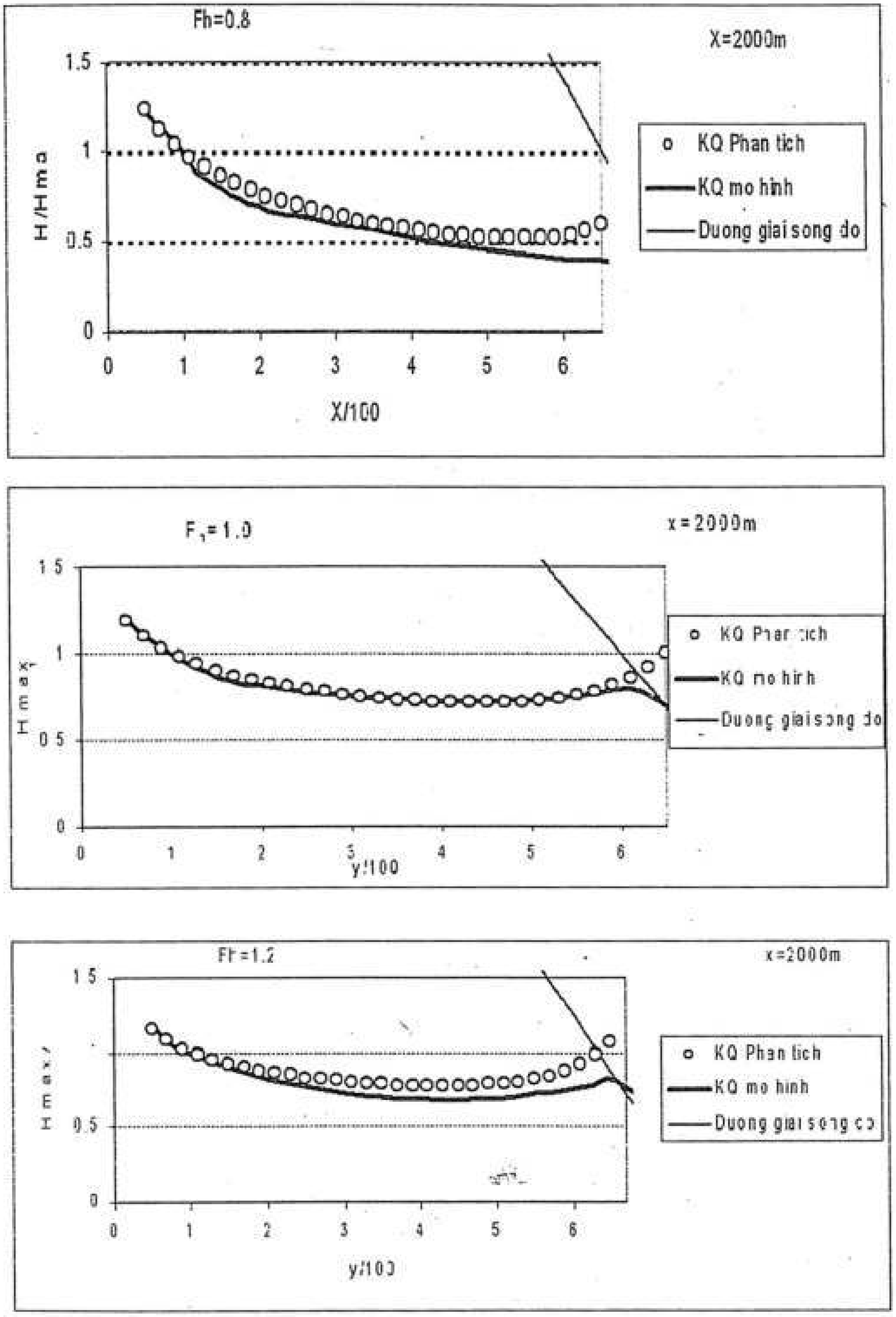

Hình 5. So sánh giữa kết quả tính toán của mô hình và kết quả phân tích giải tích

6. Kết luận

Mô hình tính sóng do tầu sinh ra lan truyền vào vùng ven bờ dựa trên phương trình Bousinesq 2D và sử dụng điều kiện biên sóng tầu của Tanimoto (2000) đã được phát triển. Mô hình đã mô phỏng được một số hiện tượng khi sóng lan truyền vào bờ cũng như đặc điểm của trường sóng khi tầu chạy trên một kênh phẳng, có đáy thoải. Hiện tượng sóng leo bờ cũng như xác định mối quan hệ giữa độ cao sóng cực đại với hình dáng, trọng lượng và vận tốc của tầu cũng như sẽ được nghiên cứu thêm. Những nghiên cứu sâu về sóng tầu sẽ rất có ý nghĩa trong các ngành giao thông, đóng tầu, quy hoạch xây cảng và nuôi trồng thuỷ sản.

Tài liệu tham khảo

1. Chen, Q., Kirby, J.T., Dalrymple, R.A., Kennedy, A.B. and Chawla, A.. Bousinesq Modeling of wave transformation, breaking and runup.II:2D. Journal of waterway, Port coastal, and Ocean Engineering/January/February, 48-55, 2000.
2. Chen, X.-N. & Sharma, S.D. . A slender ship moving at a near-critical speed in a shallow channel. J. Fluid Mechanics 291: 263-285,1995.
3. Kennedy, A. B, Chen, Q., Kirby, J. T., & Dalrymple, R. A. . Boussinesq modeling of wave transformation, breaking and runup. I: One dimension. J. Waterway of Port, Coastal and Ocean Engineering 126: 39-47, 2000.
4. Madsen, P.A., Sorensen, O.R.. A new form of the Boussineq equations with improved lineardispersion characteristic: Part 2. A slowly varying bathymetry. Coastal Eng.18, 183-204,1992.
5. Tanimoto, K., Kobayashi, H. & Ca, V.T.. Ship waves in a shallow and narrow channel. Proc. of 27th Conference on Coastal Engineering 2: 1141-1154, 2000.

CỘNG HÒA XÃ HỘI CHỦ NGHĨA VIỆT NAM
Độc lập – Tự do – Hạnh phúc

GIẤY XÁC NHẬN LÀ TÁC GIẢ CHÍNH CỦA BÀI BÁO KHOA HỌC

Tạp chí: Khí tượng thủy văn

Tên bài báo: Nước dâng do bão - công tác triển khai dự báo nghiệp vụ tại Việt Nam (2006). Tạp chí Khí tượng Thủy văn, số 543, trang 32-41

Tác giả: Trần Hồng Lam, Nguyễn Tài Hợi, Nguyễn Bá Thủy

Chúng tôi công nhận TS. Nguyễn Bá Thủy là người đóng góp chính trong các nội dung của bài báo này và xác nhận TS. Nguyễn Bá Thủy là tác giả chính của bài báo.

Họ và tên tác giả	Chữ ký	Ngày/tháng/năm
TS. Trần Hồng Lam	[signature]	28/6/2019
TS. Nguyễn Tài Hợi	[signature]	26/6/2019
TS. Nguyễn Bá Thủy	[signature]	3/7/2019

000103

Tạp chí

ISSN 0866 - 8744

Số 543 * Tháng 3 - 2006

KHÍ TƯỢNG THỦY VĂN

Scientific and Technical Hydro-Meteorological Journal

22-3 NGÀY NƯỚC THẾ GIỚI: NƯỚC VÀ VĂN HOÁ

23-3 NGÀY KHÍ TƯỢNG THẾ GIỚI: PHÒNG CHỐNG VÀ GIẢM NHẸ THIÊN TAI

TRUNG TÂM KHÍ TƯỢNG THỦY VĂN QUỐC GIA

National Hydro-Meteorological Service of Vietnam

TỔNG BIÊN TẬP: **TS. BÙI VĂN ĐỨC**

TẠP CHÍ KHÍ TƯỢNG THỦY VĂN
Số 4, Đặng Thái Thân, Hà Nội
Điện thoại: 04 8244118; E-mail: ducbv@fpt. vn

MỤC LỤC

In tại Xí nghiệp in Số 3 - NXB Bản đồ. Giấy phép hoạt động báo chí số 25/GP-BVHTT. Bộ VHTT cấp ngày 05-4-2004. Khổ 19cmx27cm - 60 trang.

Giá bán: 10.000đ

NƯỚC DÂNG DO BÃO - CÔNG TÁC TRIỂN KHAI DỰ BÁO NGHIỆP VỤ TẠI VIỆT NAM

TS. **Trần Hồng Lam**, TS. **Nguyễn Tài Hợi**, ThS. **Nguyễn Bá Thuỷ**
Trung tâm Khí tượng Thuỷ văn Biển

Nước dâng do bão được xem như sự biến đổi mực nước có chu kỳ dài dưới tác dụng của gió và khí áp lên khu vực bão xuất hiện. Ở đây khái niệm nước dâng do bão được coi là sự chênh lệch mực nước biển khi có và không có bão ảnh hưởng. Các tham số bão, địa hình đường bờ, sự quay của quả đất và tính chất thuỷ triều là những yếu tố quyết định độ dâng của mực nước biển. Hiện tượng nước dâng do bão đã gây thiệt hại lớn về người và tài sản. Để giảm thiểu thiệt hại thì việc xây dựng một quy trình dự báo nghiệp vụ nước dâng do bão là một trong những nhiệm vụ cấp bách hàng đầu của ngành khí tượng thuỷ văn. Trong bài báo này nhóm tác giả giới thiệu mô hình dự báo nghiệp vụ Delft3D-Flow đã được sử dụng tại Trung tâm Khí tượng Thuỷ văn Biển để bạn đọc tham khảo.

1. Tầm quan trọng của nghiên cứu và dự báo nước dâng do bão

Trên thế giới những nơi bị ảnh hưởng nặng của nước dâng do bão như vùng vịnh Bengal, đặc biệt là Băngladet (nước dâng trong năm 1990 lên cao tới hơn 7m đã làm hơn 400.000 người thiệt mạng) tại vùng biển Caribe, nước dâng cao nhất ghi được là 8m trong cơn bão Floria (Mỹ) làm 5000 người chết; cơn bão Katrina đổ bộ vào bang New Orleans đã gây nước dâng 6m, làm 10.000 người chết và 30.000 người mất nhà cửa, thiệt hại nhiều tỷ đô la. Tại khu vực Đông Bắc Á, các nước Nhật Bản, Triều Tiên và Trung Quốc cũng chịu nhiều thiệt hại do nước dâng, trong đó mực nước dâng cao nhất đo được tại Triều Tiên tới 5,2m. Ở Việt Nam, nước dâng do bão cũng gây thiệt hại lớn về người và của, mực nước dâng lớn nhất ghi được trong cơn bão DAN năm 1989 là 3,6m. Có thông tin cho rằng trong lịch sử đã ghi nhận mực nước dâng do bão năm 1881 tại Hải Phòng làm thiệt mạng khoảng 300.000 người (?). Gần đây nhất là tháng 9 năm 2005, bão Damrey gây nước dâng lớn tới 2,05m tại Nam Định gây vỡ đê và thiệt hại lớn mặc dù Chính phủ cùng toàn dân đã chuẩn bị đối phó rất kỹ với cơn bão này.

Ngoài bão thì gió mùa cũng gây ra hiện tượng nước dâng, tại Việt Nam trong những đợt gió mùa mạnh (cấp 6, 7) và kéo dài 2 đến 3 ngày mực nước dâng lên khoảng 30 - 40cm. Nước dâng do bão đặc biệt nguy hiểm khi xuất hiện vào đúng thời kỳ triều cường, mực nước tổng cộng dâng cao, kết hợp với sóng to đã tràn qua đê vào đồng ruộng, đây chính là nguyên nhân gây thiệt hại nặng nề về người và của. Tại Việt Nam, trong năm 2005 có 4 cơn bão gây nước dâng cao thì 2 cơn (bão số 2 - Washi và bão số 7 - Damrey) nước dâng xẩy ra đúng vào lúc triều cường nên thiệt hại do 2 cơn bão này tại các tỉnh Hải Phòng và Nam Định là rất lớn.

Nhận thức được tầm quan trọng của vấn đề này, việc nghiên cứu và dự báo nước dâng do bão đã và đang được quan tâm một cách hết sức đặc biệt.

2. Các phương pháp dự báo nước dâng do bão

Trong những năm gần đây do ảnh hưởng của biến đổi khí hậu toàn cầu, thiên tai ngày một gia tăng, đặc biệt là bão, kèm theo lũ lụt và nước dâng do bão. Vì vậy, vấn đề tính toán và dự báo nước dâng do bão có thể xảy ra cho từng khu vực là một trong những biện pháp tích cực để đưa ra biện pháp phòng tránh và những giải pháp cần thiết nhằm giảm thiểu thiệt hại. Trên thế giới có rất nhiều mô hình dự báo nước dâng do bão ở các quy mô khác nhau tùy thuộc vào khả năng của các máy móc, thiết bị, khả năng về cơ sở dữ liệu và người sử dụng v.v....Mỗi công nghệ dự báo nước dâng do bão lại có mức độ hiện đại, bao quát, cụ thể khác nhau.

Hiện nay chúng ta đã và đang sử dụng 3 phương pháp chính để tính toán và dự báo nước dâng do bão:

Phương pháp thống kê khá đơn giản và cho kết quả tương đối khả quan. Nhưng nhược điểm của phương pháp này là phải dựa vào chuỗi số liệu nước dâng và bão đã có cho những khu vực cụ thể, do vậy phạm vi áp dụng thường bị hạn chế.

Phương pháp đưa ra toán đồ trên cơ sở các cơn bão chuẩn để dự báo (phương pháp SPLASH) đã khắc phục được những khiếm khuyết của phương pháp thống kê, tuy nhiên những tham số hoá khi xây dựng bộ biểu đồ luôn luôn bị giới hạn. Vì vậy, độ chính xác không cao.

Phương pháp dùng mô hình số trị thuỷ động hai, ba chiều ưu điểm là luôn cho kết quả đầy đủ về trường mực nước theo không gian và thời gian. Phương pháp này đang được dùng phổ biến nhất trên thế giới và đã áp dụng vào Việt Nam.

Tại các nước chịu nhiều thiệt hại bởi nước dâng do bão như: Mỹ, Nhật, Nga, Trung Quốc... đã tự xây dựng các phần mềm tính toán dự báo nước dâng. Một số nước như Ấn Độ, Bănglađet, Phillipin đã mua các phần mềm dự báo của các trung tâm nghiên cứu về nước dâng do bão nổi tiếng như Delft Hydraulics của Hà Lan.

Hiện tại, phần mềm 3 chiều dự báo nước dâng do bão Delft3D-Flow của Hà Lan đã được sử dụng vào dự báo nghiệp vụ nước dâng do bão ở Việt Nam. Những kết quả tính toán và dự báo nghiệp vụ nước dâng do bão năm 2005 đã góp phần giảm thiểu những thiệt hại về người và của, đặc biệt là trong bão số 7.

3. Lựa chọn mô hình dự báo nghiệp vụ nước dâng do bão ở Việt Nam

Cùng với các chuyến điều tra khảo sát để xác định mức độ thiệt hại cũng như trị số nước dâng tại các khu vực bão ảnh hưởng thì việc lựa chọn một mô hình dự báo tốt là vấn đề cấp bách hàng đầu và có ý nghĩa thực tiễn.

Hiện nay, Trung tâm Khí tượng Thuỷ văn Biển đang sử dụng mô hình Delft3D-Flow dự báo nghiệp vụ nước dâng do bão ở Việt Nam. Mô hình Delft3D đã được triển khai áp dụng trong thực tiễn với tính toán thuỷ triều và dự báo nước dâng cho nhiều nước trên thế giới như Indonesia, Hồngkông, Ấn Độ. Những kết quả tính toán, dự báo tại Việt Nam cho thấy đây là một mô hình tiên tiến, có độ tin cậy và ứng dụng thực tiễn cao.

Mô hình Delft3D-Flow do Viện Thuỷ lực Delft Hà Lan thiết lập và đã được chuyển giao cho Việt Nam trong khuôn khổ dự án hợp tác giữa 2 chính phủ Việt Nam và Na Uy về "Hệ thống trạm phao và cảnh báo bão".

Delft3D-Flow là mô hình 3 chiều tính toán các quá trình không ổn định của hoàn lưu, các quá trình vận chuyển được tạo ra bởi thuỷ triều và tác động của các yếu tố khí tượng. Mục đích cơ bản của mô hình 2 chiều (2D - depth - averaged) và 3 chiều (3D) là mô phỏng quá trình lan truyền thuỷ triều và dòng chảy gió bao gồm sự ảnh hưởng của mật độ do tác động không ổn định của phân bố nhiệt độ và độ muối trong vùng biển nông, vùng ven bờ, vùng cửa sông, vùng sông và hồ. Mô hình hướng tới một quan điểm là quy mô ngang được xác định có ý nghĩa hơn quy mô thẳng đứng.

Những ứng dụng cơ bản của mô hình 2 chiều là mô phỏng thuỷ triều, nước dâng do bão, sóng do động đất, dao động mực nước tại các công trình, lan truyền ô nhiễm, các quá trình này được coi là đồng nhất theo phương thẳng đứng. Những ứng dụng thực tế của mô hình trên thế giới cần phải kể đến là các dự án áp dụng mô hình vào dự tính thuỷ triều và nước dâng do bão ở một số nước trên thế giới.

Mô hình Delft3D-Flow được thiết lập dựa trên việc giải hệ phương trình nước nông không ổn định. Hệ phương trình bao gồm: các phương trình động lượng theo phương ngang, phương trình liên tục và các phương trình vận chuyển. Các phương trình được giải trên hệ toạ độ đề các và hệ toạ độ cầu. Để áp dụng cho tính toán và dự báo thuỷ triều, nước dâng do bão ở Việt Nam, mô hình đã sử dụng 2 lưới tính; 1 lưới vuông có độ phân giải thô (27,7km) và 1 lưới cong với độ phân giải cao khi vào gần bờ (4km). Trên các biên lỏng của lưới tính, 8 sóng thuỷ triều chính được thiết lập và mô hình sử dụng số liệu quan trắc mực nước các trạm ven bờ Việt Nam để hiệu chỉnh.

Một số ưu điểm nổi bật của mô hình Delft3D-Flow trong dự báo nước dâng do bão:

Vừa tính đồng thời cả thuỷ triều và nước dâng. Mô hình tính chập các sóng triều chứ không tính sóng lẻ, ưu điểm này rất có ý nghĩa vì nước ta nhiều khu vực thuỷ triều có biên độ dao động lớn do vậy mô hình sẽ khắc phục được hiệu ứng tương tác phi tuyến giữa nước dâng và thuỷ triều.

Trong tính toán và dự báo nước dâng do bão, mô hình đã kết hợp trường gió nền với trường gió bão để tính toán do vậy đã giải quyết được trong trường hợp có nhiều hình thế thời tiết trên khu vực dự báo.

4. Quy trình dự báo nghiệp vụ nước dâng do bão

Việt Nam là quốc gia chịu nhiều thiệt hại do nước dâng, vì vậy không thể không có một quy trình dự báo nghiệp vụ hiện tượng này. Trong quy trình nghiệp vụ dự báo nước dâng do bão, các công đoạn như thu thập thông tin bão, tính toán nước dâng, thiết kế và phát bản tin được thực hiện trình tự, liên hoàn sao cho các thông tin được cập nhật sớm nhất đến người dân.

Trong năm 2005, kể từ sau cơn bão số 2, việc triển khai dự báo nghiệp vụ nước dâng do bão đã được thực hiện ở Trung tâm Khí tượng Thuỷ văn Biển. Quy trình sẽ được vận hành khi có các thông tin về bão hình thành trên Biển Đông và có xu thế di chuyển vào ven bờ Việt Nam thì việc tính toán, dự báo và phát bản tin sẽ được thực hiện, trong một ngày có 4 dự báo vào các thời điểm sau khi nhận được các thông tin dự báo về bão mới nhất ở thời điểm 01h, 06h, 13h và 19h giờ Việt Nam. Quá trình dự báo được tiến hành cho tới khi bão đổ bộ vào bờ hoặc bão tan hoặc di chuyển ra ngoài lãnh thổ Việt Nam.

Mô hình sử dụng nguồn số liệu chính được lấy từ Trung tâm Dự báo Khí tượng Thuỷ văn Trung ương (KTTVTƯ) phát dự báo bão cho 24 giờ, được cập nhật thường xuyên trên Internet với hầu hết các tham số bão quan trọng, đồng thời để có những dự báo xa hơn (72 giờ), các số liệu về dự báo của các Trung tâm dự báo Bão trên thế giới như JMA, Hồngkông cũng được cập nhật và bổ xung. Tuy nhiên, có một số khó khăn trong dự báo nước dâng năm 2005 như sau:

Bản tin dự báo bão của Trung tâm Dự báo KTTVTƯ có thời hạn là 24 giờ, như vậy để có những dự báo dài hơn chúng tôi khắc phục bằng việc cập nhật các thông tin dự báo 72 giờ của JMA, tuy nhiên giữa 2 bản tin dự báo này có lúc không khớp nhau do vậy sẽ khó khăn cho làm dự báo nước dâng.

Còn một số tham số dự báo bão theo yêu cầu của mô hình không có trong các bản tin dự báo của Trung tâm Dự báo KTTVTƯ như bán kính gió với tốc độ gió 55m/s, 91m/s và 182m/s, trong quá trình tính toán và dự báo, các thông số này cũng được lấy bổ xung từ JMA.

Các bản tin dự báo bão thường được cập nhật muộn, thường sau 1,5 giờ so với thời điểm phân tích, kể cả thời gian xử lý và tính của mô hình (khoảng 2,0 giờ) thì sẽ chậm khoảng 3,0 giờ so với thời điểm cần dự báo. Do vậy, cần phải nâng cấp tốc độ tính toán của máy tính cũng như giảm thời gian truyền tải các thông tin về bão.

Bản tin dự báo nước dâng được lập và phát lên các phương tiện thông tin đại chúng ngay sau khi có kết quả tính toán. Tùy thuộc vào vị trí bão đổ bộ và cường độ bão mà vị trí các khu vực phát bản tin dầy hay thưa khác nhau, thông thường tại mỗi tỉnh phía bắc có từ 2 - 4 điểm được phát tin, tương ứng với khoảng 20 km đường biển, khoảng cách này được đánh giá là đã mô tả được chi tiết sự khác biệt nước dâng trong bão theo không gian.

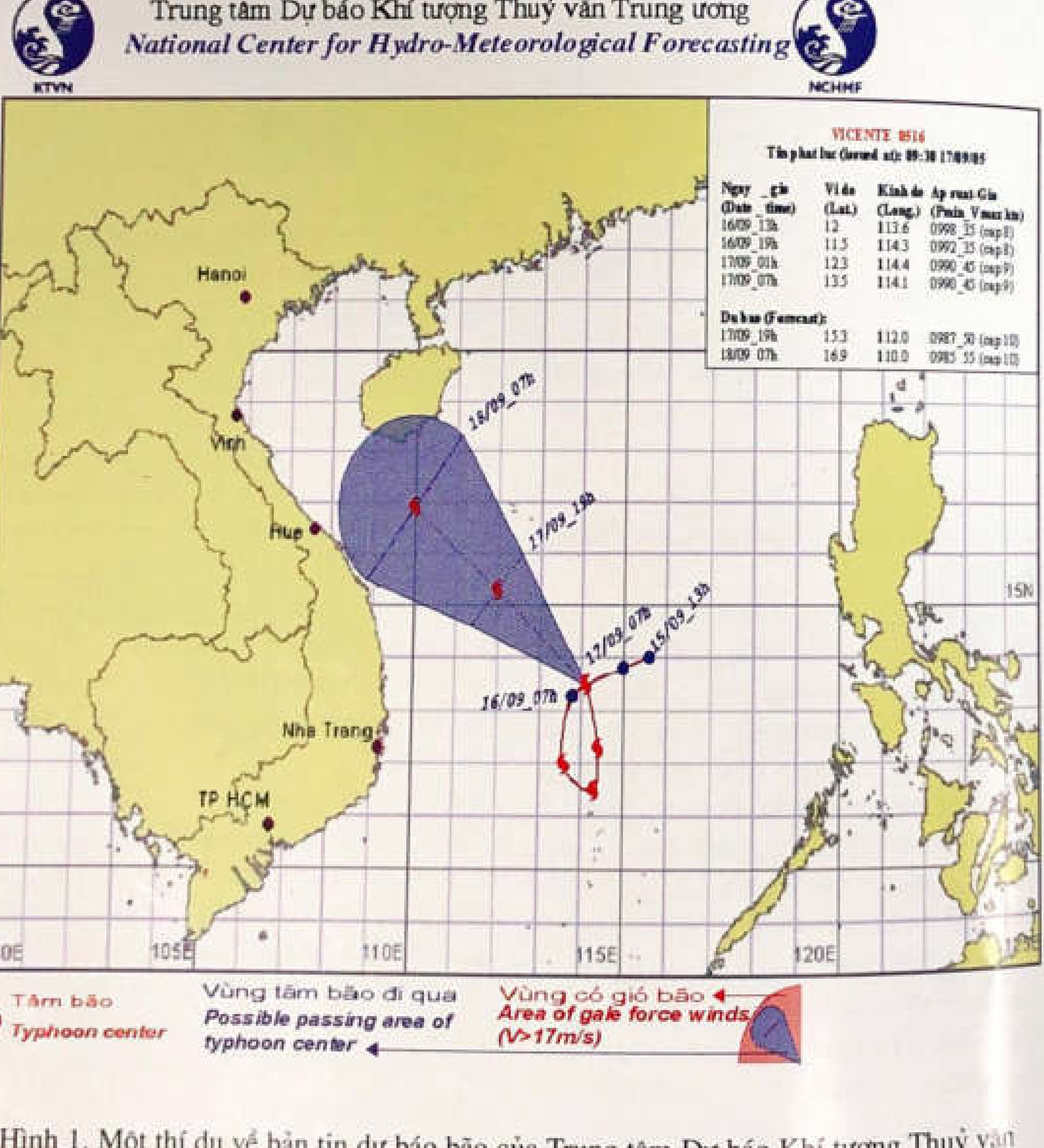

Hình 1. Một thí dụ về bản tin dự báo bão của Trung tâm Dự báo Khí tượng Thuỷ văn Trung ương phát báo cơn bão số 6 trên mạng Internet ngày 17/IX/2005

Trong các bản tin dự báo nước dâng do bão, hiện đã có các thông tin về điểm phát tin dự báo, độ cao nước dâng. Trong thời gian tới, việc truyền hình ảnh bản đồ phân bố nước dâng, cũng như xây dựng kịch bản ngập lụt do nước dâng tại các vùng đất thấp có thể xảy ra cần được tiến hành khẩn trương để đưa vào dự báo và cảnh báo.

Bảng 1. Một thí dụ về bản tin dự báo nước dâng do bão được thực hiện từ Trung tâm Khí tượng Thuỷ văn Biển gửi lên Trung tâm Dự báo KTTV TƯ

Trung tâm Khí tượng Thủy văn Biển	Cộng hòa xã hội chủ nghĩa Việt Nam Độc lập - Tự do - Hạnh phúc

Hà Nội, ngày 1 tháng 11 năm 2005

BẢN TIN DỰ BÁO NƯỚC DÂNG DO BÃO SỐ 8 LÚC 16H30 NGÀY 1/11/2005

(Theo số liệu Dự báo bão của Trung tâm Dự báo Khí tượng Thuỷ văn Trung ương phát lúc 14h30 ngày 1/11/2005 trên mạng Internet và số liệu dự báo 72 giờ của JMA trên Internet)

Bản tin số: 13

Tên tỉnh	Vị trí	Mực nước cực đại có thể xảy ra theo (m) (thuỷ triều + nước dâng)	Nước dâng lớn nhất có thể xảy ra (m)	Thời gian
Thanh Hoá	Tĩnh Gia	2.6 - 3.0m	0.6 – 1.0m	23h 1/11 - 4h 2/11
Nghệ An	Diễn Châu	2.9 - 3.2m	0.8 - 1.2m	23h 1/11 - 4h 2/11
Hà Tĩnh	Cửa Sót	3.0 - 3.4m	1.0 - 1.4m	23h 1/11 - 4h 2/11
	Cửa Khẩu	2.9 - 3.2m	1.1 - 1.5m	23h 1/11 - 4h 2/11
Quảng Bình	Đồng Hới	2.5 - 2.8m	1.0 - 1.3m	22h 1/11 - 2h 2/11
Quảng Trị	Cửa Tùng	2.2 - 2.7m	0.8 - 1.3m	20h 1/11 – 1h 2/11
Huế	Thuận An	2.1 - 2.6m	0.8 - 1.3m	20h 1/11 – 1h 2/11
Quảng Nam	Hội An	2.1 - 2.5m	0.7 - 1.1m	18h – 23h 1/11
	Tam Kỳ	2.1 - 2.5m	0.7 - 1.1m	18h – 23h 1/11
Quảng Ngãi	Dung Quất	2.0 - 2.3m	0.4 - 0.7m	17h – 23h 1/11

Lưu ý:

Các tỉnh ven biển từ Thanh Hoá đến Quảng Ngãi, đề phòng nước dâng kết hợp với triều lên cao từ 2 đến 3,4 m (trong đêm nay 1/11 và sáng mai 2/11).

Bản tin dự báo tiếp theo sẽ được phát báo sau khi nhận được số liệu dự báo bão của Trung tâm Dự báo Khí tượng thuỷ văn Trung ương.

Trung tâm Khí tượng Thuỷ văn Biển

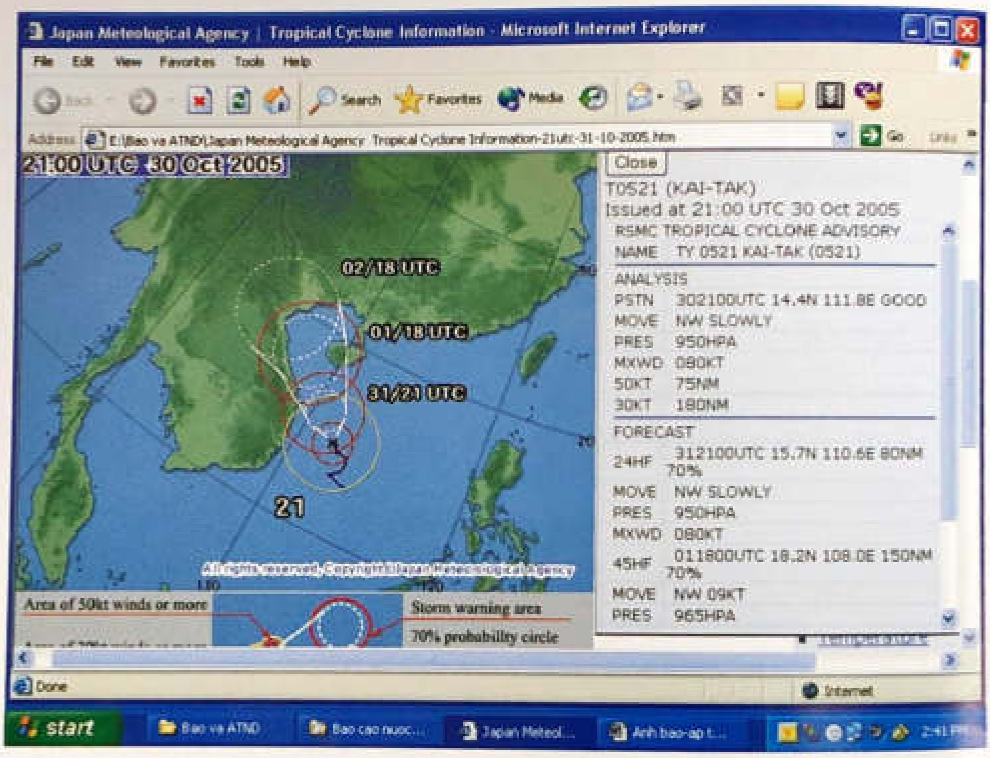

Hình 2. Một thí dụ của bản tin dự báo bão của JMA trong bão số 8 phát trên mạng Internet ngày 30/X/2005

5. Kết quả tính toán, dự báo nước dâng do bão năm 2005

Năm 2005 có thể nói là năm điển hình về tần suất bão ảnh hưởng vào Việt Nam cũng như cường độ và sức tàn phá của nó. Những cơn bão gây nước dâng lớn đáng kể nhất trong năm 2005: bão số 2 có trị số nước dâng lớn nhất tại Đồ Sơn-Hải Phòng là 1,85m, bão số 6 gây nước dâng lớn nhất là 1,8m tại Sầm Sơn-Thanh Hoá và 2,01m là trị số nước dâng lớn nhất do bão số 7 gây ra tại Hải Hậu - Nam Định. Giữa kết quả tính toán dự báo bằng mô hình và kết quả điều tra khảo sát có sai số chấp nhận được.

Kể từ sau bão cơn số 2, phân công trực dự báo và phát bản tin dự báo nước dâng đã được Trung tâm Biển thực hiện rất nghiêm túc và khẩn trương đặc biệt là trong bão số 7, cơn bão có tên quốc tế là Damrey được coi là mạnh nhất trong vòng 9 năm qua với khí áp ở tâm có lúc tới 955mb, tốc độ gió giật 146m/s. Bão số 7 đã được theo dõi thường xuyên và phát các bản tin dự báo nước dâng xa (72 giờ) trên cơ sở các kết quả dự báo của các trung tâm dự báo bão trong và ngoài nước. Do có được những thông tin dự báo xa về sự nguy hiểm của bão số 7, cùng với các ngành liên quan, công việc chuẩn bị đối phó với bão số 7 rất khẩn trương và kịp thời. Đúng như phân tích, bão số 7 rất mạnh nhưng có đường đi đơn giản, do vậy các bản tin dự báo rất kịp thời và có độ chính xác khá cao đặc biệt là khi bão đã di chuyển gần vào bờ. Trên các hình và bảng dưới đây trình bầy kết quả của tính toán dự báo và kết quả điều tra của bão số 2, 6, 7 và số 8. Có thể thấy rằng kết quả dự báo bằng mô hình khá phù hợp với thực tế và đã phản ánh được độ tin cậy của mô hình Delf3D-Flow. Trong dự báo nước dâng do bão, chất lượng dự báo phụ thuộc rất nhiều vào kết quả dự báo bão. do vậy sự phối hợp giữa các cơ quan dự báo với nhau là điều rất cần thiết.

Bảng 2. Sai số gặp phải trong tính toán nước bão tại các trạm hải văn trong bão số 2, số 6, số 7 và số 8

Trạm	Thực đo (m)	Tính toán (m)	Sai số (%)
Hòn Dấu (trong cơn bão số 2)	1,4	1,1	15
Hòn Dấu (trong cơn bão số 6)	1,0	0,7	30
Hòn Dấu (trong cơn bão số 7)	1,2	1,5	25
Đồng Hới (trong cơn bão số 8)	0,8	1,0	20

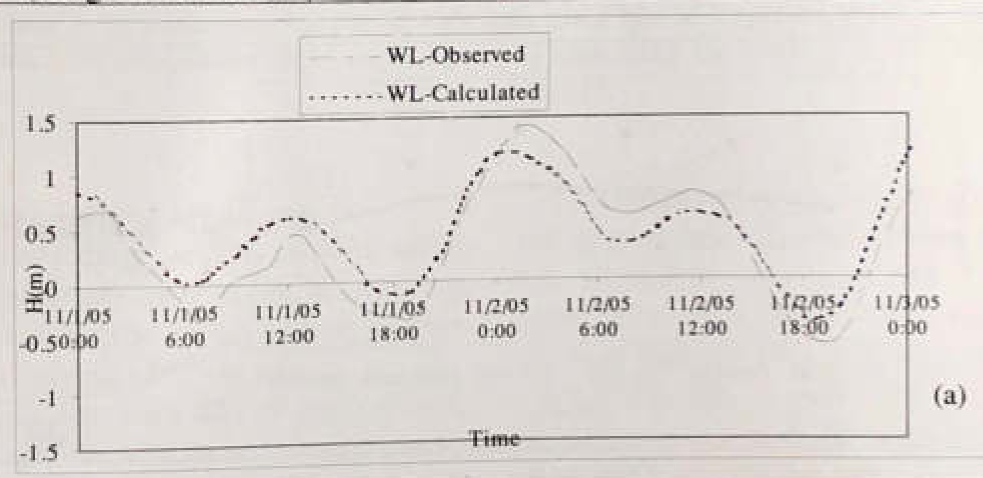

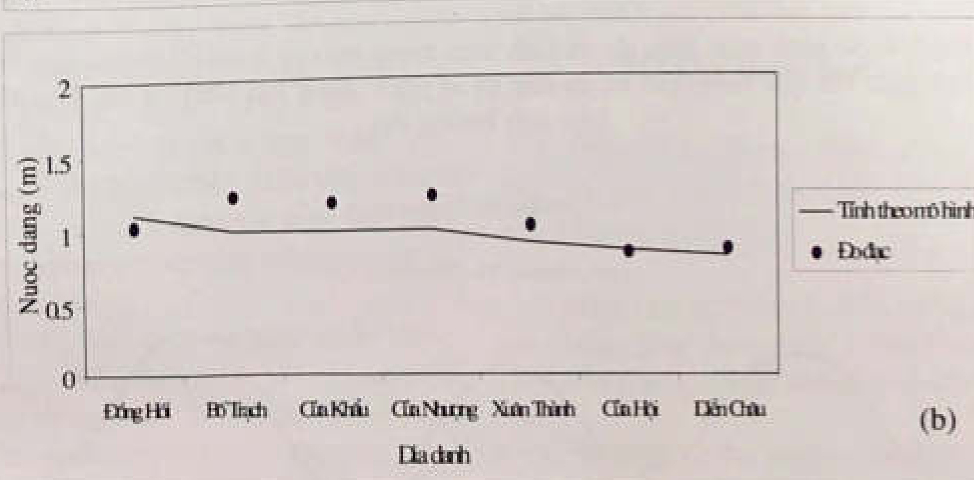

Hình 6. So sánh mực thực đo và tính toán trong bão số 8 tại Đồng Hới (a); So sánh giữa kết quả tính toán và đo đạc trị số nước dâng lớn nhất tại các khu vực bão ảnh hưởng (b).

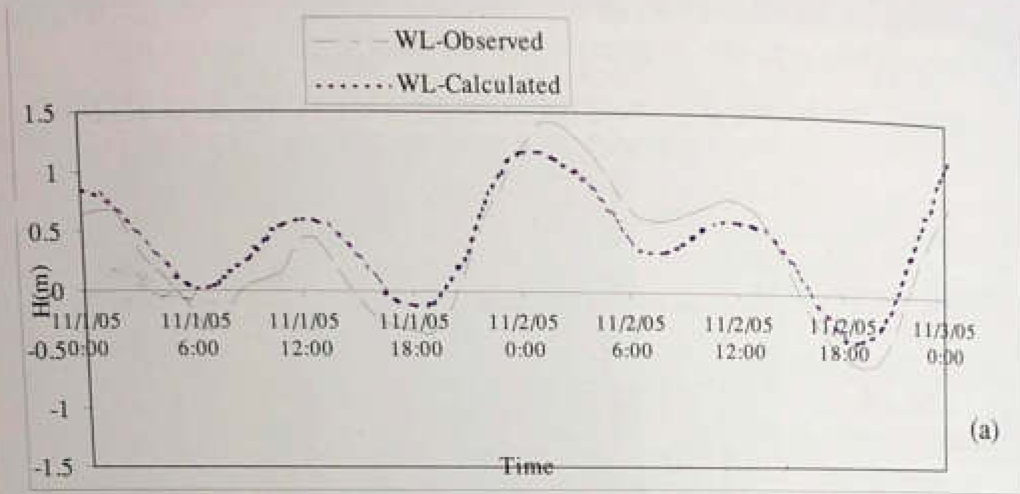

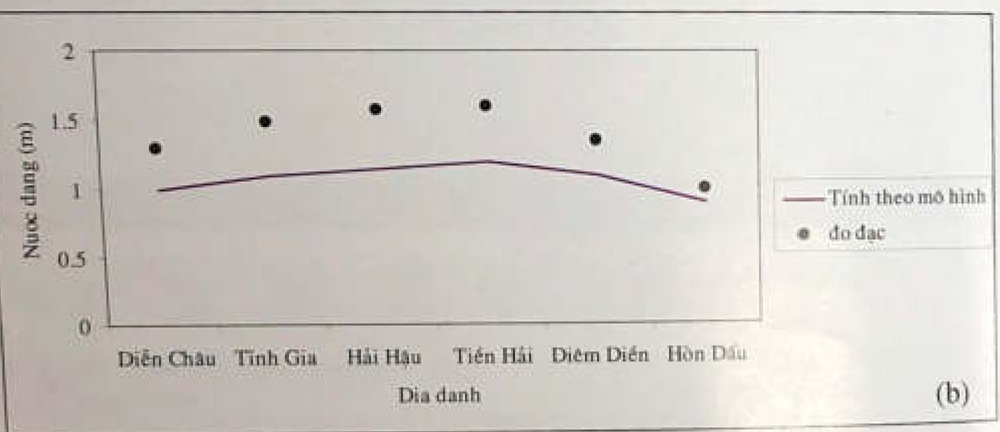

Hình 4. So sánh mực thực đo và tính toán trong bão số 6 tại Hòn Dấu (a); So sánh giữa kết quả tính toán và đo đạc trị số nước dâng lớn nhất tại các khu vực bão ảnh hưởng (b).

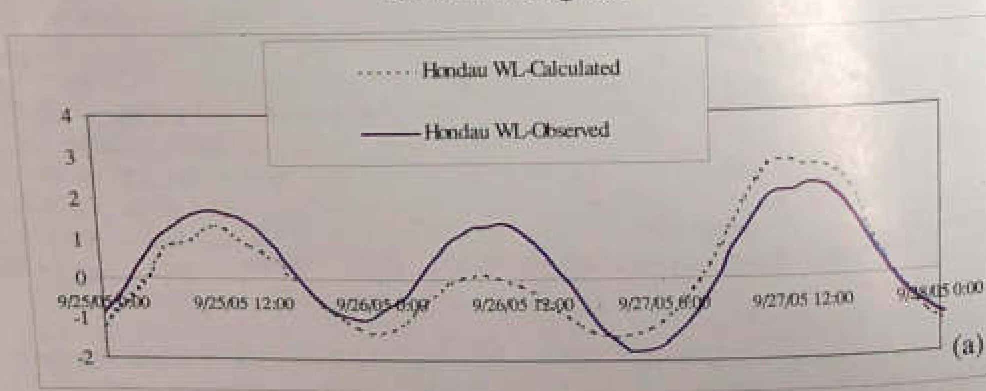

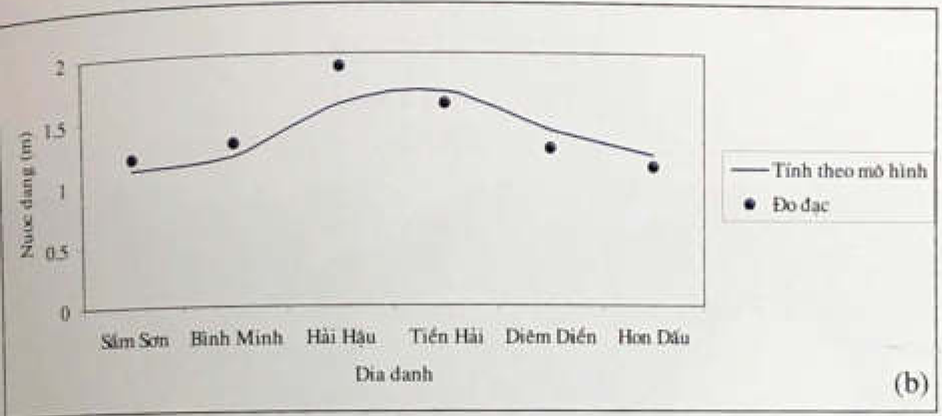

Hình 5. So sánh mực thực đo và tính toán trong bão số 7 tại Hòn Dấu (a); So sánh giữa kết quả tính toán và đo đạc trị số nước dâng lớn nhất tại các khu vực bão ảnh hưởng (b).

6. Kết luận và kiến nghị

Nước dâng do bão là hiện tượng thiên tai rất nguy hiểm, do vậy cần phải có một hệ thống dự báo và cảnh báo kịp thời và chính xác.

Cần lựa chọn đầu tư trang bị một mô hình dự báo có chất lượng cao và xây dựng một quy trình dự báo nước dâng hoàn chỉnh cho Việt Nam. Có thể khẳng định rằng mô hình Delft3D-Flow đã đáp ứng được yêu cầu của dự báo trong thời điểm này. Cần có sự phối hợp và hợp tác giữa các cơ quan dự báo khí tượng trong và ngoài nước.

Những kết quả dự báo nước dâng và phát bản tin nước dâng do bão trong năm 2005 là kịp thời, với độ chính xác tương đối cao. Do vậy, cần phát huy và triển khai theo hướng tích cực này.

Tuy nhiên, để nâng cao độ chính xác của dự báo cần chú ý xem xét một số vấn đề liên quan như: chất lượng dự báo bão, công tác hiệu chỉnh mô hình tính cho từng khu vực, từng cơn bão đặc thù và cuối cùng là cần bổ xung các mô hình dự báo ven bờ có độ phân giải chi tiết hơn.

Tài liệu tham khảo

1. Phạm Văn Ninh - Nước dâng do bão và gió mùa. Nhà xuất bản Đại học Quốc gia Hà Nội.

2. Báo cáo dự báo và điều tra khảo sát nước dâng bão năm 2005. Trung tâm Khí tượng Thuỷ văn Biển –2005.

3. The SCM Regional Model and VCM detailed Model – Report WL/ Delft Hydraulics.

Tạp chí

ISSN 0866 - 8744

Số 534 - Tháng 6 - 2005

KHÍ TƯỢNG THỦY VĂN

Scientific and Technical Hydro-Meteorological Journal

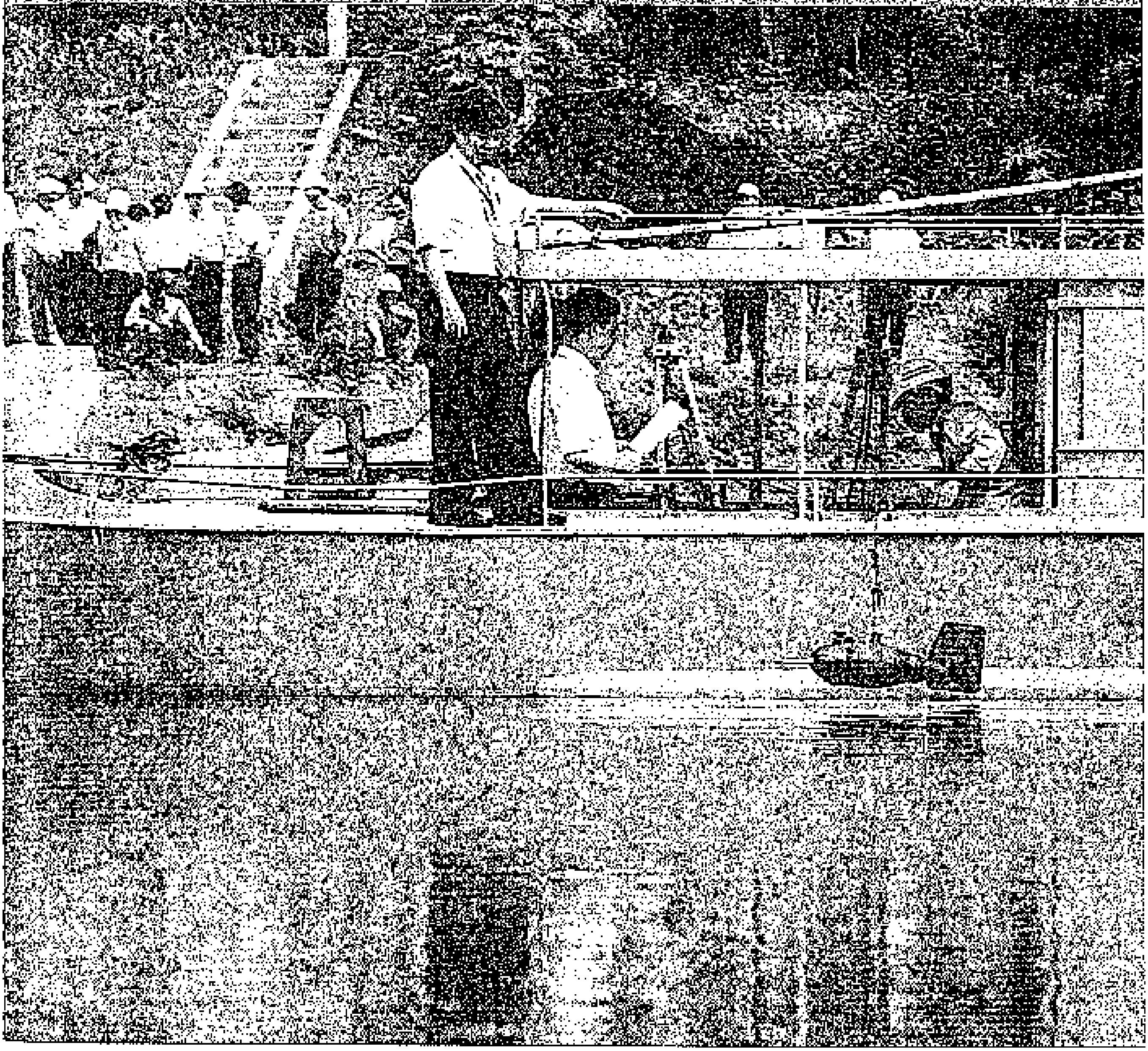

TRUNG TÂM KHÍ TƯỢNG THỦY VĂN QUỐC GIA

National Hydro-Meteorological Service of Vietnam

CONTENTS

Page

MÔ HÌNH SÓNG LAN TRUYỀN VÀO VÙNG VEN BỜ THEO PHƯƠNG TRÌNH BOUSSINESQ HAI CHIỀU

ThS. Nguyễn Bá Thủy

Trung tâm Khí tượng Thủy văn Biển

ThS. Vũ Hải Đăng

Phân viện Hải dương học Hà Nội

Mô hình tính sóng ven bờ dựa trên phương trình Boussinesq 2 chiều của Madsen và Sorensen (1992) đã được ứng dụng và phát triển cao hơn. Mô hình đã mở rộng tính cho sóng đổ (wave breaking) thông qua việc kết hợp với mô hình năng lượng rối của của Kenedy và Chen (2000). Việc tính sóng leo bờ (wave runup) được sử dụng kỹ thuật biên khe hẹp của Tao (1983) và Kenedy (2000). Mô hình đã được kiểm chứng và tính toán thử nghiệm cho 3 trường hợp: không có sóng đổ, có sóng đổ và kết hợp tính sóng đổ và sóng leo. Kết quả tính toán thử nghiệm được so sánh với các số liệu thí nghiệm của Kirby và Chawla (1996) và Bowen (1968) mô hình được đánh giá có độ tin cậy cao.

1. Mở đầu

Sóng biển là một nhân tố quan trọng trong việc xác định hình thái vùng ven bờ phục vụ cho quy hoạch, thiết kế các công trình ven bờ. Hiện nay, đã có một số mô hình thông dụng được sử dụng vào tính toán trường sóng ven bờ như mô hình RCPWAVE, mô hình SWAN. Các mô hình này dựa trên việc giải phương trình dốc thoải (mild slope) và cho kết quả rất tốt trong điều kiện địa hình dốc thoải và không phức tạp. Tuy nhiên, một trong những hạn chế của các mô hình trên là không tính đến hiện tượng phản xạ sóng, độ cao sóng leo và không mô tả được bản chất thật của quá trình sóng đổ. Phương trình Boussinesq đã được sử dụng rộng rãi cho việc tính toán sóng lan truyền từ vùng nước sâu vào vùng ven bờ và cho kết quả tính toán có độ tin cậy cao. Phương trình mô tả được sự kết hợp các hiện tượng trong quá trình sóng phát triển và lan truyền như hiện tượng nước nông, khúc xạ, nhiễu xạ và phản xạ, điều này chứng tỏ một số mô hình tính toán trước đó đã có những hạn chế nhất định. Tuy nhiên, bản thân phương trình Bousinesq không thể tính được cho trường hợp sóng đổ khi lan truyền vào vùng nước nông cũng như sóng leo bờ. Việc kết hợp với mô hình nhớt, rối và sử dụng kỹ thuật biên khe hẹp đã giúp cho mô hình giải quyết được vấn đề phức tạp trên.

2. Phương trình Boussinesq hai chiều

Mô hình tính sóng 2 chiều được dựa trên việc giải phương trình Boussinesq 2 chiều của Madsen và Sorensen (1992). Đây là phương trình đã được cải tiến những đặc trưng về biến đổi sóng tuyến tính ở vùng nước sâu từ phương trình Bousinesq nguyên thủy của Penegrine (1967). Trong trường hợp tính sóng 2 chiều, hệ phương trình:

(a) Phương trình liên tục

$$\frac{\partial \zeta}{\partial t}+\frac{\partial Q_x}{\partial x}+\frac{\partial Q_y}{\partial y}=0 \qquad (1)$$

(b) Phương trình động lượng

- Theo phương x

$$\frac{\partial Q_x}{\partial t}+\frac{\partial}{\partial x}\left(\frac{Q_x^2}{D}\right)+\frac{\partial}{\partial y}\left(\frac{Q_xQ_y}{D}\right)+gD\frac{\partial \zeta}{\partial x}=\left(\beta+\frac{1}{3}\right)h^2\left(\frac{\partial^3 Q_x}{\partial t\partial x^2}+\frac{\partial^3 Q_y}{\partial t\partial x\partial y}\right)+\beta g h^3\left(\frac{\partial^3\zeta}{\partial x^3}+\frac{\partial^3\zeta}{\partial x\partial y^2}\right)$$
$$+h\frac{\partial h}{\partial x}\left(\frac{1}{3}\frac{\partial^2 Q_x}{\partial t\partial x}+\frac{1}{6}\frac{\partial^2 Q_y}{\partial t\partial y}\right)+h\frac{\partial h}{\partial y}\left(\frac{1}{6}\frac{\partial^2 Q_y}{\partial t\partial x}\right)+\beta g h^2\left\{\frac{\partial h}{\partial x}\left(2\frac{\partial^2\zeta}{\partial x^2}+\frac{\partial^2\zeta}{\partial y^2}\right)+\frac{\partial h}{\partial y}\frac{\partial^2\zeta}{\partial x\partial y}\right\}+R_{bx} \qquad (2)$$

- Theo phương y

$$\frac{\partial Q_y}{\partial t}+\frac{\partial}{\partial y}\left(\frac{Q_y^2}{D}\right)+\frac{\partial}{\partial x}\left(\frac{Q_xQ_y}{D}\right)+gD\frac{\partial \zeta}{\partial y}=\left(\beta+\frac{1}{3}\right)h^2\left(\frac{\partial^3 Q_y}{\partial t\partial y^2}+\frac{\partial^3 Q_x}{\partial t\partial x\partial y}\right)+\beta g h^3\left(\frac{\partial^3\zeta}{\partial y^3}+\frac{\partial^3\zeta}{\partial x^2\partial y}\right)$$
$$+h\frac{\partial h}{\partial y}\left(\frac{1}{3}\frac{\partial^2 Q_y}{\partial t\partial y}+\frac{1}{6}\frac{\partial^2 Q_x}{\partial t\partial x}\right)+h\frac{\partial h}{\partial y}\left(\frac{1}{6}\frac{\partial^2 Q_x}{\partial t\partial y}\right)+\beta g h^2\left\{\frac{\partial h}{\partial y}\left(\frac{\partial^2\zeta}{\partial x^2}+2\frac{\partial^2\zeta}{\partial y^2}\right)+\frac{\partial h}{\partial x}\frac{\partial^2\zeta}{\partial x\partial y}\right\} \qquad (3)$$

Trong đó:

ζ - dao động mực nước, Q_x, Q_y - tích phân của vận tốc theo hướng x và y, h - độ sâu thời điểm ban đầu, d - độ sâu tức thời (d=h+ζ), g - gia tốc trọng trường, β - hệ số phân tán (β=0,15).

3. Mô hình sóng đổ hai chiều

Một trong những hạn chế của phương trình Boussinesq là bản thân nó không thể tính được sóng đổ và sóng leo bờ. Do vậy, phương trình Boussinesq cần kết hợp với các mô hình tính toán khác. Trong mô hình này, quá trình sóng đổ được mô phỏng bằng mô hình nhớt, rối. Quá trình này diễn ra rất mạnh ở fron phía trước của sóng. Trong mô hình này, năng lượng tiêu tán do độ nhớt, rối được sử dụng theo phương pháp của Kennedy và Chen (2000). Khi đó 2 thành phần nhớt, rối theo phương x và y (R_{bx}, R_{by}) được cộng vào thành phần vế phải của phương trình động lượng, trong khi đó phương trình liên tục được giữ nguyên.

Thành phần gây sóng đổ được diễn tả theo phương trình:

$$R_{bx}=\frac{\partial}{\partial x}\left(\nu\frac{\partial Q_x}{\partial x}\right)+\frac{1}{2}\left[\frac{\partial}{\partial y}\left(\nu\frac{\partial Q_x}{\partial y}\right)+\frac{\partial}{\partial y}\left(\nu\frac{\partial Q_y}{\partial x}\right)\right] \qquad (4)$$

$$R_{by}=\frac{\partial}{\partial y}\left(\nu\frac{\partial Q_y}{\partial y}\right)+\frac{1}{2}\left[\frac{\partial}{\partial x}\left(\nu\frac{\partial Q_x}{\partial y}\right)+\frac{\partial}{\partial x}\left(\nu\frac{\partial Q_y}{\partial x}\right)\right] \qquad (5)$$

Độ nhớt rối được tính:

$$\nu=B\delta_b(h+\zeta)\frac{\partial\zeta}{\partial t} \qquad (6)$$

Trong đó: δ_b - hệ số kích thước pha trộn, thường được lấy theo giá trị thực nghiệm bằng 1,2, hệ số B - đại lượng kiểm soát quá trình phân tán năng lượng khi sóng đổ xuất hiện, đại lượng này biến đổi một cách nhuần nhuyễn trong khoảng từ 0 tới 1, để tránh quá trình đổ bị sốc.

4. Mô hình biên di động, sóng leo

Trường hợp tính sóng leo bờ, một trong những nhiệm vụ phức tạp là việc xác định biên di động khi sóng truyền thẳng vào bờ. Việc xác định vị trí đường biên ven bờ cho mô hình tính, toàn bộ miền tính toán được mở rộng cho đến vị trí mà tại đó giá trị lớn nhất của sóng leo có thể đạt tới. Phương pháp này đã được Kennedy (2000) đã cải tiến từ phương pháp của Tao (1983) và mô hình đã vận dụng phương pháp này. Ý tưởng của phương pháp này: phần biên cứng là rỗng hoặc chứa nhiều khe hẹp, nhờ đó nước do sóng chuyển động có thể dâng lên bờ. Độ rộng của khe hẹp càng bé, tính bảo toàn động lượng càng cao và mô hình có độ chính xác cao hơn. Sử dụng phương pháp này, độ rộng của kênh truyền sóng được tính theo công thức:

$$b(\zeta)=\begin{cases}1, & \geq z^{*}\\ \delta+(1-\delta)e^{-\lambda(\eta-z^{*})/ho} & \zeta<z^{*}\end{cases} \tag{7}$$

Trong đó: δ - độ rộng của khe hẹp, λ - hệ số điều khiển quá trình biến đổi của diện tích kênh truyền sóng, h_0 - độ sâu, z^* - giá trị mực nước mà tại đó b=1.

Diện tích mặt cắt được được xác định theo công thức cải tiến của Kenedy (2000):

$$A(x,y,t)=A(\zeta)\equiv\int_{h}^{\eta} b(z)dz \tag{8}$$

$$\text{Hay: } A(\zeta)=\begin{cases}(\zeta-z^{*})+\delta(z^{*}+ho)+\dfrac{(1-\delta)ho}{\lambda}(1-e^{-\lambda(1+z^{*}/ho)}) & \zeta\geq z^{*}\\ \delta(\zeta+ho)+\dfrac{(1-\delta)ho}{\lambda}e^{-\lambda(\eta-z^{*})/ho}(1-e^{-\lambda(1+z^{*}/ho)}) & \zeta<z^{*}\end{cases} \tag{9}$$

Giá trị z^* được tính theo công thức:

$$z^{*}=\frac{-h}{(1-\delta)}+ho\left(\frac{\delta}{1-\delta}+\frac{1}{\lambda}\right) \tag{10}$$

Kết hợp phương trình Bousinesq 2 chiều với mô hình sóng đổ và sử dụng kỹ thuật biên khe hẹp, hệ phương trình cuối cùng của mô hình tính như sau:

(a) Phương trình liên tục

$$b\frac{\partial\zeta}{\partial t}+\frac{\partial Q_x}{\partial x}+\frac{\partial Q_y}{\partial y}=0 \tag{11}$$

(b) Phương trình động lượng

- Phương trình theo phương x

$$\frac{\partial Q_x}{\partial t}+\frac{\partial}{\partial x}\left(\frac{Q_x^{\,2}}{A}\right)+\frac{\partial}{\partial y}\left(\frac{Q_xQ_y}{A}\right)+gA\frac{\partial\zeta}{\partial x}-R_{bx}+E_x+\ldots=0 \tag{12}$$

- Phương trình theo phương y

$$\frac{\partial Q_y}{\partial t}+\frac{\partial}{\partial x}\left(\frac{Q_xQ_y}{A}\right)+\frac{\partial}{\partial y}\left(\frac{Q_y^{\,2}}{A}\right)+gA\frac{\partial\zeta}{\partial y}-R_{by}+E_y+\ldots=0 \tag{13}$$

Trong đó: R_{bx}, R_{by} - thành phần gây sóng đổ theo phương x và y đã được mô tả trong mục 3. E_X và E_y - thành phần gây hấp thụ sóng để tránh hiện tượng phản xạ từ biên. b và A - bề rộng và diện tích tương đối của kênh truyền sóng. Hệ phương trình trên được sai phân hoá trung tâm theo thời gian và sai phân tiến theo không gian với các điểm tính được xác định theo ô lưới hình chữ nhật. Phương pháp ẩn hướng luân phiên ADI (Alternating Direction Implicit) đã được áp dụng cho việc giải hệ phương trình sai phân.

5. Kiểm chứng độ tin cậy của mô hình

Để có thể đánh giá độ tin cậy của mô hình, tác giả đã thử nghiệm mô hình cho trường hợp sóng lan truyền qua 1 đảo ngầm, hình tròn xoáy trôn ốc và so sánh với kết quả của thí nghiệm. Trong thí nghiệm này, cả hai trường hợp; không có sóng đổ và có sóng đổ, sẽ được kiểm chứng. Việc sử dụng bể thí nghiệm như trên để kiểm chứng độ chính xác của mô hình là sự lựa chọn chính xác và khắt khe nhất để đánh giá độ tin cậy của mô hình. Thí nghiệm được thực hiện bởi Chawla và Kirby(1996). Hình 1 mô tả bể thí nghiệm, tại đó các máy thu số liệu về độ cao sóng được đặt theo các mặt cắt A-A đến G-G. Bể sóng có chiều dài là 20m, chiều rộng là 18,2m. Tâm của đảo được đặt tại vị trí x=5m, y=8,98m. Sóng được truyền từ biên phía bên trái của bể, phía phải của bể được đạt một lớp hấp thụ sóng có bề dầy 3m. Bán kính của đảo được xác định theo phương trình:

$$(x-5)^2 + (y-8,98)^2 = (2,57)^2 \tag{14}$$

Trong đó h_0 là độ sâu của bể thí nghiệm

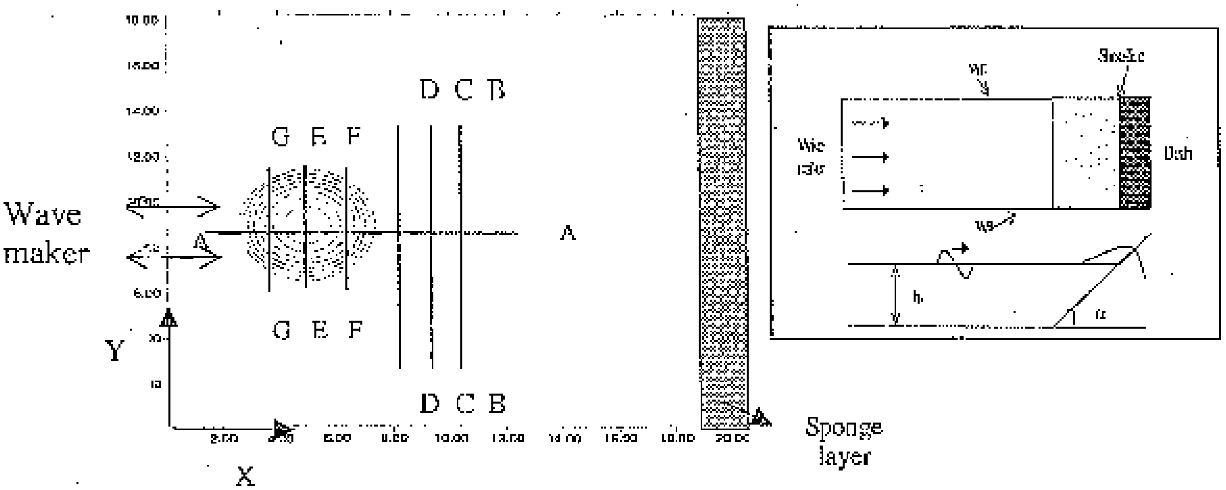

Hình 1. Sơ đồ bể thí nghiệm của Chawla & Kirby (bên trái) và Bowen (bên phải)

Độ sâu của các điểm trên đảo được xác định theo phương trình:

$$h = h_0 + 8.73 - \sqrt{82.81 - (x-5)^2 - (y-8.98)^2} \tag{15}$$

a. Trường hợp không có sóng đổ (non-breaking wave)

Trong trường hợp này độ cao sóng đầu vào tại biên là 1,18cm, chu kỳ là 1,0 giây, mực nước trong bể có độ sâu là 45cm, tương ứng lúc này tại tâm của đảo nơi có mực nước thấp nhất là 8cm. Bước lưới tính theo không gian được chọn là 0,05, 0,1m theo hướng x, y tương ứng và 0,1 giây là bước thời gian tính toán. Mô hình được chạy ổn định trong 40 giây. Kết quả tính toán và số liệu thực nghiệm trên các mặt cắt được biểu diễn trên hình 2.a. Dọc theo mặt cắt A - A, tác giả nhận thấy rằng: mô hình đã dự báo rất tốt trường sóng phía trước và sau đảo. Sự hội tụ phía mặt sau của đảo xuất hiện là do hiện tượng khúc xạ sóng khi lan truyền qua đảo. Độ cao sóng lớn nhất được quan trắc đạt gấp 2,68 lần độ cao sóng đầu vào. Dọc theo các mặt cắt ngang B - B đến G - G, mô hình đã phản ánh rất tốt quá trình biến đổi theo phương ngang của trường sóng, các giá trị thí nghiệm và kết quả tính toán hầu như là trùng khớp.

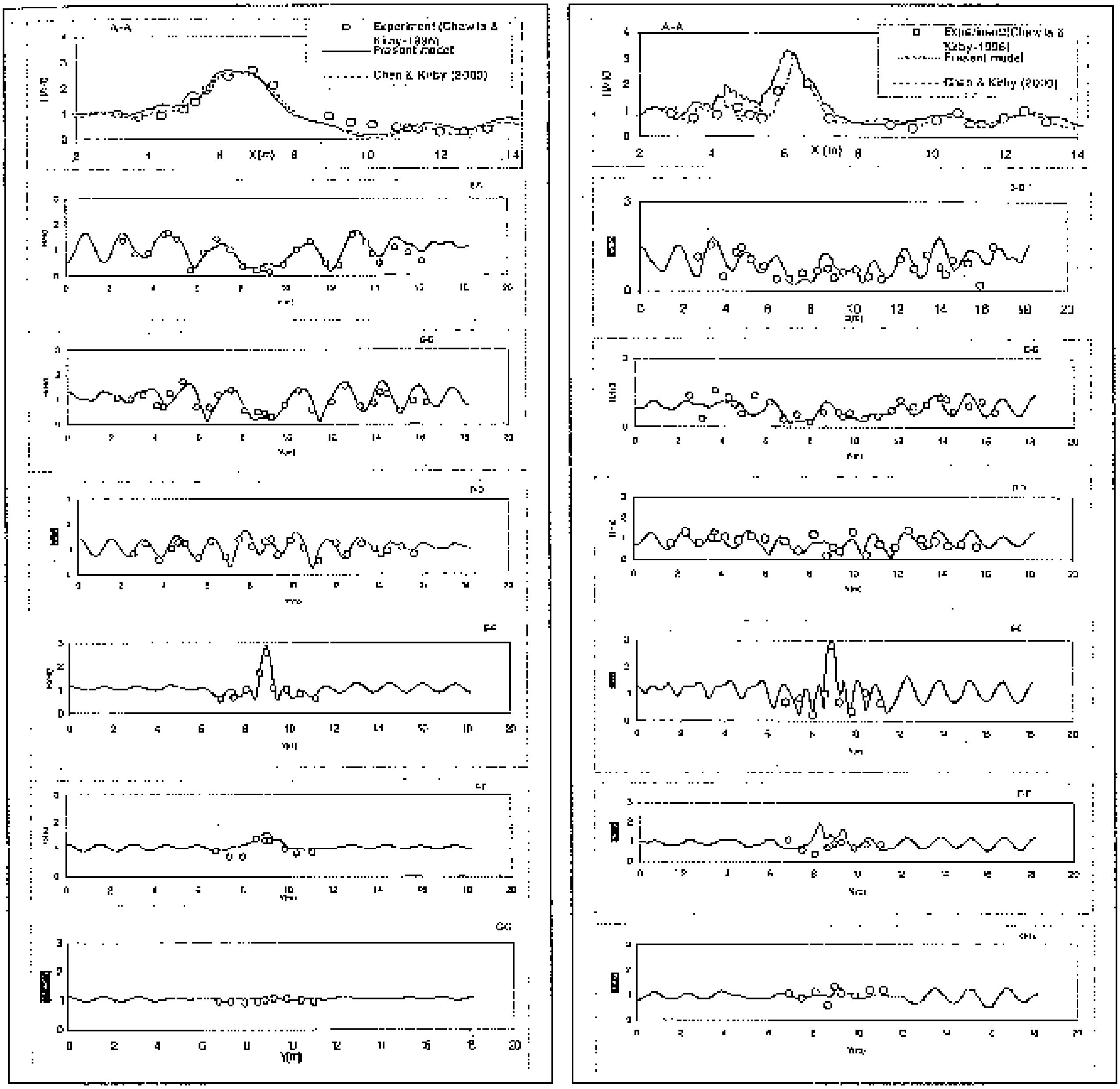

(a). Trường hợp không xuất hiện sóng đổ (b). Trường hợp có sóngđổ

Hình 2. So sánh giữa kết quả tính toán và số liệu thực nghiệm trường hợp sóng lan truyền qua đảo ngầm *b. Trường hợp có sóng đổ xuất hiện (breaking wave)*

Trường hợp thử nghiệm mô hình có sóng đổ, độ sâu của bể thí nghiệm được giảm xuống còn 39,5cm, độ cao và chu kỳ sóng tại biên tương ứng là 2cm và 1,0 giây. Do bởi mặt phía sau của fron sóng trong trường hợp sóng đổ là rất dốc, nên yêu cầu chọn bước lưới có độ mịn hơn là cần thiết để có thể xác định được chính xác vị trí sóng bắt đầu đổ, tác giả đã chọn lưới không gian theo hướng x, y là 0,025cm và bước thời gian là 0,1 giây được dùng cho tính toán. Trên hình 2.b biểu diễn kết quả tính toán của mô hình và so sánh với số liệu thực đo. Trường hợp này một vài hiện tượng bí ẩn được khám phá. Thứ nhất, tác giả thấy rằng: độ cao sóng không đạt cực đại tại đỉnh đảo khi thay vào đó là giá trị cực đại lại xuất hiện ở phía sau đảo, đây là đặc tính do hiện tượng khúc xạ gây nên. Thứ hai, hiện tượng sóng đổ và phân kỳ đã làm giảm độ cao sóng, sự giảm độ cao sóng trong trường hợp có sóng đổ nhanh hơn trường hợp không có sóng đổ xuất hiện. Mô hình tính toán cũng đã cho kết quả tương đối tốt sự biến đổi của trường độ cao sóng theo phương ngang. Kết quả tính toán trong 2 trường hợp, đồng thời được so sánh với kết quả tính toán của Chen và Kirby (2000) khi họ sử dụng phương trình Bousinesq phi tuyến tính cho cùng điều kiện thí nghiệm trên.

c. Sóng đổ và sóng leo bờ (breaking and run-up waves)

Để có thể kiểm tra độ chính xác của mô hình cho trường hợp sóng đổ và sóng leo bờ cùng xuất hiện, tác giả đã sử dụng kết quả thí nghiệm của Bowen (1968) để kiểm chứng độ tin cậy của mô hình. Trong thí nghiệm của Bowen, bể sóng được thiết kế với độ dốc là 0,082, độ sâu của bể là 50cm. Mô hình đã sử dụng các tham số sóng đầu vào để kiểm chứng độ tin cậy với độ cao là 0,065m, chu kỳ là 1,14 giây. Các tham số về mô hình sóng leo được sử dụng trong trường hợp này là $\delta = 0{,}005$ và λ=100. Tác giả cũng nhận thấy rằng: để mô hình có thể chạy được ổn định thì việc lựa chọn bước thời gian cho tính toán ngắn là rất cần thiết, ở đây bước thời gian dt=0,002 giây. Kết quả tính toán và thực đo được biểu diễn trên hình 3. Trên hình 3.a biểu diễn sự biến đổi theo không gian của đỉnh sóng, bụng sóng và đường mực nước trung bình, các đường hình tròn bé là kết quả của số liệu thí nghiệm. Trên hình 3.b, sự so sánh giữa kết quả tính toán và số liệu thực đo của độ cao sóng. Tác giả nhận thấy rằng: mô hình đã diễn tả được các hiện tượng về sóng nước nông, sóng đổ, sóng leo và cho kết quả với độ tin cậy cao, mặc dù giá trị về độ cao sóng hơi nhỏ khi so sánh với thực nghiệm tại điểm sóng đổ xuất hiện và đường độ cao sóng sau khi đổ không được dốc như đường thực nghiệm.

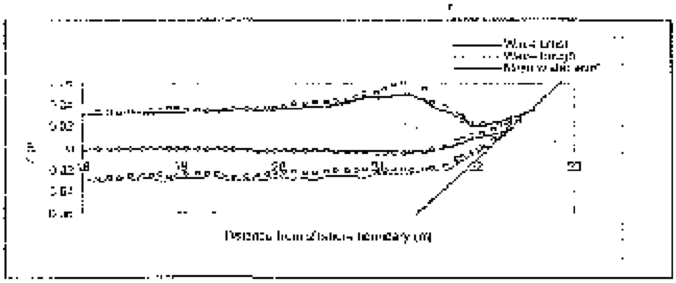

(a) Đỉnh sóng, bụng sóng và mực nước trung bình

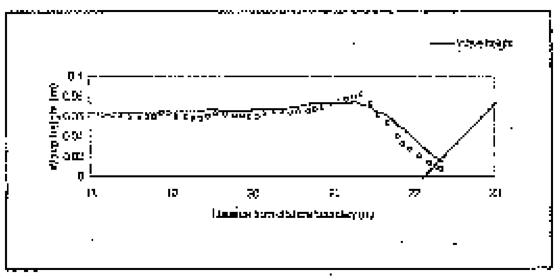

(b). Độ cao sóng

Hình 3. So sánh giữa kết quả tính toán và số liệu thí nghiệm của Bowen

6. Kết luận

Mô hình tính sóng lan truyền vào ven bờ dựa trên phương trình Boussinesq 2 chiều đã được ứng dụng phát triển. Mô hình đã được hoàn thiện bằng việc kết hợp với mô hình sóng đổ và sóng leo. Kết quả tính toán thử nghiệm và so sánh với giá trị thí nghiệm đã phản ánh được độ tin cậy của mô hình. Một trong nhưng ưu điểm của mô hình khi so sánh với các mô hình khác đã được sử dụng trước đây, mô hình đã tính được hiệu ứng do phản xạ, tính sóng leo và đã mô tả được quá trình sóng đổ có độ tin cậy cao. Tuy nhiên, một số hạn chế của mô hình cũng cần được nêu ra, đó là thời gian tính toán lâu, độ ổn định của mô hình dựa trên phương trình Bousinessq không cao. Việc ứng dụng mô hình vào tính toán các điều kiện thực tế gặp nhiều phức tạp và đó cũng là vấn đề các báo báo tiếp theo sẽ đề cập.

Tài liệu tham khảo

1. Chen, Q., Kirby, J.T., Dalrymple, R.A., Kennedy, A.B. and Chawla, A., 2000. Boussinesq Modeling of wave transformation, breaking and runup.II:2D. Journal of waterway, Port coastal, and Ocean Engineering/January/February, 48-55.
2. Kennedy. A. B, Chen, Q., Kirby, J. T., & Dalrymple, R. A. 2000. Boussinesq modeling of wave transformation, breaking and runup. I: One dimension. *J. Waterway of Port, Coastal and Ocean Engineering* 126: 39-47.
3. Madsen, P.A., Sorensen, O.R.,1992. A new form of the Boussinesq equations with improved lineardispersion characteristic: Part 2. A slowly varying bathymetry. Coastal Eng.18, 183-204.
4. Madsen, P.A., Sorensen, O.R., Shaffer, H.A., 1997. Surf zone dynamics simulated by a Boussinesq type model. Part I. Model description and cross-shore motion of regular waves. Coastal Eng. 32, 255-288

3. HỘI THẢO QUỐC TẾ (5)

Proceedings of the Twelfth International Summer Symposium

18 September 2010
Funabashi, Japan

International Activities Committee
Japan Society of Civil Engineers

Proceedings of the Twelfth International Summer Symposium

18 September 2010
Tokyo, Japan

International Activities Committee
Japan Society of Civil Engineers

ISSN 1345-8507

Published by International Activities Committee, Japan Society of Civil Engineers
Yotsuya 1-Chome, Shinjuku-ku, Tokyo 160-0004 Japan

CONTENTS

Category B: Hydraulic, Coastal and Environmental Engineering

Category C: Geotechnical Engineering

DAMAGE LENGTH OF VEGETATION DUE TO TSUNAMI ACTION-NUMERICAL MODEL FOR TREE BREAKING

Nguyen Ba Thuy[1], Norio Tanaka[2] and Katsutoshi Tanimoto[3]

1) Graduate School of Science and Engineering, Saitama University
255, Shimo-okubu, Sakura-ward, Saitama City, Saitama 338 – 8570, Japan
Email: thuybanguyen@yahoo.com

2) Graduate School of Science and Engineering, Saitama University
255, Shimo-okubu, Sakura-ward, Saitama City, Saitama 338 – 8570, Japan
Email: tanaka01@mail.saitama-u.ac.jp

3) Emeritus Professor, Saitama University
255, Shimo-okubu, Sakura-ward, Saitama City, Saitama 338 – 8570, Japan
Email: tanimotok@coda.ocn.ne.jp

INTRODUCTION

Previous studies have revealed that coastal vegetation can play a significant role in reducing the tsunami energy and damage to humans and properties. Based on the field observation in Sri Lanka and Thailand after India Ocean tsunami in 2004, Tanaka et al. (2009) pointed out that *Pandanus odoratissimus* is especially effective in providing protection from tsunami damage due to its density and complex aerial root structure, but it is not strong enough to preclude the risk of breaking due to the action of a high tsunami. The threshold height of breaking point is at the top of aerial root. Tanaka et al. (2009) proposed an empirical formula for breaking moments of various tropical trees including *P. odoratissimus*. The tsunami force is directly related to the damage of trees, however, the tsunami force and bending moment on trees were not discussed in previous studies in detail. The present study therefore to develop the numerical model considering the tree breaking effect. The objective of this study is to elucidate the damage length, reduction of water depth and tsunami force behind the coastal forest of *P. odoratissimus*.

MATERIAL AND METHODS

Governing equations are based on two dimensional non-linear long wave equations including drag force to the vegetation (Tanaka et al. 2009). For more details of the numerical model, and its validation using experimental data, refer to Thuy et al. (2009).

<u>*Tsunami force and tsunami bending moment*</u>

The tsunami force vector ($\vec{F}^{*}$) in the present paper is defined by the following equation:

$$\vec{F}^{*} = \frac{1}{2}\rho d\vec{V}\left|\vec{V}\right| \tag{1}$$

On the other hand, the tsunami bending moment vector ($\vec{M}_{Tree}$) at a critical height (h_c=2 m in this study) of the tree from the ground surface is expressed as follows:

$$\begin{aligned} \vec{M}_{Tree} &= \frac{1}{2}\rho C_{D\text{-}ref} b_{ref} \vec{V}\left|\vec{V}\right| \int \alpha\beta(z_{ij}-h_c)dz_{ij}, \quad h_c < z_{ij} \le H_{Tree} \\ &= 0, \qquad\qquad\qquad\qquad\qquad\qquad z_{ij} \le h_c \end{aligned} \tag{2}$$

Where $\vec{V}$ is the depth-averaged velocity vector; d the total water depth; ρ the water density; b_{ref} and C_{Dref} are the reference projected width and reference drag coefficient of the trunk at z_G=1.2 m from the ground surface; α and β are the additional coefficient that express the effect of cumulative width and effect of leaves or aerial roots on the drag in each height, respectively.

Topography and vegetation conditions
The bed profile is shown in Fig 1(a), which is varied by 4 slopes (S=1/10, 1/100, 1/50 and 1/500) in the tsunami direction. The water depth at wave generating boundary is 100 m. The forest was assumed to extend infinitely in the direction perpendicular to the tsunami direction. Fig. 1(b) shows the variation of α, β, and C_{D-all} of *P. odoratissimus* (Tanaka et al. (2009) for tree height H_{Tree}=6 m, where b_{ref}=0.155 m, and C_{D-ref}=1.0. The reference drag coefficient of 1.0 was adopted for a trunk with a circular section for high Reynolds number. The value of drag coefficient C_{D-all} varied with the total depth d (inundation depth) because the projected width and the drag coefficient vary with the height from the ground surface. In the present paper, the runup of only the first wave was analyzed because it has the largest runup height among continuous waves.

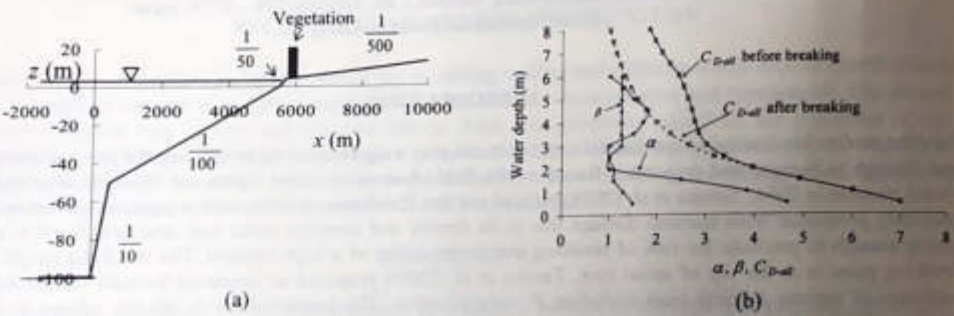

Fig. 1. (a) Cross section of bathymetry and topography, (b) vertical distribution of α, β and C_{D-all}.

RESULTS AND DISCUSSIONS

1. Tsunami bending moment on a tree.
Fig. 2(a) shows the time variations of inundation depth d, mean velocity V, tsunami force F^*, and tsunami moment M_P in front of the forest by the numerical simulation without considering tree breakage. The conditions were selected as H_{F0}=5 m (H_{F0}, water depth in front of vegetation in the case of no vegetation), tsunami period T=1200 s, forest width =100 m, H_{tree}= 6 m, h_c=2 m, and tree density γ=0.2 trees/m^2.

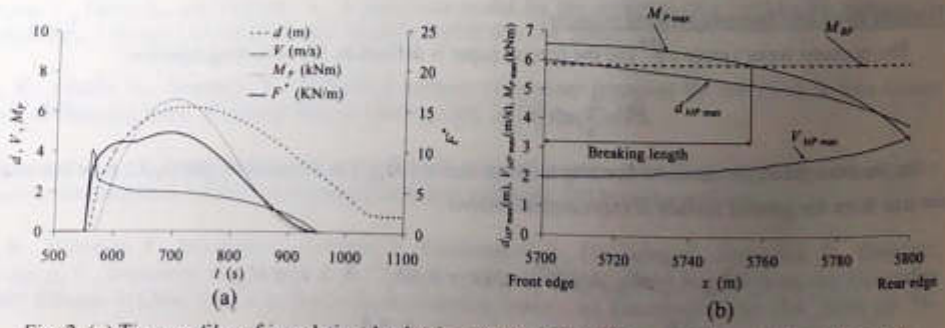

Fig. 2. (a) Time profiles of inundation depth (d), mean velocity (V), tsunami force (F^*) and bending moment (M_P) at front of vegetation, (b) spatial variation of maximum bending moment ($M_{P\max}$), representative water depth ($d_{MP\max}$) and velocity ($V_{MP\max}$).

As observed in this figure, the temporal maxima of hydraulic property appear at different times. In particular, the maximum of V appears early in the tsunami arrival while the inundation depth is low, and consequently, the tsunami force and moment were not maximum. Fig. 2(b) shows spatial distribution of the maximum tsunami moment (M_{Pmax}), representative velocity (V_{MPmax}) and representative water depth (d_{MPmax}) along the forest, where the representative velocity and water depth are defined as values at the temporal maximum of the tsunami moment. The breaking moment of the *P. odoratissimus* (M_{BP}=5.85 kNm) is indicated by a dotted line. According to the result, tsunami moment is decreased from the front to the behind due to the decrease in water depth inside the vegetation. Therefore, the vegetation at the front region has higher probability to damage by the tsunami force than the other locations in the belt. The damage length of forest is about 57.5m (57.5%).

2. Damage length of vegetation-numerical model for tree breaking.

In this section, the numerical model for tree breaking was preliminary considered for the same conditions in section 1. In the numerical model, the tree will be broken when the tsunami bending moment on a tree exceed the threshold value, where the threshold breaking moment was estimated based on the empirical formula (Tanaka et al. 2009), and 5.85 kNm for the condition of H_{tree}=6 m and b_{ref}=0.155 m. The procedure was done at each time step during the runup of a tsunami. After tree breaking, the remaining part of the tree is the aerial root, and the depth averaged drag coefficient was considered for this part (Fig. 1(b)). In the model, the impact from broken part of the tree (already destroyed by tsunami) to the surviving trees not be considered. However, trees destroyed by tsunamis become floating debris, that can damage standing tree. The drafted tree effect would be discussed in future study. Figs. 3 (a) and (b) show the comparison of time profile of water depth and velocity in front and behind the forest for two models: with breaking (B.M.) and without breaking (N.B.M.). The velocity, water depth behind the forest is increased after tree breaking owing to the reduction in drag resistance. However, in front of vegetation, the water depth decreases while the velocity increases due to the reduction of the reflection from vegetation. In relation with water depth and velocity, the tsunami force and bending moment on a tree behind the forest are increased in the model of tree breaking (Fig. 4 (a) and (b)).

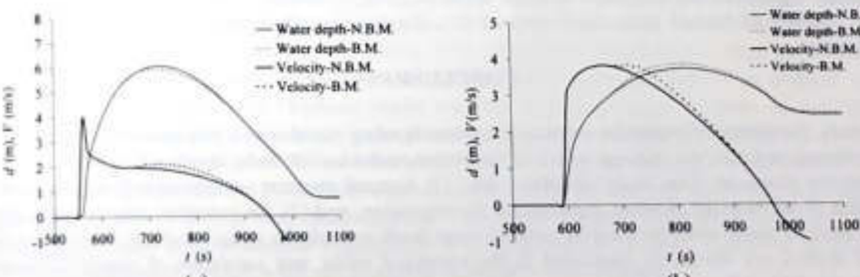

Fig. 3. Time profile of water depth and velocity. (a) in front of forest, (b) behind the forest.

Fig. 5(a) shows spatial distribution of the maximum tsunami moments (M_{Pmax}) along the forest for two models. According to the result, the damage length of forest by B.M. is about 77.5m (77.5%) and increased in comparison with N.B.M. due to the decrease in vegetation resistance in the front area where vegetation is broken. Fig. 5(b) shows the relationship between the tsunami water depth in front of vegetation in the case of no forest and the reduction of water depth (d_{max}/d_{max0}), tsunami force (F^{*}_{max}/F^{*}_{max0}) behind the forest and survival rate of *P. odoratissimus* (number of broken trees/total tree), where subscript 0 indicates the case of no forest. The results show that trees start breaking at water depth of 4.8m (Fig. 5(b), I.B.). When tsunami water depth reaches to 5.5 m all the trees are broken. The reduction rate in water depth and tsunami force increase when the tsunami water depth exceeds the initial breaking of water depth.

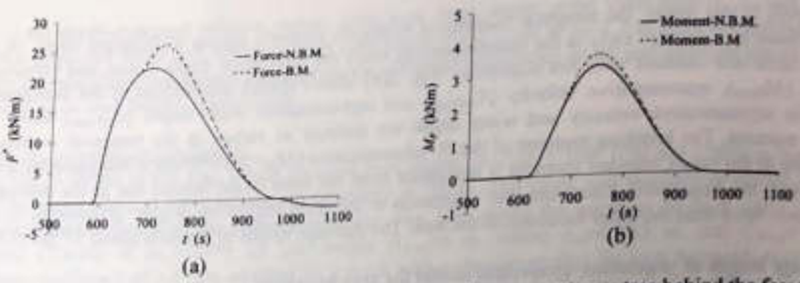

Fig. 4. Time profile of (a) tsunami force, and (b) bending moment on a tree behind the forest.

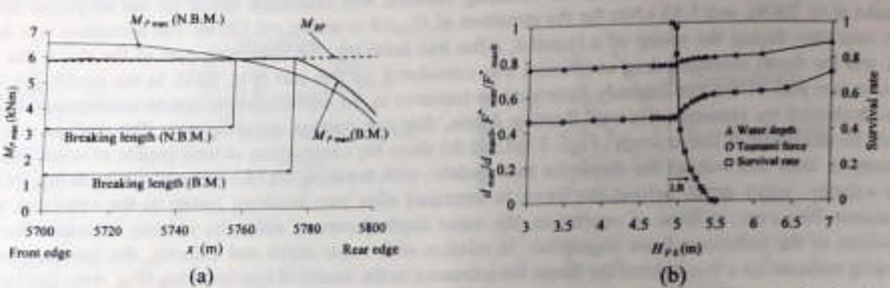

Fig. 5. (a) Damage length for two numerical model, (b) relationship between tsunami water depth (at the front of vegetation) and reduction of water depth (d_{max}/d_{max0}), tsunami force (F^*_{max}/F^*_{max0}) and survival rate (number of broken trees /total tree) of *P. odoratissimus*. Subscript 0 indicates the case of no vegetation.

CONCLUSIONS

In this study, the numerical model for estimating tsunami bending moment on a tree and including tree breakage was developed, and then the damage length of vegetation, reduction of water depth and tsunami force behind the forest are discussed. This study elucidated that: (1) tsunami moment is decreased from the front to the behind due to the decrease in water depth inside the vegetation, and (2) the reduction rate in water depth and tsunami force increases when the incident tsunami water depth exceeds the initial breaking. For future study, the effect of drafted tree should be considered in the numerical mode, and validation of numerical model with experiment and filed data is needed.

ACKNOWLEDGEMENT

This study is funded in part by the JSPS AA Science Platform Program.

REFERENCES

Tanaka, N., Nandasena, N. A. K., Jinadasa, K. S. B. N., Sasaki, Y., Tanimoto, K. Mowjood, M. I. M., 2009. Developing effective vegetation bioshield for tsunami protection, Journal of Civil and Environmental Engineering Systems, 26, 163-180.

Thuy, N.B., Tanimoto, K., Tanaka, N., Harada K., Iimura, K., 2009. Effect of open gap in coastal forest on tsunami run-up – Investigations by experiment and numerical simulation, Ocean Engineering, 36, 1258-1269.

CONSENT LETTER

To whom it may concern

Journal title: Proceedings of Civil Engineering in the Ocean, JSCE

Article title: Effects of forest and tsunami conditions on potential tsunami forces around a coastal forest with a gap (2010). Proceedings of Civil Engineering in the Ocean, JSCE, Vol. 26, pp. 291-296. (in Japanese, abstract in English)

Authors: Nguyen Ba Thuy, Katsutoshi Tanimoto, Norio Tanaka, Kosuke Iimura

I am the supervisor of Dr. Nguyen Ba Thuy during doctor course in Saitama University, Japan from October 2007 to September 2010.

On behalf of all co-authors I would like to inform you that we are totally aware and agree that the content of this paper is one part on the doctor thesis of Dr. Nguyen Ba Thuy, and he is principal author for this paper.

On behalf of all co-authors

Norio Tanaka
Dr. Engineering, Prof.
Graduate School of Science and Engineering, Saitama University
255 Shimo-okubo, Sakura-ku, Saitama
338-8570, Japan

海洋開発論文集, 第26巻, 2010年6月

切れ間を有する海岸林付近の潜在的津波力に及ぼす樹林および津波条件の影響

EFFECT OF FOREST AND TSUNAMI CONDIONS ON POTENTIAL TSUNAMI FORCES AROUND A COASTAL FOREST WITH A GAP

N. B. THUY[1]・飯村耕介[2]・田中規夫[3]・谷本勝利[4]
N. B. THUY, Kosuke IIMURA, Norio TANAKA and Katsutoshi TANIMOTO

[1] 工修 埼玉大学大学院理工学研究科（〒338-8570 埼玉県さいたま市桜区下大久保255）
[2] 学生会員 工修 埼玉大学大学院理工学研究科（〒338-8570 埼玉県さいたま市桜区下大久保255）
[3] 正会員 工博 埼玉大学教授 大学院理工学研究科（〒338-8570 埼玉県さいたま市桜区下大久保255）
[4] フェロー会員 工博 埼玉大学名誉教授（〒338-8570 埼玉県さいたま市桜区下大久保255）

Numerical simulations of tsunami runup have been carried out to investigate the effects of forest conditions (width and tree density) and incident tsunami conditions (period and height) on potential tsunami forces around a coastal forest of *Pandanus odoratissimus* trees with a gap. The potential tsunami force is defined as the total drag force on a virtual high column with unit width and unit drag coefficient. The potential tsunami force at the gap exit is enhanced greatly and the maximum in the spatial distribution in most cases. The potential tsunami forces at four representative points at front and back of forest including the center of gap exit were analyzed for various conditions and formulated as function of forest and tsunami conditions in the non-dimensional form. The potential tsunami forces calculated by the curve-fit formula agree with the simulated potential tsunami forces within 10% error.

Key Words : *Tsunami runup, coastal forest, potential tsunami force, Pandanus odoratissimus*

1. まえがき

2004年インド洋大津波後の調査で，Mascarenhas と Jayakumar [1]は海岸林内の道路背後で被害が大きいことを指摘した．また，Fernando ら [2]は破壊された珊瑚礁の切れ間背後での被害が大きいという調査結果を受けて，実験により切れ間出口での流速が大きくなることを示した．そうした現地調査や実験結果を背景に，Nandasena ら [3]はスリランカや東南アジアの海岸において広く分布しているアダン(*Pandanus odoratissimus*)林を対象として，汀線に直角方向に切れ間があるときの津波遡上に関する二次元数値計算を行い，その出口において流速が速くなることを確認し，さらに谷本ら [4]は切れ間幅を系統的に変化させたときの数値計算を行い，出口での流速が最も増幅される幅があることを示した．続いて，Thuy ら [5]は先の Fernando ら [2]に類した実験を行い，数値計算結果が実験結果によく合うことを検証している．

しかしながら，既往研究では津波条件等が限定されているなどの難点があるほか，被害に直接関係する津波による力についてはいまだ十分に議論されていないのが現状である．そのため，本研究では，アダンによる樹林帯に切れ間がある場合を対象とした二次元数値計算を行い，樹林条件（密度，樹林幅）および入射津波条件が樹林帯付近における潜在的な津波力にどのように影響するかを明らかにし，特に，結果の無次元表示を試みる．

2. 数値計算の方法と計算条件

(1) 基礎方程式と数値計算法

数値計算法はThuy ら[5]および谷本ら[4]と基本的に同じであるが，基礎方程式は津波力計算の便宜から水深平均流速を用いた非線形長波方程式に変えている．ただし，水深平均流速を用いても，全水深が非常に小さいときの流速を除き，主要な計算結果に違いはなく，数値計算モデルの実験的検証と現地スケールへの適用に対する考え方に変わりはない．

平均流速を用いたときの樹林による抵抗力ベクトル$\vec{F}$は次式のとおりである．

$$\vec{F} = \gamma \frac{1}{2} \rho C_{D\text{-}all}(d) b_{ref} \vec{V} \left| \vec{V} \right| d \qquad (1)$$

ここに，γは樹林密度（単位面積あたりの樹木の本数），ρは水の密度，$C_{D\text{-}all}(d)$は樹木の水深平均抵抗

係数（dの関数），b_{ref}は樹木の基準投影幅（胸高での幹の直径），$\vec{V}$は流速ベクトル，dは全水深（没水深）である．$C_{D\text{-}all}$は次式で与える（田中・佐々木[7]）．

$$C_{D\text{-}all}(d)=C_{D\text{-}ref}\frac{1}{d}\int_0^d \frac{b(z_G)}{b_{ref}}\frac{C_D(z_G)}{C_{Dref}}dz_G \qquad (2)$$

ここに，$C_{D\text{-}ref}$は基準抵抗係数（胸高での幹に対する抗力係数で与える），bおよびC_Dは地面からの高さz_Gでの幹と枝の投影幅およびそこでの樹木の抗力係数である．このように，$C_{D\text{-}all}$は高さ方向における抗力係数の変化ばかりでなく，投影幅の変化を含んだもので，全水深（没水深）の関数であるところに特色がある．

数値計算は基礎式を差分式に変換して行うが，本論文での差分間隔Δx，Δyは2.5mである．

(2) 対象とする海岸と津波および樹林条件

対象としたのは図-1に示した断面が汀線方向（y軸方向）に一様に続く海岸であり，そこに津波がまっすぐ（x軸方向）に来襲する条件である．汀線付近は基準面（z=0m）までが1/100勾配，基準面上+4.0mまでが1/50勾配であり，続く陸地の勾配は1/500である．この断面形状は比較的緩勾配の海岸における砕波帯と浜の典型的地形を念頭に単純化したもので，特定の地点を対象としたものではない．

津波来襲時の潮位は+2.0mとし，入射津波は水深100mの沖側境界で押し波スタートの正弦波で与えており，周期Tを600～3600s，波高H_Iを2～8mの範囲で変化させる．ただし，沖側境界をどこにとるかは任意性があるので，本論文では飯村ら[8]と同様に入射津波高を樹林なしの場合の汀線(z=2.0m)での津波高H_{sf0}で表す．図-2にT=1200s，H_I=6mの場合の汀線における第1波水位が最大になったときの水位ζ，流速Vおよび$\sqrt{gd}$（g：重力の加速度）の空間分布を例示しているが，この条件でのH_{sf0}は6.94mである．また，これにより遡上津波の先端部は射流であることがわかる．

海岸樹林は1/500斜面の沖側端（z=4.0m）から幅B_Fにわたってあるものとし，図-3のような平面配置を考える．図中，L_Fは汀線方向の長さ，b_Gは切れ間の幅であり，本研究ではL_F=200m，b_G=15mに固定する．この条件では切れ間の影響が汀線直角方向の両境界に波及せず無限に続く樹林帯に幅15mの切れ間がある条件と考えることができる．また，b_G=15mは出口での流速がほぼ最大となる条件を設定したものである．対象とした樹木は熱帯海岸樹のアダンで気根があり，図-4に示したような抵抗特性を有している．これは2004年インド洋大津波，2006年ジャワ津波に際しての樹木特性や破壊事例の調査結果[7]をもとに作成したものである．図中，H_{Tree}は

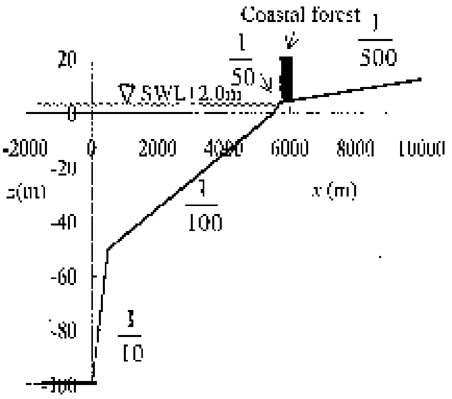

図-1 対象とする海岸地形

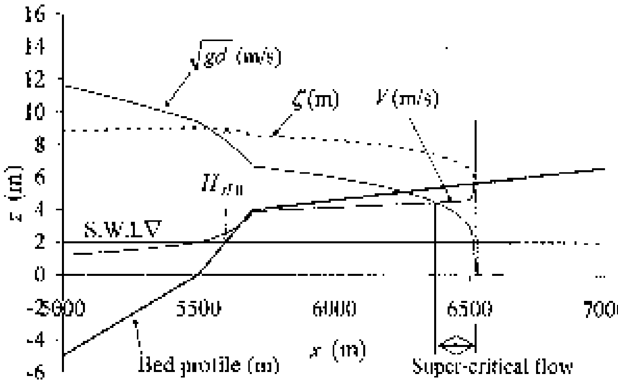

図-2 汀線での水位が最大時の水位，流速および$\sqrt{gd}$

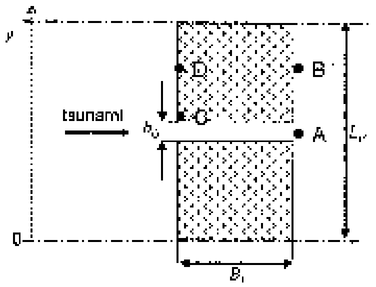

図-3 海岸樹林の配置と樹林条件

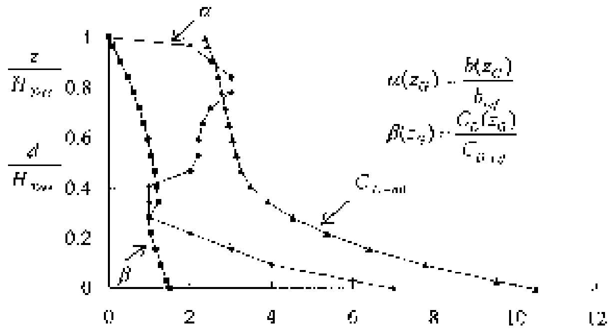

図-4 対象とする樹種アダンの抵抗特性

樹高で，本研究ではほぼ最大に生長したアダンを考え，H_{Tree}=8m，b_{ref}=0.2mとし，基準抗力係数$C_{D\text{-}ref}$は1.0とする．

数値計算では，樹林幅B_Fを0～200m，樹林密度γを0～0.4本/m^{2}の範囲で変化させる．なお，図-3中のA～Dは計算結果を示す代表点である．A，Bは樹林背後，C，Dは樹林最前列での地点であり，

その座標は A (x=5700+B_F+1.25m, y=100m), B (x=5700+B_F+1.25m, y=156.25m), C (x=5701.25m, y=108.75m), D (x=5701.25m, y=156.25m)である．地点B，D は切れ間の影響がほとんどない地点として選定している．

3．結果と考察

(1) 津波力の平面分布の例

本論文では次式で定義する潜在的津波力 $\vec{F}^*$ を議論する．

$$\vec{F}^* = \frac{\vec{F}}{\gamma C_{D-all}(d)b_{ref}} = \frac{1}{2}\rho\vec{V}\left|\vec{V}\right|d \tag{3}$$

これは単位幅，単位抗力係数を有した十分に高い仮想柱体に働く全抗力（単位：N/m）を表しており，通常津波による流体力として用いられている値の1/2 に相当する．これは，実際の樹木やその他障害物に働く全抗力を求めることが可能な潜在的津波力であり，たとえば単独の樹木に働く抗力による津波力 $\vec{F}_{Tree}$ は次のように表せる．

$$\begin{aligned}\vec{F}_{Tree} &= C_{D\text{-}all}(d)b_{ref}\vec{F}^*, \qquad H_{Tree} \geq d \\ &= C_{D\text{-}all}(H_{Tree})b_{ref}\frac{H_{Tree}}{d}\vec{F}^*, \quad H_{Tree} < d\end{aligned} \tag{4}$$

図-5 は代表的樹林帯および津波条件（B_F=100m, γ=0.226 本/m^2, T=1200s, $H_{s/0}$=6.94m）での潜在的津波力の時間的最大値 F^*_{max}（以降，これを単に津波力と呼ぶ）の樹林帯付近における分布を示したものである．津波力は既往研究 [4]で示した流速の変化に呼応して切れ間付近で顕著に変化し，その空間的最大値は切れ間出口に現れていることがわかる．ちなみに，前出の**図-3** に示した代表地点 A，B，C，D での値はそれぞれ，76.5，12.2，9.0，7.3kN/m であり，樹林帯最前列での津波力は後端での値より小さい．これは樹林帯による反射により樹林帯最前列付近では流速が減じることによっている．

(2) 樹林条件による津波力の変化

図-6，7 に代表的津波条件（T=1200s，$H_{s/0}$=6.94 m）のもとでの樹林幅（γ は 0.226 本/m^2 に固定），樹林密度（B_Fは 100m に固定）による津波力（添字A，B，C，D でそれぞれの地点を表している）の変化を示している．切れ間出口中央地点 A での津波力 F^*_{maxA} は樹林幅および樹林密度が大きくなるにつれて増大するが，**図-6** の樹林幅による変化では B_F=80m 付近で極大値に達した後に減少，**図-7** の密度による変化では一定値に近づくという違いがある．これは次のように説明できる．

まず，**図-8** は切れ間入り口での流入量($\overline{Q}_{in\,max}$)，出口での流出量($\overline{Q}_{out\,max}$)，側方からの流入量($\overline{Q}_{side\,max}$)，地点 A での津波力が最大時の没水深(d_{F^*max})および流速(V_{F^*max})の樹林幅による変化を示したものである．ただし，ここに流入・流出量は時間変化における最大値を切れ間幅 b_G=15m で割った平均値である．樹林幅が大きくなるにつれて，入り口での流入量は減少し一定値に近づくのに対し，側方からの流入量は増大し一定値に近づく変化を示す．その結果，出口での流出量は初め増大し，最大値に達した後に減少しており，津波力の変化と同様である．しかしながら，最大となる樹林幅は違っており，津波力のほうが大きいところまで増大している．これは，同図に示しているように，没水深は減少するものの流速は増大しており，津波力は流速の 2 乗に比例するので，流出量が減ってもある程度までは津

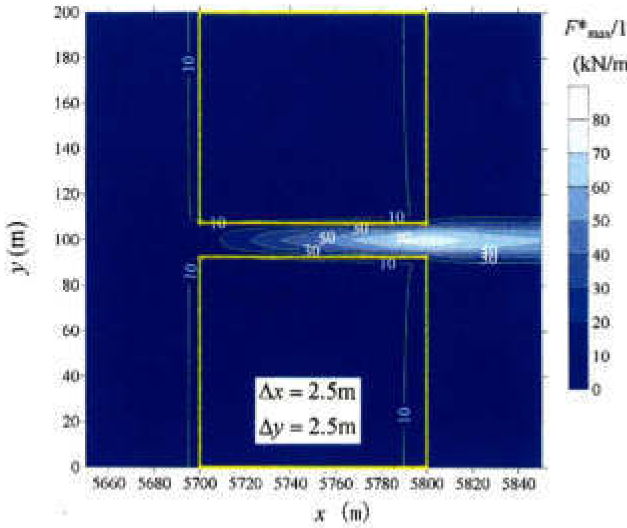

図-5 潜在的津波力の時間的最大値F^*_{max}の平面分布の例

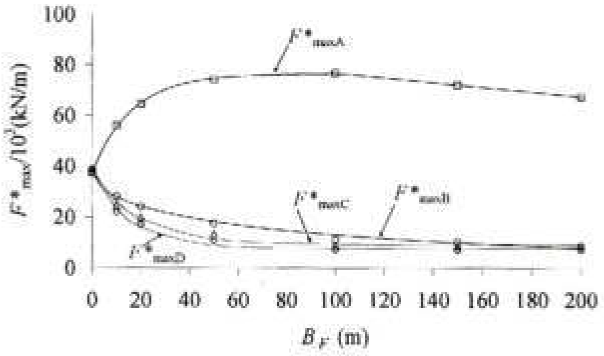

図-6 樹林幅による津波力の変化（γ=0.226本/m^2）

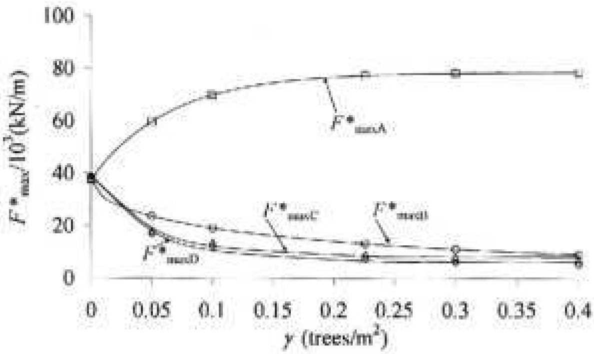

図-7 樹林密度による津波力の変化（B_F=100m）

波力が増大する結果となることによっている．なお，樹林幅が大きくなるにつれて出口位置は遠くへ移動するため，津波が達しないような極限まで考えると津波力は 0 まで減少する．本条件の場合，B_f=1000m 程度で，津波遡上は樹林帯内で終息し，出口までには至らない．

一方，図-9 は流入・流出量，浸水深および流速の密度による変化を示したものである．いずれも樹林幅の場合と類似な傾向を示しているが，この場合，切れ間出口の位置は固定されているので，それぞれ一定値に近づく変化となっている．極限的には樹林帯は空隙のない壁体に帰着し，そのため，密度が増大するにつれて壁体切れ間出口での津波力に近づく変化を示すことになる．本条件(B_f=100m)の場合，不透過壁体のときの津波力が最大となることを確かめている．なお，地点 A での津波力最大時の流れは樹林帯なしの場合を除いて，図-8，9 の場合ともに射流である．

以上の地点 A での変化に対し，地点 B，C および D での津波力の変化は単調な減少である．いずれも樹林幅，樹林密度増大による樹林抵抗の増大によって樹林帯背後では津波が減衰すること，樹林帯前方では反射の増大のため最前列での流速が減少することによっている．この中で，図-7 の地点 B の結果は，対象地形や樹種等条件は異なるものの，樹林密度を変化させて数値計算を行った Hiraishi and Harada[7] による結果とよく類似している．これらの地点での津波力は検討条件の範囲内では，地点 B での津波力が大きく，次いで切れ間入り口に接する地点 C，地点 D での津波力の順に小さくなる．このように樹林帯最前列の津波力は比較的小さいことが特色として指摘される．ただし，地点 B での津波力は，地点 A と同様に樹林幅が大きくなるにつれて最終的には 0 まで減少する．なお，図中の曲線は数値計算結果に当てはめた式による関係であるが，後で無次元表示に対する式を示すので，ここでは提示を省略する．

(3) 津波条件による津波力の変化

図-10，11 は代表的樹林条件（B_f=100m，γ=0.226 本/m²）での入射津波高 H_{si0}（T=1200s に固定），周期 T（H_{si0}=6.94m に固定）による津波力の変化を示したものである．図中，F^*_{max0} は樹林がない場合の地点 A における津波力である．津波力は本条件の範囲では容易に予測されるように入射津波高が大きいほど大きくなり，周期が長くなるほど小さくなっている．図中の曲線は，

$$F^*_{max} = a_{Hf}\left(H_{si0} - H_{cf}\right)^{b_{Hf}} \tag{5}$$

$$F^*_{max} = a_{Tf}\exp\left\{-b_{Tf}\left(\frac{T}{T_{rep}} - 1\right)\right\} \tag{6}$$

の関数で当てはめた式による変化である．ここに，a_{Hf}，a_{Tf}は有次元係数，b_{Hf}，b_{Tf}は無次元指数，H_{cf}

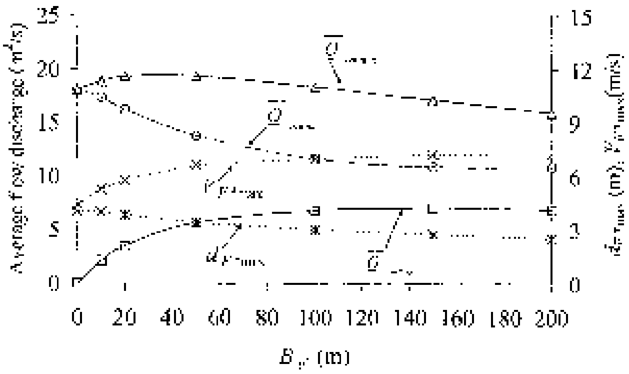

図-8　切れ間への流入・流出流量と地点Aにおける浸水深および流速（γ=0.226本/m²）

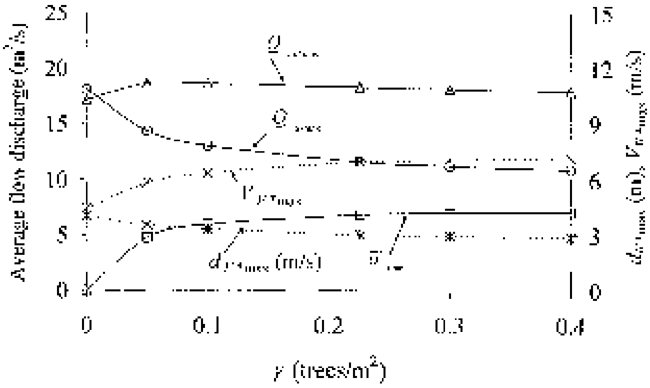

図-9　切れ間への流入・流出流量と地点Aにおける浸水深および流速（B_f=100m）

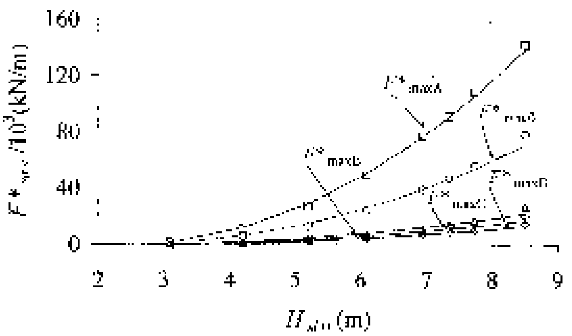

図-10　入射津波高による津波力の変化（B_f= 100m，γ=0.226，T=1200s）

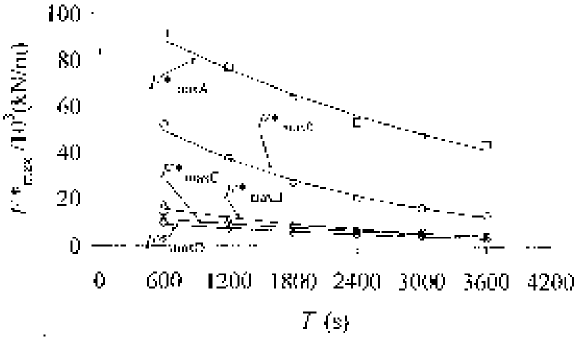

図-11　津波周期による津波力の変化（B_f= 100m，γ=0.226，H_{si0}=6.94m）

は津波が到達する限界の入射津波高，T_{rep} は津波の代表周期である．このうち H_{cf} は厳密に言えば樹林条件および地点の関数であるが，本研究の範囲ではそれほど変化しないので，本検討範囲での平均的な値である 2.5m に固定している．また，b_{Hf}は津波力が津波高の２乗に比例すると考え２としている．代表周期は任意性のあるところであるが，本研究では 20 分を考え，T_{rep}=1200s とする．そうした上での当てはめ曲線であるが，適合度は良好である．

(4) 無次元化の試み

首藤[10]は樹林条件を表すのに樹林厚を定義し，田中ら[11]はそれに樹種による抵抗特性の違いを取り入れた式を提案した．式 (7) はそれを SI 単位系に変更して書き換えたものである．

$$B_{dNall} = \gamma(1\times B_F) b_{ref} C_{D-all} = \gamma B_F b^*_{ref} C_{D-all} \tag{7}$$

ここに，B_{dNall}は樹林厚（単位：m），b^*_{ref}は数値は樹木の基準投影幅 b_{ref} に同じであるが，表記を簡単にするため単位を m²/本とした便宜的なものである．C_{D-all} を与える浸水深としては飯村ら[8]と同様に汀線での津波高を用いる．

本研究では，これを次のように代表津波条件に対する長さスケールを導入して無次元化する．

$$\frac{B_{dNall}}{T_{rep}\sqrt{gH_{rep}}} = \frac{\gamma B_F b^*_{ref} C_{D-all}(H_{rep})}{T_{rep}\sqrt{gH_{rep}}} \tag{8}$$

ここに，H_{rep} は汀線における代表津波高で，任意性があるところであるが，本研究では 7m と設定する．したがって，この無次元パラメータは津波条件は入っているものの固定条件であり，単に樹林条件を表すにすぎない．なお，上式の分母は周期 T_{rep} の長波の水深 H_{rep} における波長に相当する．

一方，津波力は次のように無次元化する．

$$\frac{F^*_{max}}{\rho g H_{i0}^2} = \alpha_f f_{Hf} f_{Tf} \tag{9}$$

ここに，α_fは無次元値，f_{Hf}，f_{Tf} は入射津波高 H_{i0}，津波周期 T に関する無次元関数であり，それぞれ次のように与える．

$$f_{Hf} = \left(\frac{1-H_{cf}/H_{i0}}{1-H_{cf}/H_{rep}}\right)^{b_{Hf}} = 2.42\left(1-\frac{2.5}{H_{i0}}\right)^2 \tag{10}$$

$$f_{Tf} = \exp\left\{-b_{Tf}\left(\frac{T}{T_{rep}}-1\right)\right\} \tag{11}$$

これについては後で説明を加える．

図-12，13 は地点 A，B および C，D での全シミュレーション結果について，式(8)の値を横軸にとり，式(9)の無次元値 α_f（地点を表す A，B，C，D の添字を付加）を縦軸にプロットしたものである．地点 A については樹林幅による変化と樹林密度による変化に先の図-6，7 の説明で述べたような違いがあることから，さらに BF，γ の添字を付して区別している．また，無次元関数 f_{Tf} に含まれる未定係数 b_{Tf} については，A，B，C，D の添字を付加して，地点ごとに次のように与えている．

$$b_{TfABF} = 0.318 + 0.268\exp\left(-3888\frac{\gamma B_F b^*_{ref} C_{D-all}(H_{rep})}{T_{rep}\sqrt{gH_{rep}}}\right) \tag{12}$$

$$b_{TfA\gamma} = 0.296 + 0.292\exp(-72.3\gamma b^*_{ref}) \tag{13}$$

$$b_{TfB} = 0.526 \tag{14}$$

$$b_{TfC} = b_{TfD} = 0.400 \tag{15}$$

このうち，地点 A については樹林幅，樹林密度により区別をしている他か，樹林条件の関数としている．これは切れ間出口での流速が二次元効果を強く受けることと，樹林幅の変化により移動する地点であることによる．他の地点については，B，D 地点は一次元的（切れ間の影響を受けない）であること，C は固定点であることにより定数で与えている．なお，α_f は式(9)からわかるように，入射津波による汀線での全静水圧に比例した値で無次元化した遡上域での津波力を無次元関数 f_{Hf}，f_{Tf} で除して補正した値であり，本論文ではこれを単に無次元津波力と呼ぶ．

このように無次元関数 f_{Hf}，f_{Tf}は横軸の津波条件

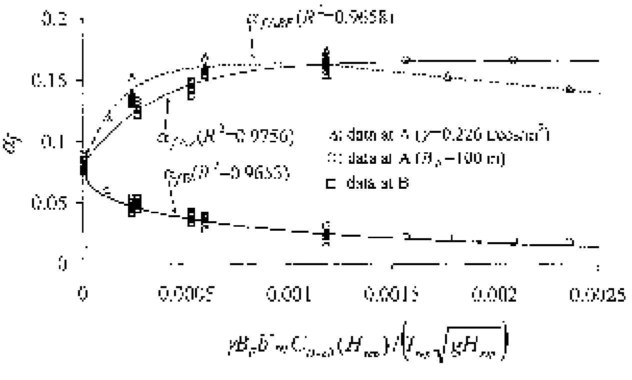

図-12　無次元樹林厚に対する無次元津波力（地点A，B）

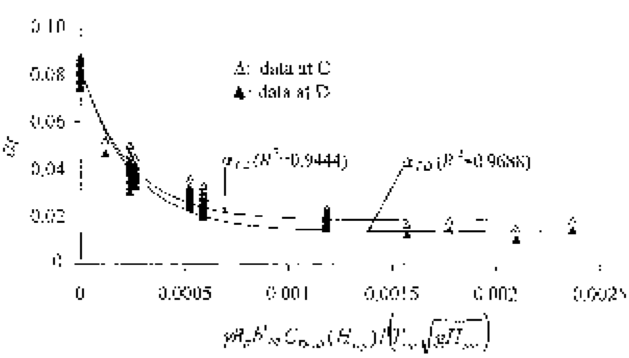

図-13　無次元樹林厚に対する無次元津波力（地点C，D）

を代表津波条件の値に固定化したことによる津波力の補正関数で，これにより樹林条件が同じであれば津波高あるいは周期による変化は横軸の同じ位置にプロットされ，無次元津波力は代表津波条件による値とほぼ同じ値をとるように基準化したものである．

図-12，13 の曲線はそうした無次元津波力に対する次のような当てはめ式による関係を表している．

$$\alpha_{fmax}=\min\left\{\begin{array}{l}0.164-0.0833\exp\left(-5747\dfrac{B_{dWall}}{T_{rep}\sqrt{gH_{rep}}}\right)\\[2ex] 0.183-16.9\dfrac{B_{dWall}}{T_{rep}\sqrt{gH_{rep}}}\end{array}\right\} \tag{18}$$

$$\alpha_{fav}=0.167-0.0852\exp\left(-2719\frac{B_{dWall}}{T_{rep}\sqrt{gH_{rep}}}\right) \tag{19}$$

$$\alpha_{fb}=0.0794\exp\left(-31.1\left[\frac{B_{dWall}}{T_{rep}\sqrt{gH_{rep}}}\right]\right) \tag{20}$$

$$\alpha_{fr}=0.0186-0.0633\exp\left(-4216\frac{B_{dWall}}{T_{rep}\sqrt{gH_{rep}}}\right) \tag{21}$$

$$\alpha_{g1}=0.0139+0.0678\exp\left(-4048\frac{B_{dWall}}{T_{rep}\sqrt{gH_{rep}}}\right) \tag{22}$$

式(18)中の min は中括弧内の上段，下段の式による値のうち小さい値をとることを意味する．

図-14 は当てはめ式による津波力とシミュレーションによる津波力の相関である．多様な条件での結果であるためばらついているが，ほぼ±10%の誤差に収まっている．

4．むすび

本研究において，切れ間を有する海岸樹林付近での樹林および津波条件による潜在的津波力の変化を明らかにした．津波力は切れ間で流速が大きくなることから切れ間付近で顕著に変化し，切れ間出口で最大となる．その切れ間出口での津波力は樹林抵抗（樹林幅，樹林密度）が大きくなるにつれて増大するが，樹林幅増大については出口が遠ざかるため最大に達した後は減少傾向を示す．切れ間から十分離れた地点や樹林前端での津波力は樹林抵抗が大きくなるにつれて減少する．津波条件の影響については波高が大きくなるほど，また周期が短いほど大きくなる．これら津波力の結果に対する無次元当てはめ式による計算値は誤差ほぼ±10%の範囲でシミュレーション結果に一致する．今後，さらに津波力により樹木に働く破断モーメント等の検討が必要である．

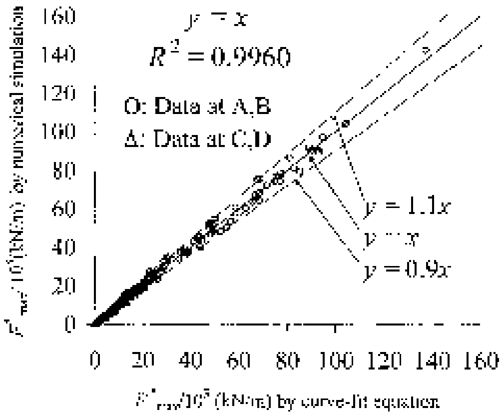

図-14　当てはめ式とシミュレーション結果の最大津波力の相関

参考文献

1) Mascarenhas, A. and Jayakumar, S.: An environmental perspective of the post-tsunami scenario along the coast of Tamil Nadu, India: Role of sand dunes and forests, Journal of Environmental Management, Vol.89, pp.24-34, 2008.

2) Fernando, H.J.S., Samarawickrama, S.P., Balasubramanian, S., Hettiarachchi, S.S.L., Voropayev, S.: Effects of porous barriers such as coral reefs on coastal wave propagation, Journal of Hydro-environment Research, Vol.1, pp.187-194, 2008.

3) Nandasena, N.A.K., Tanaka, N. and Tanimoto, K.: Perspective of coastal vegetation patches with topography variations for tsunami protection in 2D-numerical modeling, Annual Journal of Hydraulic Engineering, Vol.52, pp.133-138, 2008.

4) 谷本勝利，田中規夫，Thuy, N.B.，Nandasena, N.A.K.，飯村耕介：津波遡上に対する海岸樹林内通路の影響－2 次元数値計算による検討－，海洋開発論文集，第 24 巻，pp.87-92，2008.

5) Thuy, N.B., Tanimoto, K., Tanaka, N., Harada, K. and Iimura, K.: Effect of open gap in coastal forest on tsunami run-up - investigations by experiment and numerical simulation, Ocean Engineering, Vol.36, pp.1258-1269, 2009.

6) 谷本勝利，田中規夫，Thuy, N.B.，飯村耕介，原田賢治：海岸樹林端部付近における津波の流れ－実験と数値計算－，海岸工学論文集，第 56 巻，pp.361-365，2009.

7) 田中規夫，佐々木寧：2006 年ジャワ津波災害において海岸林が果たした役割とその破断・なぎ倒し限界，水工学論文集，第 51 巻，pp.1445-1450，2007.

8) 飯村耕介，田中規夫，谷本勝利，田中茂信：海岸樹林による津波減災効果の評価式の提案，海岸工学論文集，第 56 巻，pp.366-370，2009.

9) Hiraishi, T. and Harada, K.: Greenbelt tsunami prevention in South-Pacific region, Report of the Port and Airport Research Institute, Vol.42, No.2, pp.3-25, 2003.

10) 首藤伸夫：防潮林の津波に対する効果と限界，第 32 回海岸工学講演会論文集，pp.465-469，1985.

11) 田中規夫，佐々木寧，湯谷賢太郎，Samang Homchuen：津波防御に関する樹林帯幅と樹種の影響について－インド洋大津波におけるタイでの被災調査－，海岸工学論文集，pp.1346-1350，2005.

Proceedings of Coastal Dynamics 2009

48. TSUNAMI FLOW VELOCITY BEHIND THE COASTAL FOREST WITH AN OPEN GAP–EFFECTS OF TSUNAMI AND TREE CONDITION

Nguyen Ba Thuy, Norio Tanaka, Katsutoshi Tanimoto, Kenji Harada and Kosuke Iimura

Doi: https://doi.org/10.1142/9789814282475_0050

Claim

Restore content access
This functionality works only for purchases made as a guest

Coastal Dynamics 2009
Paper No. 384223

TSUNAMI FLOW VELOCITY BEHIND THE COASTAL FOREST WITH AN OPEN GAP– EFFECTS OF TSUNAMI AND TREE CONDITION

Nguyen Ba Thuy[1], Norio Tanaka[2], Katsutoshi Tanimoto[3], Kenji Harada[4] and Kosuke Iimura[5]

Abstract

In this paper, the effects of tsunami condition, forest density and forest width on tsunami flow velocity behind the coastal forest with an open gap were investigated by numerical simulations. A numerical model based on two-dimensional nonlinear long-wave equations was developed to account for the effects of drag and eddy viscosity forces due to the presence of vegetation. The numerical model was validated with good agreement by the experimental results. The numerical model was then applied to the coastal forest of *Pandanus odoratissimus* with a straight open gap (gap width=15m) perpendicular to the shoreline. It is found that the normalized maximum velocity behind the gap and vegetation[1] patch are greatly different. When tsunami period becomes large, the increase of velocity at the gap exit becomes large. Both forest width and forest density primarily influence on the velocity; as those increase, the normalized maximum velocity at the gap exit increases, while it decreases at the behind the vegetation patch. The enhancement of velocity at the gap exit is strongly dependent on the forest density but it is weakly influenced by the tsunami height.

Key words: Gap, tsunami velocity, *Pandanus odoratissimus,* forest density, forest width, tsunami period

1. Introduction

Many field observations, particularly after the 2004 Indian Ocean tsunami, have elucidated the effects of coastal vegetation on tsunami energy reduction (Danielsen et al. 2005, Kathiresan and Rajendran 2005, Tanaka et al. 2007, Mascarenhas and Jayakumar 2008). Currently, coastal forests are widely considered as an effective measure to mitigate tsunami damage from both economic and environmental points of view. In fact, several projects to plant vegetation on coasts as a bioshield against tsunamis have been started in Southeast Asian countries (Tanaka et al., 2008, 2009).

Related to the capacity of coastal forests to mitigate tsunami damage, many studies have been done by laboratory experiments and numerical simulations as well as field investigations. Among these, the numerical simulation is very effective, and various numerical models based on nonlinear long-wave equations have been proposed. Harada and Imamura (2005) proposed a model of the numerical simulation, in which the resistance of vegetation was evaluated by drag forces on trees and the drag coefficients of pines were estimated based on field observations and laboratory experiments. Tanaka et al. (2007) improved the expression of drag force so that the vertical stand characteristics of tree were considered more realistically, and proposed the equivalent drag coefficients for various tropical trees on the basis of field investigations in Sri Lanka, Thailand, and Indonesia. Tanaka et al. (2007) also demonstrated that *Pandanus odoratissimus* grown on beach sand is especially effective in providing protection from tsunami damage due to its density and complex aerial root structure. Tanimoto et al. (2007, 2008), Tanaka et al. (2008), and Thuy et al. (2008) used *Pandanus odoratissimus* species investigated by Tanaka et al. (2007) in their simulations.

To protect the human lives and properties from the disastrous amount of energy by tsunamis, it is important to make clear the inundation characteristics in different areas and in various conditions (i.e., tsunami condition, forest condition, coastal topography etc.). The behavior of tsunami needs to be

Graduate School of Science and Engineering, Saitama University, 255 Shimo-okubo, Sakura-ku, Saitama, 338-8570, Japan. [1] s07de059@mail.saitama-u.ac.jp, [2]tanaka01@mail.saitama-u.ac.jp, [3]tanimotok@coda.ocn.ne.jp, [4] haradak@mail.saitama-u.ac.jp, [5] s09de001@mail.saitama-u.ac.jp

elucidated clearly for evaluating the quantitative effect of vegetation on tsunami reduction and damage.

The presence of an open gap in a forest (for example a road, river etc.) may change flow pattern and amplify the current in the gap. This means that an open gap in a coastal forest has a negative effect on tsunami run-up behind the forest. On the basis of field investigations on the Indian coast after the 2004 tsunami, Mascarenhas and Jayakumar (2008) pointed out that roads perpendicular to the coast served as pathways for a tsunami to travel inland. Fernando et al. (2008) demonstrated by laboratory experiments that the exit flow velocity from a coastal perpendicular gap in submerged porous barriers simulated corals was significantly higher compared to the case with no gap.

The effect of an open gap in a coastal forest on tsunami run-up has been studied by numerical simulations and laboratory experiments. Thuy et al. (2009) conducted the experiments of a costal forest like mangrove in a wave channel of 40cm wide, and showed that the exit flow velocity in the case with a gap width of 7 cm is 1.8 times in comparison to the flow velocity without vegetation. Tanimoto et al. (2008) and Thuy et al. (2009) systematically investigated the effect of an open gap in a forest of *Pandanus odoratissimus* on tsunami run-up by numerical simulations and found that a 15 m gap width causes the highest velocity under their calculated conditions. On the other hand, both experimental and numerical results with a narrow gap showed that tsunami height behind the gap and vegetation patch is not so much different. The reduction rate of tsunami height behind the coastal forest without gap is already shown by numbers of researchers (for example, Harada et al., 2005; Tanimoto et al., 2007 etc.).

Therefore, this study focuses on the effect of tsunami height, tsunami period, forest density and forest width on flow velocity behind the vegetation patch and at the gap exit by numerical simulations. The numerical model is based on two-dimensional nonlinear long-wave equations and incorporates the *Sub-Depth Scale* turbulence model. The numerical model has been validated for the capability of numerical model. A coastal forest of *Pandanus odoratissimus* is selected for the simulation, because it is a representative coastal vegetation in South Asia and reported especially effective in providing protection from tsunami damage (Tanaka et al., 2007).

This paper introduces the most recent results of our studies at Saitama university on the effect of open gap in coastal forest to tsunami run-up, particularly including results of laboratory experiments.

2. Mathematical model and numerical method

2.1. Governing equations

The governing equations are two-dimensional nonlinear long-wave equations that include drag and eddy viscosity forces due to interaction with vegetation. The continuity and the momentum equations are respectively:

$$\frac{\partial \zeta}{\partial t}+\frac{\partial Q_x}{\partial x}+\frac{\partial Q_y}{\partial y}=0 \tag{1}$$

$$\frac{\partial Q_x}{\partial t}+\frac{\partial}{\partial x}\left(\frac{Q_x^2}{d}\right)+\frac{\partial}{\partial y}\left(\frac{Q_xQ_y}{d}\right)+gd\frac{\partial \zeta}{\partial x}+\frac{\rho g n^2}{\rho d^{7/3}}Q_x\sqrt{Q_x{}^2+Q_y{}^2}+\frac{1}{2\rho}\frac{\rho\gamma C_{D-all}b_{ref}}{d}Q_x\sqrt{Q_x{}^2+Q_y{}^2}$$
$$-2\frac{\partial}{\partial x}\left(\nu_e\frac{\partial Q_x}{\partial x}\right)-\frac{\partial}{\partial y}\left(\nu_e\frac{\partial Q_x}{\partial y}\right)-\frac{\partial}{\partial y}\left(\nu_e\frac{\partial Q_y}{\partial x}\right)=0 \tag{2}$$

$$\frac{\partial Q_y}{\partial t}+\frac{\partial}{\partial x}\left(\frac{Q_xQ_y}{d}\right)+\frac{\partial}{\partial y}\left(\frac{Q_y^2}{d}\right)+gd\frac{\partial \zeta}{\partial y}+\frac{\rho g n^2}{\rho d^{7/3}}Q_y\sqrt{Q_x{}^2+Q_y{}^2}+\frac{1}{2\rho}\frac{\rho\gamma C_{D-all}b_{ref}}{d}Q_y\sqrt{Q_x{}^2+Q_y{}^2}$$
$$-2\frac{\partial}{\partial y}\left(\nu_e\frac{\partial Q_y}{\partial y}\right)-\frac{\partial}{\partial x}\left(\nu_e\frac{\partial Q_y}{\partial x}\right)-\frac{\partial}{\partial x}\left(\nu_e\frac{\partial Q_x}{\partial y}\right)=0 \tag{3}$$

where x and y are the streamwise and transverse directions, respectively, Q_x and Q_y are the discharge flux in x and y directions respectively, t is the time, d the total water depth (d=h+ζ), h the local still water depth, ζ the water surface elevation, g the gravitational acceleration, ρ the water density, n the Manning roughness coefficient, γ the tree density (number of trees/m^2), and $C_{D\text{-}all}$ the depth-averaged equivalent drag coefficient considering the vertical stand structure of tree, which was defined by Tanaka et al. (2007) as:

$$C_{D-all}(d) = C_{D-ref}\,\frac{1}{d}\int_0^d \alpha(z_G)\beta(z_G)dz_G \tag{4}$$

$$\alpha(z_G) = \frac{b(z_G)}{b_{ref}} \tag{5}$$

$$\beta(z_G) = \frac{C_D(z_G)}{C_{D-ref}} \tag{6}$$

where $b(z_G)$ and $C_D(z_G)$ are the projected width and drag coefficient of a tree at the height z_G from the ground surface, and b_{ref} and $C_{D\text{-}ref}$ are the reference width of the trunk and the reference drag coefficient at z_G=1.2 m, respectively. The eddy viscosity ν_e is expressed in the *SDS* turbulence model as described below.

2.2. Turbulence model

The *SDS* turbulence model given by Nadaoka and Yagi (1998) is applied to evaluate the eddy viscosity with modifications related to the bottom friction and vegetation resistance.

$$\frac{\partial k_D}{\partial t} + u\frac{\partial k_D}{\partial x} + v\frac{\partial k_D}{\partial y} = \frac{1}{d}\frac{\partial}{\partial x}\left(d\,\frac{\nu_e}{\sigma_k}\frac{\partial k_D}{\partial x}\right) + \frac{1}{d}\frac{\partial}{\partial y}\left(d\,\frac{\nu_e}{\sigma_k}\frac{\partial k_D}{\partial y}\right) + p_{kh} + p_{kv} + p_{kd} - \varepsilon_D \tag{7}$$

$$p_{kh} = \nu_e\left[2\left(\frac{\partial u}{\partial x}\right)^2 + \left(\frac{\partial u}{\partial y} + \frac{\partial v}{\partial x}\right)^2 + 2\left(\frac{\partial v}{\partial y}\right)^2\right] \tag{8}$$

$$p_{kv} = \frac{gn^2}{d^{4/3}}(u^2+v^2)^{1.5} \tag{9}$$

$$p_{kd} = \frac{\gamma b_{ref} C_{D-all}}{2}(u^2+v^2)^{1.5} \tag{10}$$

$$\nu_e = c_w\,\frac{k_D{}^2}{\varepsilon_D} \tag{11}$$

$$\varepsilon_D = c_d\,\frac{k_D{}^{1.5}}{l_D} \tag{12}$$

where k_D is the kinetic energy, $l_D = \lambda\, d$ is the length scale (λ: turbulence length scale coefficient), and u and v are the depth-averaged velocity components in x and y directions, respectively. For the model parameters, standard values are adopted: c_w=0.09, c_d=0.17, and σ_k=1.0.

A set of the above equations is solved by the finite-difference method of a staggered leap-frog scheme. An upwind scheme is used for nonlinear convective terms in order to maintain numerical stability. A semi–Crank-Nicholson scheme is used for bed friction, drag, and eddy viscosity terms. On the offshore sides, a wave generation zone with a constant water depth in which governing equations are reduced to linear long-wave equations is introduced to achieve the non-reflective wave generation by using the method of characteristics. For a moving boundary treatment, a number of algorithms are necessary so that the flow occurring when the water surface elevation is high enough can flow to the neighboring dry cells.

3. Experimental results and model validation

The laboratory experiments for long waves were carried out in a wave channel of 40 cm wide, 15 m long and 1 m wide vegetation model setting in the water, at Saitama University. The vegetation is simply modeled by wooden cylinders with a diameter of 5 mm mounted in a staggered arrangement with the density γ=2183 cylinders/m^2 and an open gap is set on the side (for more details refer to Thuy et al., 2009).

Several wave and gap width conditions were tested in the experiments. In the present paper, however, the results of relatively low waves with the period of T=20 s for the cases of without vegetation, full vegetation and with a gap width of 7 cm are presented.

Fig. 1 shows the records of flow velocity in three cases; without vegetation, full vegetation and with the presence of gap, where the record in the case of the presence of gap is the velocity at the center of gap exit. Reduction of velocity in the case of full vegetation and the enhancement of velocity in the presence of gap are clearly noticed.

Figs. 2(a) and (b) show examples of the time series of flow velocity for the case of gap presence. Both experimental and numerical results of flow velocities at (a) the center of the gap exit, and (b) the center of the end of vegetation patch are plotted. The numerical results agree fairly well with the experimental results. Experimental and numerical results show a large difference of flow velocities at the gap exit and vegetation region

The average of peak values of flow velocity obtained from the time series at all measuring points on the cross line behind the vegetation in the case of gap presence are plotted in Fig. 3. It is confirmed that the agreement between experimental and numerical results is fairly good.

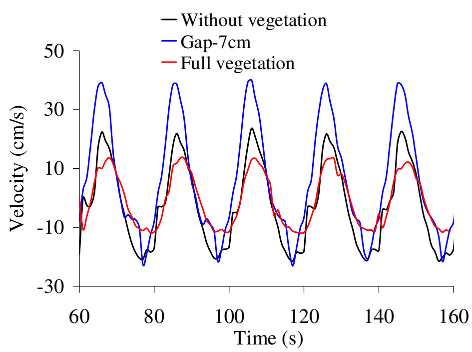

Fig. 1 Experimental records of current velocity in 3 cases.

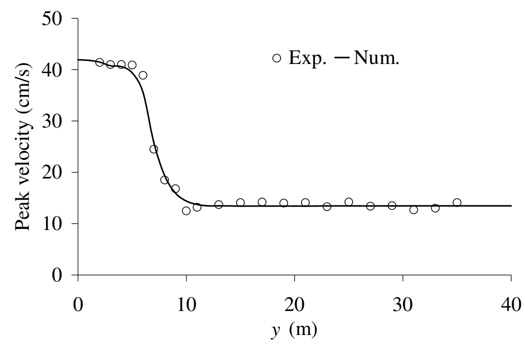

Fig. 3. Model validation for transverse distribution of peak velocity behind the vegetation.

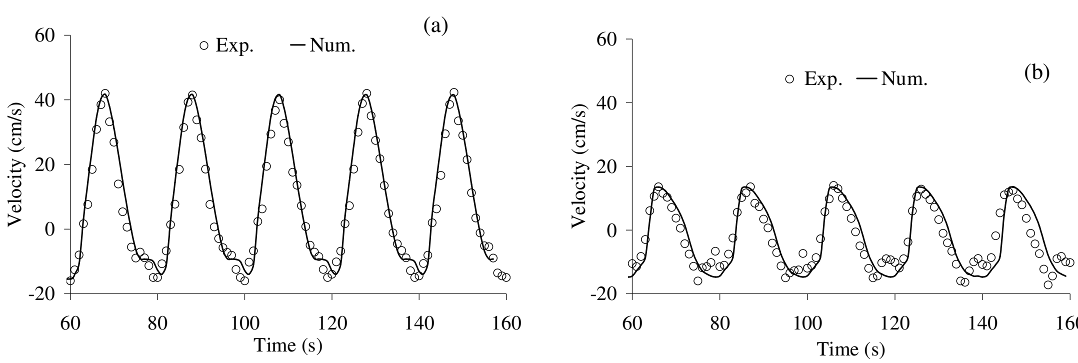

Fig. 2. Model validation for time series of flow velocity. (a) At center of gap exit, and (b) at center of vegetation end.

4. Application of numerical model- tsunami flow velocity behind coastal forest

4.1. Topography, tsunami and vegetation conditions

4.1.1. Vegetation species

In the present study, *P. odoratissimus*, a dominant coastal vegetation in South Asia, was considered as a tree species consisting of a coastal forest. As shown in Fig. 4(a), *P. odoratissimus* has a complex aerial root structure that provides additional stiffness and increases the drag coefficient. Fig. 4(b) shows the α, β, and $C_{D\text{-}all}$ of *P. odoratissimus* modified slightly from those proposed by Tanaka et al. (2007) to the following conditions: the tree height H_{Tree}=8 m, the reference diameter b_{ref}=0.2 m, the density γ=0.2 trees/m^2, and the reference drag coefficient $C_{D\text{-}ref}$=1.0. In the figure, z_G indicates the height from the ground surface.

(a) *Pandanus odoratissimus.*

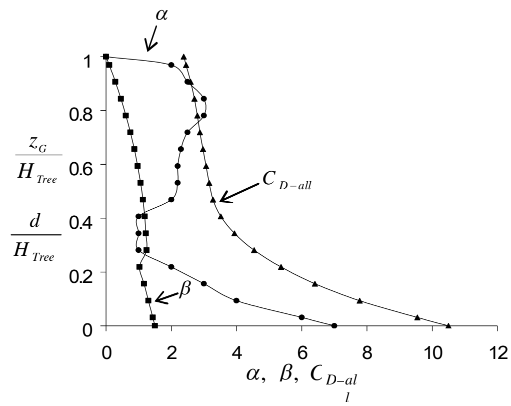

(b)

Fig. 4. Characteristics of *P. odoratissimus*. (a) Photographs of a stand, and (b) vertical distribution of α, β, and $C_{D\text{-}all}$.

4.1.2. Topography and coastal forest conditions

A uniform coastal topography with the cross section perpendicular (x-axis) to a straight shoreline, as shown in Fig. 5(a), was selected as a model case. The bed profile of the domain consists of 4 slopes S=1/10, 1/100, 1/50, and 1/500. The offshore water depth at an additional wave generation zone with a horizontal bottom is 100 m below the datum level of z=0. The tide level at the attack of a tsunami is considered to be 2 m, and therefore the still water level is located at 2 m above the datum level. The direction of the incident tsunami is perpendicular to the shoreline. In the present paper, the tsunami height and velocity of the first wave only are discussed.

Coastal forest starts at the starting point of the slope of 1/500 on the land, where the height of the ground is 4 m above the datum level (2 m above the tide level at tsunami attack). The forest is assumed to extend in the direction of the shoreline (y-axis) with the same arrangement of gaps and vegetation patches with an along-shore unit length of L_F, as shown in Fig. 5(b). Both side boundaries, shown by dot-and-dash lines in the figure, are mirror image axes in which no cross flow exists. The coastal forest length L_F is fixed as 200m. According to Thuy et al. 2009, this length is long enough to avoid the effect of flow from the other ends of the vegetation patch in the direction parallel to the shoreline. The gap width b_G is 15m at the middle of the forest length. The coastal forest width B_F is fixed as 200 m, except for the cases considering the effect of forest width. In the present study, velocities at point A (the middle at the end of open gap) and at point B (the middle at the end of vegetation patch) are discussed.

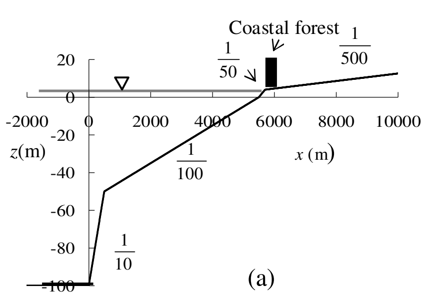

(a)

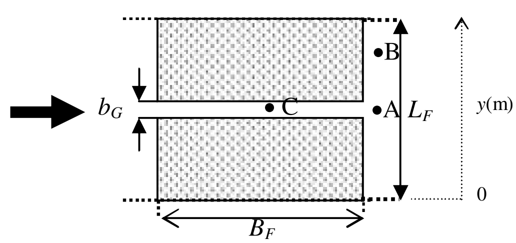

(b)

Fig. 5. Schematic of the topography for numerical simulation. (a) Cross section of topography, (b) sketch of forest and gap arrangement, and definition of important parameters b_G, B_F and L_F. A, B and C show location for the output of numerical simulation.

In the numerical calculation, a uniform grid size in x and y directions was set as 2.5 m and the time interval was 0.04 s. The Manning roughness coefficient (n) was set as 0.025, which is widely used in numerical simulations of tsunami run-up (for example, Harada and Imamura 2005). The turbulence length scale coefficient (λ) was set as 0.08, the same value obtained from the experimental calibration.

4.2. Tsunami behind the coastal forest

Fig. 6(a) shows the time profile of flow velocity in three cases; without vegetation, full vegetation and the presence of gap at point A for the case of incident wave height at the offshore boundary, H_I=6m and tsunami period, T=20 minutes. These results are consistent with the experimental results. The maximum velocity is 2.5 times in comparison with the case with full vegetation and 1.7 times in the case with no vegetation. The increases of velocity at the end of the gap are related to the inflow from both sides of the open gap. It can be examined in Fig. 6(b), where the time variation of the discharge flux averaging with the gap width ($\overline{Q}_{in}$ at the inlet, $\overline{Q}_{out}$ at the outlet, and $\overline{Q}_{side}$ at the sides), where $\overline{Q}_{side}$ is defined as the value of total in-flow (positive) from both sides to the gap divided by the gap width and called the average inflow from (both) sides. Consequently, $\overline{Q}_{out}$ corresponds to a summation of $\overline{Q}_{in}$ and $\overline{Q}_{side}$ with consideration of their phase differences and is strongly dependent on the inflow coming from both sides.

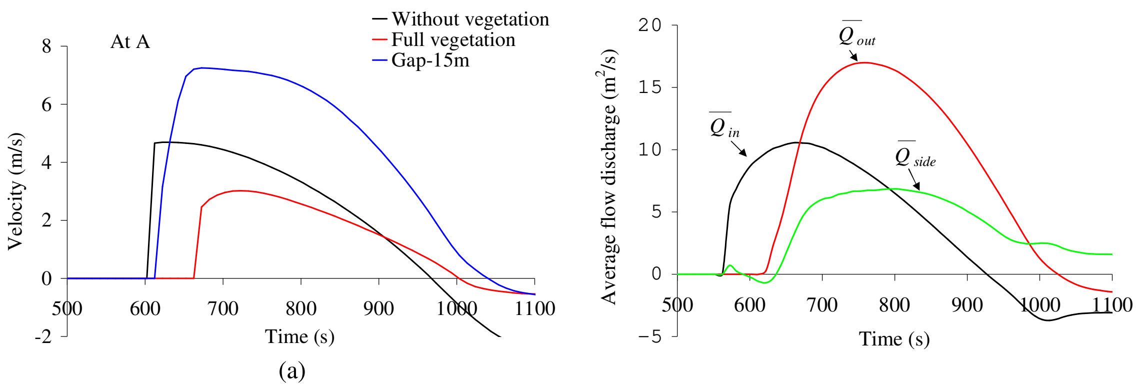

Fig. 6. (a) Time profile of velocity in three cases of vegetation arrangement at location A, and (b) time profile of average discharge flux. $\overline{Q}_{in}$ at the inlet, $\overline{Q}_{out}$ at the outlet, and $\overline{Q}_{side}$ at the sides.

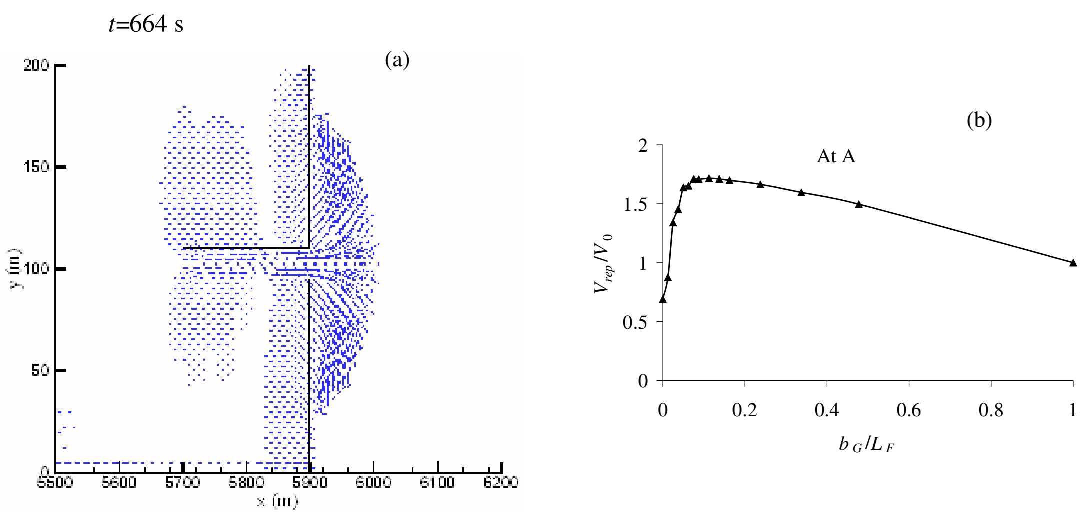

Fig. 7. (a) Flow pattern at 664 s, (b) variation of normalized representative velocity (Thuy et al. 2009).

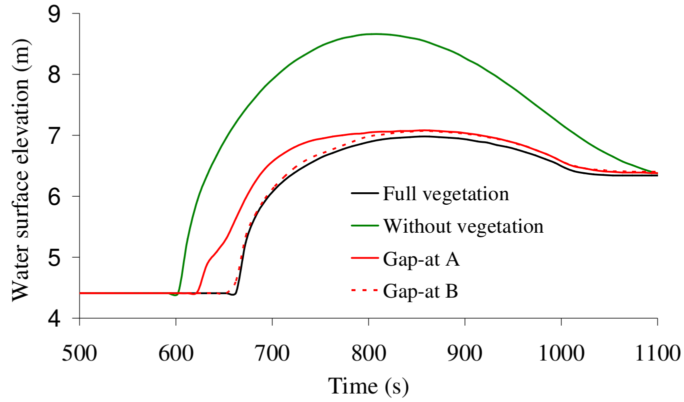

Fig. 8. Time profile of water surface elevation in three cases of vegetation arrangement.

Fig. 7(a) illustrates the flow patterns at t=664 s. The flow in the gap is fast and reaches the end quickly to spread out from the exit. However, the enhancement of velocity behind the gap is dependent on the width of the open gap. Tanimoto et al. (2008) and Thuy et al. (2009) systematically investigated and found that in the same conditions of topography and tree as Section 4.1 and with H_I=6 m, and T= 20 minutes, a gap width of 15 m causes the highest velocity. Fig. 7(b) shows the normalized representative flow velocity (V_{rep}/V_1) at location A against the normalized gap width (b_G/L_F), where the representative flow velocity V_{rep} is the velocity at the time when the discharge flux reaches the maximum in the time variation, and V_0 is the representative flow velocity for the case of without vegetation. (Thuy et al., 2009). Fig. 8 shows the time profiles of water surface elevation above the datum level at point A in three cases; without vegetation, full vegetation and the presence of gap (locations A and B in Fig. 5(b)). It confirmed that the presence of 15 m of open gap width in coastal forest has small influence on tsunami height behind the vegetation in comparison with the case of full vegetation, and the tsunami heights behind the gap and behind the vegetation patch are almost same. Therefore, for later discussion, the inundated depths at point A only are shown.

4.3. Effect of tsunami height and tsunami period

Fig. 9(a) shows the change of normalized maximum flow velocity (V_{max}/V_1) at locations A and B by the tsunami height, H_I=2, 3, 4, 5, 6 m, where V_{max} is the temporal maximum flow velocity at A or B, and V_1 is the maximum flow velocity for the case of without vegetation. In this figure, the forest density and tsunami period are fixed as 0.2 trees/m^2 and 20 minutes, respectively. The velocity at location B decreases due to the drag of vegetation, while at location A, it increases due to the enhancement of inflow from vegetation sides to the gap, except for the case H_I =2 m. However, the change rate is not large as the tsunami height exceeds 3 m. The decrease of velocity in comparison with the case without vegetation in the case H_I = 2 m (see Fig. 9(b)) is due to the prevalent out flow (negative value) from gap to vegetation sides. It can be confirmed in Fig. 10(a), where the time profile of average flow discharge passing to the gap from both vegetation sides is shown. In Fig. 10(a), a dominant flow with direction from vegetation sides to the gap occurring in process of tsunami propagation for the case H_I =3 m, while, the opposite direction is dominant when H_I =2 m. The occurrence of dominant flow from gap to vegetation sides is due to a large value of the depth average drag coefficient generated by complex aerial root structure of *P. odoratissimus* when the inundation depth becomes small (see Fig. 9(b) and 4(b)), that slows the flow in the vegetation patch. Consequently, the outflow from the gap to vegetation patches dominates as a whole to reduce the flow velocity at the exit. These flows are corresponding to considerable slope of water surface elevation occurred in the process of tsunami propagation as confirmed in Fig. 10(b), where the time series plots of water surface elevation at cross sections at the middle of forest width (location C in Fig.5(b)) are shown. The change of normalized maximum inundation depth (d_{max}/d_1) by the tsunami height is also shown in Fig. 9(a), where d_{max} is the maximum inundation depth at location A, and d_1 is the maximum inundation depth for the case of without vegetation. It is almost same to the normalized maximum velocity at location B.

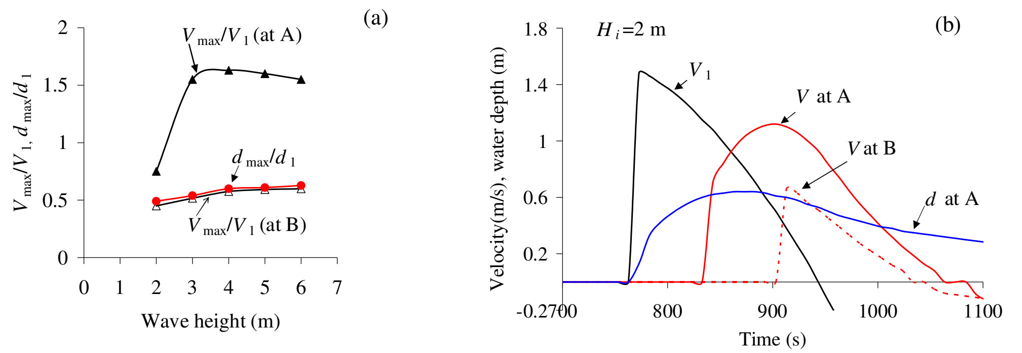

Fig. 9. (a) Variation of normalized maximum velocity and maximum inundation depth by tsunami height, (b) time profile of velocity and water depth for the case of H_I=2 m. V_1 denoted the case of without vegetation.

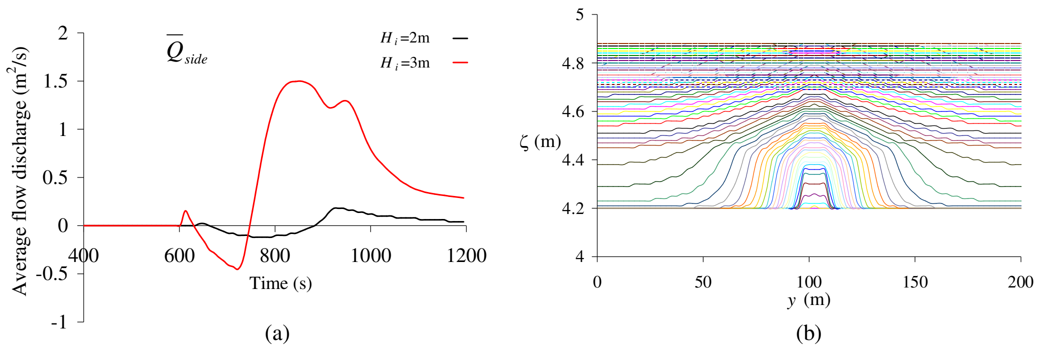

Fig. 10. (a) Time profile of average discharge flux, (b) time series plots of cross sections water surface elevation at C.

In order to examine the effect of tsunami period to velocity reduction behind the coastal forest, the conditions of tsunami height and forest density are selected as 6 m and 0.2 trees/m,^{2} and the tsunami period is varied as 10, 20, 30, 40, 50 and 60 minutes. Fig. 11(a) shows the variation of maximum velocity at point A, point B and V_1 by the tsunami period. The velocities decrease as the tsunami period becomes large. As the tsunami period becomes large, the difference between the velocity at point B and V_1 becomes smaller, while the difference between the velocity at point A and V_1 becomes larger. In Fig. 11(b), consequently, the change of normalized velocity at point B is small, and the normalized velocity at point A increases as the tsunami period increases. The flow velocity at point A becomes a double of velocity in the case of no vegetation when tsunami period exceeds 50 minutes. Numerical results also show that, the effect of tsunami period on the change of normalized maximum inundation depth is very small (see Fig. 11(b))

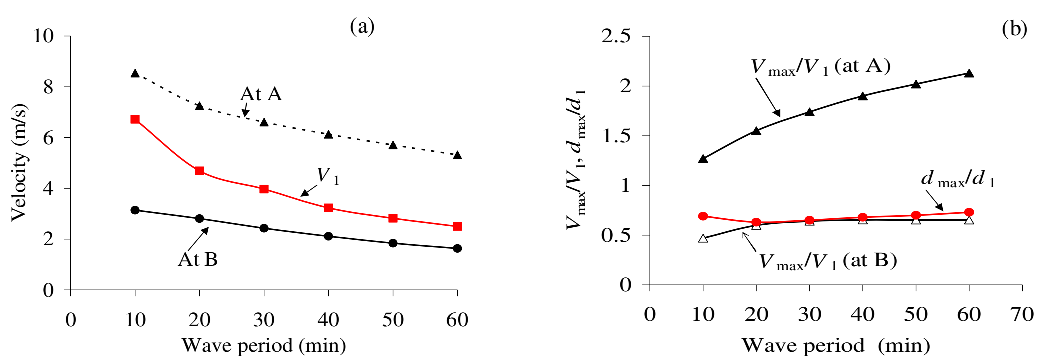

Fig. 11. (a) Variation of maximum velocity by tsunami period, (b) variation of normalized maximum velocity(V_{max}/V_1) and normalized maximum inundation depth (d_{max}/d_1) by tsunami period.

4.4. Effect of forest density and forest width

The effect of forest density is discussed in the conditions that the tsunami height and tsunami period are fixed as 6 m and 20 minutes, and the forest density varies as 0.05, 0.1, 0.2, 0.3 and 0.4 trees/m^2. Fig. 12(a) shows the distribution of maximum velocity along the end line of forest width in three cases of forest density. It can be seen that the increase of forest density reduces velocity behind the vegetation patch, but it increases the velocity at the gap exit. Fig. 12(b) shows the change of normalized maximum flow velocity at points A and B against the forest density. As the forest density increases, the velocity at point B decreases and increases at point A. Fig. 13 shows the normalized increase of velocity at point A relative to point B ($[V_{max(A)}$-$V_{max(B)}]$/ $[V_{maxB}]$) against the tsunami height for the forest densities of 0.1 and 0.4 trees/m^2. The amplification of flow through the gap is quite clear, and is strongly dependent on the forest density and weakly on the wave height. The change of normalized maximum inundation depth has the same tendency to the case of the change of normalized maximum velocity at point B; it decreases as forest density increases (see Fig. 12(b)).

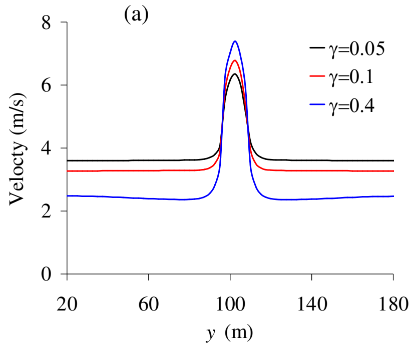

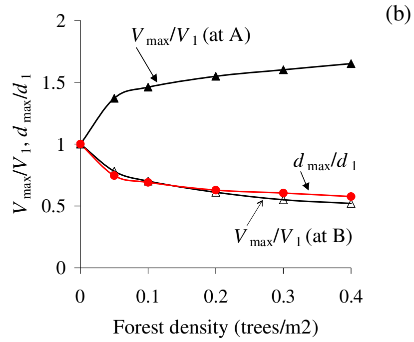

Fig. 12. (a) Cross section of velocity in three cases of forest density (γ is the tree density (number of trees/m^2)), (b) variation of normalized maximum velocity (V_{max}/V_1) and maximum inundation depth (d_{max}/d_1) by forest density.

To investigate the effect of forest width on velocity reduction, the tsunami height, tsunami period and forest density are fixed as 6 m, 20 minutes and 0.2 trees/m^2 respectively. The forest width B_F is changed as 0, 20, 50, 100, 150 and 200 m. Fig. 13 shows the normalized increase of velocities at point A and point B (now, the positions of point A and B change as the forest width changes) just behind the coastal forest. From Fig. 14, the normalized maximum velocity at point B decreases from 1.0 to 0.5 corresponding from no forest to a forest with of 200 m. However, at point A, contrary to point B, the normalized maximum velocity increases as the forest width increases, and gets to the maximum value of 1.6 at forest width of 200 m. Numerical results also show that, the change of normalized maximum inundation depth has the same tendency as the case of the change of normalized maximum velocity at point B; it decreases from 1.0 to 0.6 corresponding from no forest to a forest with of 200 m (see Fig. 14).

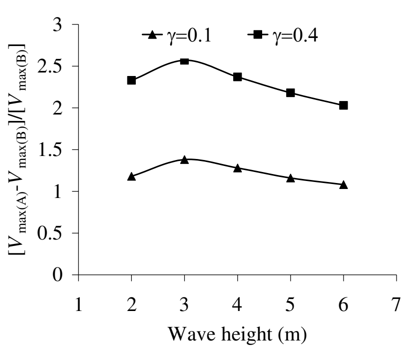

Fig. 13. Variation of normalized exit velocity by wave height. γ is the tree density (number of trees/m^2)

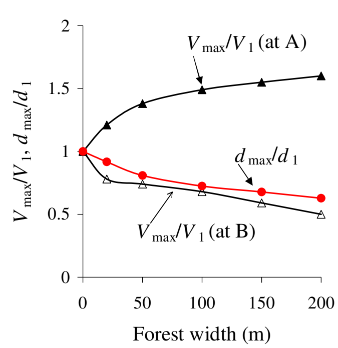

Fig. 14. Variation of normalized maximum velocity (V_{max}/V_1) and maximum inundation depth (d_{max}/d_1) by forest width. For the definition of A and B, see Fig.5(b)

5. Conclusions

The effects of tsunami height, tsunami period, forest density and forest width on the tsunami flow velocity behind the coastal forest with the presence of an open gap were discussed in this study. It is found that the normalized maximum velocity behind the gap and vegetation patch are greatly different. The changes of normalized maximum velocity at the gap exit and vegetation patch are not large as the tsunami height exceeds 3 m. When tsunami period becomes large, the normalized maximum velocity at the gap exit becomes large but behind the vegetation patch it does not so vary. The forest density and forest width primarily influence on the tsunami velocity behind the vegetation patch and at gap exit; as those increase, the normalized maximum velocity at the gap exit increases, while it decreases behind the vegetation patch. The enhancement of velocity at the gap exit is strongly dependent on the forest density but it is weakly influenced by the tsunami height. In all investigated cases, the change of normalized maximum inundation depth has the same tendency to the change of normalized maximum velocity at behind the vegetation patch.

In the present paper, only *Pandanus odoratissimus* species is selected for investigation. The mitigation of tsunami run-up behind a forest strongly depends on the vegetation species. The effect of vegetation species on tsunami run-up with the presence of open gap will be investigated in future work.

Acknowledgements

This study is partially funded by the Sumitomo Foundation. The authors wish to acknowledge Mr. N. A. K. Nandasena for his contribution in setting up the laboratory experiments.

References

Danielsen F., Sorensen M.K., Olwig M.F., Selvam V., Parish F., Burgess N.D., Hiraishi T., Karunagaran V.M., Rasmussen M.S., Hansen L.B., Quarto A., Suryadiputra N., 2005. The Asian tsunami: A protective role for coastal vegetation, *Science*, Vol. 310, 643.

Fernando, H.J.S., Samarawickrama, S.P., Balasubramanian, S., Hettiarachchi, S.S.L., Voropayev, S., 2008. Effects of porous barriers such as coral reefs on coastal wave propagation. *Journal of Hydro-environment Research*, 1, 187-194.

Harada, K., Imamura, F., 2005. Effects of coastal forest on tsunami hazard mitigation – A preliminary investigation, Tsunamis: *Case studies and Resent Development, ed. K. Satake* (Advances in natural and Technological Hazards Research, Springer), 279-292.

Kathiresan, K., Rajendran, N., 2005. Coastal mangrove forests mitigated tsunami, Short note, *Estuarine, Coastal and Shelf Science* 65, 601 – 606.

Mascarenhas, A., Jayakumar, S., 2008. An environmental perspective of the post-tsunami scenario along the coast of Tamil Nadu, India: Role of sand dunes and forests, *Journal of Environmental Management*, 89, 24-34.

Nadaoka, K., Yagi, H., 1998. Shallow - water turbulence modeling and horizontal larger-eddy computation of river flow. *Journal of Hydraulic Engineering*, 124(5), 493-500.

Tanaka, N., Sasaki, Y., Mowjood, M.I.M., Jinadasa, K.B.S.N., 2007. Coastal vegetation structures and their functions in tsunami protection: Experience of the recent Indian Ocean tsunami, *Landscape and Ecological Engineering*, Vol. 3, 33-45.

Tanaka, N., 2008. Vegetation bioshields for tsunami mitigation: review of the effectiveness, limitations, construction, and sustainable management, *Landscape and Ecological Engineering*, Springer, Vol. 5, 71-79.

Tanaka, N., Nandasena, N. A. K., Jinadasa, K. S. B. N., Sasaki, Y., Tanimoto, K. Mowjood, M. I. M., 2009. Developing effective vegetation bioshield for tsunami protection, *Journal of Civil and Environmental Engineering Systems*, 26(2), 163-180.

Tanimoto, K., Tanaka, N., Nandasena, N. A. K., Iimura, K, Shimizu, T., 2007. Numerical simulation of tsunami prevention by coastal forest with several species of tropical tree, *Annual Journal of Coastal Engineering*, JSCE, Vol. 54 (2), 1381-1385. (in Japanese).

Tanimoto, K., Tanaka, N., Thuy, N. B., Nandasena N. A. K., Iimura, K., 2008. Effect of open gap in coastal forest on tsunami run-up – investigation by 2-dimensional numerical simulation, *Annual Journal of Civil Engineering in the Ocean*, JSCE, Vol. 24, 87-92. (in Japanese).

Thuy, N. B.,Tanimoto, K., Tanaka, N., Harada. K., Iimura, K.. Effect of open gap in coastal forest on tsunami run-up-Investigation by experiment and numerical simulation, 2009. *Journal of Ocean Engineering*. (revise).

PROCEEDINGS OF COASTAL ENGINEERING, JSCE

Online ISSN : 1884-8222
Print ISSN : 0916-7897
ISSN-L : 0916-7897

Journal home Journal issue About the journal

Current issue

Showing 1-50 articles out of 294 articles from the selected issue

Download PDF (691K)

Effect of Coastal and River Forests on Tsunami Run-up in River

Katsutoshi TANIMOTO, Norio TANAKA, N. B. THUY, Kosuke IIMURA

2008 Volume 55 Pages 226-230
Published: October 10, 2008
Released: June 04, 2010

DOI https://doi.org/10.2208/proce1989.55.226

JOURNALS FREE ACCESS

Hide abstract

The effect of coastal and river forests on tsunami run-up in a river has been investigated by numerical simulations basedon two-dimensional non-linear long wave equations. A simple coastal and river topography is considered where theriver course is straight and perpendicular to the shore line. The coastal forest zone consists of *Rhizophora apiculata* woods of 200m wide in the offshore side from the shore line at high tide and *Pandanus odoratissimus* woods of 100mwide on the backshore. In the river, *Rhizophora apiculata* woods of 1000m long are placed on the high water channelnear the river mouth. The results of numerical simulations with and without forests suggest the possibility that the coastaland river forests can reduce the run-up not only on the coast but also in the river.

Download PDF (677K)

Application of Three-dimensional Non-hydrostatic Numerical Model to Tsunamis in Coastal Areas

Takashi TOMITA, Kazuhiko HONDA

2008 Volume 55 Pages 231-235
Published: October 10, 2008
Released: June 04, 2010

DOI https://doi.org/10.2208/proce1989.55.231

JOURNALS FREE ACCESS

Show abstract

Download PDF (1245K)

Basic Study of Effects of Mesh Division on Run-up Tsunami Simulation

Yoichi MURASHIMA, Fumihiko IMAMURA, Syunichi KOSHIMURA

2008 Volume 55 Pages 236-240
Published: October 10, 2008
Released: June 04, 2010

DOI https://doi.org/10.2208/proce1989.55.236

Environmental Hydraulics and Sustainable Water Management

Volume 1:
Environmental Hydraulics

Edited by J.H.W. Lee & K.M. Lam

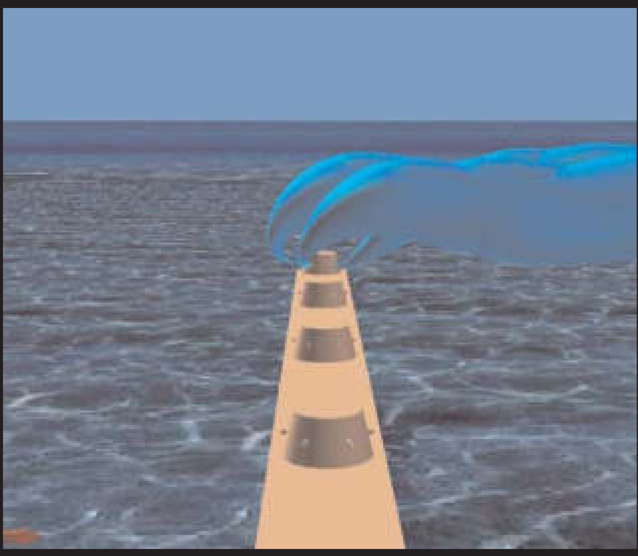

PROCEEDINGS OF THE 4TH INTERNATIONAL SYMPOSIUM ON ENVIRONMENTAL HYDRAULICS AND THE 14TH CONGRESS OF ASIA AND PACIFIC DIVISION, INTERNATIONAL ASSOCIATION OF HYDRAULIC ENGINEERING AND RESEARCH, 15–18 DECEMBER 2004, HONG KONG

Environmental Hydraulics

Edited by

J.H.W. Lee
The University of Hong Kong, China

K.M. Lam
The University of Hong Kong, China

Volume 1

A.A. BALKEMA PUBLISHERS LEIDEN / LONDON / NEW YORK / PHILADELPHIA / SINGAPORE

Taylor & Francis
Taylor & Francis Group
6000 Broken Sound Parkway NW, Suite 300
Boca Raton, FL 33487-2742

Version Date: 20140416

International Standard Book Number-13: 978-1-4822-6286-5 (eBook - PDF)

Visit the Taylor & Francis Web site at
http://www.taylorandfrancis.com

and the CRC Press Web site at
http://www.crcpress.com

8.2 Waves/coastal processes – II

8.3 Case studies/modelling

Environmental Hydraulics and Sustainable Water Management – Lee & Lam (eds)
© 2005 Taylor & Francis Group, London, ISBN 04 1536 546 5

Transformation of ship waves on a sloping coast

K.T. Dam, K. Tanimoto, N.B. Thuy & Y. Akagawa
Saitama University, Saitama, Japan

ABSTRACT: The characteristics of shoaling, refraction, and breaking are understood fairly well for ordinary wind waves and ocean swells. However, it has been not much investigated how ship waves are propagated by shoaling, refraction, and breaking on a coast. In present paper, the transformation of ship waves on a sloping coast with straight, parallel depth contours is discussed on the basis of simulated results by a 2-D numerical model. Based on numerical results, an applicable analytical formula to predict maximum wave height on the slope is introduced. In the proposed formula, the maximum wave height is the product of relative shoaling coefficient, relative refraction coefficient, relative damping coefficient, and the reference wave height defined at an appropriate distance from the sailing line. The maximum wave height estimated by the proposed method agrees well with numerical simulation results.

1 INTRODUCTION

Waves generated by navigating ships contain a massive amount of energy that can seriously damage the marine environment, degradation of coastal structures, and being responsible for nuisance or damage to beach users as well as other floating bodies. Recently, ship waves are in particular attentions of not only environmental managers, coastal and port authorities, but also naval architects as well as shipbuilders. So far, many investigations have been done with the aim to predict the characteristics of these waves as a function of ship hull geometry, ship speed, water depth, and the distance from the sailing line.

Havelock (1908) extended the work of Kelvin (1877) to show that the decay of ship waves is proportional to y^{-n}, where y is the distance from the sailing line and n is a constant value. Havelock predicted that in sub-critical speed, the divergent waves decay have an exponent of $n = 0.33$. Sorensen (1969) used model test to show that the bow wave data generally similar to this predicted rate of decay. This approach is more practical for coastal engineering purposes and results only in an additional constant in the equation. For super-critical ship speed, Kofoed-Hansen et al. (1999) suggested that the value of $n = 0.55$ can be used. Furthermore, based on experimental result, Whittaker et al. (2001) proposed the lowest value of $n = 0.2$ for shallow water.

However, the transformation due to shoaling, refraction, and breaking must be considered in addition to damping by the distance, when ship waves propagate on a sloping coast. Especially, the wakes generated by ships operating at critical and super-critical speeds, with wave heights noticeable higher, wave periods longer, and associated with shoaling and breaking, are being much more serious and complicated. To investigate how like and how different in propagation between ship waves and ordinary wind waves, in the present study, the transformation of ship waves on a coast is discussed on the basis of simulated results. The effect of shoaling, refraction, and breaking is evaluated to estimate the maximum height of ship waves. It was initially verified that, although ship waves are nonlinear and unsteady, the finite amplitude wave theory and the Snell's law can be applied to predict the maximum wave height, which is generated by a defined ship travels on a sloping coast.

2 METHOD AND RESULTS OF NUMERICAL SOLUTION

2.1 *Numerical method*

The simulation method is used to solve numerically Boussinesq-type equations (Madsen & Sørensen 1992) with a moving ship boundary (Tanimoto et al. 2000). In the coordinate system Oxy, where the origin O lies on the immobilized water-plane, the x-axis points in the direction of ship's forward motion, the y-axis pointing toward the shore, the governing equations are written as:

$$\frac{\partial \zeta}{\partial t}+\frac{\partial Q_x}{\partial x}+\frac{\partial Q_y}{\partial y}=0 \tag{1}$$

$$\begin{aligned}&\frac{\partial Q_x}{\partial t}+\frac{\partial}{\partial x}\left(\frac{Q_x^2}{D}\right)+\frac{\partial}{\partial y}\left(\frac{Q_xQ_y}{D}\right)+gD\frac{\partial \zeta}{\partial x}=\left(\beta+\frac{1}{3}\right)h^2\left(\frac{\partial^3 Q_x}{\partial t\partial x^2}+\frac{\partial^3 Q_y}{\partial t\partial x\partial y}\right)+\beta g h^3\left(\frac{\partial^3 \zeta}{\partial x^3}+\frac{\partial^3 \zeta}{\partial x\partial y^2}\right)\\&+h\frac{\partial h}{\partial x}\left(\frac{1}{3}\frac{\partial^2 Q_x}{\partial t\partial x}+\frac{1}{6}\frac{\partial^2 Q_y}{\partial t\partial y}\right)+h\frac{\partial h}{\partial y}\left(\frac{1}{6}\frac{\partial^2 Q_y}{\partial t\partial x}\right)+\beta g h^2\left\{\frac{\partial h}{\partial x}\left(2\frac{\partial^2 \zeta}{\partial x^2}+\frac{\partial^2 \zeta}{\partial y^2}\right)+\frac{\partial h}{\partial y}\frac{\partial^2 \zeta}{\partial x\partial y}\right\}+R_{bx}\end{aligned} \tag{2}$$

$$\begin{aligned}&\frac{\partial Q_y}{\partial t}+\frac{\partial}{\partial y}\left(\frac{Q_y^2}{D}\right)+\frac{\partial}{\partial x}\left(\frac{Q_xQ_y}{D}\right)+gD\frac{\partial \zeta}{\partial y}=\left(\beta+\frac{1}{3}\right)h^2\left(\frac{\partial^3 Q_y}{\partial t\partial y^2}+\frac{\partial^3 Q_x}{\partial t\partial x\partial y}\right)+\beta g h^3\left(\frac{\partial^3 \zeta}{\partial y^3}+\frac{\partial^3 \zeta}{\partial x^2\partial y}\right)\\&+h\frac{\partial h}{\partial y}\left(\frac{1}{3}\frac{\partial^2 Q_y}{\partial t\partial y}+\frac{1}{6}\frac{\partial^2 Q_y}{\partial t\partial x}\right)+h\frac{\partial h}{\partial y}\left(\frac{1}{6}\frac{\partial^2 Q_y}{\partial t\partial y}\right)+\beta g h^2\left\{\frac{\partial h}{\partial y}\left(\frac{\partial^2 \zeta}{\partial x^2}+2\frac{\partial^2 \zeta}{\partial y^2}\right)+\frac{\partial h}{\partial x}\frac{\partial^2 \zeta}{\partial x\partial y}\right\}+R_{by}\end{aligned} \tag{3}$$

Herein, $\zeta(x, y, t)$ is the water surface elevation, Q_x (x, y, t) and Q_y (x, y, t) the depth-integrated velocity components in x and y directions, respectively, t the time, h (x, y) the still water depth, D (x, y, t) is the total depth $(D=\zeta+h)$, g is the gravitational acceleration, and β is the correction factor of the dispersion term $(\beta=1/15)$.

To simulate surf zone hydrodynamics, energy dissipation due to wave breaking is modeled by introducing two additional eddy viscosity terms (R_{bx} and R_{by}) into the momentum equations (Kennedy et al. 2000), these momentums mixing terms are given as:

$$R_{bx}=\frac{\partial}{\partial x}\left(v\frac{\partial Q_x}{\partial x}\right)+\frac{1}{2}\left[\frac{\partial}{\partial y}\left(v\frac{\partial Q_x}{\partial y}\right)+\frac{\partial}{\partial y}\left(v\frac{\partial Q_y}{\partial x}\right)\right] \tag{4}$$

$$R_{by}=\frac{\partial}{\partial y}\left(v\frac{\partial Q_y}{\partial y}\right)+\frac{1}{2}\left[\frac{\partial}{\partial x}\left(v\frac{\partial Q_x}{\partial y}\right)+\frac{\partial}{\partial x}\left(v\frac{\partial Q_y}{\partial x}\right)\right] \tag{5}$$

The eddy viscosity v is defined as:

$$v=B\delta_b(h+\zeta)\frac{\partial \zeta}{\partial t} \tag{6}$$

where δ_b is a mixing length coefficient with an empirical value of 1.2. The quantity B that controls the occurrence of energy dissipation is smoothly varied from 0 to 1.0 to avoid an impulsive start of breaking (Schäffer et al. 1993).

The equations are solved by implicit finite difference techniques with the variables defined on a space staggered rectangular grid. The Alternating Direction Implicit (ADI) algorithm is used in the solution to avoid the necessity for iteration. By using the ADI method, the system of implicit finite difference equations is reduced to a tridiagonal system of equations for each grid line in the model, and then will be solved by the Double Sweep algorithms, a very fast and accurate form of Gauss elimination.

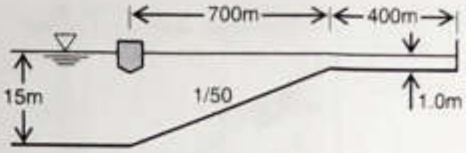

Figure 1. Cross section of computational channel.

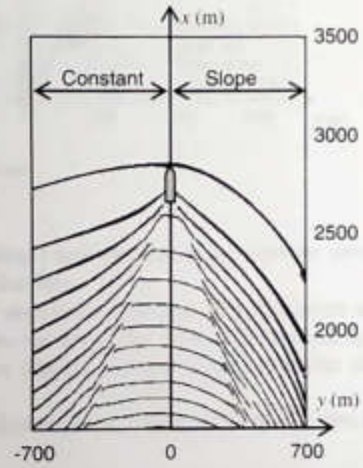

Figure 2. Top view of wave crests.

The ship considered in the present study is measured 82 m in length, 14.6 m in width, and the draft is 5.88 m. The ship, as shown in the Figure 1, is steadily traveling on an open coast with straight and parallel contours. Computational grid size in both x and y-directions are 2.5 m. The channel length is 4000 m from the ship start position. The ship is assumed to start from rest and accelerate uniformly to a final velocity. Since the main interest in the present study is the wave propagation far from the ship, therefore, a slender ship theory (Chen & Sharma 1995) is assumed to give the boundary conditions at the ship location.

The most important parameter for the characterization of ship waves in shallow water is depth Froude number. The depth Froude number (F_h) is defined as the ration of ship speed to the wave propagation speed in shallow water. In the present study, ship speed is ranged from 7.28 m/sec to 14.45 m/sec, the corresponding depth Froude numbers (F_h) from 0.6 to 1.2, respectively.

2.2 *Numerical results and discussions*

Figure 2 shows the top view of simulated waves crests for the case of critical ship speed ($F_h = 1.0$). In the figure, the darker (bigger) spot the higher elevation of wave crest. In constant water depth, the distance between waves crests increases with distance from the sailing line. In the slope side, however, this tendency is not occurred due to shoaling and refraction effects. On sloping coast, the effect of wave refraction is clearly observed in the wave pattern. It may cause the decrease in the wave height as the water depth becomes shallow. Besides, the effect of wave shoaling increases the wave height.

The largest and most energetic waves are produced at approximately $F_h = 0.95$. Wave heights are sharply increased when F_h from 0.8 to 0.95. However the decay rate of near-critical wave differs greatly from the decay rate of super-critical wave. It can be seen from these results that the maximum wave height on the sloping coast is not only dependent upon its transverse distance from

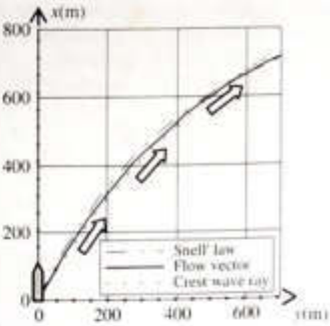

Figure 3. Wave rays on sloping coast.

the sailing line (due to wave decay) and interaction between the divergent and transverse waves, but also due to shoaling and refraction.

In constant water depth, the dominant directions of propagation are mostly alike. Meanwhile, on sloping coast, these directions (or tan β) are apparently changed according to the distance from the sailing line. The inclination (dx/dy) of wave direction on the slope can be formulated as a function of y.

With $y = 100$ m value as a reference level, based on the Snell's law, the value of tan β at a certain position is given by:

$$\tan\beta = \sqrt{\frac{\left(C/C_1 \times \sin\beta_1\right)^2}{1-\left(C/C_1 \times \sin\beta_1\right)^2}} \tag{7}$$

In which, C is wave celerity at the optional position of y. C_1 and β_1 is the reference wave celerity and wave angle at the reference location of $y = 100$ m.

Figure 3 illustrates the plotted wave rays on the slope that obtained from three different methods. The dash-dot curve is the wave ray obtained from Snell's law. The continuously dark curved line is the wave ray created from flow vectors. And the dashed curve is the wave ray that constructed from wave crest lines. As shown in the figure, these methods give almost the same result. In other words, on a gently sloping coast, ship waves refracted as same as the way the ordinary waves did. Therefore, the Snell's law can be applied for ship waves and the relative refraction coefficient K_r' is given by:

$$K_r' = \left[1+\left\{1-\left(\frac{C}{C_1}\right)^2\right\}\tan^2\beta_1\right]^{-1/4} \tag{8}$$

3 ANALYTICAL SOLUTION FOR MAXIMUM WAVE HEIGHT

3.1 *Analytical formula for maximum wave height*

To predict maximum wave height on slope, an analytical formula is proposed as follows:

$$H_{max} = K_s' \times K_r' \times K_d' \times H_1 \tag{9}$$

In which, K_s', K_r', K_d' are the relative shoaling, refraction, and damping coefficients, respectively. H_1 is reference maximum wave height at $y = 100\,\text{m}$. The relative refraction coefficient K_r' can be obtained from the Equation 8, on the basis of the Snell's law. To compute the relative shoaling coefficient K_r', the finite amplitude wave theory (Goda 1985) is used, as follows:

$$K_s' = K_s / K_{s1} \tag{10}$$

where:

$$K_s = K_{si} + \left(0.0015 \times (h/L_0)^{-2.9} \times (H_0/L_0)^{1.3}\right) \tag{11}$$

$$K_{si} = \frac{1}{\sqrt{\tanh\dfrac{2\pi h}{L} + \dfrac{2\pi h}{L}\left(1 + \tanh^2\dfrac{2\pi h}{L}\right)}} \tag{12}$$

$$L_0 = gT_1^2 / 2\pi \tag{13}$$

$$H_0 = H_1 / K_{s1} \tag{14}$$

$$L = \frac{gT_1^2}{2\pi}\tanh\frac{2\pi h}{L} \tag{15}$$

In which, g (m/s^2) is the acceleration of gravity; h (m) is still water depth at y; T_1, H_1 are reference wave period and reference maximum wave height at $y = 100\,\text{m}$.

Finally, the relative damping coefficient can be obtained from the following formula:

$$K_d' = (y/100)^{-n} \tag{16}$$

In the present study, we found that the value of $n = 0.2$ gives best agreement of the model evaluated based on analytical results.

3.2 *Comparison between analytical formula and simulation results*

Figure 4 presents the comparison between numerical simulation and analytical solution results for three cases: $F_h = 0.8$, $F_h = 1.0$ and $F_h = 1.2$. In sub-critical speed ($F_h = 0.8$), the wave height gradually decreases until slope end, this scenario is caused by combined interaction between shoaling and damping effects. On the other hand, in critical and super-critical regimes, the maximum wave height on slope reduces by the damping and refraction at first, then increases by shoaling, and finally markedly decreased after break. The relative maximum wave height from simulated result (circle mark) agrees well with the one calculated by analytical formula (thickly solid line), except in very shallow water depth. In the figure, the straight thin line indicated limited breaking wave height due to limitation of water depth, which is proposed by Goda (1985).

3.3 *Reference value of maximum wave height, wave period, and angle of wave direction*

Reference components of maximum wave height ($F_h = 1.0$, at $x = 2000\,\text{m}$, $y = 100\,\text{m}$) are presented in Figure 5. These reference components can be formulated as a function of F_h. The approximate exponential functions (which are displayed as the solid curves) are shown in the figure.

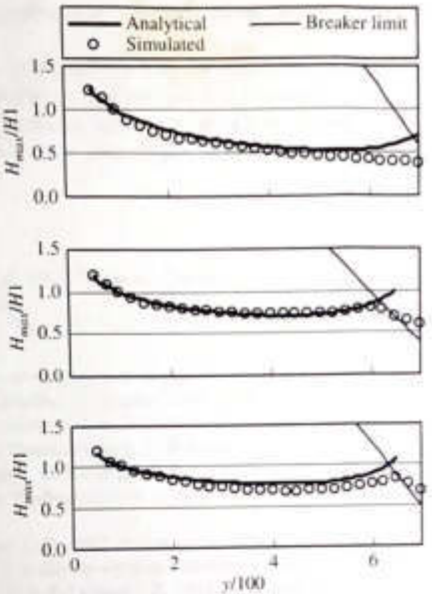

Figure 4. Simulated and analytical results.

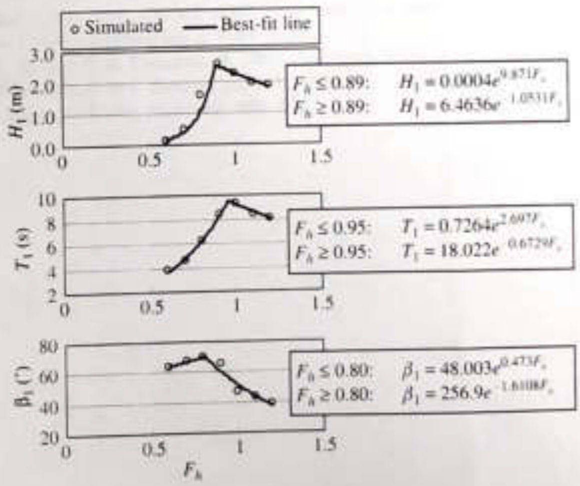

Figure 5. Reference components of maximum wave height.

4 CONCLUSIONS

Linear wave theory provides a good prediction of shoaling and refraction of ship waves. To estimate the maximum wave height on a sloping coast at a given distance from the sailing line; the proposed analytical formula (Eq. 9) can be applied. For shallow water depth, to compute the relative damping coefficient, the value of $n = 0.2$ is suggested. The relative shoaling coefficient is calculated by using the finite amplitude wave theory, and to calculate the relative refraction coefficient, the Snell's law is used.

The reference values of maximum wave components, such as: maximum wave height, wave period, and incidence angle can be formulated as a function of depth Froude number. However, to generalize the proposed formula, further investigations including lab data and field data for various ships geometric conditions (e.g. ship length, ship draft) are essentially needed.

REFERENCES

Chen, X.-N. & Sharma, S.D. 1995. A slender ship moving at a near-critical speed in a shallow channel. *J. Fluid Mechanics* 291: 263–285.

Goda, Y. 1985. *Random Seas and Design of Maritime Structures*. Tokyo: University of Tokyo Express: 41–86.

Havelock, T.H. 1908. The propagation of groups of waves in dispersive media, with application to waves on water produced by a traveling disturbance. *Proc. of the Royal Society of London* LXXXI: 398–430.

Kennedy, A.B., Chen, Q., Kirby, J. T. & Dalrymple, R. A. 2000. Boussinesq modeling of wave transformation, breaking and runup. I: One dimension. *J. Waterway of Port, Coastal and Ocean Engineering* 126: 39–47.

Kofoed-Hansen, H., Jensen, T., Kirkegaard, J. & Fuchs, J. 1999. Prediction of wake wash from high-speed craft in coastal areas. *Hydrodynamics of High Speed Craft. The Royal Institution of Naval Architects London*: 1–10.

Madsen, P.A. & Sørensen, O.R. 1992. A new form of Boussinesq equations with improved linear dispersion characteristics – Part 2: A slowly-varying bathymetry. *Coastal Engineering* 18: 183–204.

Schäffer, H. A., Madsen, P. A. & Deigaard, R. 1993. A Boussinesq model for waves breaking in shallow water. *Coastal Engineering* 20: 185–202.

Sorensen, R.M. 1969. Waves generated by model ship hull. *J. Waterways, Harbours Division, Proc. of the American Society of Civil Engineering* 95 (No. WW4): 513–538.

Tanimoto, K., Kobayashi, H. & Ca, V.T. 2000. Ship waves in a shallow and narrow channel. *Proc. of 27th Conference on Coastal Engineering* 2: 1141–1154.

Whittaker, T.J.T., Doyle, R. & Elsaesser, B. 2001. An experimental investigation of the physical characteristics of fast ferry wash. *In V. Bertram (Editor), HIPER'01 2nd International Euro Conference on High Performance Marine Vehicles, Hamburg*: 480–491.

GIAI ĐOẠN SAU KHI BẢO VỆ LUẬN ÁN TIẾN SĨ (17/09/2010)

4. TẠP CHÍ QUỐC TẾ (7)

geosciences

MDPI

Article

Monsoon-Induced Surge during High Tides at the Southeast Coast of Vietnam: A Numerical Modeling Study

Nguyen Ba Thuy [1,*], Tran Quang Tien [1], Cecilie Wettre [2] and Lars Robert Hole [2]

1 Vietnam National Hydrometeorolocical Forecasting Center, No. 8 Phao Dai Lang, Dong Da, Hanoi, Vietnam; tqt.quenha@gmail.com
2 Division of Oceanography and Maritime Meteorology, Norwegian Meteorological Institute, Bergen, Norway; ceciliew@met.no (C.W.); lrh@met.no (L.R.H.)
* Correspondence: thuybanguyen@gmail.com; Tel.: +84-4-3267-3199 (ext. 708)

Received: 26 September 2018; Accepted: 21 January 2019; Published: 31 January 2019

check for updates

Abstract: In this study, monsoon-induced surge during high tides at the Southeast coast of Vietnam was analyzed based on the observed tide data at the Vung Tau station in the period between 1997—2016. Specifically, the surge was determined by removing the astronomical tide from the observed total water level. The two-dimensional Regional Ocean Model System (ROMS 2D) was applied to simulate the surge induced by monsoons during spring tide. The surge observations showed that the change of peak surge did not follow a clear trend, of either an increase or decrease, over time. A peak surge of over 40 cm appeared mainly in October and November, although the peak of the astronomical tide was higher in December. ROMS 2D was validated with the observational data, and the model could sufficiently reproduce the wind-induced surge during high tides. This study therefor ere commends for ROMS 2D to be used in operational forecasts in this area.

Keywords: spring tide; surge; monsoon; ROMS 2D

1. Introduction

Compared with other coastal areas in Vietnam, the Southeast coast is less affected by natural hazards coming from the sea such as storms and tropical low pressure systems. However, the region has certain geographical characteristics such as low plains and a large estuary system which make this area vulnerable to increased sea levels during spring tide (Tuan, 2000) [1]. This phenomenon has become more and more intense as the weather has become more variable in recent years; the maximum daily rainfall trend is increasing and the frequency of monsoons is rising on the South coast of Vietnam (e.g., Tan and Thanh, 2013) [2].

Seawater intrusion is dependent on the thetidal regime in coastal estuarine areas and the surge due to winds caused by tropical depressions and typhoons. The observed sea level ($H_{observed}$) is the sum of astronomical tide (H_{tide}) and surges (H_{surge}) due to other factors, mainly typhoons, low pressure zones, or strong monsoons ($H_{observed} = H_{tide} + H_{surge}$). In the coastal areas of the Southeast, the phenomenon of flooding during high tide (spring tide) occurs frequently from October to February; these are months with high tide amplitudes. In addition, these are the months when the activities of storms, tropical low pressure systems, and strong monsoon sareat the highest (Du et al., 2016) [3]. In recent years, the spring tides in Ho Chi Minh City have caused serious flooding in many parts of the city, affecting life and productivity. In November 2010, the high tide samplified, causing the entire 252 km east and west coastal line of Ca Mau province to be flooded up to 0.5m in depth for periods of about 2–3 h per day, as shown in Figure 1a (Minh and Lan, 2012) [4]. The spring tide in October 2013 caused a historic rise in water level at Vung Tau station (420 cm). Seawater intruded into Ho Chi Minh City, causing serious flooding for several days (Figure 1b) (Minh and Lan, 2012) [4].

(a) (b)

Figure 1. Flooding due to spring tides in the South province of Vietnam. (**a**) The center of Ca Mau province at the spring tide in 31 October 2010. (**b**) Ho Chi Minh City during the historic spring tide in 26 October 2011.

In addition to the astronomical tide and the flooding caused by rain, it is possible that the flooding in Ho Chi Minh City had a significant contribution from the monsoon-induced surge. Consequently, there is significant motivation to study the monsoon-induced surge in combination with the spring tide in this area.

For several decades, climate change impact studies have focused on storm surge studies in Vietnam (e.g., Sao, 2008; Thang, 1999; Thuy, 2003; Chien et al., 2015; Thuy et al., 2014) [5–9]. Conventional two-or three-dimensional nonlinear shallow water equations have been used. However, the monsoon-induced surge has not been subject to much study, especially not in terms of numerical modeling. According to research by Ninh et al., in addition to typhoons, the monsoons also caused significant storm surges and, during strong monsoons (winds of force 6–7 on the Beaufort scale) with a duration of 2 to 3 days, significant surge heights of about 30–40 cm, sometimes higher, occurred [10]. Based on the analysis of water levels for many years at the tidal stations in Vietnam, Thanh [11] showed that in addition to astronomical tide fluctuations, there are fluctuations of sea levels in coastal areas and islands where the duration of the rise and fall is mainly influenced by the wind regime, especially in the Northeast monsoon season. The majority of the observed fluctuations have an amplitude of less than 50 cm; however, the magnitude of the rise due to monsoon winds can reach 30–40 cm (Thanh, 2011) [11]. When assessing the after-runner storm surge due to typhoon Kalmaegi (2014) which landed on coastal Hai Phong (Northern Vietnam), Thuy et al. [12] concluded that the strong Southwest monsoon is the main cause for this phenomenon. Analyzing two historic spring tide phases in Ho Chi Minh City in October 2010 and November 2011, Minh and Lan [4] concluded that the spring tide in Ho Chi Minh city was related to the strong Northeast monsoon. The main cause of the high sea levels, was due to high waves generated by strong winds that pushed water into the river mouths on the high tide days, resulting in an abnormal sea level rise.

In this study, the monsoon-induced surge in the spring tide phases at the Southeastern coast of Vietnam was analyzed based on water level observations at the Vung Tau station. Next, wind-induced surge in two spring tide phases was simulated by a numerical model. A harmonic analysis method was applied to remove the astronomical tide from the observed water level in order to determine the surge. The Regional Ocean Model System in 2D (ROMS 2D) was applied to simulate monsoon-induced surge on the coast in order to evaluate the model's ability to forecast surges in the area.

2. Materials and Methods

2.1. Study Area and Data

In the study area, tidal cycles are semidiurnal, and tidal amplitudes tend to decrease from the northern coast of the Province of Binh Thuan to the southern coast of the Province of Ca Mau, as shown in Figure 2. The largest tidal amplitudes from Binh Thuan to Ca Mau are approximately 300–400 cm. There is only one tide station setup at Vung Tau. The location of the station is at longitude 107°04′ and latitude 10°20′ (Figure 2). The datum of tide observation is at the lowest tide in one tide circle (18.6 years).

Figure 2. The study area and location of Vung Tau station.

To analyze the water level and surge height in the study area, the observed water levels at Vung Tau station over 30 years (1987–2016) were collected. To evaluate the capability of ROMS 2D to predict surges generated by monsoons, the wind and pressure re-analyses from the European Centre for Medium-Range Weather Forecasts (ECMWF) were used as inputs for the monsoon-induced surge prediction model.

2.2. Research Method

2.2.1. Harmonic Analysis of Astronomical Tide

The surge height was determined by subtracting the astronomical tide from the observed water level (total water level) according to the following formula:

$$\mathrm{H_{surge}} = \mathrm{H_{observation}} - \mathrm{H_{tide}} \tag{1}$$

where $\mathrm{H_{surge}}$ is the surge height, $\mathrm{H_{observation}}$ is the total water level height, and $\mathrm{H_{tide}}$ is the astronomical tide height.

The harmonic analysis method was used to estimate the astronomical tide. In this method, the tide height z at any time t is the sum of the tidal oscillations of the component (called tidal waves):

$$z_t = A_0 + \sum_{i=1}^{r} f_i H_i \cos[q_i t + (V_0 + u)_i - g_i] \tag{2}$$

where A_0 is the average water level, f_i is the coefficient of variation of the tidal component i, H_i is the harmonic constant of the tidal component i, q_i is the constant angle of the tidal component i, $(V_0 + u)_i$ shows astronomical parts of angle of component i which represents the time angle of the assumed astronomical object at time t, g_i is the harmonic constant of angle of component i, and r is the number of components. f_i and $(V_0 + u)_i$ are time dependent (t). When we have the observed water level z_t, the task of tide analysis is to determine the set consisting of harmonic constants H and g for each tidal component of the station.

To analyze the tide components, one year of tide gauge data from Vung Tau station was used to obtain the amplitude and phase of 68 tidal constituents.

2.2.2. The ROMS 2D Ocean Model

ROMS is a regional ocean model and was developed by Rutgers University, the University of California (USA) and contributors worldwide [13]. As an open source model, ROMS is widely used for a diverse range of applications over a variety of spatial regions and time periods, from the coastal strip to the world's oceans on multiple time scales. ROMS is based on the latest advanced numerical methods and is best applied to mesoscale systems or those systems that can be mapped at high resolution such as at 1 km to 100 km grid spacing. The model solves hydrodynamic equations for free-surface waters with complex bottom terrain on a horizontal orthogonal curve system and integrated topography in the vertical direction. Tides are introduced in the model by prescribing, in all grid cells, the elevation induced by the harmonic constituents. The harmonic constituents are taken from the model TPXO 7.2 [14], provided by Oregon State University, that predicts tidal levels for thirteen constituents of eight primary (M2, S2, N2, K2, K1, O1, P1, Q1), two long period (Mf, Mm), and three non-linear (M4, MS4, MN4) harmonic constituents on a 1440 × 721, 1/4 degree resolution full global grid. To focus on the monsoon-induced surge in this study and for calculation speed, the 2D version of ROMS was chosen.

Our numerical simulation domain covers the whole South China Sea: −2.5–26° N, 97.0–125.0° E (Figure 3a). The curved grid is constructed with 498 × 498 gridlines with a resolution that varies in the direction of longitude from 2.6 to 6.6 km and in the direction of latitude from 3.7 to 8.0 km, following the detailed trend of the coast (Figure 3b). The General Bathymetry Chart of the Ocean (GEBCO) of the British Ocean Data Center was used to extract the bathymetry for offshore domains. Coastal topography maps with scales of 1/100,000 published by the Vietnam Administration of Seas and Islands were used for the domain details near the coast (Thuy et al., 2017) [9]. A time step of 10 s was selected for simulations in the case of both the tide-only and for the case of combined surge and tide.

The wind and pressure used in ROMS 2D were retrieved from there-analysis product ERA Interim as provided by the European Centre for Medium-range Weather Forecasts (ECMWF) with wind at 10m and atmospheric pressure at the sea surface in Network Common Data Form (NetCDF) format, with a global resolution of0.125° × 0.125° at 6-hourly intervals [15]. ROMS 2D interpolates the wind and pressure data to the orthogonal congruent coordinate system corresponding to the time step of the modeling time.

The wind stress τ_S is usually estimated by the following equation:

$$\tau_S = \rho_a C_D \vec{U}_{10} \left| \vec{U}_{10} \right| \quad (3)$$

where ρ_a is the density of air, C_D is the drag coefficient, and $\vec{U}_{10}$ is the wind speed (m/s) at 10 m height. For monsoon-induced surge simulations, the formula for C_D from Large and Pond [16] is as follows:

$$C_D = \begin{cases} 1.2 \times 10^{-3} \text{ for } 4 < U_{10} < 11 \text{ ms}^{-1} \\ 10^{-3}(0.49 + 0.065U_{10}) \text{ for } 11 < U_{10} < 25 \text{ ms}^{-1} \end{cases} \quad (4)$$

This algorithm has been used in many studies, such as in Dorman et al. [17], Samelson et al. [18], and Koracin et al. [19], and in particular for studies of storm surge in the South China Sea (Penget et al. [20] and Biet et al. [21]).

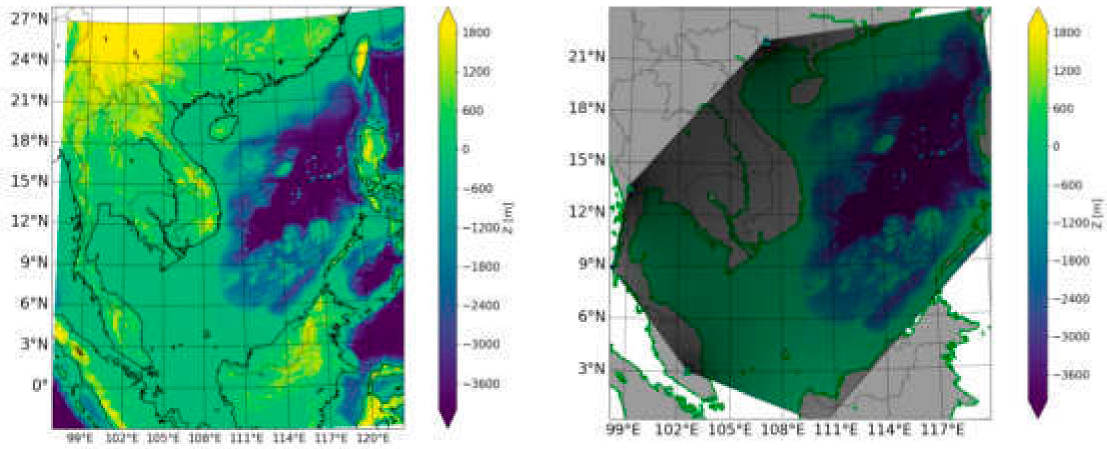

(a) (b)

Figure 3. (**a**) The domain of the grid and bathymetry. (**b**) Grid for the South China Sea and coastal areas of Vietnam.

3. Results and Discussion

3.1. Astronomical Tide and Total Water Level at the Southeast Coast of Vietnam

Figure 4 shows the peak astronomical tide of the months in 2016 and the peak of observed water levels at Vung Tau station in the period of 1987–2016. The highest of peak astronomical tides are in the months of January, February, March, October, November, and December. In this region, the main activities of typhoons, tropical depressions, and Northeast monsoons are also concentrated in these months. Therefore, in the first and last months of the year, the total water level will be high due to a combination of astronomical tides and the surges, as also shown in Figure 4. Figure 4 also shows that even though the peak of astronomical tide was smaller in October and November than in December, the total water level was higher. The Southeast coast consists of low land regions with a very gentle slope where a rise of only tens of centimeters of water level can significantly increase the risk of flooding and salt water intrusion. Note that the inundation height (Figure 5) corresponding to warning level III in this area is 400 cm. Because of the potentially serious impact of monsoon-induced surge, this study will therefore focus on the months from October to February.

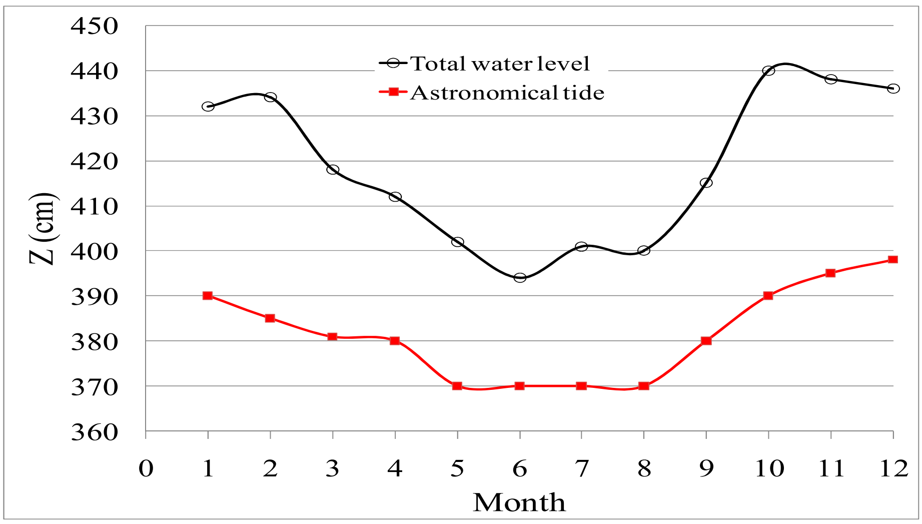

Figure 4. The peak astronomical tide of month in 2016 and maximum observed water level in the period 1987–2016.

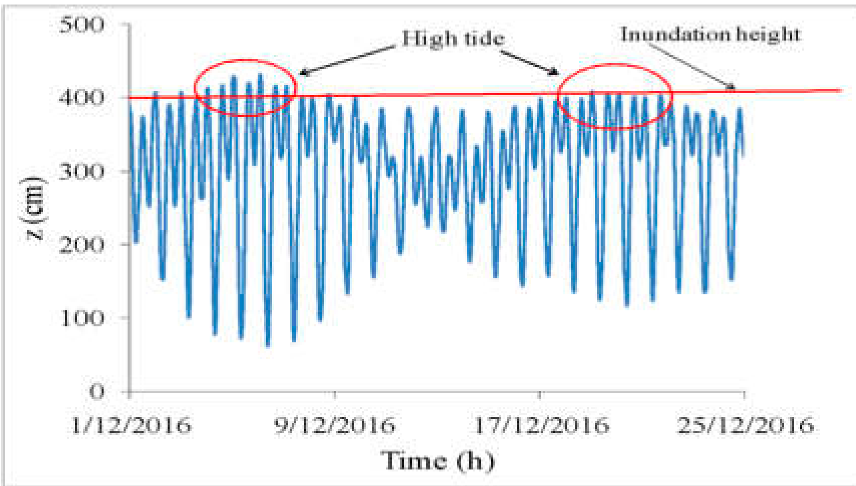

Figure 5. Time profile of water level variation at Vung Tau station in December 2016.

In general, at Vung Tau station, there are two spring tide phases in a month. This is illustrated in Figure 5, where the time profile of observed water levels in December 2016 is shown. Therefore, this study mainly focuses on the analysis of the surge during the spring tide days.

3.2. Surge Induced by Monsoon and Tropical Cyclones in the Southeast Coast of Vietnam

The surge height induced by monsoons and tropical cyclones was determined by subtracting the astronomical tide from the observed water level on all days of high tide. Figure 6a shows a time series of the observed water levels, astronomical tides, and surges in the last days of October and early November 2010. This is the time when the highest water was recorded at Vung Tau station. Changes in observed water level and surge show that even on days that were not high tide days, wind-induced surge contributed a considerable part of the rise in total water level extremes. The observed water levels, astronomical tides, and surge heights in the case of typhoon Linda's landfall in November 1997 are shown in Figure 6b. Although the typhoon did not make landfall on the days with the highest astronomical tides, the storm surge height of about 45 cm contributed to a peak of total water reaching up to 420 cm.

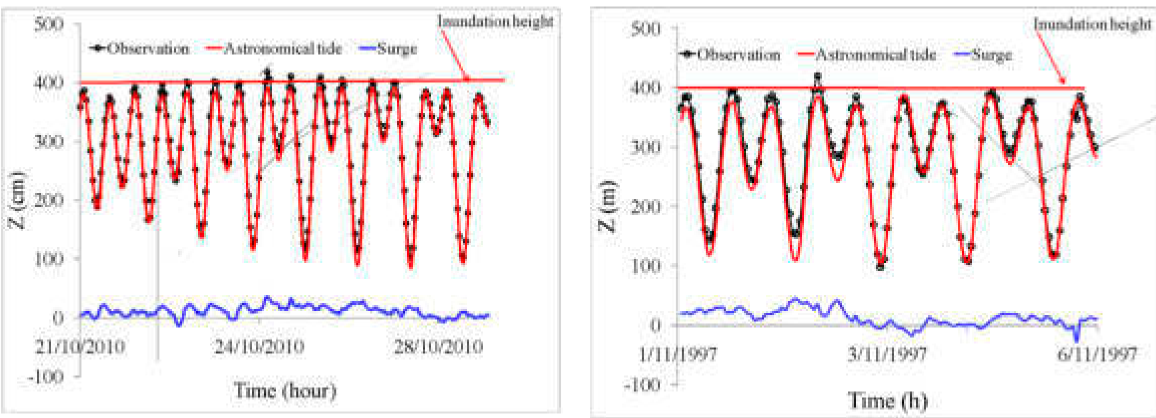

(a) (b)

Figure 6. Time series of observed water levels, astronomical tides and surges in Vung Tau (**a**) during spring tide phase in late October and early November 2010 and (**b**) during typhoon Linda (November 1997).

Figure 7a–e shows the highest of the peak surges at Vung Tau station during the spring tide days in January, February, October, November, and December in the period of 1987–2016.A frequency analysis of the surge levels over 30 years was carried out as shown in Table 1. Based on the results of the analysis, some comments on the surge height at Vung Tau station during this period are as follows:

1. The surge heights do not follow a clear trend with regards to the time of increasing or decreasing heights.
2. Surge levels of 20 to 30 cm are predominant on the coasts, comprising 39.5% of the total number, followed by surge heights of less than 20 cm. Surge heights of over 40 cm occurred mainly in October and November in which the highest surge of 54 cm occurred in November 1995. This is the reason why, in October and November, although the peak tide was smaller than in December, the total water level was higher than in December.

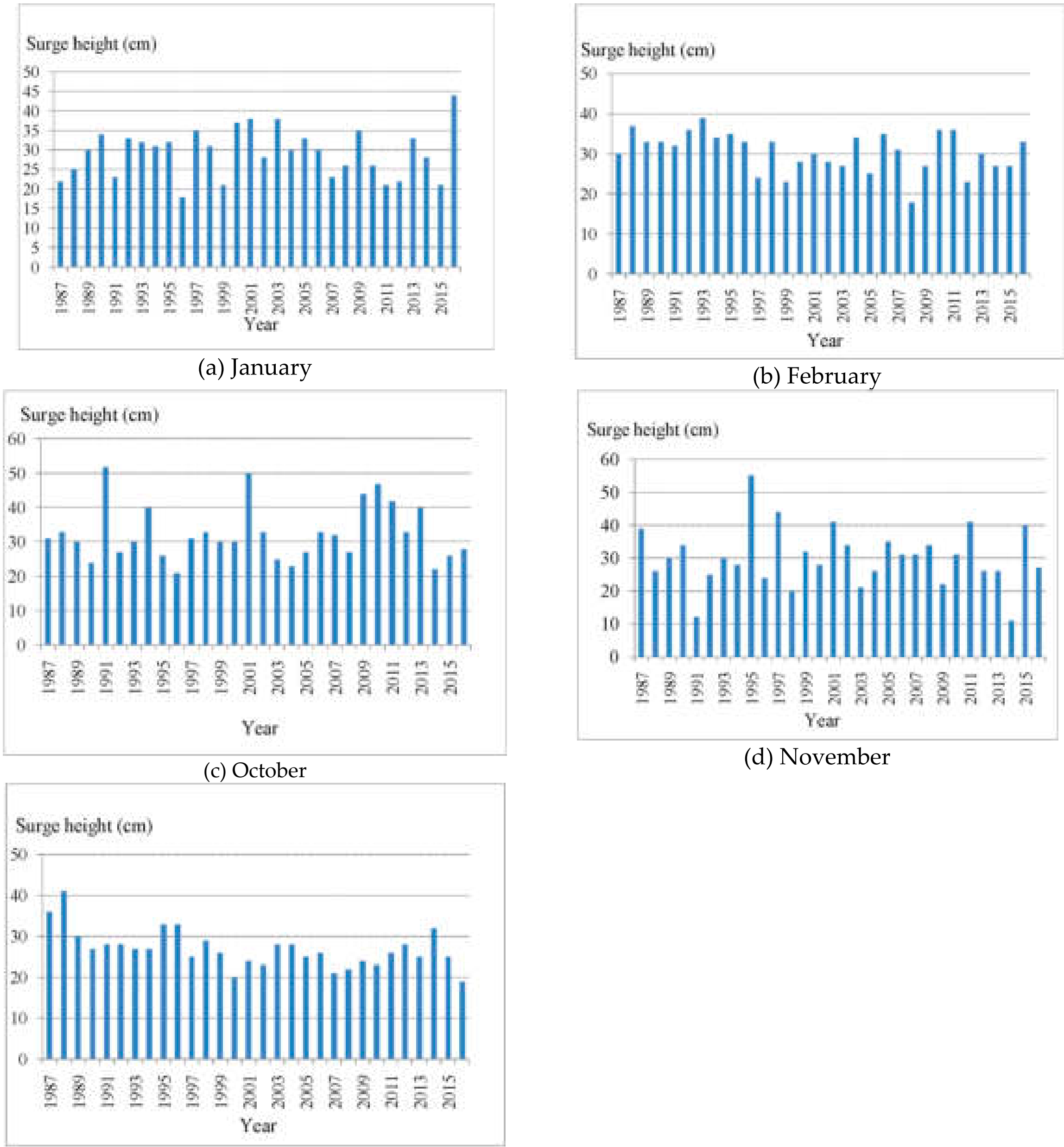

(a) January (b) February (c) October (d) November (e) December

Figure 7. Surge heights at Vung Tau station in 1987–2016. (**a**) January, (**b**) February, (**c**) October, (**d**) November and (**e**) December.

Table 1. Frequency of surge levels in Vung Tau station in 1987–2016.

Surge Height (cm)	Frequency	Percentage (%)
$H_{ND} < 20$	159	42.7
$20 \leq H_{ND} < 30$	147	39.5
$30 \leq H_{ND} < 40$	52	13.9
$H_{ND} > 40$	14	3.7

The analysis of astronomical tide, total water level, and surge at Vung Tau station shows that in the Southeast coast of Vietnam, the largest surges occur between October and February. This area is less affected by typhoons and tropical low pressure systems, so the monsoon-induced surges are very significant. The contribution of the monsoon-induced surge will increase the total water level and consequently increase the impact of total water level on the low-lying terrain. Since the terrain is low and flat, it means that only a small increase in water level will have the potential to increase the inundation and salt intrusion in the area. Therefore, being able to predict the monsoon-induced surge in the spring tide phases in this coastal area becomes very important. The forecasting of monsoon-induced surges needs to be implemented in a numerical prediction model, and the model needs to be validated prior to use for operational forecasting. The validation of the numerical model for predicting monsoon-induced surges is presented in the section below.

3.3. Results of Simulations of Monsoon-Induced Surgeduring Spring Tides in the Southeast Coast of Vietnam

3.3.1. Validation of the Numerical Model for Tide

First, the model needs to be verified and validated for tide in the study area. Figure 8 shows the comparison of the tides calculated by ROMS 2D for three values of the Manning coefficient (n = 0.02, 0.023, and 0.028) with harmonic analysis data at Vung Tau station in July 2016. Note that in this case, the datum is at the mean sea level, and the two methods used the same thirteen tide constituents. A roughness coefficient of 0.023 gives the smallest error between numerical results and the harmonic analysis data. By using this coefficient, the numerical model was validated for April and November 2016. The results in Figure 9a,b shows that the model simulates both the phases and the tide amplitudes quite well, with maximum errors of around 44 cm (37 cm).Typical values for Root Mean Square Error (RMSE) are 19 cm (17 cm), and the correlation index is 0.93 (0.95) for April (November).Therefore, the roughness coefficient obtained from the tidal validation will be used in the simulation of monsoon-induced surge below.

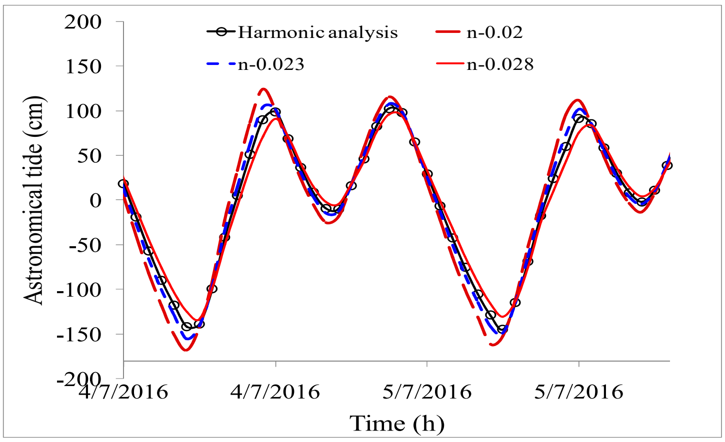

Figure 8. Comparison of tides predicted by two-dimensional Regional Ocean Model System (ROMS 2D) for three values of the Manning coefficient (n) with harmonic analysis at Vung Tau station in July 2016.

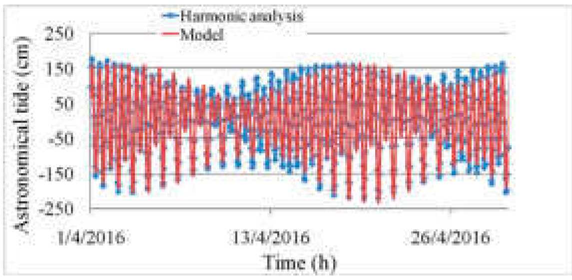

(a)

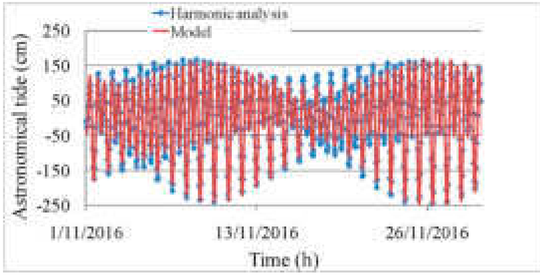

(b)

Figure 9. Comparison of tides predicted by ROMS 2D with harmonic analysis at Vung Tau in (**a**) April 2016 and (**b**) November 2016.

3.3.2. Validation of the Numerical Model for Surge Induced by Monsoon

In order to evaluate the capability of ROMS 2D in predicting monsoon-induced surge in the Southeast coast of Vietnam, we selected the days of two recorded spring tide phases, one at the end of October and early November 2010 and one at the end of October 2013. We conducted two sets of numerical simulations: one of tide-only and one of surge with tide. As shown in Figure 10, firstly, the case of surge with tide was simulated. Secondly, the tide-only simulation was conducted to extract the surge level, taking into account the surge and tide interaction as follows: $H_{surge} = H_{surge+tide} - H_{tide}$. Finally, the surge was computed at the mean sea level.

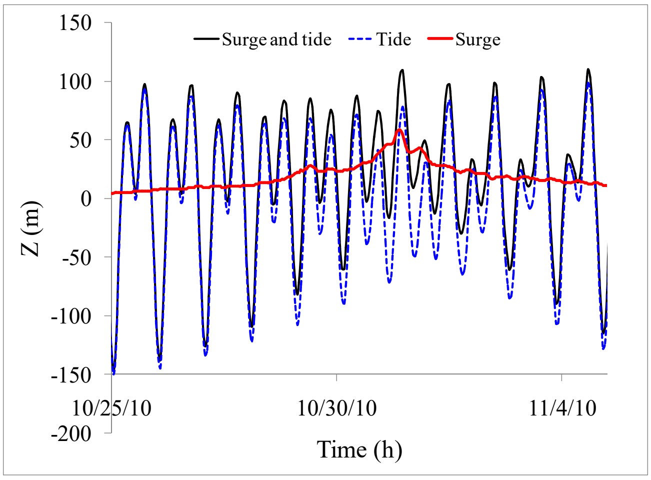

Figure 10. Time series of calculated only tides (“Tide”), surges coupled with tides (“Surge + Tide”), and surges with "Tide" extracted from “Surge + Tide” at Vung Tau station during the period of 25 October to 4 November 2010.

Monsoon-Induced Surges during the Spring Tide in Late October and Early November 2010

During this spring tide phase, the sea level started to rise from 29 October to end on 1 November 2010. There were several times when the surge height was over 40 cm; the highest was 47 cm at 08:00 on 30 October 2010. Figure 11a,b shows the wind and pressure re-analysis field at 07:00 on 27 October (Figure 11a) and at 07:00 on 31 October 2010 (Figure 11b). During this time, the Northeast monsoon came far to the south and the wind speed increased to level 6–7 on the Beaufort scale (10–18 m/s) on 31 October. The high wind speed and long duration led to the generation of large and persistent water rises in this high tide period, which resulted in the inundation of many areas along the Southeast coast, including Ho Chi Minh City, located 40 km from the coast.

The simulation of surge induced by strong winds from 25 October to 3 November 2010, shows that the maximum surge height in this area is up to 70 cm on the Southeastern coast of Vung Tau

(Figure 12). In order to establish a comparison, the frequency of the simulated data was changed from 10 s (time step of the model) to one hour (period between two measurements). The comparison of surge heights calculated by model and observations at Vung Tau station are shown in Figure 13. The maximum errors were around 28 cm, and typical values for RMSE were 10 cm with a peak surge of 7 cm.

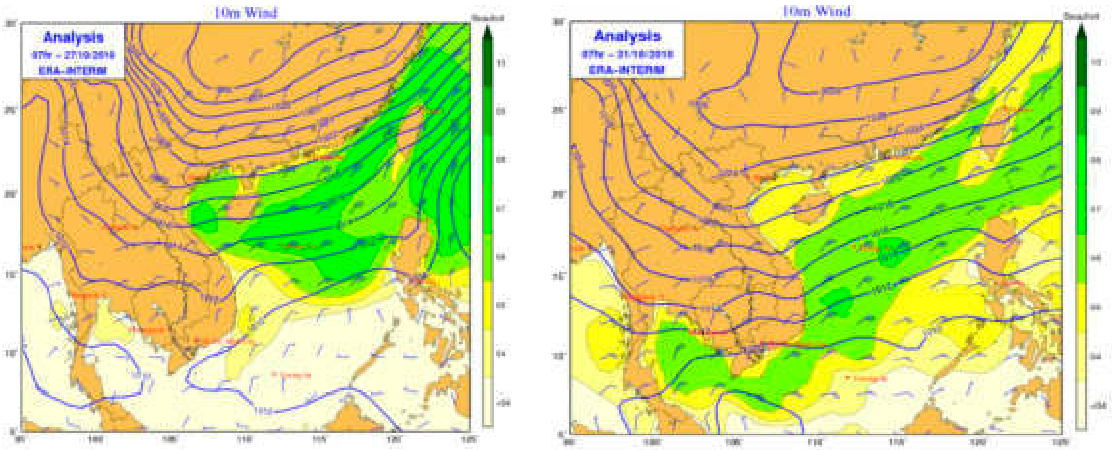

(a) (b)

Figure 11. Wind and pressure re-analyzed on (**a**) 27 October 2010 and (**b**) 29 October 2010.

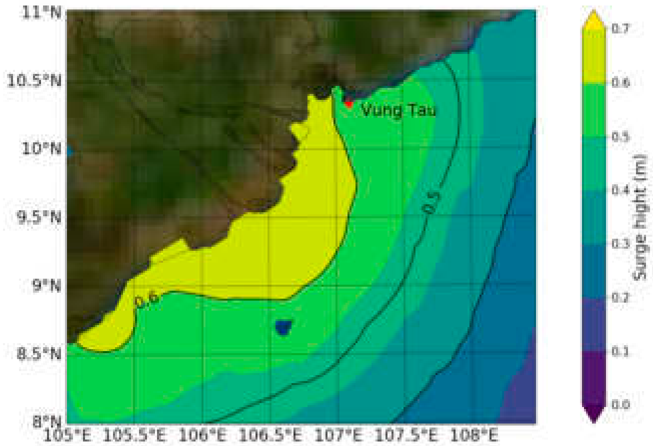

Figure 12. Maximum surge height due to monsoon during 25 October to 3 November 2010.

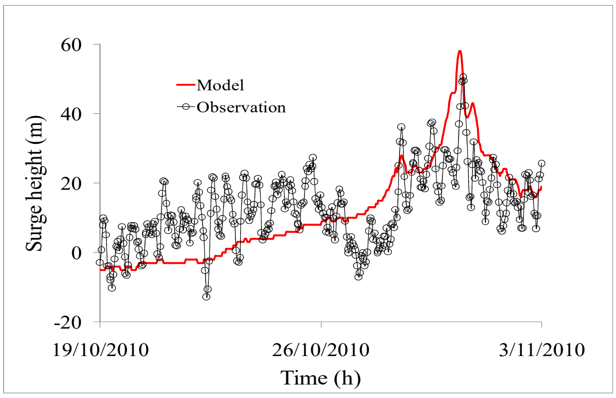

Figure 13. Comparison between numerical and observed surge heights at Vung Tau station during 25 October to 3 November 2010.

Monsoon-Induced Surges during the Spring Tide in October 2013

The second spring tide phase used for the numerical validation was on the dates at the end of October 2013. A historic high tide was recorded in Ho Chi Minh City, with a maximum water level at Vung Tau station of 420 cm, which was over the threshold inundation depth at the area. At that time, the Northeast monsoon came far to the South, as illustrated by the re-analysis of wind and pressure (Figure 14a,b). Strong winds and high tide combined with heavy rain were the cause of record flooding in the Southeast coast of Vietnam. Figure 15 shows the spatial distribution of the peak surge levels simulated by the ROMS 2D model. The maximum surge level reached up to 0.7 m on the coastal areas. The results of the series of simulations are shown in Figure 16, which presents comparisons between observations (OBS-Surge) and calculations (Model-Surge) at Vung Tau station. From the results, a similar tendency was found between model and observation, although the values for RMSE were 18 cm and errors of peak surge were 17 cm.

The errors of surge simulation may come from two sources: (1) insufficient resolution of wind field re-analysis; and (2) the surge height, in the case of monsoon, was not high, and there was noise from analyzed surge observation data. Despite this fact, the model can be used for forecasting the surge height during the monsoon.

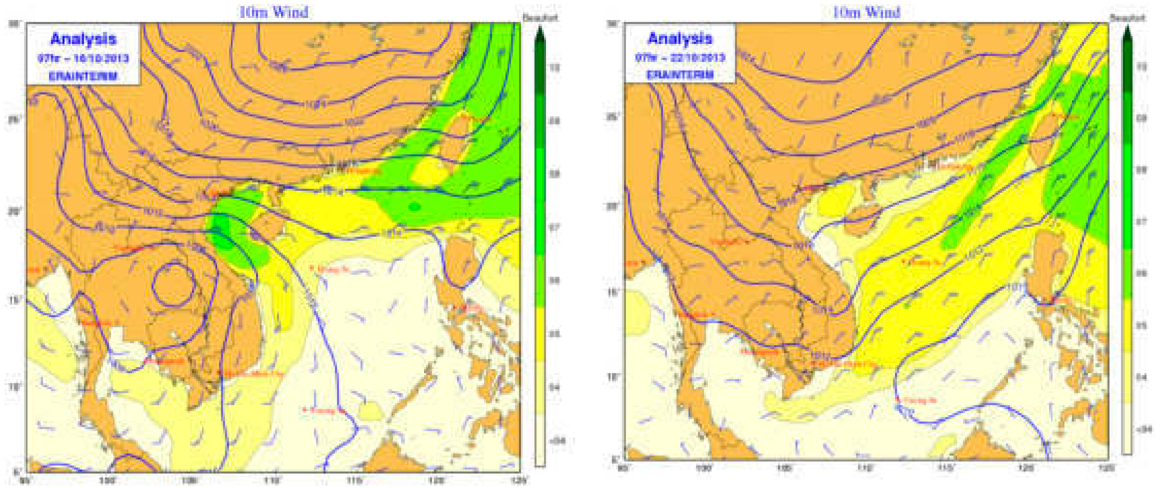

(a) (b)

Figure 14. Wind and pressure re-analyzed on (**a**) 16 October 2013 and (**b**) 22 October 2013.

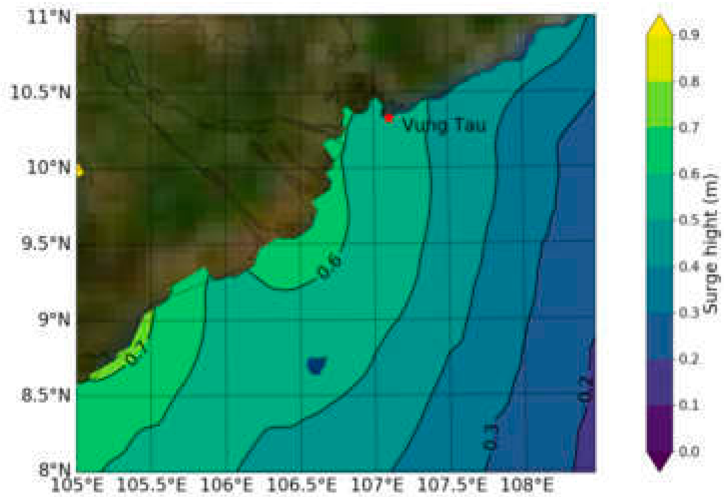

Figure 15. Maximum surge during 16–26 October 2013.

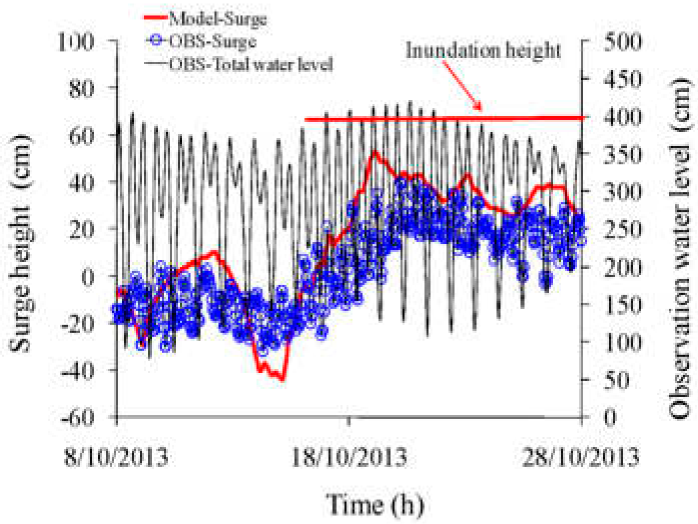

Figure 16. Comparison between numerical and observed surge heights at Vung Tau station during 16–28 October 2013.

4. Conclusions

The Southeast coast of Vietnam has a dense population and many important economic facilities along its coastline, which are vulnerable to storm surges due to the low plains and a large estuary system. High sea levels are possible during the strong Northeast monsoon surges (October–February) if they coincide with spring tides. This would usually lead to floods in the coastal areas. In this study, the monsoon-induced surge during spring tides in the Southeast coast of Vietnam was analyzed based on observed tides at the Vung Tau station. In particular, the surge was determined by removing the astronomical tidal oscillations from the observed water level. A harmonic analysis was used to calculate the astronomical tide. The observed water level data over 30 years (1987–2016) was collected for analysis. Next, ROMS 2D was used to simulate the surge heights in two spring tide phases in order to assess the capacity of the model to simulate surge height. The main results are summarized as follows:

1. The change of peak surges does not show a clear trend.
2. Surge levels of 20 to 30 cm are predominant on the coasts, comprising 39.5% of the total number. Peak surge heights over 40 cm occurred mainly in October and November. This is a reason why most of the high spring tide in this area occurred in October and November even though the peak tide was smaller than in December.

ROMS 2D implemented for the South Coast of Vietnam has reproduced relatively well the wind-induced surge during high tides. Therefore, we conclude that it is possible to apply this model for the operational forecast of monsoon-induced surges in this area.

In this study, monsoon-induced surge at the shore line has been considered. A very interesting subject to be considered for future research would be to use a coupled river and ocean model in order to investigate the effect of river conditions on surges in addition to the coastal and river site inundation.

Author Contributions: N.B.T. and T.Q.T. collected field data and analyses. N.B.T, L.R.H. and C.W. developed the study design. L.R.H. and C.W. provided expert knowledge used in data analysis and interpretation. All co-authors contributed to the writing of the manuscript.

Acknowledgments: This research is funded by Vietnam National Foundation for Science and Technology Development (NAFOSTED) under grant number 105.06-2017.07 (method and numerical model) and by the Ministry of Science and Technology of Vietnam under grant number ĐTĐL-C.35/15 (re-analyses and tide data), and partially funded by the Norwegian Agency for Development Cooperation (NORAD; Hole and Wettre), which the authors gratefully acknowledge.

Conflicts of Interest: The authors declare no conflict of interest.

References

1. Tuan, L.A. Hydro-Meteorology on the Plain in Mekong River. Ph.D. Thesis, Can Tho University, CanTho, Vietnam, 2000.
2. Tan, P.V.; Thanh, N.D. Climate Change in Vietnam: Some Research Findings, Challenges and Opportunities in International Integration. *Vietnam Natl. Univ. J. Sci.* **2013**, *29*, 42–55, (In Vietnamese, Abstract in English).
3. Du, D.T.; Hole, L.R.; Tran, A.D.; Hoang, D.C.; Thuy, N.B. Verification of forecast weather surface variables over Vietnam using the National Numerical Weather Prediction System. *Adv. Meteorol.* **2016**, *2016*. [CrossRef]
4. Minh, P.T.; Lan, L.T.X. Analyze the spring tide in Ho Chi Minh City from 2006 to 2011. *Sci. Tech.-Meteorol. J.* **2012**, *347*, 26–30. (In Vietnamese)
5. Sao, N.T. Storm surge predictions for Vietnam coast by Delft3D model using results from RAMS model. *J. Water Resour. Environ. Eng.* **2008**, *23*, 39–47.
6. Thang, N.V. Building Scheme for Storm Surge Prediction in Hai Phong Coastal Zone. Ph.D. Thesis, Vietnam Institute of Meteorology, Hydrology and Environment, Hanoi, Vietnam, 1992.
7. Thuy, V.T.T. Storm surge modeling for Vietnam's coast. Master's Thesis, Delft Hydraulic, Delft, The Netherlands, 2003.
8. Chien, D.D. Researching the Scientific Basis to Assess the Storm Surge in the Sea Areas from Quang Binh to Quang Nam. Ph.D. Thesis, University of Science-Vietnam National University, Hanoi, Vietnam, 2015.
9. Thuy, N.B.; Cuong, H.D.; Tien, D.D.; Chien, D.D.; Kim, S.Y. Assessment of changes in sealevel caused by Typhoon No. 3 in 2014 and forecast problems. *Sci. Tech.-Meteorol. J.* **2014**, *647*, 16–20. (In Vietnamese)
10. Ninh, P.V.; Quynh, D.N.; Manh, D.V. *Surge Induced by Strong Monsoon*; Project of 48B.02.02; Institute of Mechanics-Vietnam: Hanol, Vietnam, 1991.
11. Thanh, H.T. The Variation of Sea Level in Coastal Zone of Vietnam. Ph.D. Thesis, Institute of Meteorology, Hydrology and Environment, Hanoi, Vietnam, 2011.
12. Thuy, N.B.; Sooyoul, K.; Chien, D.D.; Dang, V.H.; Cuong, H.D.; Wettre, C.; Hole, L.R. Assessment of Storm Surge along the Coast of Central Vietnam. *Coast. Res. J.* **2017**, *33*, 518–530. [CrossRef]
13. Regional Ocean Modeling System (ROMS). Available online: www.myroms.org (accessed on 20 July 2017).
14. TPXO Global Tidal Solutions. Available online: http://volkov.oce.orst.edu/tides/ (accessed on 20 July 2017).
15. ERA-Interim. Available online: https://www.ecmwf.int/en/forecasts/datasets/archive-datasets/reanalysis-datasets/era-interim (accessed on 3 January 2018).
16. Large, W.G.; Pond, S. Open Ocean Momentum Flux Measurements in Moderate to Strong Winds. *J. Phys. Oceanogr.* **1981**, *11*, 324–336. [CrossRef]
17. Dorman, C.E.; Holt, T.; Rogers, D.P.; Edwards, K. Large-scale structure of the June–July 1996 marine boundary layer along California and Oregon. *Mon. Weather Rev.* **2000**, *128*, 1632–1652. [CrossRef]
18. Samelson, R.M.; Barbour, P.; Barth, J.; Bielli, S.; Boyd, T.; Chelton, D.; Kosro, P.; Levine, M.; Skyllingstad, E.; Wilczak, J. Wind stress forcing of the Oregon coastal ocean during the 1999 upwelling season. *J. Geophys. Res.* **2002**, *107*. [CrossRef]
19. Koracin, D.; Dorman, C.E.; Dever, E.P. Coastal perturbations of marine layer winds, wind stress, and wind stress curl along California and Baja California in June 1999. *J. Phys. Ocean* **2004**, *34*, 1152–1173. [CrossRef]
20. Peng, S.; Li, Y.; Xie, L. Adjusting the Wind Stress Drag Coefficient in Storm Surge Forecasting Using an Adjoint Technique. *J. Atmos. Ocean Technol.* **2015**, *30*, 590–608. [CrossRef]
21. Bi, X.; Gao, Z.; Liu, Y.; Liu, F.; Song, Q.; Huang, J.; Huang, H.; Mao, W.; Liu, C. Observed drag coefficients in high winds in the near offshore of the South China Sea. *J. Geophys. Res. Atmos.* **2015**. [CrossRef]

Simplified formulae for designing coastal forest against tsunami run-up: one-dimensional approach

Nguyen Ba Thuy, N. A. K. Nandasena, Vu Hai Dang & Norio Tanaka

Natural Hazards
Journal of the International Society for the Prevention and Mitigation of Natural Hazards

ISSN 0921-030X
Volume 92
Number 1

Nat Hazards (2018) 92:327-346
DOI 10.1007/s11069-018-3197-z

Springer

Nat Hazards (2018) 92:327–346
https://doi.org/10.1007/s11069-018-3197-z

ORIGINAL PAPER

Simplified formulae for designing coastal forest against tsunami run-up: one-dimensional approach

Nguyen Ba Thuy[1] · N. A. K. Nandasena[2] · Vu Hai Dang[3] · Norio Tanaka[4]

Received: 25 April 2015 / Accepted: 1 February 2018 / Published online: 8 February 2018

Abstract In the present study, laboratory experiments were conducted to validate the applicability of a numerical model based on one-dimensional nonlinear long-wave equations. The model includes drag and inertia resistance of trees to tsunami flow and porosity between trees and a simplified forest in a wave channel. It was confirmed that the water surface elevation and flow velocity by the numerical simulations agree well with the experimental results for various forest conditions of width and tree density. Further, the numerical model was applied to prototype conditions of a coastal forest of *Pandanus odoratissimus* to investigate the effects of forest conditions (width and tree density) and incident tsunami conditions (period and height) on run-up height and potential tsunami force. The modeling results were represented in curve-fit equations with the aim of providing simplified formulae for designing coastal forest against tsunamis. The run-up height and potential tsunami forces calculated by the curve-fit formulae and the numerical model agreed within ± 10% error.

Keywords Tsunami run-up · Coastal forest · *Pandanus odoratissimus* · Tsunami force

✉ Nguyen Ba Thuy
thuybanguyen@gmail.com

1 Vietnam National Hydrometeorological Forecasting Center, No 8 Phao Dai Lang, Dong Da, Hanoi, Vietnam

2 Department of Civil and Environmental Engineering, Faculty of Engineering, University of Auckland, Private Bag 92019, Auckland 1142, New Zealand

3 Institute of Marine Geophysics and Geology, 18 Hoang Quoc Viet, Cau Giay, Hanoi, Vietnam

4 Graduate School of Science and Engineering, Saitama University, 255 Shimo-okubo, Sakura-ku, Saitama 338-8570, Japan

1 Introduction

After the Indian Ocean tsunami in 2004, a number of studies have explained effects of coastal forests in reducing the tsunami run-up and the damage to humans and property based on post-tsunami surveys (for example, Danielsen et al. 2005; Kathiresan and Rajendran 2005; Tanaka et al. 2007). Nandasena et al. (2012) reported that coastal forests consisting of pine trees on the northeast coast of Japan played an important role not only to reduce in tsunami energy but also to trap solid objects like concrete slabs detached from sea walls, and boats from marinas during the 2011 Great East Japan (Tohoku-Oki) tsunami. They investigated hypothetical arrangements of coastal forests with other mitigating methods for tsunami energy reduction in advanced numerical modeling. Currently, coastal forests are increasingly considered to be an effective measure to mitigate tsunami damage from both economic and environmental points of view, despite there is still debating on its effective role due to the absence of adequate studies (Kerr and Baird 2007). In fact, several projects to plant vegetation on coasts as a bio-shield against tsunamis have been started in South and Southeast Asian countries (Tanaka et al. 2009; Tanaka 2009).

The reduction of tsunami damage behind a coastal forest depends on the vegetation species and their properties (tree height, diameter, density, and vertical configuration), extent (along-shore length and cross-shore) and arrangement of forest (uniform or staggered), local tsunami conditions (flow depth and flow velocity) and local topography (Nandasena et al. 2008; Tanaka et al. 2009). Related to the forest arrangement, Mascarenhas and Jayakumar (2008) pointed out that roads perpendicular to beaches in a coastal forest served as a passage for the tsunami to travel inland for example in many places in Tamil Nadu, India, during the of 2004 Indian Ocean tsunami. Nandasena et al. (2012) also pointed out the difference between straight and crooked roads in coastal forests, perpendicular to the beach, in terms of tsunami energy reduction in numerical modeling for the case of the 2011 Great East Japan tsunami. In their simulation, the maximum flow velocity was increased 1.37 and 1.79 times behind the straight road when the tsunami moved inland and the tsunami moved seaward, respectively, compared to that of the bare land. However, the flow velocity did not increase through the crooked road, and the maximum flow velocity behind it was roughly equal to that of the bare land (Nandasena et al. 2012).

Tanaka et al. (2007) pointed out that *Pandanus odoratissimus* is especially effective in providing protection from tsunami damage due to its density and complex aerial root structure, but its strength is not so strong above the exposed root system and hence it has a risk of breaking due to the action of high tsunamis. In previous studies by numerical simulations, however, tsunami forces acting on each tree are not discussed. The tsunami forces are directly related on the damage of the trees. Therefore, when designing a coastal forest to reduce tsunami energy, the magnitude of the tsunami force on trees becomes a key parameter to be considered. Advanced numerical models may calculate these forces, with some assumptions. However, these numerical models are not readily available for stake holders.

In this paper, therefore, we introduce simple formulae derived from advanced one-dimensional numerical modeling to calculate tsunami force on forests and reduction in run-up due to forests on uniform slopes for different tsunami conditions. The numerical model is based on a one-dimensional nonlinear long-wave equations (Nandasena et al. 2008). Laboratory experiments on long-period sinusoidal waves around a simplified forest model with various width and tree density were conducted in a wave channel in order to validate the applicability of the numerical model. Then, the model was applied to a coastal forest of *P. odoratissimus* with effects of forest conditions (width and tree density) and incident tsunami conditions (height and period) to discuss the tsunami force and reduction in run-up on a typical ground slope. Finally, simple equations were proposed based on the modeling results to predict tsunami run-up reduction due to coastal forest, forces on the trees and forces behind the forest. An application of these simple equations in a real case is also presented.

2 Mathematical model and numerical method

2.1 Governing equations

The governing equations are modified one-dimensional nonlinear long-wave equations that include drag and inertia forces due to interaction with trees, and porosity between trees (Nandasena et al. 2008). The continuity and the momentum equations are, respectively:

$$\theta_{\mathrm{d}}\frac{\partial \zeta}{\partial t}+\frac{\partial Q_x}{\partial x}=0 \tag{1}$$

$$\theta_{\mathrm{d}}\frac{\partial Q_x}{\partial t}+\frac{\partial\left(\frac{Q_x^2}{d}\right)}{\partial x}+\theta_{\mathrm{d}}gd\frac{\partial d}{\partial x}+\theta_{\mathrm{d}}^{3/2}gd\frac{\partial z}{\partial x}+\theta_{\mathrm{b}}\sqrt{\theta_{\mathrm{d}}}\frac{\tau_x}{\rho}+\frac{\theta_{\mathrm{d}}^{3/2}}{\rho}\sum_{i=1}^{k}f_{xi}=0 \tag{2}$$

where Q_x is the discharge, ζ the water surface elevation measured from a datum, d the water depth, z the bed elevation measured from the datum, τ_x the bed resistance (given by Manning's equation), $\sum_{i=1}^{k} f_{xi}$ the total resistance on fluid generated by trees, g the gravitational acceleration, ρ the density of sea water, θ_{d} the depth-averaged porosity between trees at water depth d, θ_{b} the bed porosity between trees. Total resistance by trees is assumed to be equal to sum of the drag and inertia forces as follows (For more details, refer to Nandasena et al. 2008)

$$F_D=\gamma\frac{1}{2}C_{\text{D-all}}b_{\mathrm{ref}}d\frac{Q_x^2}{d^2\theta_{\mathrm{d}}} \tag{3}$$

$$F_I=\gamma\rho C_{\mathrm{M}}\forall\frac{D\left(Q_x/d\sqrt{\theta_{\mathrm{d}}}\right)}{Dt} \tag{4}$$

where γ is the tree density (number of trees/m^2), C_{M} the inertia coefficient (= 2.0) (Imamura et al. 2008; Nandasena et al. 2008), and $C_{\text{D-all}}$ the depth-averaged equivalent drag coefficient considering the vertical stand structure of tree, which was defined by Tanaka et al. (2007) as:

$$C_{\text{D-all}}(d)=C_{\text{D-ref}}\frac{1}{d}\int_0^d \alpha(z_{\mathrm{G}})\beta(z_{\mathrm{G}})\mathrm{d}z_{\mathrm{G}} \tag{5}$$

$$\alpha(z_{\mathrm{G}})=\frac{b(z_{\mathrm{G}})}{b_{\mathrm{ref}}} \tag{6}$$